

An Experimental Investigation of Damage Detection of CFRP Using an Electrical Re- sistance Change Method



The
University
Of
Sheffield.

By

AHMED SHIHAB AHMED AL-SAAD I

**A THESIS PRESENTED FOR THE DEGREE OF
DOCTOR OF PHILOSOPHY**

IN THE

**COMPOSITE SYSTEM INNOVATION CENTRE
DEPARTMENT OF MATERIALS SCIENCE AND ENGINEERING**

DECEMBER 2018

ACKNOWLEDGEMENTS

ACKNOWLEDGEMENTS

First I would like to thank Dr. Simon Hayes, and Dr. Jose Luis Sosa for their supervision over my PhD.

I would like to express my sincere gratitude for Dr. James Meredith for his assistance with materials and tools and for all his valuable advice. I would like to thank Mr. Paul Roger for his contributions. I would like to thank all the people who critically contributed to my research.

I would like to express my love and gratitude and give a special appreciation to my mother, my sisters and my brothers for being there for me and for their support for what has been a challenging few years.

I would like to thank Professor Constantinos Soutis and Professor Russell J. Hand for my viva and for their valuable comments.

In conclusion I would like to acknowledge the financial contribution of the Higher Committee for Education Development in Iraq (HCED) for making this work possible.

ABSTRACT

The increasing demands on lightweight materials in the aerospace industry led to expansion in the use of carbon fibre composite laminates. Carbon fibre composite laminates have attracted the aerospace industry due to their high specific properties. While carbon fibre composite laminates have shown excellent resilience for most types of loads, it can be vulnerable to impact events. This in turn led designers to increase safety factors for carbon fibre composite laminates. This increases the costs of adopting components made of carbon fibre composite laminates. The need for unconventional carbon fibre composite laminates has emerged to improve the reliability and safety of carbon fibre composite laminates components and decrease the costs. This thesis presents the results of the development of electrical self – sensing carbon fibre composite laminate panels which can detect, locate and quantify damage due to impact events. The main aims are boosting the reliability, decreasing the costs of composite components by decreasing safety factors and reducing unnecessary inspection costs and unscheduled maintenance.

The current electrical sensing system uses a four – probe electrical resistance method, where the electrical current was injected into the carbon fibre composite laminate panels through two electrodes (outer electrodes) and the voltage was measured between inner electrodes (sensing electrodes). The sensing system was tested on two types of woven fabric carbon fibre reinforced – epoxy composite laminate panels. These panels were fabricated using the autoclave processing and vacuum assisted resin transfer moulding techniques. The electrical sensing system uses two sensing mats that are sensing mat 1 and sensing mat 2, the main difference between them being the size of the electrodes and the distance between the electrodes. Electrical contact between the sensing mats and the carbon fibre composite laminate panels was made using a Silver – Epoxy conductive adhesive, where the sensing mats attached to the bottom surface of the panels.

To investigate the damage sensitivity of the sensing system for carbon fibre composite laminate panels fabricated by both the autoclave processing and the vacuum assisted resin transfer moulding technique, the panels with various thicknesses from 0.84 – 3.5 mm, were impacted at 0.409 – 10 J to generate barely visible impact damage, the impact energy required was estimated so as to cause barely visible impact damage.

It was found that due to occurrence of damage the electrical resistance changed, the degree of the electrical resistance change depends on the damage size and type. C – scan, optical and fluorescent microscopic images were adopted to identify the damage type, damage size, and damage extent and to validate discussions. Further calculations to estimate energy required to cause fibre breakage were conducted using data obtained from standard tensile and flexural tests. It was found that the sensitivity of the current sensing system decreases when the panel thickness increases, and this imposed a new challenge on the current sensing system. With the help of C – scan data a relationship between change in electrical resistance and the damage area was found and an inverse analysis was undertaken, where the size of damage was predicted from changes in electrical resistance. The sensing system demonstrated its capabilities in detecting, locating and quantifying damage in woven fabric carbon fibre reinforced – epoxy composite laminates panels. The current sensing system can also monitor changes in the electrical resistance due to deflection, however the electrical resistance changes were reversible.

PUBLICATIONS

PUBLICATIONS

- A. Alsaadi, S. A. Hayes (2016) “*Electrical Self-Sensing of Damage within Composite Structures*” conference proceeding paper, 17th European Conference on Composite Materials, Munich, Germany, June 2016.
- A. Alsaadi, J. Meredith, T. Swait, J. L. Curiel - Sosa S. A. Hayes (2018) “*Damage Identification in Carbon Fibre Reinforced Polymer Plates Using Electrical Resistance Technique*” submitted to Composite Structures, Elsevier.
- A. Alsaadi, J. Meredith, S. Hayes, J. L. Curiel-Sosa (2018) “*An Electrical Resistance-Based Structural Health Monitoring System for CFRP Laminates*” Manuscript submitted to IEEE Sensors Journal.

SYMPOSIUM

- Materials Science and Engineering Department, the University of Sheffield – Smart Materials, Sep 2016

TALKS

- Materials Science and Engineering Department, the University of Sheffield, Self – healing and Self – sensing carbon fibre composite laminates. Jun 2015
- 17th European Conference on Composite Materials (ECCM17) – Electrical self-sensing of damage within composite structures. Jun 2016

NOMENCLATURE

Acronyms

Alternative current (AC)

Analogue to digital converter (ADC)

Autoclave processing panel that is made of four plies (AB)

Autoclave processing panel that is made of eight plies (AC)

Autoclave processing panel that is made of twelve plies (AD)

Autoclave processing panel that is made of sixteen plies (AE)

Barely visible impact damage (BVID)

Bisphenol A Epichlorohydrin (DGEBA)

Catalytic chemical vapour deposition (CCVD)

Carbon fibre composite laminate (CFRP)

Contrary (contra)

Complementary (comp)

Data acquisition system (DAQ)

Degree of cure (DOC)

Direct current (DC)

Differential scanning calorimetry (DSC)

Digital signal processor (DSP)

Extrinsic Fabry – Perot interferometric (EFPI)

Extruded polyacrylonitrile (ex – PAN)

Flexible circuit board (FCB)

Fibre Bragg grating (FBG)

Grip at grip top (GAT)

Lateral gage various (LGV)

Lateral gage middle (LGM)

Lateral gage middle (LGM)

Lateral gage middle (LGM)

Tension and compression at the loading nose top and bottom (TAB) (CAT)

Tension at the loading nose bottom (TAB)

Ultimate tensile strength (UTS)

Ultraviolet (UV)

Vacuum assisted resin transfer moulding processed panel that is made of four plies (VB)
 Vacuum assisted resin transfer moulding processed panel that is made of eight plies (VC)
 Hydroxyl compound (MOH)
 Kinetic energy (KE)
 Non – destructive test (NDT)
 Non – destructive evaluation (NDE)
 Out of autoclave (OoA)
 Polytetrafluoroethylene (PTFE)
 Resin transfer moulding (RTM)
 Revolutions per minute (RPM)
 Silicon carbide (SiC)
 Polyacrylonitrile (PAN)
 Potential Energy (PE)
 Scanning electron microscope (SEM)
 Vacuum assisted resin transfer moulding (VARTM)
 Volatile organic compounds (VOC)

Superscript

° Degrees

Greek symbols

η Electrical resistivity
 η_c Electrical resistivity of composite
 η_f Electrical resistivity of fibre
 η_m Electrical resistivity of matrix
 η_t Through – thickness electrical conductivity
 σ_{11} Normal stress in the fibre direction
 σ_{13} Shear stress in the longitudinal direction
 σ_{22} Normal stress in transverse direction
 σ_{23} Shear stress in the transverse direction
 σ_f Flexural stress
 ε_f Flexural strain
 β_o Heating or cooling rate
 Ψ Universal gas constant
 μ_o Viscosity constant

μ Viscosity
 δ Deflection
 ρ Density of carbon fibre composite laminate
 ρ_{sp} Relative density of carbon fibre composite laminate
 w_p Weight of the pan
 φ_f Fibre content
 φ_r Resin content
 φ_v Void content
 ρ_f Density of the carbon fibre
 ρ_r Density of the resin
 β_1 Regression coefficient
 κ Impact damaged area
 ξ Global electrical resistance

Roman symbols

A cross section area
 a Weight of the specimen in air
 b Weight of the specimen in the water
 C_c Electrical conductance of composite
 C_m Electrical conductance of matrix
 C_f Electrical conductance of fibre
 E Young's modulus
 E Activation energy
 E_p Potential energy
 E_f Flexural Modulus
 V Voltage
 I Current
 m Mass
 g Gravity force
 h Height
 P Load
 J Current density
 R Electrical resistance
 R_o Electrical resistance before impact
 R_i Electrical resistance after impact

w Specimen width

t Thickness

T_g Glass transition temperature

T_o Starting temperature

t Time

L Distance between electrodes

V_f Fibre volume fraction

V_{f_0} Fibre volume fraction at zero compaction pressure

V_{f_∞} Ultimate fibre volume fraction at infinite compaction pressure

w_f Fibre mass

TABLE OF CONTENTS

TABLE OF CONTENTS

ACKNOWLEDGEMENTS	I
ABSTRACT	II
PUBLICATIONS	IV
NOMENCLATURE	V
TABLE OF CONTENTS	IX
LIST OF FIGURES	XIII
LIST OF TABLES	XVII
CHAPTER 1	1
1.1 Aims of the Thesis	3
1.2 Outline	4
CHAPTER 2	7
2.1 Constituents and Manufacture	7
2.1.1 Dry Carbon Fibre	7
2.1.2 Epoxy Resins	8
2.1.3 Pre-impregnated Carbon Fibres (prepreg)	10
2.1.4 Resin Transfer Moulding (RTM)	11
2.1.5 Vacuum Assisted Resin Transfer Moulding (VARTM)	12
2.2 Damage Problems	14
2.2.1 Barely Visible Impact Damage (BVID) Generation	15
2.2.1.1 Impact Parameters	15
2.2.1.2 Carbon Fibre Composite Laminates Parameters	16
2.2.1.3 Selection of impact energies (barely visible impact damage loads)	18
2.3 Structural Response of Carbon Fibre Composite Laminate During the Impact Events (Damage Development)	19
2.3.1 Matrix damage	19
2.3.2 Delamination	19
2.3.3 Fibre damage	21
2.4 Non-Destructive Testing and Smart Sensing	21

2.4.1	Thermography Methods	22
2.4.2	Acoustic Methods	23
2.4.3	Fibre-Optic Methods	24
2.4.4	Electrical Methods	26
2.5	Electrical Conduction of Carbon Fibre Reinforced Polymer	34
2.5.1	Ohm's Law	34
2.5.2	Current Density	35
2.6	Electrical Resistance Sensing Techniques	35
2.6.1	Electrical Sensitivity in CFRP Laminate	35
2.6.2	Two-Probe Sensing Technique	37
2.6.3	Four-Probe Sensing Technique	38
2.6.4	Piezoresistivity in Carbon Fibre	40
2.7	Summary	43
CHAPTER 3		45
3.1	Materials	45
3.1.1	Epoxy Resin Systems	45
3.1.1.1	IN-2 Epoxy Infusion Resin	45
3.1.2	Copper Clad Laminates (Pyralux FR8510R)	49
3.1.3	Carbon Fibres	50
3.1.3.1	Carbon Fibres Tairyfil TC-35	51
3.1.3.2	Carbon Fibres Toray FT300B	51
3.2	Experimental Set ups and Procedures	52
3.2.1	Differential Scanning Calorimetry	52
3.2.1.1	Degree of Cure	52
3.2.1.2	Kinetic Parameters by Differential Scanning Calorimeter Using Isothermal Method	53
3.2.2	Scanning Electron Microscope	54
3.2.2.1	Specimen Preparation	54
3.2.2.2	Scanning Electron Microscope Setup	55
3.2.3	Resistivity Measurement of the Sensing System	55
3.2.3.1	Resistivity test setup	55
CHAPTER 4		57
4.1	Differential Scanning Calorimetry	57
4.1.1	Degree of Cure	57
4.1.2	Kinetic Parameters by Differential Scanning Calorimeter Using Isothermal Method	58
4.2	Scanning Electron Microscope Characterization	59
4.3	Sensing System Resistivity	61
CHAPTER 5		62
5.1	Vacuum Assisted Resin Transfer Moulding	62
5.1.1	Fabricating Process	62

5.2	Autoclave processing	65
5.2.1	Fabricating Process	66
5.3	Producing Sensing Mats	68
5.3.1	Fabricating Procedure	68
5.4	Attaching Sensing Mats to the Carbon Fibres Composite Laminates	72
5.4.1	Attaching Sensing Mats to Carbon Fibre Composite Laminate Panels Using Conductive Epoxy	72
 CHAPTER 6		 76
6.1	Specimens and Experimental Procedures	76
6.1.1	Microscopical Examination of Carbon Fibre Composite Laminate Panels	76
6.1.1.1	Specimen preparation and optical microscope setup	76
6.1.2	Flexural Properties of Carbon Fibre Composite Laminates	78
6.1.2.1	Specimen preparation and test setup	78
6.1.3	Tensile Properties of Carbon Fibre Composite Laminates	80
6.1.3.1	Specimen Preparation and Test Set up	80
6.1.4	Fibres, Resin Volume Fraction and Void Contents	81
6.1.4.1	Samples preparation	82
6.1.4.2	Carbon fibre composite density	82
6.1.4.3	Acid digestion method	83
6.2	Results and Discussions	86
6.2.1	Microscopical Examination of Carbon Fibre Composite Laminate Panels	86
6.2.1.1	Voids, resin rich areas, bundles drops, and number of plies analysis	86
6.2.1.2	Electrical connection analysis	90
6.2.2	Flexural Strength of Carbon Fibre Composite Laminate Panels	94
6.2.3	Tensile Strength of Carbon Fibre Composite Laminate Panels	96
6.2.4	Fibres, Resin Volume Fraction, and Void Contents in Carbon Fibre Composite Laminate Panels	99
 CHAPTER 7		 101
7.1	Damage Generation (Drop – Weight Impact Test)	101
7.2	Damage Detection in Carbon Fibre Composite Laminates	102
7.2.1	Data Acquisition System	102
7.2.2	Through – Thickness Electrical Resistance Measurements and Electrical Conductivity Calculations	104
7.2.3	Surface Electrical Resistance Measurements and Global Electrical Resistance Calculations	106
7.2.4	Electrical Resistance Change Due to Flexural Loads	116
7.2.5	Non-Destructive Testing Technique (C-scan)	117
7.2.5.1	Specimen preparation and C-scan setup	117
7.2.6	Destructive Testing Technique (Fluorescent Microscope Test)	120
7.2.6.1	Sample Preparation and Machine Setup	120
7.3	Results and Discussions	123
7.3.1	Through – Thickness Electrical Resistivity Measurements and Electrical Conductivity Calculations	123
7.3.2	Changes in Electrical Resistance Due to Flexural Loads	125

7.3.3	Damage Detection in Woven Fabric Carbon Fibre Reinforced Composite Laminates	128
7.3.4	Quantification of Damage	144
7.3.5	Damage Location	152
7.3.6	Summary of the Findings	158
CHAPTER 8		160
8.1	Summary and Conclusions	160
8.2	Future work	162
REFERENCES		163
APPENDIX A		177
1.	Tensile Test for Carbon Fibre Composite Laminates Panels	177
2.	Flexural Tests for Carbon Fibre Composite Laminates Panels	180
APPENDIX B		183

LIST OF FIGURES

LIST OF FIGURES

Figure 2-1: Schematic model of PAN-based fibre transverse cross-section [46].	8
Figure 2-2: Synthesising epoxy resin from reacting epichlorohydrin with hydroxyl compounds in the presence of a catalyst.	9
Figure 2-3: Shows the curing stages of an epoxy resin by an amine hardener [53].	10
Figure 2-4: A schematic of typical resin transfer moulding [62].	12
Figure 2-5: An illustration showing a typical setup of VARTM [66].	13
Figure 2-6: The impact damage pattern for [0, 90] composite laminates [1].	18
Figure 2-7: shows the low velocity impact damage pattern for woven fabric carbon fibre composite laminates.	18
Figure 2-8: Schematic of impact test and expecting failure modes, both modes are suspecting to occur at low-velocity impact events [107].	21
Figure 2-9: Schematic shows the sound energy travels through the sample and it is either reflected by the backside of the sample or it is reflected earlier if a flaw or crack was found.	24
Figure 2-10: The mechanisms that could cause fracture in optical fibres [154].	26
Figure 2-11: Schematic shows practical structure of carbon/epoxy composite [188].	36
Figure 2-12: Voltage contour for a cross-ply laminate [33].	37
Figure 2-13: Two-probe electrical resistance technique.	37
Figure 2-14: a. Image showing National Instruments cDAQ 9172 with NI9219 modules, b. Four-probe electrical resistance method where the DAQ system configured.	38
Figure 2-15: a. shows equipotential lines for the configuration b, b. schematic shows the internal current distribution[181].	39
Figure 2-16: Typical curves for ex-PAN carbon fibres showing the resistance changes due to applied strains [42]. ΔR represents the change in electrical resistance due to applied strain and R represent the typical resistance of an unloaded carbon fibre.	41
Figure 2-17: Temperature dependence of the resistivity of ex-PAN [199].	42
Figure 2-18: Schematic variation of room temperature electrical resistivity versus heat treatment temperature [42]. o is ex-rayon, solid o is stretched rayon; Δ and ∇ ex-PAN fibres, \diamond ex-pitch fibres and the solid line is CCVD fibres.	42
Figure 3-1: Prepared sample for SEM examination.	54
Figure 3-2: Photograph showing a representation of the four-probe technique.	56
Figure 3-3: Schematic model of the experimental setup that is used to measure the resistivity for Pyralux FR8510R. The thickness dimensions have been magnified for the purpose of clarifications.	56
Figure 4-1: Curing reaction IN-2 Epoxy infusion resin as function of temperature.	58
Figure 4-2: Curing reaction of VTC401 resin as function of temperature.	58
Figure 4-3: Arrhenius plot that represents the relationship between the heating rate and glass transition temperature for IN-2 Epoxy infusion resin.	59
Figure 4-4: SEM micrographs of carbon fibres showing the surface and transverse cross section of Formosa Tairyfil TC-35. a. shows a low magnification image b. shows a high magnification image where the transverse cross section features appear clearly. Image dimensions is 1024 x 943 pixels.	60
Figure 4-5: SEM micrographs of carbon fibres showing the surface and transverse cross section of Toray FT300B. a. shows a low magnification image 12000x b. shows a high magnification image 20000x where the transverse cross section features appear clearly. Image dimensions is 1024 x 943 pixels.	60
Figure 5-1: A typical schematic diagram shows the setup for a VARTM technique.	63
Figure 5-2: A typical vacuum assisted resin transfer moulding setup.	64
Figure 5-3: Prepreg stacks prepared for autoclave processing.	66
Figure 5-4: Autoclave processing cycle for prepreg VTC 401.	67
Figure 5-5: Sensing mat 1 designed using Photoshop CC 2017.	68
Figure 5-6: Sensing mat 2 designed using Photoshop CC 2017.	69
Figure 5-7: Preparation steps for producing sensing mats that are designed specifically for damage sensing in carbon fibres composite laminates. The image on the right shows the artwork for the	

sensing mat that is going to be printed on the Pyralux FR8510R covered with photosensitive film that is shown in on left image.	69
Figure 5-8: Pyralux FR8510R that was covered with photo-resistive film.	70
Figure 5-9: Steps to produce sensing mats a) sensing mat 1 pattern, b) the sensing mat after exposing to UV light, c) the sensing mat after developing, d) ready to use sensing mat. The total thickness of ready to use sensing mats dimensions is 0.068 μm	71
Figure 5-10: Schematic representing directions of grinding and polishing steps.	73
Figure 5-11: Graphs showing the finish of the same sample before and after abrasion process.	73
Figure 5-12: The panels were enveloped in a vacuum bag and subjected to 1 bar of vacuum pressure.	74
Figure 5-13: Experimental set ups for electrical resistance measurements of a test specimen before being subjected to a low velocity impact test.	75
Figure 6-1: Experimental setup for flexural test according to ASTM D7264/D7264M.	79
Figure 6-2: Flexural loading diagram according to ASTM D7264/D7264M.	79
Figure 6-3: View of tensile test frame, Zwick/Roell Z020.	81
Figure 6-4: Precision balance to measure the density of carbon fibre composite laminates.	82
Figure 6-5: Set up used to measure the constituent content of carbon fibre composite laminate.	84
Figure 6-6: SEM image shows the surface of the carbon fibre and residual resin for Tairyfil TC-35 carbon fibre.	85
Figure 6-7: SEM image shows the surface of the carbon fibre and residual resin for VTC 401 carbon fibre.	85
Figure 6-8: Cross sections of a 2 x 2 mm twill weave CFRP laminates panel, reflected-light bright-field illumination, 5x objective. a) represents 4 plies CFRP laminates b) represents 8 plies CFRP laminates. Samples were made by a vacuum assisted resin transfer moulding technique (VARTM).	87
Figure 6-9: Entrapped air, resin rich areas, bundles termination and number of plies in CFRP laminate panels that were made with 2 x 2 mm twill weave carbon fibres by an autoclave. a) represents 4 plies of prepreg VTC401, b) represents 8 plies of prepreg VTC401, c) represents 12 plies of prepreg VTC401, and d) represents 16 plies of prepreg VTC401. A reflected light bright-field illumination, 5x magnification.	89
Figure 6-10: Cross-section of CFRP laminate panels that were made by a vacuum assisted resin transfer moulding (VARTM), through-thickness electrical conduction due to fibre – fibre contacts are shown in a) 4-ply panel (VB) that was examined using bright-field illumination, 20x objective, and b) 8-ply panel (VC) that was examined using bright-field illumination, 10x objective.	91
Figure 6-11: Cross-section of CFRP laminate panels that were made from prepreg VTC401 by using an autoclave processing technique. The electrical contacts between adjacent plies occurred due to fibre – fibre contacts that can be seen in all images. a) 4-ply panel (AB), b) 8-ply panel (AC), c) 12-ply panel (AD), and d) 16-ply panel (AE). All the panels were examined using bright-field illumination, 10x objective apart from the panel that was showed in a that was examined under 20x objective.	93
Figure 6-12: Three-point flexural test for AB panel, the average $\sigma_f = 790 \text{ MPa}$	94
Figure 6-13: Tensile stress-strain curve for AC panel.	97
Figure 7-1: Schematic diagram of 4-wire resistance circuit.	103
Figure 7-2: Data collection flow chart using NI cDAQ-9127 and NI9219 modules.	104
Figure 7-3: Schematic diagram illustrate through – thickness electrical resistance experimental set ups.	106
Figure 7-4: Electrical resistance measurement map using sensing mat 1 a) electrical resistance along 0° and b) electrical resistance along 90°	107
Figure 7-5: Flexural test and specimen configuration.	116
Figure 7-6: Experimental set-up; 1. Digital camera to monitor the movement of the specimen and record the deflection, 2. DAQ system to measure electrical resistance data from the CFRP laminate, 3. CFRP laminate, 4. Flexural testing rig.	117
Figure 7-7: DolphiCam C08 transducer.	118
Figure 7-8: C – scan, B – scan, and A – scan images for a) damage free CFRP laminates (AE panel) and b) the same panel but impacted at 10 J. In C – scan TOF image in top right corner, the dark blue colour represents the back face of the panel and the light blue colour represents the top surface roughness. B – scan images in the left top corner and bottom middle represent the depth of damage through – thickness. A – scan in the bottom left corner shows reflection of ultrasound wave due to damage.	119
Figure 7-9: Dependence of through – thickness electrical resistivity of CFRP laminate panels on thickness and fibre volume fraction. The electrical resistivity was measured using sensing mat 1.	124

Figure 7-10: Dependence of through – thickness electrical resistivity of CFRP laminate panels on thickness and fibre volume fraction. The electrical resistivity was measured using sensing mat 2.	125
Figure 7-11: Changes in electrical resistance due to deflection at 2, 4, 6, and 8 mm in AC panel. The electrical resistance readings were acquired using sensing mat 1.	126
Figure 7-12: Changes in electrical resistance due to deflection at 2, 4, 6, and 8 mm in VC panel. The electrical resistance readings were acquired using sensing mat 1.	127
Figure 7-13: Changes in electrical resistance due to deflection at 2, 4, 6, and 8 mm in AC panel. The electrical resistance readings were acquired using sensing mat 2.	128
Figure 7-14: Changes in electrical resistance due to deflection at 2, 4, 6, and 8 mm in VC panel. The electrical resistance readings were acquired using sensing mat 2.	128
Figure 7-15: The percentage change in electrical resistance in carbon fibre composite laminate panels due to impact damage using sensing mat 1.	129
Figure 7-16: Impact damage distribution in CFRP laminates panel (AB). The panel was subjected to 0.405 J impact energy using a semi-spherical impactor with a 13 mm diameter head. The damage is a combination of matrix cracks and delamination.	130
Figure 7-17: Impact damage distribution in different CFRP laminates. The panels were subjected to 1.426 J of impact energy using a semi-spherical impactor with a 13 mm diameter head.	134
Figure 7-18: Montage image of impact damage of AB panel. The panel was subjected to drop weight impact at 1.426 Joules. Epi-fluorescence, 390-440 nm excitation, 4x objective.	134
Figure 7-19: Montage image of impact damage of AC panel, the panel was mounted in with EpoDye. Epi-fluorescent, 4x objective. The laminate was subjected to a 1.426 Joules impact energy.	135
Figure 7-20: Impact damage distribution in different CFRP laminates. The panels were subjected to 3.33 J of impact energy using a semi-spherical impactor with a 13 mm diameter head.	137
Figure 7-21: Montage image of impact damage of VB panel, epi-fluorescence, 4x objective. The laminate was subjected to low velocity impact at 3.33 Joules.	138
Figure 7-22: Montage image of impact damage of AC panel, epi-fluorescence, 4x objective. The laminate was subjected to low velocity impact at 3.33 Joules.	138
Figure 7-23: Montage image of impact damage of VC panel, epi-fluorescence, 4x objective. The laminate was subjected to low velocity impact at 3.33 Joules.	138
Figure 7-24: Impact damage distribution in CFRP laminates panels (AB, VB, AC, VC, AD and AE). The panels were subjected to 4.96 J impact energy using a semi-spherical impactor with a 13 mm diameter head.	141
Figure 7-25: Montage image of impact damage of AC panel, epi-fluorescence, 4x objective. The laminate was subjected to low velocity impact at 4.96 Joules.	142
Figure 7-26: Montage image of impact damage of VC panel, epi-fluorescence, 4x objective. The laminate was subjected to low velocity impact at 4.96 Joules.	142
Figure 7-27: Impact damage distribution in CFRP laminates panels (AD and AE). The panels were subjected to 9.96 J impact energy using a semi-spherical impactor with a 13 mm diameter head.	143
Figure 7-28: The percentage changes in electrical resistance in CFRP laminate panels due to impact damage using sensing mat 2.	144
Figure 7-29: Illustration of damage identification and quantification using the electrical resistance change method. The figure illustrates the bottom face of a CFRP laminate panel where sensing mat 2 was attached. The panel was subjected to impact energy on the upper face of the composite panel.	146
Figure 7-30: Relationships between the damaged areas and the percentage in electrical resistance changes for AB panel using both sensing mats. 0.607 J impact energy was excluded from the graph to be used for inverse analysis later in this section.	148
Figure 7-31: Relationships between the damaged areas and the percentage in electrical resistance change for VB panel using both sensing mats.	148
Figure 7-32: Relationships between the damaged areas and the percentage in electrical resistance change for AC panel using both sensing mats.	149
Figure 7-33: Relationships between the damaged areas and the percentage in electrical resistance change for VC panel using both sensing mats.	149
Figure 7-34: Relationships between the damaged areas and the percentage in electrical resistance change for AD panel using both sensing mats.	150
Figure 7-35: Relationships between the damaged areas and the percentage in electrical resistance change for AE panel using both sensing mats.	150

Figure 7-36: C – scan image for AB panel impacted at 0.607 J.	151
Figure 7-37: Representation of damage identification technique using electrical resistance change method.....	153
Figure 7-38: Damage location in AB panel that was impacted at a) 0.406 J, b) 0.607 J, c) 1.426 J, d) 3.333 J, and e) 4.96 J. The arrows on C – scan image at the top left and right corners represent the current flow direction.	154
Figure 7-39: Damage location in AC panels that were impacted at a) 1.426 J, b) 3.333 J, and c) 4.96 J. The C-scan images at the top left and right corners show the damage profile, the arrows around C-scan images show the current flow direction.	155
Figure 7-40: Damage location in AD panels that were impacted at a) 4.96 J, and b) 9.996 J. The C-scan images at the top left and right corners show the damage profile, the arrows around C-scan images show the current flow direction.	155
Figure 7-41: Damage location in AE panels that were impacted at a) 4.96 J, and b) 9.996 J. The C-scan images at the top left and right corners show the damage profile, the arrows around C-scan images show the current flow direction.	156
Figure 7-42: Damage location in VB panels that were impacted at a) 1.426 J, b) 3.33 J, and c) 4.96 J. The C-scan images at the top left and right corners show the damage profile, the arrows around C-scan images show the current flow direction.	157
Figure 7-43: Damage location in VC panels that were impacted at a) 1.426 J, b) 3.33 J, and c) 4.96 J. The C-scan images at the top left and right corners show the damage profile, the arrows around C-scan images show the current flow direction.	158
Figure A-1: Stress – Strain curve for AB panel, the average UTS = 607.33 MPa and E = 55 GPa. E was calculated at a strain range of 0.002 in the region between 0.002 and 0.004 for specimen 1, 0.004 and 0.006 for specimen 2, and 0.006 and 0.008 for specimen 3.	177
Figure A-2: Stress – Strain curve for AC panel, the average UTS = 620.6 MPa and E = 57.744 GPa. E was calculated at a strain range of 0.002 in the region between 0.002 and 0.004 for all the specimens.	177
Figure A-3: Stress – Strain curve for AD panel, the average UTS = 690 MPa and E = 57.46 GPa. E was calculated at a strain range of 0.002 in the region between 0.0052 and 0.0072 for all the specimens.	178
Figure A-4: Stress – Strain curve for AE panel, the average UTS = 735.5 MPa and E = 57.33 GPa. E was calculated at a strain range of 0.002 in the region between 0.002 and 0.004 for all the specimens.	178
Figure A-5: Stress – Strain curve for VB panel, the average UTS = 419 MPa and E = 53 GPa. E was calculated at a strain range of 0.002 in the region between 0.003 and 0.005 for all specimens.	179
Figure A-6: Stress – Strain curve for VC panel, the average UTS = 450 MPa and E = 55 GPa. E was calculated at a strain range of 0.002 in the region between 0.004 and 0.006 for all the specimens.	179
Figure A-7: Three-point bending test for AB panel. The average σ_f = 790 MPa.	180
Figure A-8: Three-point flexural test for AC panel. The average σ_f = 810 MPa.	180
Figure A-9: Three-point flexural test for AD panel. The average σ_f = 870 MPa.	181
Figure A-10: Three-point flexural test for AE panel. The average σ_f = 890 MPa.	181
Figure A-11: Three-point flexural test for VB panel. The average σ_f = 610 MPa.	182
Figure A-12: Three-point flexural test for VC panel. The average σ_f = 690 MPa.	182
Figure B-1:Electrical sensing code that was used to acquire the data from DAQ system.	183

LIST OF TABLES

LIST OF TABLES

Table 2-1: Most important parameters that determine the effectiveness of self – sensing electrical resistance system in carbon fibre composite laminates.	30
Table 3-1: Ingredient percentages of IN-2 Epoxy infusion resin.....	45
Table 3-2: Ingredient percentages of AT30 Epoxy Hardener-Slow	46
Table 3-3: curing schedules for the epoxy resin system	48
Table 3-4: Physical properties of uncured IN-2 Epoxy resin and AT30 hardener as provided by the supplier.	48
Table 3-5: Physical and mechanical properties of the cured resin at 25°C as provided by the manufacturer.	48
Table 3-6: The physical and the mechanical properties of Tariyfil TC-35 as provided by the supplier.....	51
Table 3-7: Physical and mechanical properties of FT300B as provided by the supplier	51
Table 5-1: The curing schedules for the epoxy resin system.	65
Table 5-2: Pyralux FR8510R, Coverlay FR0110 and Dry film dimensions corresponding to sensing mat sizes.....	70
Table 6-1: The primary abrading stage	78
Table 6-2: The secondary abrading stage	78
Table 6-3: The polishing stage.....	78
Table 6-4: Flexural fracture shapes and failure identification codes according to ASTM D7264/D7264M.	94
Table 6-5: Flexural properties of CFRP laminates considered in the experiments.....	96
Table 6-6: Tensile fracture shape and fracture codes according to ASTM 3039/3039M for all panels used in this work.	97
Table 6-7: Tensile properties of carbon fibre composite laminates panel used in this work.	98
Table 6-8: The fibres, resin, voids contents volume fraction for carbon fibres composite laminates panels.	99
Table 7-1: Experimental data of low velocity impact tests.....	102
Table 7-2: Electrical resistance changes due to impact events measured using both sensing mat 1 and mat 2.	109
Table 7-3: Grinding and polishing stages for CFRP laminates for fluorescence microscopy.....	121
Table 7-4: Through – thickness electrical resistivity and electrical conductivity of composites at various carbon fibre volume fractions.	123
Table 7-5: The impact energies required for fibre failure due to back surface flexure.	135
Table 7-6: Damaged areas due to various impact energies for CFRP laminate panels used in this thesis, measured by C - scan.....	145

Chapter 1

INTRODUCTION

Composite materials may be the most advanced materials in 21st century since they allows the engineers to not only designing a structure, but also designing the composite material itself [1]. These materials have gained their importance from a wide range of applications and they have showed indications for wider potential future uses. In the last few decades, an enormous amount of studies have been undertaken, which has led to understanding and greater utilization of composite materials. The drop in prices of commodities due to technological advancements, and the advancements in composite materials manufacturing techniques have helped to expand their uses [2, 3]. Most present commercial production techniques for both composite constituents, i.e. reinforcing elements and matrices, and composite end user products are subjected to competition with conventional materials such as metallic alloys and ceramics. Thereby, the economic importance of composite materials has grown sharply due to their increased demands [4, 5]. The assets that composite materials offer such as corrosion resistance, workability and tailorability outweigh their counterparts (i.e. metals and ceramics). Composite materials have been used in many engineering applications such as civil infrastructure, automotive, technology, medical, and aerospace industries [6-11]. In civil engineering, the maintenance of deteriorated, repair, damaged and substandard civil infrastructure have become a major issue for civil engineers worldwide [12]. Continuous carbon fibres are used to improve the shear strength of structural components (i.e. beams), and chopped carbon fibres are used to improve the mortar strength and reduce crack initiation and propagation [12]. In addition, composite materials have been used as a filler to reduce the cost of construction materials products such as epoxy mortars.

The transportation industry is characterised by high demands on high performance components, coupled with high service demands, as well as a high safety concern, therefore composite materials are expected to play major roles in this industry by applying specific composite materials for engines, gearboxes, chassis, aerodynamics, and suspensions. It is found that composite materials reduce fuel consumption [13], and this can have positive impacts economically and environmentally. Factors such as strength-to-weight ratio, stiffness-to-weight ratio, scalability, workability and applicability of composite materials have contributed to expand their uses. For example, composite materials have been used extensively in military transportation applications such as armoured vehicles and tanks. In addition, composite materials have been used for cosmetic purposes in the automotive industry [14-17].

Carbon fibre composite materials are deployed increasingly in aeronautical structures [18]. Laminated carbon-fibre composite materials have been used particularly in satellites, helicopters, and civil and military aircrafts. These laminated composite materials consist of at least two layers that are bonded together. Lamination is used to combine the best aspects of the constituents and bonding materials promoted by lamination are strength, stiffness, low weight, corrosion resistance, wear resistance, thermal insulation, acoustical insulation [9, 19].

However, laminated carbon fibre composite materials are susceptible to different types of damage under different types of loads [20]. Interlaminar cracks, intralaminar cracking and crack-like defects are probably the most common types of damage in composite materials [21]. Due to the nature of the laminated composite materials, these types of damage can be initiated under low amounts of loads. Thereby, the need to develop new composite systems is vital for further use of composite materials. As a result, many techniques are under development to detect and quantify different types of damage in carbon fibre reinforced polymer (CFRP) laminates.

Smart sensing composite systems are essential for economic applications of composite components as they reduce the costs of maintenance, turnaround time and safety factors. This is important because the maintenance costs is the third largest expense after the labour and fuel [22]. In addition, the smart sensing composite systems are experiencing a growing interest from different communities [23], in particular, the aerospace industry where high operational safety factors, minimisation of downtimes, and reduction of structural inspection costs are required. For large composite structures, knowing the damage location and severity are desirable. To determine the locations and the dimensions of damage in such complex structures, a reliable testing system needs to be used. Different types of damage, such as delamination, matrix cracking and fibre breakage can be detected using different sensing techniques, for instance fibre optics, acoustics, thermography or electrical techniques. These techniques are essential in improving the reliability, robustness and reducing the cost of using composite materials [24]. Many applications have deployed self-sensing techniques in practice such as remote monitoring of post-seismic building for safety where optical fibres were used [25]. Further details will be discussed in the literature review in Chapter 2.

Sensing techniques may differ in terms of expenses, levels of instrumentation, accuracy and robustness required. Many sensing techniques are in development to replace partially or completely non-destructive evaluation (NDE) techniques [26-29]. The later ones are expensive and problematic or not possible to deploy for real time monitoring. Non-destructive testing methods such as X-radiographic inspections, optical and fluorescent microscopy, acoustic emissions and ultrasonic testing have been used successfully to obtain qualitative data for the determination of a damage size and location [27, 30]. However, the quantitative characterizations are not

straight forward. The main obstacle to expanding the use of the composite material systems is that there is no such a monitoring system which is able to provide information about structural health status quickly and in a form easy to interpret by the inspectors of the structures.

The electrical resistance monitoring technique has been studied to monitor strain and identify damage in carbon fibre composites [31, 32]. The electrical resistance change technique has outweighed other methods as it employs the carbon fibre itself as a sensor to measure the changes in electrical resistances and consequently detects damage. Fundamentally, a two-probe method and a four-probe method are often used in electrical resistance measurements for self-sensing in CFRP. The two-probe method means that electrodes introduce an electrical current as well as measuring voltage, this method is simple and convenient, but it is sensitive to the quality of electrical contacts [33, 34]. The four-probe method injects an electrical current through two electrical contacts (normally outer electrodes) on the specimen and measures voltage between two different electrodes. This method is more sensitive, accurate and more precise than the two-probe method in sensing impact damage and fatigue in CFRPs, it can also present to measure subsurface behaviour [35].

Impact energies introduce different types of damage in CFRP laminates [36]. The types of damage depend on the amount of the impact energy, the type of carbon fibre, the thickness of the panel and the stacking sequence. Different types of damage can be observed in CFRP laminates, that are matrix cracking, fibre breakage and delamination. Matrix cracking happens in low impact energies (low velocity impact) and it triggers the delamination [37]. The matrix cracking causes a small but detectable change in electrical resistance and so does delamination. However, fibre breakage occurs at high impact energies and causes a significant increase in the electrical resistance [38]. In the electrical resistance technique, the carbon fibre works as a sensor, and that has made this technique extremely attractive.

1.1 Aims of the Thesis

The aim of this work is to demonstrate the applicability of the four-probe electrical resistance technique in detecting barely visible impact damage in woven fabric reinforced carbon fibre/epoxy composite panels that are fabricated by the vacuum assisted resin transfer moulding (VARTM) and the autoclave processing techniques. All aspects pertinent from examining the constituents of the carbon fibre/epoxy composite laminates to produce carbon fibre/epoxy composite panels will be described in the first instance. The suitability of the sensing technique

as an economically viable replacement for conventional non-destructive testing techniques will be investigated.

1.2 Outline

This thesis is structured in the following manner:

Chapter 2: literature Review

This chapter gives a brief introduction on carbon fibre composite laminates in terms of their constituents and fabrication procedures. This chapter also presents the damage problems in carbon fibre composite laminates with emphasis on barely visible impact damage (BVID). Then it describes the structural response of carbon fibre composite laminates for impact events. Smart sensing techniques are reviewed throughout this chapter. Details of the electrical smart sensing techniques and the electrical conduction in carbon fibre composite laminates are provided.

Error! Reference source not found.: Methodology

This chapter presents materials considered for use in this work, and techniques carried out to characterize the materials. Sample preparation along with standard testing methods, machines and tools used in this project are described.

Error! Reference source not found.Chapter 4: Results of Characterization Procedures for Raw Materials

This chapter presents and discusses the results for the experiments of the raw materials. It discusses the results of differential scanning calorimetry (DSC) to measure the degree of cure and the activation energy. Scanning Electron Microscope (SEM) images for carbon fibre filaments are presented and discussed. This chapter ends with discussion of the results of the sensing system resistivity.

Chapter 5: Producing Composite Panels

The first section of this chapter describes the vacuum assisted resin transfer moulding technique that was used to fabricate the CFRP panels. The second section presents in detail the

manufacturing of CFRP panels using the autoclave processing technique. The third section details the manufacturing process for sensing mats. The last section shows how self – sensing CFRP panels were produced.

Chapter 6: Examination of Composite Panels

This chapter aims to address most important characteristics that affect the electrical conduction in CFRP laminate panels. The first section of this chapter addresses the most critical aspects that have a significant effect on the surface, through – thickness, and volume electrical conduction of the CFRP laminate panels. Details of the experimental set ups are described. The second section of this chapter presents the results and discussions and provides a platform for further discussion in Chapter 7.

Chapter 7: Damage Generation and Damage Detection in Composite Panels

This chapter has three sections; the first section details the generation of barely visible impact damage in the CFRP laminate panels. The second section describes the use of a surface electrical resistance method to detect, quantify, and locate damage. In this section as well, a through – thickness electrical resistivity and electrical conductivity and surface electrical resistance are measured and described in this chapter to support the discussions. The last section presents results and discussions where parameters that effect the electrical resistance sensing technique, are plotted against the change in electrical resistance and a conclusion is drawn.

Chapter 8: Conclusion and Future Work

This chapter summarises the most important findings of this work as well as the contribution to the knowledge and presents ideas for future work.

Chapter 2

LITERATURE REVIEW

This chapter introduces carbon fibre composite laminates as a function of their constituents, which are a reinforcing element and a matrix. It provides details about different manufacturing techniques that are being used to fabricate carbon fibre composite laminates. This chapter also addresses the most common damage problems that may occur in carbon fibre composite laminates and presents a detailed review about non-destructive testing and smart sensing: optical methods, tomography, acoustic methods and electrical methods. The smart materials section is particularly focused on the electrical methods, which make up the subject of the rest of the thesis. Details of most important aspects that govern the electrical methods such as types of carbon fibres, laminate thicknesses, and types of electrical contacts are provided. The electrical conduction principles in carbon fibres are mentioned briefly in this chapter, alongside piezoresistivity of carbon fibres and electrical conduction mechanisms in carbon fibre composite laminates. The electrical resistance sensing technique is highlighted in the last section of this chapter, as it is the means that is used to detect damage in this work.

2.1 Constituents and Manufacture

2.1.1 Dry Carbon Fibre

Carbon fibre holds a unique place in modern industries as it is a possible solution when fuel consumption optimisation and light weight structures are required [13]. Products made of carbon fibres are considered as life time products since they have a high fatigue life [39, 40]. This property along with other key properties, such as light weight, high strength and high stiffness have encouraged industries, such as aviation, automotive and renewable energy industries to adopt composites in their products. That in turn has expanded the market share for the composite industry [41].

Carbon fibres can be classified depending on a precursor (the starting polymer) and a manufacturing technique. For instance, carbon fibres can be produced by extruding an organic precursor, such as polyacrylonitrile (ex – PAN), pitch (ex – pitch) and rayon, through a nozzle into continuous filaments, followed by graphitization at temperatures up to 3500°C to convert polymer chains to graphite sheets. There are other four techniques for producing carbon fibres that are catalytic chemical vapour deposition (CCVD), carbon coated filaments, filaments produced from

carbon arcs, and ion bombardments [42, 43], all of which produce graphite sheets with no need for a further heat treatment.

The present work focuses on aerospace applications for CFRP where continuous carbon fibres with low modulus (200 – 300 GPa) and high strength (5.8 GPa) are required, as a result, PAN-based carbon fibres were chosen. For the time being the predominant raw material for carbon fibres in the market is Polyacrylonitrile. Polyacrylonitrile is easy to be spun into highly oriented carbon fibres. PAN-based carbon fibres turn out to be more economical due to a low cost precursor and a simple fabrication technique [44]. Polyacrylonitrile (C_3H_3N)_n, which has been used on a commercial scale, is a copolymer [45]. Thus, the carbon fibres are collective of highly ordered and amorphous zones of their precursors as shown in Figure 2-1.

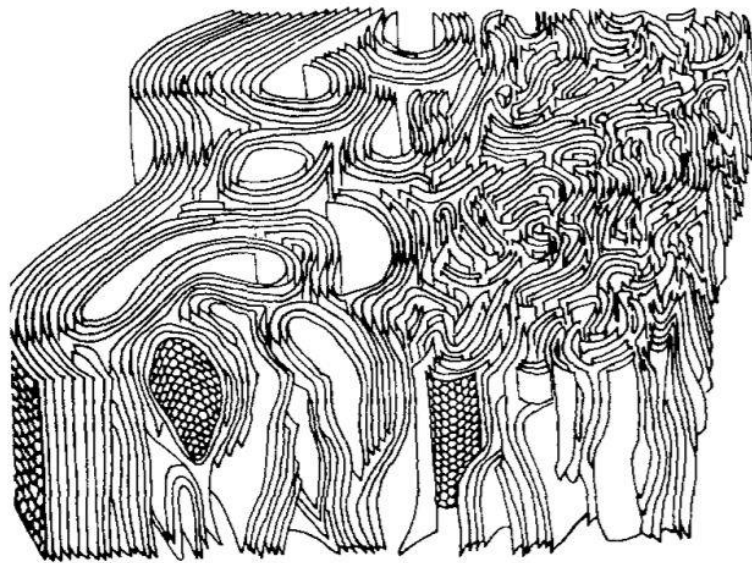


Figure 2-1: Schematic model of PAN-based fibre transverse cross-section [46].

2.1.2 Epoxy Resins

Another element in CFRP laminates is a matrix. In the aerospace industry, matrices used, are mostly epoxy and phenolic resins due to their desirable mechanical properties such as tensile, compression and toughness properties [47]. This is despite that fact that epoxy resins are more expensive than many other resins, but their high glass transition temperature has helped to increase their usage. The relative size of the market for epoxy resins is 12% relative to the overall resins market, but only 7.5% of this amount is used as reinforced resins [48]. The global epoxy market is predicted to reach \$17bn by 2018 [5].

Epoxy resins can be synthesised by many ways that are described in detail in [48, 49]. Reacting a halohydrin with hydroxyl compounds to manufacture epoxy rings are the most important

routes as shown in Figure 2-2. The figure shows epichlorohydrin reacts with hydroxyl compounds like phenols or aliphatic alcohols. MOH may vary, it could be potassium or sodium hydroxide. MOH is important to neutralize a halogen acid that is HCl in this reaction, when the epoxy ring is formed. Therefore, MOH should be used in a stoichiometric concentration. Details about epoxy types used in this work along with their physical and mechanical properties will be presented in Section 3.1.1

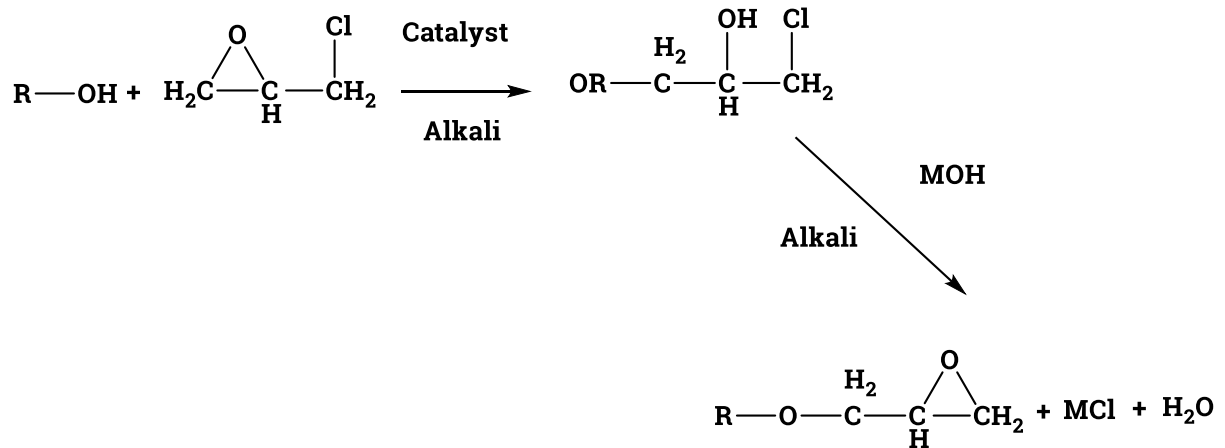


Figure 2-2: Synthesising epoxy resin from reacting epichlorohydrin with hydroxyl compounds in the presence of a catalyst.

Curing agents or hardeners are essential to convert liquid resins to hard and infusible thermoset networks, as they promote cross-linkings of epoxy resins [50]. There are many types of curing agents that are available in the market. The final properties of epoxy resins determine the type curing agent required. Amines are the most popular curing agents that are used with epoxy resins [51]. Amine curing agents are classified according to hydrocarbons involved, they can be aliphatic, alicyclic, and aromatic amines.

Aliphatic amines are used to cure epoxy resins at room temperature, it generates large quantities of heat and it has low usable time [48]. Cured epoxy resins have very good mechanical properties, high bonding properties and heat resistance up 100°C, Figure 2-3. The figure shows that the active hydrogen in primary amine reacts with an epoxy group that lead to form a secondary amine that in turn reacts to with an epoxy group to cure. The last stage is the polymerization process that occurs when a tertiary amine reacts with an epoxy group. The aromatic amines have been developed to achieve high heat resistance and chemical resistance [52]. The curing process initiates at room temperature; however epoxy resins require post curing, the first stage is carried out at 80°C to lessen heat generation then heating to a high temperature 150-170°C.

Autoclave processing is the chosen method to fabricate carbon fibre composite laminates for high performance applications, especially complex structures for the aerospace industry [58]. This manufacturing technique involves cutting thin-layers of prepreg and layering them up in a mould to form the required shape and then the uncured part is placed in a vacuum bag and then the whole component is inserted into an autoclave to be cured at high temperature under high pressure. More details about this technique will be discussed in Section 5.2. On the other hand there are many disadvantages to using the autoclave that are a high turnaround time, high investment cost, the tooling usually costs at least £400k [59], huge footprint, and excessive energy consumption. All those factors combine to become where the driving force to find an alternative curing process for curing parts for low performance industries. To overcome those challenges, many manufacturing techniques were developed with an eye on producing cost effective aerospace parts. These include resin transfer moulding (RTM), vacuum assisted resin transfer moulding (VARTM) and out-of-autoclave processing (OoA) techniques [60, 61].

2.1.4 Resin Transfer Moulding (RTM)

The need for a net shape, repeatability and high volume production in the automotive industries were the impetus to adopt RTM in composite manufacturing in the mid-1980s [60]. The principle is to have a unidirectional or woven fibre preform structures inside a net shaped mould and then the resins pushed inside the mould under a high pressure to bond the fibres together. The mould consists of two parts (male-female). The mould flanges are compressed a sealing tap which seals the mould and prevents resin leaks as shown in Figure 2-4. The resin (the matrix) must have certain properties to be used in RTM, those properties are low viscosity and fast curing resins. RTM depends on the clamping force that is applied on the mould to withstand the resin injection pressure without opening or distorting [60].

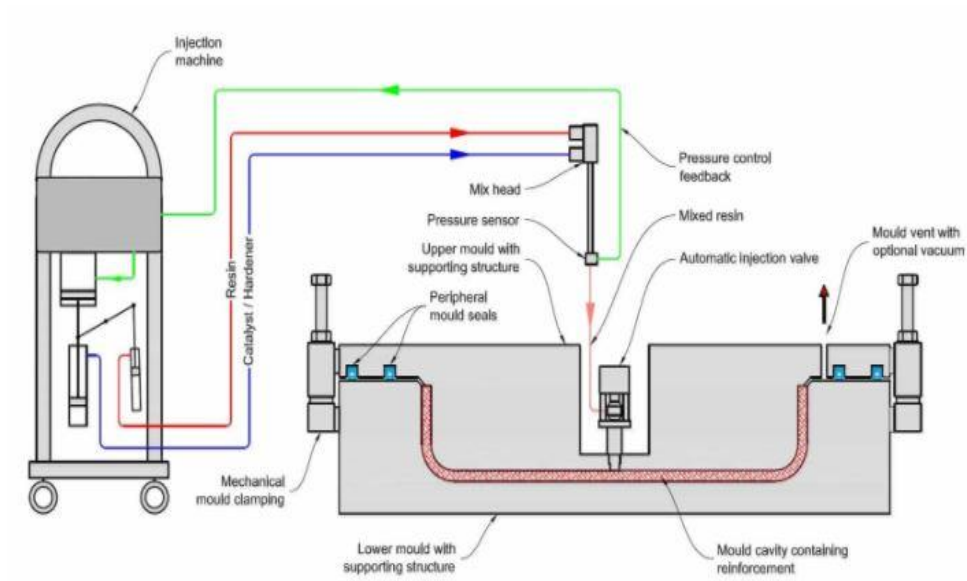


Figure 2-4: A schematic of typical resin transfer moulding [62].

2.1.5 Vacuum Assisted Resin Transfer Moulding (VARTM)

VARTM is a liquid composite moulding (LCM) process that has the ability to produce a large-scale, complex, highly-integrated fibre reinforced polymer used in boat hulls, rotor blades, armoured vehicles and aerospace applications. Also, it has potential to be cost-effective and provides a good work environment [63-65]. VARTM process integrates the advantages of high quality, repeatability and clean handling of the resin transfer moulding (RTM) process with the benefits of flexibility and scalability of open-mould hand layup processing without volatile organic compound (VOC) emission [57]. VARTM utilizes the difference between atmosphere and vacuum pressure to infuse a liquid resin into to a preform while RTM uses positive injection pressure and rigid mould equipment. VARTM is cost effective over a conventional autoclave moulding process, as it uses a simple mould construction and low clamping forces [57]. A typical setup of VARTM is shown in Figure 2-5.

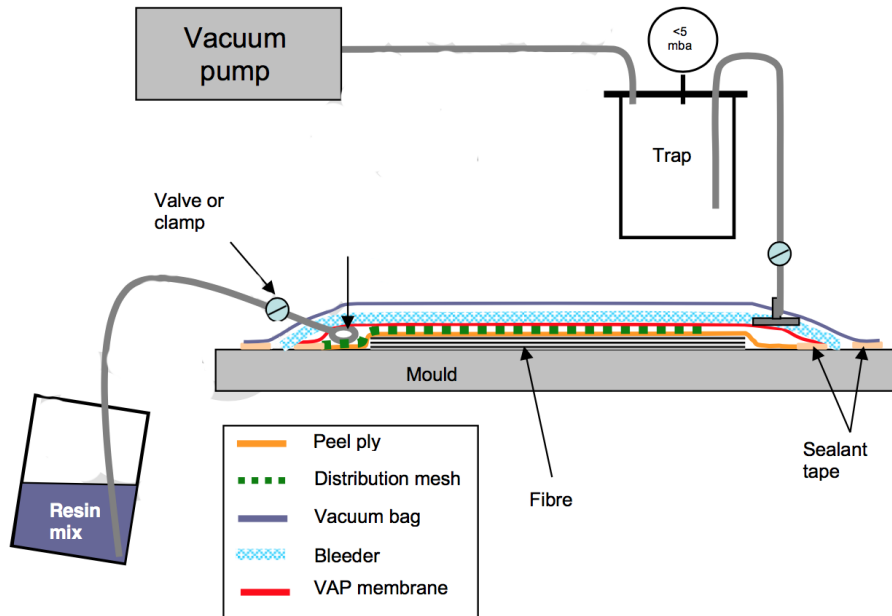


Figure 2-5: An illustration showing a typical setup of VARTM [66].

Figure 2-5 illustrates a dry fibre reinforcement, which is known as a preform, covered by peel ply cloths and resin distribution media. All combinations are placed over a one-side mould then they are enveloped and sealed with a flexible plastic bag and sealing tape. Applying a vacuum pressure through a vent creates negative pressure, which provides a resin driving force. The resin infuses the preform through a spiral tube from an inlet port and is smoothly distributed into the preform. The peel plies are used to peel off the resin distribution media and the vacuum bag after curing, while the main purpose of using resin distribution media is to speed up the resin infusion process [67].

In VARTM, the resin flow should be well controlled to prevent forming defects like dry spot and micro-voids [68]. Dry spots are caused by air entrapment that can occur for many reasons, for instance an improper mould design or the resin infusion process being too slow and the resin becoming viscous before reaching the vent. Other causes are complex shapes, a leakage in the vacuum bag or there is an impermeable insert inside the preform [69]. In terms of complex shapes, it is not easy to flow resin around corners or between joints [70], while the most common reason for dry spot is the leakage in the vacuum bag, that can be due to damage in the vacuum bag, resin supply tubes, connectors or leakage near sealing tapes [57]. Besides dry spots, which is a visible defect, micro-voids can form due to incompatibility in resin flow. The resin flow between tows is governed by Darcy's law while the resin flow inside a tow is governed by capillary effect [71]. Vacuum pressure is another parameter that can affect the micro-void content level [72]. The effect of compaction pressure on fibre volume fractions is given by,

$$P_{\text{comp}} = a \frac{\left(\left(\frac{V_f}{V_{f_0}}\right) - 1\right)}{\left(\left(\frac{1}{V_f}\right) - \left(\frac{1}{V_{f_\infty}}\right)\right)^4} \quad 2-1$$

Where a , V_f , V_{f_0} and V_{f_∞} are the preform constant, fibre volume fraction, fibre volume fraction at zero compaction pressure and the ultimate fibre volume fraction at infinite compaction pressure, respectively [57]. Many ways have been used to monitor and control the flow of resin in VARTM. Some researchers used an electrical current to monitor and control the flow and degree of cure in VARTM [73-75]. Optic fibres were used also to monitor the flow and cure of the resin in VARTM [76], whereas, others use photogrammetry analysis techniques to control resin infusion in the vacuum infusion process [77]. In addition, methods such as dielectric and SMART-weave sensing techniques have been used for the same purpose [78]. The dielectric sensing technique either uses a reusable sensor where it is located on a mould or a vacuum bag or an embedded sensor. The dielectric method is mainly used to measure gelation point and viscosity profile.

The SMARTweave consists of a sensor grid, and software program that collects a real-time data, the sensor grid is laid up in the VARTM and/or RTM mould, and it is used to map the flow of the resin inside the mould. During this study, it has been found that most researchers have focused their work only on monitoring resin flow during the impregnating process in VARTM or RTM, except Lekakou et al. [79] who used optic fibres to monitor a resin flow front and composite curing, in addition using the same sensors to monitor composite damage later on. However, the drawbacks of using optic fibres will be discussed later in Section 2.4.3. For the first time as part of this study, electrical resistance self-sensing composites are made using VARTM.

2.2 Damage Problems

Barely visible impact damage (BVID) represents an obstacle for a large number of carbon fibre applications. When a structure made of fibre reinforced composite materials, such as CFRP, are subjected to low velocity impact, the CFRP is capable of absorbing and dissipating the incident energy in either elastic deformation or in form of damage [80]. Impact performance of the composite laminates is vital to determine their appropriate selection for a specific application [81]. In addition, the impact response of laminated composites will provide the designer with information about the damage tolerance in a presumed composite structure [82]. Barely Visible Impact Damage (BVID), as a result of low velocity impact, occurs in carbon fibre composite laminates when an object such as a tool dropped accidentally on a carbon fibre composite structure. This damage may also be caused by debris on runways for an aircraft. This damage causes a

significant reduction in the mechanical properties of carbon fibre composite laminate, especially compression after impact properties [83].

As a result of the impact, the carbon fibre composite laminate may suffer three types of damage that are matrix cracking, delamination, and fibre breakage [84]. All three forms of damage will cause a reduction in the compression strength of a composite laminate. Delamination, in particular, might cause a significant degradation in compression strength (up to 50%) since it will encourage the plies to act independently. Barely visible impact damage (BVID) represents a challenge for composite materials, polymer matrix composites particularly, because minor damage could produce a visible dent in a metallic panel but can cause unseen damage (delamination) to a composite panel [85].

2.2.1 Barely Visible Impact Damage (BVID) Generation

This section provides a description of the theory of low-velocity impacts. To evaluate the damage behaviour of the carbon fibre composite laminates, two main factors are determining the impact performance of the carbon fibre composite laminate structure both of which should be considered. The first factor is the impact parameters that influence the damage mechanism. The impact parameters in the drop-weight impact test, which is used in this work, are the mass of the foreign object that impacts the carbon fibre composite laminates, the area of the foreign object, and the velocity of the foreign object [85].

The second factor is the materials characteristics that determine the damage tolerance in carbon fibre composite laminates and the failure mechanism. The material characteristics are the fibre type, fibre volume fraction, fibre tow structure, the weave, stitching, the matrix properties and toughness and the fibre-matrix interfacial properties [85]. On the other hand, the response of carbon fibre composite structures is governed by the geometry, thickness, stacking sequence and lay-up procedure. The following sections present a comprehensive explanation of the methods and procedures that were used to analyse and capture the data.

- Impact parameters
- Carbon fibre composite laminates parameters
- Selection of impact energies (Barely visible impact damage loads)
- Structural response of carbon fibre composite laminate during the impact events (damage development)

2.2.1.1 Impact Parameters

Impact parameters are impact velocity, impactor area and the weight of the dropped mass. The low-velocity impact that was used in this work is less than $10 \text{ m}\cdot\text{s}^{-1}$ [86], that means there is no

penetration of targets (carbon fibre composite laminate panels) achieved. Low-velocity impact refers to events where, during the contact duration between the impactor and the target, the entire structure responds to the waves that propagate to the boundary and are reflected several times [81, 87]. The response reflects different types of deformations. The carbon fibre composite laminates are capable of absorbing and dissipating incident energies in either elastic deformation or in form of damage [88, 89]. The damage generated during those events is barely visible impact damage (BVID). The damage can be in different forms that are delamination, matrix cracking, fibre/matrix debonding or/and fibre rupture.

2.2.1.2 Carbon Fibre Composite Laminates Parameters

The response of carbon fibre composite laminates to impact damage can be complex [84]. Carbon fibre composite laminates consist of three main elements that are the reinforcing component (carbon fibres), the bonding component (the epoxy matrix), and a fine interphase region between fibre and matrix. The way the carbon fibre composite laminates deform and fail depends upon the both mechanical and chemical properties of the carbon fibre composite constituents [90].

Under low-velocity impact events, carbon fibre composite laminates may suffer from different types of damage that includes delamination, interlaminar matrix cracking, fibre-matrix interface debonding, fibre pull-out and fibre fracture [91]. The capability of these failure modes on absorbing the impact energy depends on the constituent's properties under a fixed loading mode of low-velocity impact events. As can be seen in the ultrasonic C-scan technique and fluorescent microscope in Section 7.3.3, delamination, matrix cracking, and fibre-matrix interphase debonding result in low fracture energies. Whereas, fibre fracture failure mode results in significantly greater energy dissipation.

The carbon fibre composite laminates in this study were made from Toray FT300B, in case of prepreg VTC401, and Formosa TC35 3K, in case of VARTM. Toray FT300B 3K and Formosa TC35 3K that have diameters of 7 μm ; therefore, their ability to absorb the low-velocity impact energies is higher than fibres with small diameters. Also, the damage is more localized with energy being dissipated over an area immediate to the region of impact [42]. However, they have a lower fibre failure strain than small diameter fibres. The carbon fibres that were used are twill weave that means their capability to absorb and dissipate the impact energy locally is higher than their counterparts, such as unidirectional carbon fibres as shown with the ultrasonic C-scan technique Section 7.3.3.

The functions of the epoxy matrix in carbon fibre composite laminates are protection, alignment, stabilization, and stress transfer from one fibre to another. Generally speaking, the stiffness and

the strength of the epoxy matrix is considerably lower than those for reinforcing fibres. The fibres are responsible for carrying most of the load in structural parts. However, the role of the epoxy matrix is critical [92]. For instance, damage to the epoxy matrix due to impact-induced delamination can reduce the load-bearing capability of the carbon fibre composite laminates by up to 50% [19]. Both epoxy resin systems (IN-2 Epoxy infusion resin and VTC401) that are used in this study, are toughened epoxy resin systems. The first system contains 1,6 bis (2,3-epoxy-propoxy) hexane in its formula which improves the toughness of this system, while the latter is toughened epoxy resin matrix, the plasticizing modifier of the system is not known to the users as it is commercially secret.

One of the most important factors that control the mechanical performance of the carbon fibre composite is the interphase [92], which is the strength of the bond between the epoxy matrix resin and the reinforcing element (the carbon fibres). Normally, the carbon fibres pass through an oxidation process to improve the level of adhesion with epoxy resin. In the VARTM process, an ultra-low viscosity epoxy resin was used with a viscosity of 225 mPa.s. A further reduction of the epoxy resin viscosity was induced due to the infusion at an elevated temperature of 40°C. The final viscosity of the resin during the infusion was 27.88 mPa.s. That reduction in the viscosity of epoxy resins decreases the surface tension of the epoxy resin and increases the wettability of the carbon fibres consequently, which in turn is expected to improve the fibre matrix adhesion.

Stacking sequence also helps to determine the impact damage failure [93]. For example, in unidirectional carbon fibre composite laminates that are subjected to a low-velocity impact event the main damage type is splitting, that in turn leads to a peanut-shaped curve in cross-play composites, as shown in Figure 2-6. As a result, these materials are not suitable for applications where impact events might occur. However, a 2x2 mm twill weave carbon fibres mat was used in this study, as it was found that this material offers superior impact resistance and improved residual strengths [89, 94]. It increases the flexibility of the carbon fibre composite laminates, also it absorbs considerably more energy and dissipates the rest of the energy locally [95]. The damage pattern of this material is more localized as shown in Figure 2-7 and in the C-scan section (Section 7.3.3).

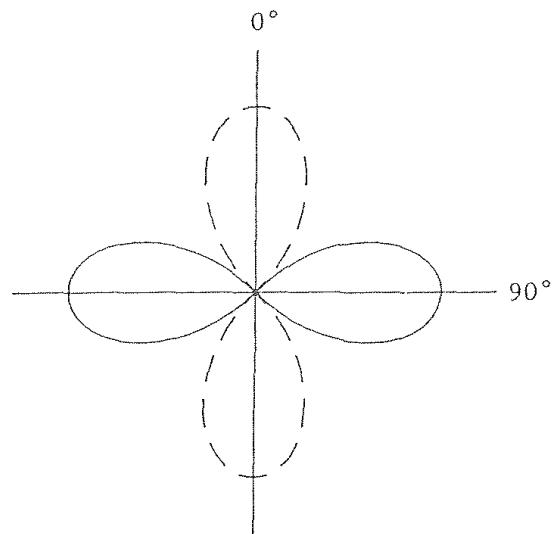


Figure 2-6: The impact damage pattern for [0, 90] composite laminates [1].

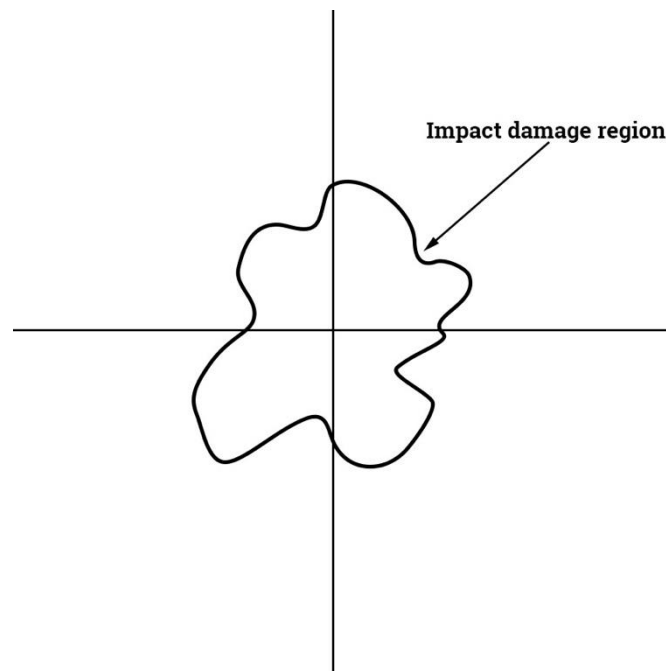


Figure 2-7: shows the low velocity impact damage pattern for woven fabric carbon fibre composite laminates.

2.2.1.3 Selection of impact energies (barely visible impact damage loads)

The vast majority of impact test work reported in the literature was undertaken in the range between 1 to 5 Joules [81]. It is found that these amounts of impact energies may cause minimal damage in the carbon fibre composite laminates. Also, the most recent standards for Boeing and Airbus state that barely visible impact damage (BVID) should be defined as a residual indentation that ranges between 0.25 – 1 mm [96, 97]. In addition, the foreign object should not

be bigger than 25.4 mm in diameter. Also, those standards state that BVID should not be found during heavy maintenance general visual inspection using typical lighting conditions from a distance of 1.524 m. As will be seen later in optical microscopy and C-scan sections, the damage for the woven fabrics is predominantly delamination and fibre breakage and the deformation is more localized [94, 98]. Also, it depends on the curvature of the impactor tip.

2.3 Structural Response of Carbon Fibre Composite Laminate During the Impact Events (Damage Development)

In spite of the fact that delamination and fibres breakage are the main damage modes in the woven carbon fibre composite laminates, there are other types of damage modes that may occur (matrix cracking and penetration). The latter happen either when the impact energy is high or under high velocity impact events, both cases are out of the scope of this work.

2.3.1 Matrix damage

Matrix damage is the first type of damage that may occur during low-velocity impact events. Matrix damage may take two forms either matrix cracks or debonding between carbon fibres and epoxy matrix. The main reason that leads to matrix damage is the mismatch between the matrix (epoxy matrix) and reinforcing element (carbon fibres) [81]. Damage is usually oriented in planes parallel to the fibre direction in unidirectional carbon fibre composite laminates [99]. However, and as seen later in the fluorescent microscopy Section 7.1.3, the matrix damage in woven fabric carbon fibre/epoxy composite laminates initiates in the upper layer under the edges of the impactor. The matrix cracks on the bottom layer occur due to bending load and sometimes they are called bending cracks. Bending cracks are induced by high tensile bending stress and they characteristically growing through the thickness (in the vertical direction).

2.3.2 Delamination

Delamination can be defined as a crack which runs in the resin-rich area between the adjacent plies in composite laminates, the minimum size is approximately 0.07 μm in graphite/epoxy laminates [100, 101]. Delamination may be attributed to many reasons, one of the reasons is that there is a bending stiffness mismatch between adjacent layers [102, 103] that may be more likely in the unidirectional carbon fibre composite laminates. It is also found there is a connection between matrix cracks and delamination [103]. However, delamination is also affected by other parameters such as material properties, stacking sequence, and laminate thickness. The research has proved the relationship between matrix cracks and delamination [84, 104, 105]. It

is observed that delamination initiation only occurs in the presence of matrix cracks [106], at that point, a threshold energy must be reached. Scanning electron microscope revealed for the first time the association between matrix cracks and delamination, it is shown that the delamination does not always run exactly in the interface region, however it can run slightly on either side [8]. In the unidirectional carbon fibre composite laminates, the matrix crack initiates when the impact energy exceeds the ultimate strength of the layer that is in contact with the impactor. Then the cracks propagate through the surface layer due to shear stress. When it reaches the interface, it is halted by a change in the direction of the fibres, therefore, it continues growing between the layers as a delamination due to interlaminar normal and shear stress [107].

In woven carbon fibre reinforced epoxy laminates, it is noticed that the material that is located directly under the impactor is compressed by translating over thickness in a time frame much less than that required for the overall response of the structure. Woven carbon fibre reinforced laminate deformation is highly localized, causing large transverse and normal stresses which can cause the damage to propagate and fail eventually. Impact events create a compression stress wave at the front face of the laminate that in turn, travels through the thickness of the laminate. This wave is reflected from the back surface as a tension wave which can cause failure at the first weakest interface, as a result, chipping and splintering of the parts of the rear ply may occur [107].

At low-velocity impact events, woven carbon fibre/epoxy composite laminates can respond by bending and failing, either by shear resulting in delamination or flexural failure depending on short or long beam [108], respectively as shown in Figure 2-8. Delamination growth is suspected to be governed by interlaminar longitudinal shear stress σ_{13} and transverse in-plane stress σ_{22} in the layer below the delaminated interface, and by the interlaminar transverse shear stress σ_{23} in the layer above the interface [109]. It is worth mentioning here that delamination causes less degradation in the tensile properties, while its effect on the compression properties is significant, especially compression after impact.

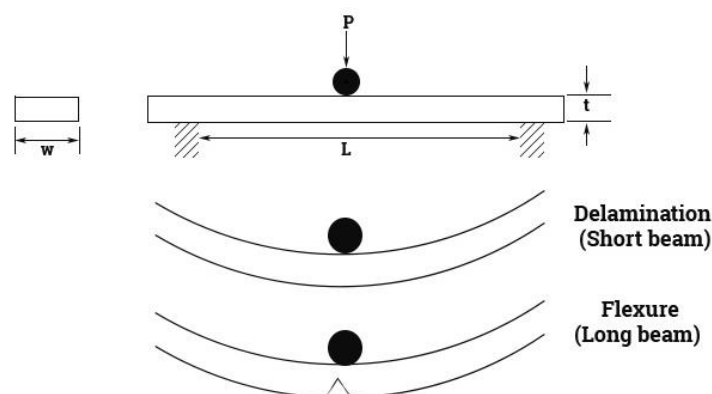


Figure 2-8: Schematic of impact test and expecting failure modes, both modes are suspecting to occur at low-velocity impact events [107].

2.3.3 Fibre damage

Generally, fibre failure mode occurs after matrix cracking and delamination, it is the last of the fracture process. In low-velocity impact events, it unlikely to happen; however, it might occur under the impactor due to locally high stresses that is mainly controlled by shear forces. Also, it may occur at the rear face of the plate (non-impacted face) due to high bending stresses. The fibre failure mode is the start for more serious damage that is penetration mode, fibre failure mode may lead to catastrophic failure [110]. The required energy to cause back surface flexure failure is given by Equation 2 – 2.

$$\text{Energy} = \frac{\sigma_f^2 w t L}{18 E_f} \quad 2-2$$

Where σ_f is the flexural strength, E_f is flexural modulus (in this work Young's modulus was used in the calculations), w is the width, L is unsupported length and t is the specimen thickness. Since the supporting plate is circular in shape, therefore, $w = L = 78$ mm.

2.4 Non-Destructive Testing and Smart Sensing

Self-monitoring systems are an essential tool to improve the reliability of composites, reduce maintenance costs that come from taking parts out-of-service to test them and overcome limitations of non-destructive tests (NDTs). Damage in composite materials can be varied, it takes many forms such as a matrix-cracking, fibre breakage and delamination [33, 111, 112]. By far, delamination is the most important form of damage due to it causing a considerable reduction in a composite's compressive strength and stiffness [113]. Indeed, delamination and catastrophic propagation is the major concern to the aerospace industry, since it can occur due to different scenarios during the life of a composite structure, fabrication processes or maintenance operations.

For example, events such as instruments dropping on structures, hail falling on surfaces, accidents with birds, and rocks or debris being kicked up at high velocities into the aircraft. Such damage is totally undetectable by visual tests, either damage is occurring between laminae or it is too small to be seen by normal eye [112]. This damage can grow during subsequent loading cycles, so it is important to detect it at an early stage (delamination initiation stage) to avoid a disastrous failure that is caused by a drastic reduction in mechanical properties. Impact damage may be the main cause for delamination, in addition to matrix cracking and fibre breakage [114].

Low velocity impacts are expected to occur during many occasions like manufacturing processes or uses of a composite structure. Extensive efforts have been directed to investigate damage effects on properties of composites.

For low velocity impacts such as drop weight, pendulum and flyer plate, where the impactor velocity is less than 10 m/s, damage is usually not visually detectable, but can result in a significant strength reduction. The absence of visible surface damage creates special difficulties in adopting conventional damage characterization methods. It is then necessary to develop experimental techniques to detect the presence of damage and record its nature, size, shape, and through-the-thickness distribution [16]. These techniques can be used for in-service inspections to ensure structural safety.

Hence, early detection of damage and its severity and location are key factors. Non-destructive testing techniques (NDT) such as thermography, ultrasonic C-scan, eddy current and X-Ray have been used to provide the location and size of defects within composite structures [115-117]. These tests might provide precise results about damage size, shapes and locations; However, they need special equipment and surface preparations. In reality, it might be difficult to use these techniques to test composite structures in-service due to complexity of composite materials, which are normally formed by layers of dissimilar materials, but they can be used to detect damage in certain parts of composite structures. Fibre reinforced composite materials with reinforcing elements like carbon, glass and Kevlar are increasingly used in a wide range of both low and high technology engineering applications. To meet these increases in using of composite materials in different applications like aerospace applications, developing new monitoring systems become more essential [118].

2.4.1 Thermography Methods

A thermal approach has been used in a variety of applications such as examination of subsurface defects and the study of microstructural damage in composites using thermo-physical properties [119-121], observation of coating thickness and covered structures. The main interest here is to show how this approach has been used to test the integrity of composite structures, the vast majority of research in this area uses infrared to monitor heat flux at composite material surfaces [122]. This approach utilizes radiated energy to obtain subsurface defect and/or damage information. The thermography can be divided into two approaches: passive and active thermography.

In passive thermography no external heat source is required, where the defects or damage in composite are naturally at higher or lower temperature than the background, while in active ther-

mography, an external heat source is needed to apply heat pulse to a composite material surface that will generate heat flow inside the material. In the case that there are defects, flaws or damage it will affect the homogeneity of the heat flow [123, 124]. Non-contact, non-destructive and fast examination techniques are the most important characterizations, and that makes the thermography method attractive as a non-destructive inspection technique [125].

Due to developments in thermal data interpretations, using thermography in the field of composites becomes increasingly important in both carbon fibre composites [126] and glass fibre composites [127]. However, the thermographic method has many limitations, for instance, difficulties of use with complex and large structures, cost of equipment, highly skilled operators, the ability to detect defects and damage that only make a measurable change in thermal properties and thermal losses due to emissivity.

2.4.2 Acoustic Methods

The propagation of an ultrasonic pulse in an object is scattered or reflected from any interface that separates regions of differing acoustic impedance [128]. If there are any defects, flaws or damage that will affect the manner in which an ultrasonic pulse is transmitted, the pulse will be scattered or reflected, and the location of the discontinuities can be determined (Figure 2-9). If there is no damage, the pulse will reflect from the far surface of an object. Ultrasonic methods such as C-scan are widely used in aerospace applications for non-destructive evaluation (NDE) of structure [38].

Ultrasonic methods are useful to characterize damage or a defect and give an integrated picture, see Section 7.3.3. Ultrasonic methods are suitable for in-line (during the manufacturing process) and end-of-line (finished products) quality control. Ultrasonic methods are providing vital information about the damage and/or defects profile, size and severity. However, there are many limitations to use these methods for in-situ composite monitoring systems [129]. For example, they are expensive and they are point methods, therefore, it is difficult to apply them over the entire area of large structures [130].

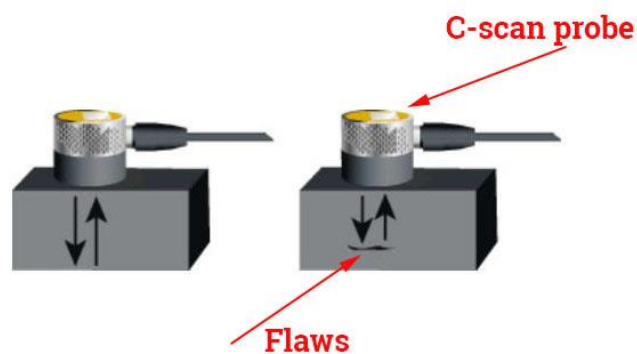


Figure 2-9: Schematic shows the sound energy travels through the sample and it is either reflected by the backside of the sample or it is reflected earlier if a flaw or crack was found.

Other type of sonic methods is acoustic emission [131]. The basic idea is detecting an energy emission (sound wave) that emits from a material due to deformation or damage occurrence. For instance, when a piece of wood is stressed, an audible cracking sound can be heard before the wood breaks. This phenomenon can be extended to other materials and including composite materials [132]. By monitoring spontaneous noise that is generated in a composite material due to applying load, matrix cracking, fibre breakage and delamination can be detected, located and characterized [133-136].

The acousto-Ultrasonic method is a combination of both acoustic and ultrasonic testing technique. This technique is mainly used to assess damage that is distributed over a large area but they are not suitable for detecting small damage such as delamination in a large area [137]. In these approaches (acoustic emission and acousto-ultrasonic), each probe needs a dedicated digital signal processor (DSP) with an internal analogue to-digital converter (ADC) and that adds more cost to this approach [138].

2.4.3 Fibre-Optic Methods

Fibre-optic sensors are tools in which light is transmitted to and from a monitoring region using fibre-optic links [139-141]. They may be easily integrated into composite structures to produce smart composite structures that enable sensors to approach interior composite structures and probe them easily [140]. It is found that these fibre optic sensors have a limited effect on a composite structure in terms of failure stresses [35]. Intrinsic fibre optic sensors with the help of one of optical property such as intensity, wavelength, phase or state of polarization can measure the strain, temperature, pressure and detect damage in composite structures.

Optical fibre properties (intensity, wavelength, phase or state of polarization) should be modulated to measure strain, temperature, pressure or detect damage in large structures. There are some difficulties associated with the use of optical fibres, for example to monitor strain within the structure requires a perfect bonding between fibre optic sensors and composite structures to experience the same strain gradient in host composite structures. Fibre optic sensors have been used increasingly to monitor fabrication strains during the fabrication process [142]. However, there are limitations in using fibre optic sensors because they cause a local distortion and resin-rich regions. That can happen when the optical fibre diameter is bigger than the thickness of the ply [143].

There are several optic-based ways to monitor strain, like Extrinsic Fabry-Perot interferometric (EFPI) sensor [144, 145] and Fibre Bragg grating (FBG) sensor [145]. EFPI is phase modulated

optical fibre sensors, these sensors use the principle that reflected monochromatic light will interfere with the light from the original source that in turn will cause measurable light and dark fringes dependant on strain. A Fabry-Perot interferometer has been proved to be capable of detecting impact damage on composite materials [146]. The ability of the Fabry-Perot interferometer of locating damage was demonstrated by Schindler [147] with the help of a neural network. FBG sensors are a popular choice in smart composite structures, since they are easy to use (they are wavelength based sensors, they operate on the principle that is detecting a narrowband of reflected light that its frequency changes depending on strain) [148, 149]. Those sensors can be used to characterize defects in composites or to monitoring strain [148, 150]. They are available in various lengths from 2 – 20 mm, they have a high failure strain, and they are being easy for multiplexing [151]. However, the measured strain that is acquired from FBG sensors require complex analysis to obtain accurate axial strains since the measured strain is three-dimensional nature [140].

Both the FBG and EFPI have been used in sensing techniques in composites including structural health monitoring systems, strain/stress measurements and cure monitoring systems. The latter can be in form of pressures and/or temperatures [151, 152]. Once the optic fibres have been incorporated inside composite structures, they are affected by strain generated during cure and heating and that in turn limits their applications. However, the FBG has been adopted by aerospace and civil companies [153].

One problem with optical fibre sensors is that failure of a fibre interrupts the sensing, meaning that sensing capability is lost [139]. The possible ways that optical fibres fractures in response to external loads are: the optical fibres will fracture because of large bending-induced tensile stresses, disregarding whether the composite matrix has damaged. The optical fibres could fracture in the path of delamination, where transverse shear stresses can be triggered in the optical fibres. Finally, the optical fibres can fail due to matrix cracking either in tension or shear as shown in Figure 2-10.

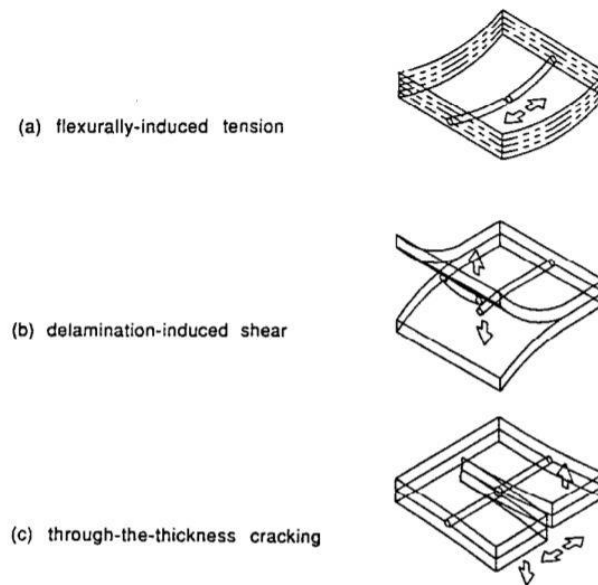


Figure 2-10: The mechanisms that could cause fracture in optical fibres [154].

2.4.4 Electrical Methods

Detection and monitoring systems that are mentioned above are either incorporating sensors into the composites structure, such as a Fibre Bragg grating (FBG) or attaching or inserting sensors to the composites, such as acoustic methods and the Fabry Perot Interferometer (FPI). Once those sensors have been integrated into composite structures, a new challenge will have to be overcome that is establishing a relationship between changes in physical properties of sensors and changes in properties of composite structures being monitored (such as temperature, pressure, stiffness etc.).

An alternative way, which may be more natural, to obtain a smart material is to use composite material constituents as a sensor. This is highly possible in polymer matrix carbon fibre reinforced composites since they consist at least two elements that are carbon fibre (a highly conductive material, its conductivity is 1.5×10^5 S/cm) and matrix that is highly insulating, for example the electrical conductivity of the epoxy matrix is 10^{-13} - 10^{-15} S/cm that depends on many factors, such as temperature, inclusions and the epoxy resin types [155]. Transverse electrical conduction occurs in carbon fibre reinforced-epoxy composites due to waviness of carbon fibres. The waviness is contributed to the difference in the coefficient of thermal expansions $70 - 78 \times 10^{-6} \text{ K}^{-1}$ and $-9.1 \times 10^{-7} \text{ K}^{-1}$ for epoxy resins and carbon fibres respectively [156, 157].

The same concept extends to through thickness electrical conduction, however the through-thickness electrical conduction is much less than transverse electrical conduction since it strongly depends on the amount of pressure that is used in the fabrication technique as shown

in Section 6.1.1. When carbon fibres break and/or when an epoxy matrix cracks, it prevents previously touching fibres from contacting, then a change in electrical properties will occur due to a decrease in fibre – fibre contacts [33]. There is directionality in electrical properties of composite materials, electrical resistance of a composite material in the longitudinal direction differs from the electrical resistance in the transverse and through-thickness directions; this property has been deployed to investigate damage mechanisms [130].

The features (i.e. strain monitoring, damage monitoring, and damage detection) determine the type of electrical currents being used. Direct current (DC) is suitable to monitor fibre fracture and delamination processes [130, 158, 159], since those types of damage produce a measurable change in electrical resistance. While alternative current (AC) may be used to monitor matrix cracks, transverse cracks, fibre/matrix debonding, and delamination [155, 160, 161]. AC (based on dielectric analysis) is mainly used to monitor a resin infusion process during liquid moulding processes [78, 162] and thermoset resins cure [78, 163].

DC (based on electrical resistance analysis) is used to monitor stiffness variations in carbon fibre reinforced – epoxy composites. DC used in either real-time monitoring systems to monitor strain and damage growth such as fatigue [129, 158, 164] or damage detection such as delamination due to low velocity impact events [165, 166]. The amount of electrical resistance of carbon fibre composite – epoxy laminates relies on many factors that are carbon fibre (FT300B, Tairyfil TC-35, etc.), reinforcing pattern (unidirectional, cross-ply, quasi-isotropic or woven fabric reinforced carbon fibre composites), electrical connection methods (copper plate, silver plate, copper wires, etc.) [117, 167, 168], electrical measurement methods (two-probe or four-probe electrical measurement system), fibre volume fraction and fabrication techniques (autoclave processing technique, vacuum assisted resin transfer moulding (VARTM), etc.). Table 2-1 presents the main parameters affecting on electrical resistance sensing techniques and their consequences on percentage changes in electrical resistance.

Table 2-1: Most important parameters that determine the effectiveness of self – sensing electrical resistance system in carbon fibre composite laminates.

Author	Carbon Fibre Composite Type	Carbon Fibre Volume Fraction %	Dimensions (mm)	Electrical Contact Type	Test Type	Direct Current (mA)	Electrical Measurement System	Electrical Resistance (ΔR) Ω	Re-	Percentage Change ($\Delta R/R_0$)		
Abry et al. [155]	[0/90] _s	Not available	100 x 10 x 2.2	Copper plate	Bending	10	2-probe strain damage	0.009	9			
	[90/0] _s							0.0045				
K. Schulte [158]	[0] _B	Not available	190 x 25 x 1	Copper plate	Tensile	50	2-probe real-time monitoring system	0.332 – 0.345	4			
	[0/90] _s		190 x 25 x 2		Fatigue			0.3 – 0.316			5.3	
P. E. Irving et al. [129]	0°	59.8	270 x 25 x 2	Copper strip	Tensile	30	4-probe real-time monitoring system	0.003 – 0.004	1.5 – 1.8			
	90°		270 x 25 x 2					1			6 - 16	1.6 – 3
	[0/90]		270 x 25 x 2					30			0.005 – 0.01	1 – 2
	0°	270 x 25 x 2	30		0.03 – 0.04	10 – 15						
	90°	59.8	270 x 25 x 2		Fatigue	1	4-probe real-time monitoring system	60 – 160	10 – 15			
	[0/90]	270 x 25 x 2	30		0.05 – 0.1	10 – 15						

Author	Carbon Fibre Composite Type	Carbon Fibre Volume Fraction %	Dimensions (mm)	Electrical Contact Type	Test Type	Direct Current (mA)	Electrical Measurement System	Electrical Resistance (ΔR) Ω	Re-	Percentage Change ($\Delta R/R_0$)
De Baere et al. [124]	[0/90] _{4s}	Not available	270 x 30 x 2.5	Rivet	Tensile	100	2-probe real-time monitoring system	0.0064 - 0.0088		1.25 – 1.31
T. J. Swait et al. [165]	[90/0] _{2s}	60	110 x 110 x 2	FCB	Low velocity impact	0.5	2-probe damage detection system	1.5 – 8		0.14
Hart et al. [166]	[0/45/-45/90] _{2s}	Not available	152.4 x 152.4 x 2	Copper strips	Low velocity impact	Vary	4-probe damage detection system	3.73 x 10 ⁻⁵ – 8.2 x 10 ⁻⁵		0.403 – 0.672
	[0/45/-45/90] _{4s}		152.4 x 152.4 x 4					1.42 x 10 ⁻⁵ – 1.09 x 10 ⁻⁴		0.163 – 0.480
S. Wang et al. [169]	[0/90]	63.5	200 x 12 x 3.2	Copper wires	Low velocity impact	0.25 – 99	4-probe damage detection system	0.888		0.1
Todoroki et al. [170]	[(0/90) _{2s}	50	200 x 105 x1	Copper plate	Indentation	30	4-probe damage monitoring system	0.00012-0.00018		0.01
Zappaloroto et al. [171]	[0°] ₁₈	Not available	225 x 25 x 2.95	Silver coating and copper plate	Mode 1	250	4-probe damage monitoring system	Not available		0 – 30
Gadomski et al. [172]	[0/90] ₂	60 – 70	160 x 25 x 3	Silver tape	Bending	20	4-probe damage monitoring system	Not available		4 – 1400
Kwon et al. [173]	[0]	Not available	100 x 16.2	Silver paste and copper wires	Bending	Not available	2-probe damage monitoring system	Not available		0 – 0.8

2.5 Electrical Conduction of Carbon Fibre Reinforced Polymer

The investigation of electrical properties of a carbon fibre reinforced polymer (CFRP) laminate is essential in order to deploy an electrical self-sensing system of CFRP in a practical use. Detection of damage in carbon fibre polymer-matrix composites have been extensively studied by electrical resistance measurements [170]. To evaluate the structural integrity of CFRP laminates, it is vital to understand how electrical resistance of CFRP changes in response to applied loads. The electrical resistance techniques have been applied successfully on unidirectional and multi-directional composite laminates such as cross-ply and quasi-isotropic CFRP laminates [32, 165, 174] to monitor either the strain or detect damage. The piezoresistivity of carbon fibres enables identification of different forms of damage such as delamination, matrix cracks, and fibre breakage due to changes in electrical resistance [175].

The electrical resistance sensing system may replace the ultrasonic methods as a non-destructive test technique [141]. Due to its great practical importance, many ways have been used to make an electrical connection between the CFRP laminates and electrodes. For example, the electrodes are co-cured with the panels or a conductive material such as silver paint, carbon cement, and silver epoxy were used [33, 111, 174]. Requirements such as low resistance, a long operating life and cost are needed to be considered when setting up a current flow at the contacts of two electrodes.

This section is organised as follows: Sections 2.5.1 and 2.5.2 present the electrical fundamentals i.e. Ohm's and current density law; Section 2.6 describes different electrical resistance sensing techniques i.e. two-probe and four-probe.

2.5.1 Ohm's Law

The ability or lack of ability of materials to conduct electrical current is one of the principal characteristics of materials. Materials are categorised by this property, that is, they are divided into conductors, semiconductors, and insulators. Their conductivities are 10^4 - 10^6 , 10^{-6} - 10^2 , 10^{-8} - 10^{-20} S/cm respectively. Materials such as metals and their alloys, silicon and ceramics are considered as conductors, semiconductors and insulators respectively. One of fundamental equations that describes electrical conduction in materials is Ohm's law [176].

This law is one of the simplest electrical laws, that can be applied to many materials such tungsten, bronze, brass, iron aluminium and copper. Ohm's law may be expressed in Equation 2-3.

$$V = IR \quad 2-3$$

Where V is the potential difference in Volts, I is current flow in a circuit in Amperes and R is the resistance of the conductor in Ohms. According to equation 2-3, the amount of current that

flows through a wire is inversely proportional to resistance, which in turn is dependent upon chemical compositions of materials.

2.5.2 Current Density

Current density is the magnitude of the electric current per cross-sectional area [177], and it can be expressed using Equation 2-4

$$J = \frac{I}{A} \quad 2-4$$

Where I is the electric current (amp) and A is the cross-sectional area (mm^2). For materials with finite resistance, the current density J is directly proportional to the electric field E in the medium. The resistivity of a material is the proportionality constant η , whose value is material and temperature dependent.

$$J = \frac{1}{\eta} E \quad 2-5$$

Where $E = \frac{V}{L}$ (the voltage difference between two points divided by the distance separating them).

2.6 Electrical Resistance Sensing Techniques

A general method of measuring resistivity of an electrically conductive solid material is to measure potential differences between electrodes under a constant electrical current condition. However, several set-ups exist for electrodes arrangements, they differ in absolute values and tendencies [178-180]. An experimental study on the effect of an electrode set-up was carried out by Wang et. al [180]. This study, as well as other studies [181, 182], explained the difference in absolute values and tendency in two different set-ups: two-probe and four-probe techniques using a direct current (DC). Two-probe and four-probe techniques are the subject of the following sections.

2.6.1 Electrical Sensitivity in CFRP Laminate

The structure of a material is considered to be sensitive to its condition when it consists of sensors that are providing in-service data about the material itself or its operation environment. Thus this would improve the durability and reliability as well as widen the adoption of composite laminates in general and CFRP laminates in particular [180]. However, there are a few requirements that in-service health monitoring sensors need to meet. For example, they must not cause damage to the structure (i.e. they are small in size), they offer the possibility of being

located in remote and inaccessible areas of the structure and they must have the ability to transmit the information to a central processing unit.

This data must be in a direct relation with the physical process being monitored and properties and performances that are to be maintained. The data, which is being provided, must compete in sensitivity with the data obtained by conventional non-destructive evaluation techniques (NDE) and it must cover a sufficient area of a structure. The best way to achieve all of that requirements is to use a material that has the ability to monitor itself. CFRP laminates consist of, at least, two different components that are the epoxy, which is highly insulating (the electrical conductivity (σ) $\approx 1.5 \times 10^{-15}$ S/cm, and the carbon fibre, which is highly conductive $\sigma \approx 1.5 \times 10^5$ S/cm. That makes it potentially a smart material by utilizing one or more of its components, CFRP laminates can be monitored during manufacturing processes [183-185] or in-service [186, 187] by measuring the electrical conductivity of carbon fibres (i.e. increase or decrease in electrical resistance as an indicator of strained or damaged CFRP laminates). In continuous carbon fibre reinforced composite laminates, the electrical conductivity in the fibre direction is very high. Therefore, the ideal conductivity can be easily estimated by multiplying electrical conductivity of carbon fibres by fibre volume fraction.

In the case of ideal carbon fibre composite laminates, the carbon fibre in a lamina is perfectly straight, perfectly aligned and evenly distributed. Each single fibre is separated from its neighbours by a thin resin layer and that leads to zero conductivity in the transverse and through-thickness directions. However, in practice carbon fibre in the lamina is wavy as shown in Figure 2-11 [33].

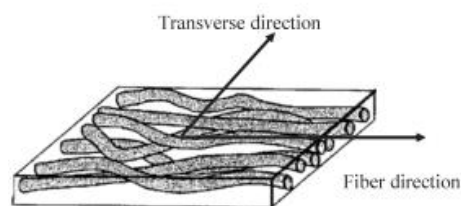


Figure 2-11: Schematic shows practical structure of carbon/epoxy composite [188].

In unidirectional carbon fibre composite laminates, the curved carbon fibres cause non-zero electrical conductivity in the transverse direction due to a large network that is formed by carbon fibre contacts with each other. However, the electrical conductivity of CFRP laminates in the transverse direction is much lower than the electrical conductivity in the fibre direction (37 – 55) S/cm [33]. Studies [33, 155] have experimentally revealed the ratio between electric conductivity in the fibre direction σ_0 to the transverse direction σ_{90} , $\sigma_{90}/\sigma_0 = 3.7 \times 10^{-2}$ and the ratio between electric conductivity in the fibre direction σ_0 to through-thickness direction σ_t , $\sigma_t/\sigma_0 = 3.8 \times 10^{-3}$ for a continuous carbon fibre composite laminate of the fibre volume fraction is 0.62.

Through-thickness conductivity of a CFRP laminate is smaller than transverse direction conductivity, although the fibre-fibre network structure is similar to the transverse direction [189]. That is attributed to thin resin rich layer that exists between laminae in a laminate. For a practical CFRP laminate, prepreg lamina are wavy as it is the case for carbon fibre as shown above in Figure 2-11. The contact between laminae leads to non-zero electric conductivity in the thickness direction. The contacts between adjacent laminae create a circular pattern flow around the positive electric electrode as shown in Figure 2-12; this is one of the factors that reduces the accuracy of this method.

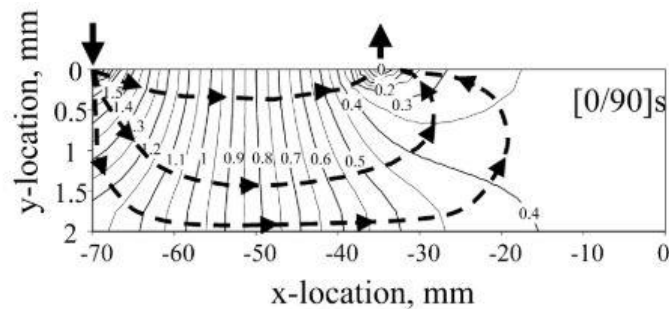


Figure 2-12: Voltage contour for a cross-ply laminate [33].

Two-probe and four-probe electrical resistance measurement methods are the most common techniques to measure the changes in electrical resistance in CFRP laminates. Both methods are detailed in the following two sections.

2.6.2 Two-Probe Sensing Technique

A two-probe technique uses two electrodes to introduce an electrical current and measure electrical resistance via corresponding changes in voltage as shown in Figure 2-13.

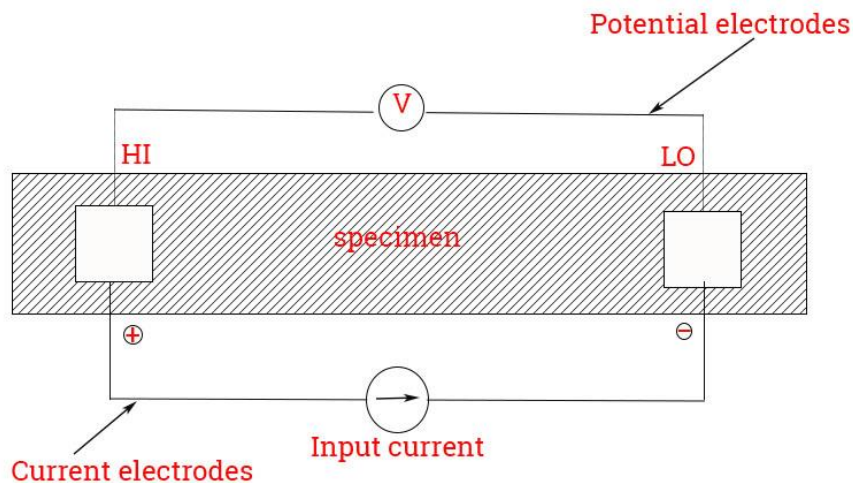


Figure 2-13: Two-probe electrical resistance technique.

This technique has been used to measure strain [112, 113, 116, 190] and to detect damage in carbon fibre reinforced polymer (CFRP) laminates [117, 124, 165]. It is simple and convenient, but it is sensitive to the quality of the electrical contacts [124]. This method has been questioned since electric resistance of a CFRP varies, some researchers reported an increase in electrical resistance [158] and others reported a decrease in electrical resistance [113, 129, 130, 168, 180] due to applied loads. The decrease in resistance is due to electrons travelling in an unexpected direction relative to the applied voltage gradient, due to backflow across a composite interface [191]. Todoroki et al [188] and Angelidis et al [174] attributed the reduction in the electrical resistance to poor electrical contact at the electrodes.

2.6.3 Four-Probe Sensing Technique

The four-probe method injects an electrical current through two electrical contacts (normally outer electrodes) on a specimen and measures voltage between two electrodes as shown in Figure 2-14. It is more effective and precise than the two-probe technique in sensing impact damage and cycling loading damage (i.e. fatigue damage in CFRPs due to the essential elimination of contact resistance from the measured resistance) [180]. In addition, it has the ability to detect sub-surface damage [35, 192]. The electric current flows in a direction perpendicular to the equipotential line, the internal current distribution is shown in Figure 2-15: a.

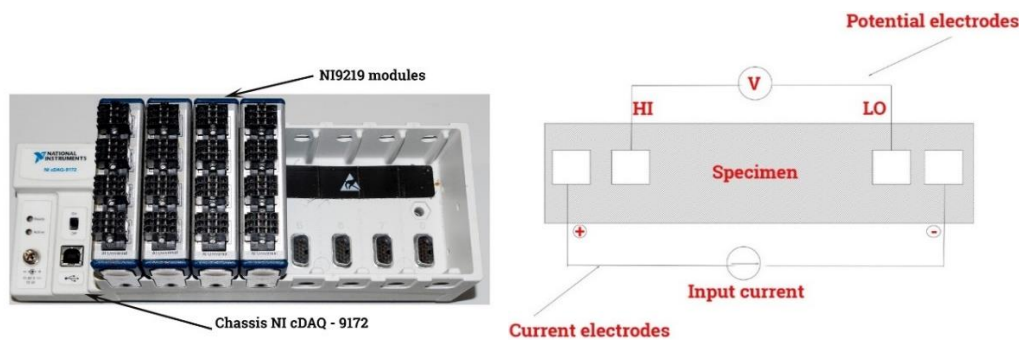


Figure 2-14: a. Image showing National Instruments cDAQ 9172 with NI9219 modules, b. Four-probe electrical resistance method where the DAQ system configured.

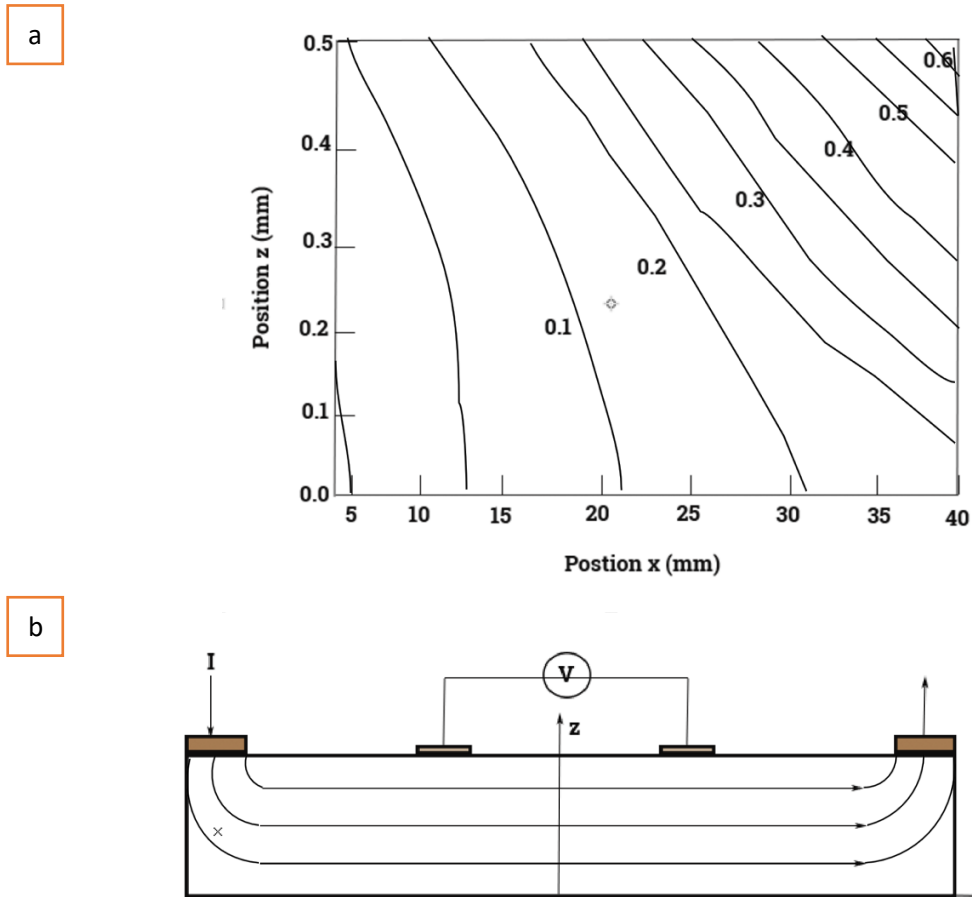


Figure 2-15: a. shows equipotential lines for the configuration b, b. schematic shows the internal current distribution[181].

As the position of voltage electrode approaches the position of the current electrode, the equipotential line approaches the surface of the specimen [181]. As a result, for the case of the two-probe technique in which the current and the voltage electrodes share the same position, the measured voltage values might be significantly affected by the condition of the specimen surface [33]. However, it is found that polishing the specimen surface will cause a considerable drop in the strength of the carbon fibre that is located at the surface of a CFRP laminate, consequently the event number of fibre breakage shows higher values than unpolished specimens [181].

It is expected that this is the difference between the resistance measurement results of a two and four-probe technique which might be caused by the effect of the surface polishing and not by the differences in the strength of the CFRP specimen. In the current work, electric resistance of panels was measured by attaching a sensing mat to the bottom surface of CFRP laminates. The occurrence of the damage will initiate at the tensile side of the CFRP laminate [155], therefore, it is desirable to attach the sensing mat to the bottom surface of a specimen.

2.6.4 Piezoresistivity in Carbon Fibre

Piezoresistivity refers to changes in electrical resistance due to applied strain in carbon fibres. This property makes the carbon fibres attractive materials since it directly indicates damage and/or strain in structural materials, such as carbon fibre reinforced laminates. This is an intrinsic property in the reinforcing element (carbon fibres), and this property can be utilized to make carbon fibre composites smart materials. Due to the vast amount of work that has been taken in this field [42, 193-195], therefore, the following discussion will focus on ex-PAN continuous carbon fibres as they are going to be used in this work, also they have been used extensively in structural applications.

It has been reported in continuous carbon fibre/epoxy laminate [196] that have an applied tensile stress in the fibre direction which causes a reversible increase in the resistance in the through-thickness direction as measured by a four-probe technique. This might be due to the increase in degree of fibre alignments and decrease in the contact points between fibres in adjacent layers. However, applying tensile strain in the fibre direction will cause a reversible decrease in electrical resistance in the fibre direction as measured by the four-probe technique. A possible explanation for that change is due to increase in the degree of alignment as it happens in the through-thickness direction. Electrical resistance in woven fabric carbon fibre reinforced composite laminates increases due to applied strain due to reduction in fibre – fibre contacts in the through – thickness direction as discussed in Section 7.3.2.

Irving et. al. [197] found that using a two-probe technique gives the opposite result. Whereas, electrical resistance of CFRP laminate increases due to applied uniaxial tension and that might be attributed to dimensional changes during tensile loads. In general, the four-probe technique might be better than the two-probe technique as it eliminates electrical contact resistance at the electrodes and it is more reliable as it measures electrical resistance accurately for conventional homogeneous electrically conductors.

It is found that the piezoresistivity of ex-PAN carbon fibre (filament) is complex [193]. Carbon fibres (filaments) show a linear increase in electrical resistance above 0.1% of strain. However, carbon fibres have variable behaviours in most cases at low strains. Typical curves for ex-PAN shown in Figure 2-16. The piezoresistivity in carbon fibres can be contributed to many reasons, one of these reasons is changes in the shape of carbon fibre under applied strain. Applying a uniaxial tensile load on a carbon fibre will decrease the diameter and increase the length of the carbon fibre consequently that would increase the resistance of a carbon fibre [42].

It is useful to study these geometric effects from changes in resistivity separately, since it can produce either a negative or positive contribution to the piezoresistance. Figure 2-16 shows

different PAN based carbon fibres that their resistivity changes with applied strain. Celion 3000 is a low modulus ($E = 200 - 300$ GPa) PAN-based carbon fibre, the resistivity (ρ) of this carbon fibre is $10^{-5} \Omega \cdot m$ at the room temperature. GY-50 is a medium modulus ($E = 350$ GPa) PAN-based carbon fibre, $\rho \approx 1.05 \times 10^{-5} \Omega \cdot m$ at the room temperature. GY-70 is a high modulus carbon fibre ($E = 500 - 700$ GPa), $\rho \approx 1.5 \times 10^{-5} \Omega \cdot m$ at the room temperature. While GR-21 is an ex-pitch carbon fibre that is not of interest in this work. Two types of a PAN-based carbon fibre were used in this work that were Toray FT300B and Tairyfil TC-35, their tensile modulus is 230 GPa and resistivity is 1.7 and $1.73 \times 10^{-5} \Omega \cdot m$ respectively.

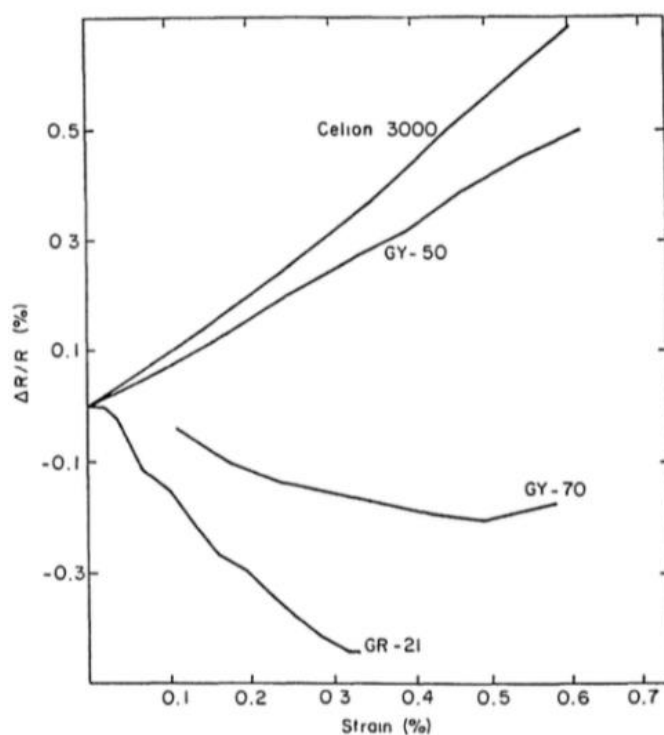


Figure 2-16: Typical curves for ex-PAN carbon fibres showing the resistance changes due to applied strains [42]. ΔR represents the change in electrical resistance due to applied strain and R represent the typical resistance of an unloaded carbon fibre.

The piezoresistivity is a function of temperature, as temperature might be used to categorize the lattice perfection of a carbon fibre. Therefore, the resistivity curves are useful and they are similar for widely different classes of carbon-based materials [198]. Figure 2-17 shows a set of resistivity as function of temperature for ex-PAN fibres. For perfect fibres, fibres with less defects, the resistivity curves approach that of single crystal graphite. Since the electrons scattering by defects are minimized but the intrinsic scattering by phonons must be considered. Nevertheless, none of the resistivity curves completely attain the low values for single crystal graphite due to residual defects remaining in the fibres [42]. At the room temperature, for different heat treatments, the resistivity curve for the CCVD fibres lies under ex-pitches fibres and ex-

PAN fibres, in that order. That might reflect the degree of difficulty to graphitize these carbons as shown in Figure 2-18.

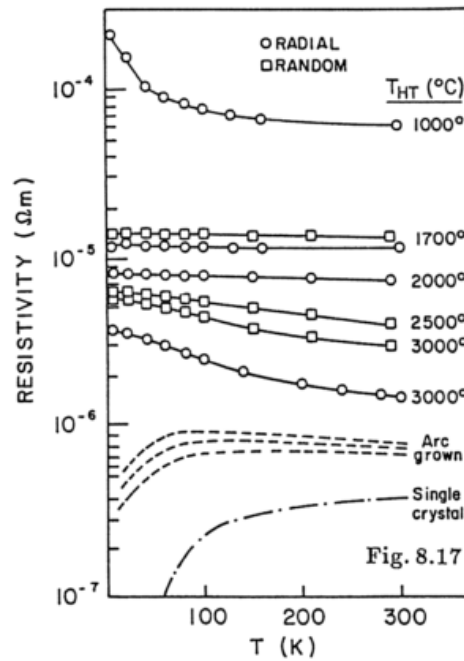


Figure 2-17: Temperature dependence of the resistivity of ex-PAN [199].

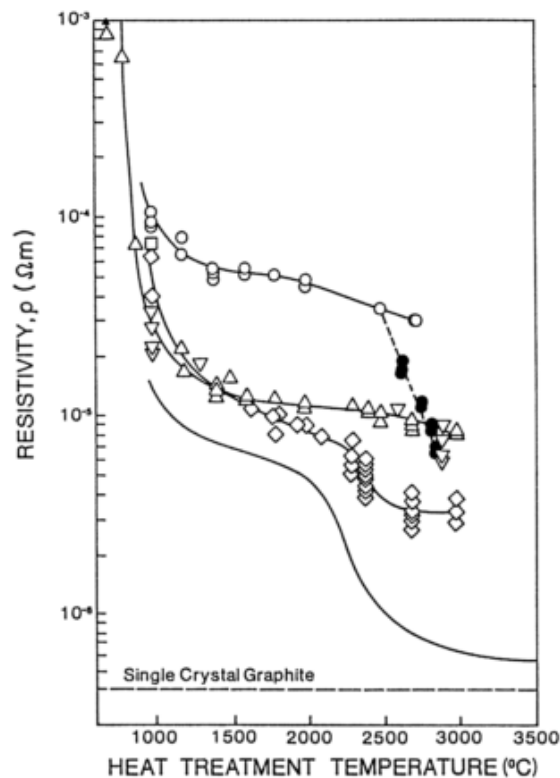


Figure 2-18: Schematic variation of room temperature electrical resistivity versus heat treatment temperature [42]. o is ex-rayon, solid o is stretched rayon; Δ and ∇ ex-PAN fibres, \diamond ex-pitch fibres and the solid line is CCVD fibres.

2.7 Summary

- This chapter presented a brief introduction to constituents and manufacturing techniques of carbon fibre composite laminates, two manufacturing techniques that were autoclave processing and vacuum assisted resin transfer moulding were described. The most familiar damage forms due to low velocity impact events, with particular emphasis on delamination, were presented with factors that have significant impacts on the type, shape, and severity of damage, such as resin matrix type, carbon fibre type, and impact parameters. The most common smart sensing systems were addressed briefly, however, the electrical smart sensing systems were detailed, and the electrical resistance sensing system was covered in detail as it presents the main object of this thesis. Critical parameters and their effects on the sensitivity of electrical resistance sensing system were presented in Table 2-1. The theory of electrical conduction in carbon fibre composite laminates were explained and laws that govern the electrical conduction were presented. Two electrical resistance measurement systems, that are two – probe and four – probe electrical resistance were described. This thesis utilized the four – probe electrical resistance measurements, therefore, the advantages of this technique were mentioned thoroughly. This chapter ended by discussing the most important electrical property that has made carbon fibre composite laminates interesting materials that is piezoresistivity.
- As evident from the literature that the electrical resistance sensing technique has shown potential contributions to improve the reliability of carbon fibre composite laminates due to its ability to monitor strain and damage due to applied loads. The vast majority of the reported literature on electrical resistance sensing technique has conducted on a bar type specimen for proof-concept purposes (technology readiness level 1 – 3). This thesis described work that tests the applicability of electrical sensing technique on a panel type specimen.
- Although previous studies have undertaken substantial efforts in applying electrical resistance technique on carbon fibre composite laminates fabricated using autoclave processing technique, the studies have shown a little effort to investigate the suitability of the electrical sensing technique to carbon fibre composite laminates fabricated using different fabricating techniques, such as a vacuum assisted resin transfer moulding

technique. This thesis explored the applicability of electrical resistance sensing technique on carbon fibre composite laminates made using VARTM processing technique.

- Extensive studies were conducted on unidirectional, cross – ply, quasi – isotropic carbon fibre composite laminates, however a little effort has been made on testing the suitability of electrical resistance sensing technique on woven fabric carbon fibre reinforced – epoxy composite laminates. The current thesis investigated the suitability of the electrical resistance sensing technique to woven fabric carbon fibre composite laminates. This thesis attempted to show the limitations in a potential use with electrical sensing system due to the lack of a sufficient theoretical background.
- Neural network and response surface method were used in the literature to locate the damage in tested specimens, both methods required a large set of data for training. This thesis proposed innovative sensing mats that divide the panels into segments and measure the local variations in electrical resistance in each segment to locate damage. The variations in electrical resistance due to damage occurrence was analysed using a simple code that utilized simple analytical methods.

Chapter 3

METHODOLOGY

This chapter provides details of constituent materials used to produce smart carbon fibre composite laminate panels. Experimental procedures to characterize physical and electrical properties of raw materials are described.

3.1 Materials

Carbon fibre composite laminate panels were manufactured using two manufacturing techniques that are a vacuum assisted resin transfer moulding (VARTM) and an autoclave processing techniques. Resin systems are detailed in Section 3.1.1, Section 3.1.2 describes copper-clad laminates that were used to make the sensing mats and carbon fibres are described in Section 3.1.3.

3.1.1 Epoxy Resin Systems

In this work two types of uncured epoxy resins were used. A liquid low viscosity epoxy resin was used to make carbon fibre/epoxy composite laminates in a vacuum assisted resin transfer moulding (VARTM). In addition, a partially cured epoxy resin (B-staged) with carbon fibres in the form of a prepreg was used to make carbon fibres/epoxy composite laminate panels in an autoclave processing technique.

3.1.1.1 IN-2 Epoxy Infusion Resin

This resin uses unique chemistry which is described below as provided by the manufacturer (Easy Composites, UK). The ingredients for the resin and the hardener are presented in Table 3-1 and Table 3-2 respectively. This resin has an ultralow viscosity, high mechanical properties, and it is a toughened epoxy resin. Due to its low viscosity and long pot life, this resin is used mainly in a resin transfer moulding (RTM) and a vacuum resin transfer moulding (VARTM).

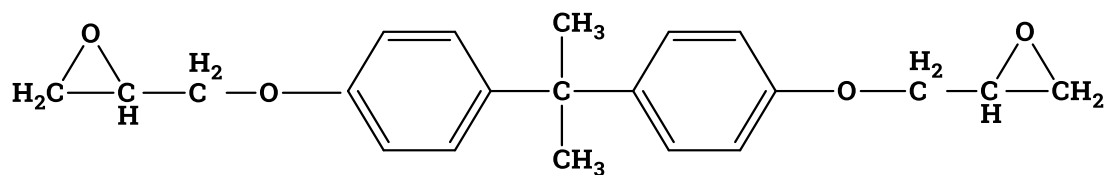
Table 3-1: Ingredient percentages of IN-2 Epoxy infusion resin.

Ingredients	Bisphenol-A-Epichlorhydrin	Bisphenol-F-Epichlorhydrin	1,6 bis (2,3-epoxypropoxy) hexane	Propylene Carbonate	Car-
Concentration %	30 - 50	30 - 50	20 - 30	5	

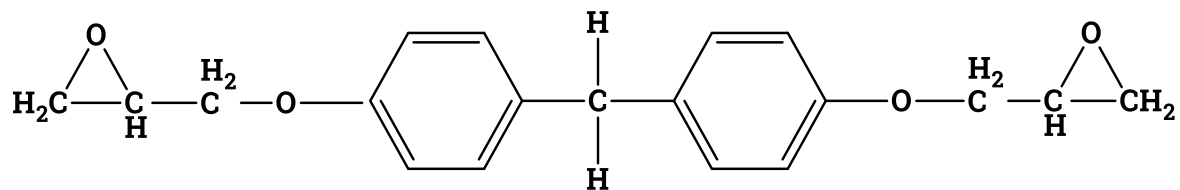
Table 3-2: Ingredient percentages of AT30 Epoxy Hardener-Slow

Ingredients	Polyoxypropyl-enediamine	3-aminomethyl-3,5,5-trimethyl-cyclohexylamine	2,2,4-(2,4,4-)methylenediamine	Trimethylehexa-	Benzyl alcohol
Concentration %	30 – 50	30 – 50	5 – 10		5

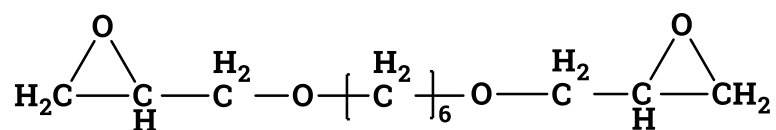
As seen in Table 3-1, the epoxy resin system that was used in this work is a mix of different epoxy resins. Each epoxy resin contributes to epoxy resin system in different ways as described below:



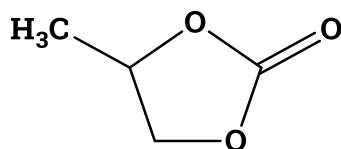
Bisphenol A Epichlorohydrin (DGEBA) resin is responsible for the mechanical properties such as modulus, but it has high viscosity due to its low flexibility in comparison with Bisphenol F Epichlorohydrin.



Bisphenol F Epichlorohydrin resin, in turn, is less viscous than Bisphenol A Epichlorohydrin but it has a higher average epoxy content than DGEBA. This chemical component contributes to the mechanical and rheological properties of the resin system by reducing the viscosity of the resin system, but its main function is increasing the chemical resistance of the resin system.



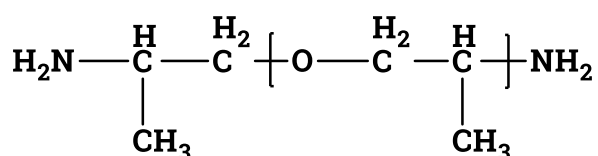
In order to preserve the physical or mechanical properties of the resin system, but reduce the viscosity, 1,6 bis (2,3-epoxypropoxy) hexane was used. This a polyfunctional reactive epoxy diluent that has the ability to reduce the viscosity of the resin system. However, the mechanical properties of the resin system are less affected by incorporation this diluent, as it does not affect the cross-link density of the system. In fact, it is found it enhances some of the properties such as the toughness [48].



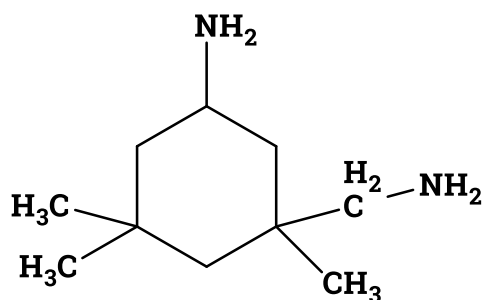
Propylene carbonate is added as a modifier, where its main function is decreasing the viscosity of the resin system. Propylene carbonate has a high molecular dipole moment (4.9D) that makes this chemical component a strong solvent, but it becomes part of the resin system [48]. That is unlike conventional solvents which leaves the mixture. Propylene carbonate reduces the mechanical properties of the resin system, but the reduction in the mechanical properties is not high due to its low percentage in the resin system 5%.

The curing agent system (hardener) that was used with the resin system is described below. It can be seen that the curing agent consists of aliphatic amines and cyclo-aliphatic amines. The aliphatic amines have a significant impact on the final product (cured resin) in terms of mechanical properties and the glass transition temperature. The aliphatic amines reduce the mechanical properties such as the modulus, but they increase the toughness of the cured resin, in addition they cause a reduction in the glass transition temperature of the cured resin relative to aromatic amines. One additional advantage for this curing agent system is that it initially cures at room temperature. However, this curing system contains other curing agents which require post curing in an oven to complete the curing reaction. The curing agent chemicals are described below.

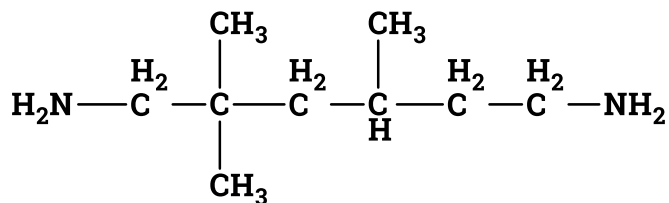
Polyoxypropylenediamine



3-aminomethyl-3,5,5-trimethylcyclohexylamine



2,2,4-(2,4,4-) Trimethylexamethylenediamine



Benzyl alcohol

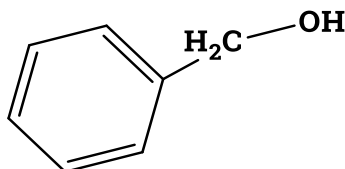


Table 3-3 presents the curing and the post curing schedules for this resin system. The properties of the resin and the hardener prior to mixing are shown in

Table 3-4. Table 3-5 shows the physical and mechanical properties for cured resin at room temperature.

Table 3-3: curing schedules for the epoxy resin system

Temperature (°C)	RT	40	50	60
Time (Hour)	24	6	6	12

Table 3-4: Physical properties of uncured IN-2 Epoxy resin and AT30 hardener as provided by the supplier.

Properties	Material	Value
Viscosity at [25] °C	Epoxy Resin	500-600 mPa.s
	Hardener	25-50 mPa.s
	Combined	225 mPa.s
Density	Epoxy Resin	1.14-1.16 g/cm ³
	Hardener	0.94-0.97 g/cm ³
	Combined	1.105 g/cm ³

Table 3-5: Physical and mechanical properties of the cured resin at 25°C as provided by the manufacturer.

Properties	Value	Test Method
Density	1.08 – 1.12 g/cm ³	ASTM D 792

Hardness	84.5-88.5 Shore D/15	ASTM D 2240
Maximum T_g	92 -98°C	ASTM D 3418
Flexural Strength	112-124 MPa	ASTM D 790
Flexural Modulus	3.15-3.55 MPa	ASTM D 790
Tensile Strength	65.5-73.5 MPa	ASTM D 638
Elongation at break	6-8 %	ASTM D 638
Maximum Strain	5-7 %	ASTM D 790
Strain at Break	6-8 %	ASTM D 790
Water Absorption (24h at room temperature)	0.12-0.2 %	ASTM D 570

3.1.2 Copper Clad Laminates (Pyradox FR8510R)

Conventional smart sensing materials that are made using electrical sensing techniques require using a lot of wires [185]. In this work sensing mats that are made of flexible circuit boards (FCBs) were used to reduce the amount of wiring required. In addition, that will make this technique versatile for aerospace applications. The electrical connection reliability using sensing mats is high since it is almost impossible to make a wrong connection. The accuracy of attaching sensing mats to surface of the carbon fibre composite laminates is higher than attaching an individual piece of copper (electrodes) to the surface.

Conventional flexible circuit boards consist of five distinct layers of materials: Dielectric film, a conductor layer, a cover layer, and two distinct adhesive layers. Commercial flexible copper-clad composite laminates sheets Pyralux FR8510R (Dupont, USA) were used in this work. Sheet Pyralux FR8510R is a single-sided composite laminate sheet that consists of an 18 μm thick of copper foil bonded to a 25 μm thick of flexible film of polyimide. This material is classified according to IPC-4562, where FR8510 is a product code and R specifies the type of copper was used in this product which is rolled-annealed copper (or sometimes called wrought).

The copper is Grade W5 that was processed according to IPC-4562A-WAM1. However, according to the manufacturer, during the manufacturing press cycle to make the Pyralux FR8510R in an autoclave it changes to grade W7. This copper (grade W7) has a maximum resistivity of 0.155 $\Omega\cdot\text{g}/\text{m}^2$. However, the Pyralux FR8510R has passed through further processing during

attaching it to carbon fibre composite laminates and the actual resistivity was measured, as presented in Section 3.2.3.

Since the substrate of the dielectric film has a significant impact on the manufacturing cost and the performance of the finished sensing mats. The insulation (dielectric film) used in this product is a 25 μm polyimide flexible film. The polyimide offers the best combination of costs and properties for this application. The polyimide film is covered with a 25 μm thick of C-staged acrylic adhesive. The laminating process to copper foil takes place with the use of heat and pressure in an autoclave to form the base laminate.

A cover layer was used in this project to isolate tracks in a sensing mat from making contacts with the carbon fibre panels this being Pyralux FR 0110 Coverlay (Dupont, USA). That material consists of a 25 μm thick layer of polyimide covered with a 25 μm thick of B-staged acrylic adhesive. B-staged acrylic adhesive's main function is to join the cover layer to the etched pattern on the base laminate. Pyralux FR8510R offers two main advantages in this project. The first advantage is reduction the amount of wiring required in the work and it increases the toughness of the carbon fibre composite laminates since it has polyimide in its structure [165].

3.1.3 Carbon Fibres

The matrix is responsible for transferring loads between the reinforcing elements in carbon fibre/epoxy composite laminates. Carbon fibres are carrying most of the loads. The mechanical properties of the carbon fibres depend greatly on the precursor used and the processing conditions employed as these factors determine the degree of alignment of the crystals. That in turns means the behaviour of the carbon fibres depend largely on their microstructure. Therefore, the microstructure of the carbon fibres, which were used in this work, was examined using scanning electron microscope as shown in Section 3.2.2. Two types of carbon fibres were used that are Taryfil TC-35 and Toray FT300B.

It is worth to mention the fact that there is limited information provided by the suppliers regarding the processing and conditions that are essential for producing the high mechanical properties carbon fibres. However, plenty of information was concluded from scanning electron microscope (SEM) that was carried out on the two types of fibres, therefore discussions in the following section is built on the information that was obtained from the SEM as well as the information that was provided by the suppliers.

3.1.3.1 Carbon Fibres Tairyfil TC-35

These carbon fibres were supplied in a 2 x 2 mm twill weave fabric, 3000 filaments in a bundle (3K), and 200 grams per square meter (gsm). The mechanical properties are provided by the supplier as shown in Table 3-6. These are ex-PAN carbon fibres. PAN refers to the starting materials that is Polyacrylonitrile. These fibres are produced by extruding the polymer through a nozzle (ex: refers to the extrusion process). The carbon fibre (filament) diameter is 7 μm ; the fibres were examined in the SEM. The examination shows that these fibres have a heterogeneous circular cross-section.

Table 3-6: The physical and the mechanical properties of Tariyfil TC-35 as provided by the supplier.

Property	Value	Unit	Test
Diameter	7	μm	
Density	1.8	g/cm^3	JISR-7601
Tensile strength	3.45	GPa	JISR-7601
Tensile modulus	230	GPa	JISR-7601
Elongation	1.5%		
Electrical resistivity	1.73×10^{-3}	$\Omega.\text{cm}$	
Sizing type	Epoxy		

3.1.3.2 Carbon Fibres Toray FT300B

These carbon fibres were supplied in a form of pre-impregnated carbon fibres with a 2 x 2 mm twill weave. The carbon fibre weight is 275 grams per square meter (gsm), it has 3000 filaments in a bundle. FT300B is an untwisted yarn that made from a twisted yarn through an untwisting process. This grade of carbon fibres is the baseline for the aerospace industry. They are PAN-based carbon fibres. Those carbon fibres have a bean-shaped cross-sectional microstructure with an internal flaw in the structure. It is expected that those flaws have a significant influence on the mechanical and electrical properties as shown in Table 3-7.

Table 3-7: Physical and mechanical properties of FT300B as provided by the supplier.

Property	Value	Unit	Test
Diameter	7	μm	
Density	1.76	g/m^3	TY01
Tensile strength	3.53	GPa	TY-030B-01
Tensile modulus	230	GPa	TY-030B-01
Elongation	1.5%		

Property	Value	Unit	Test
Electrical resistivity	1.7×10^{-3}	$\Omega \cdot \text{cm}$	
Sizing type (FT300B)	Epoxy, Phenolic and BMI		

3.2 Experimental Set ups and Procedures

This section describes the experiments that were undertaken on the materials mentioned above. This section provides details of machines and adjustments, specimen preparations and test standards.

3.2.1 Differential Scanning Calorimetry

It is essential to understand the chemistry (degree of cure) and physics (glass transition temperature) of epoxy resins used in this work. All chemical reactions and many physical transitions are associated with heat generation or heat consumption. Differential scanning calorimetry (DSC) is a fundamental tool in thermal analysis. Simply, DSC looks at how a material's heat capacity is changed by temperature. Where a sample of known mass is heated or cooled and the changes in its heat capacity are tracked as changed in the heat flow. This allows detection of transitions such as melting temperature, glass transition temperature, phase changes and degree of cure. DSC was used to determine the degree of cure for both resin systems (VTC 401 and NI-2 Epoxy Infusion Resin) used and the activation energy for IN-2 infusion resin.

3.2.1.1 Degree of Cure

DSC was used to determine the degree of cross-linking (degree of cure (DOC)) in thermosetting resin systems that were used. A Perkin Elmer 8500 DSC was used to assess the DOC. This is a heat flow DSC, it is power-controlled to measure heat flow. This machine has a double – furnace, one for a reference sample and the other for an actual sample. The movement of heat in and out of a sample is monitored and recorded as a function of temperature and time. To measure the DOC a specimen was placed in a pan in the furnace. The movement of heat in and out of the sample is monitored by temperature sensors. A feedback loop (monitoring change of temperature with time) is used to keep the sample at a given temperature while measuring the power needed to do this against a reference sample. The reference sample consists of an empty closed pan.

3.2.1.1.1 Specimen preparation and differential scanning calorimetry setup

A standard test methodology, ASTM E2160-04, was adopted in the test. A 13 mg sample of liquid IN-2 epoxy infusion resin, or a 13 mg of 100 % uncured prepreg in case of VTC401 was placed in an aluminium pan. The pan was closed by a lid (a closed pan set up was used) then

it was placed in the DSC. The sample was heated at a constant heating rate (isothermal mode) at 10° C/min from the room temperature (25° C) to a target temperature, 250° C as shown in Equation 3-1

$$T(t) = T_0 + \beta_0 \cdot t \quad 3-1$$

Where T_0 is the starting temperature of the run and β_0 the heating or cooling rate. It can be noticed that Equation 3-1 is a linear function between temperature and time. Isothermal mode was used in the experiments, therefore, the term in β_0 in Equation 3-1 is zero. In the isothermal mode if no reactions or transitions take place in the sample, therefore, there is no heat exchanged with the sample and the heat flow rate should read zero. In the reality the heat exchange of the sample and the reference sample are different since they are asymmetric. To obtain precise heat of reactions a baseline run was carried out and then subtracted from the measured curve to obtain the true reaction heat flow rate.

To determine the degree of cure (DOC), a small fragment of cured sample was placed in an aluminium pan then an open pan setup was used. The open pan was placed in the DSC. The sample was heated from the room temperature (25°C) to the targeted temperature 250° C in the isothermal mode at a constant heating rate of 10° C/min. The tests were undertaken according to ASTM E2160-04. The heat of the reactions was calculated for both samples (liquid and solid samples) in order to determine the degree of cure.

3.2.1.2 Kinetic Parameters by Differential Scanning Calorimeter Using Isothermal Method

In a VARTM technique the resin viscosity is an important element to control the infusion process and to obtain a high-quality part. Therefore, the viscosity of the IN-2 epoxy infusion resin was controlled by adjusting the infusion temperature. Hence, infusing of the resin at an elevated temperature will help to reduce the viscosity of the resin and increase the wettability of the resin to the carbon fibres. To estimate the reduction in the resin viscosity due to infusion at an elevated temperature, a method to determine kinetic parameters of the activation energy by DSC using the isothermal method, according to ASTM E2070 – 13 – test method E, was adopted.

3.2.1.2.1 Specimen preparation

5 mg of IN-2 epoxy infusion resin was placed in an aluminium pan (Perkin Elmer, US) and sealed by using a dedicated lid (Perkin Elmer, US). The total weight of the specimen was recorded to the nearest $\pm 10 \mu\text{g}$ and fed to software. Then the specimen was placed along with a reference sample in the DSC, then the DSC sample chamber was closed. Ranges of heating rates were

used (2, 5, 10, 15, 20, and 30°C/min). The sample was heated from the room temperature 25°C to 250°C in an isothermal mode as described above.

3.2.2 Scanning Electron Microscope

Scanning electron microscopy (SEM) was used to determine the relationship between microstructures and electrical properties of PAN-based carbon fibres. SEM is a useful tool for visualising micro-cracks, flaws, voids connected with fibre processing, and porous structures associated with the exfoliation process. The SEM images demonstrate the lamellar organization of graphite layers which may be circumferential or radially oriented.

3.2.2.1 Specimen Preparation

Two PAN-based carbon fibres were examined. The Tairyfil TC-35 (Formosa, Taiwan) was extracted from a 200 gsm 2 x 2 twill weave fabric (Easy Composites, UK). The FT300B (Toray, Japan) fibre was extracted from prepreg VTC401, 275 gsm, 2 x 2 twill wave fabric (SHD Composite Materials, UK) and a sample was placed in 70 % nitric acid for 90 minutes, washed with distilled water then dried in an oven (Thermo Scientific, UK) at 50°C for 1 hour in order to remove the remaining resin. The densities for the carbon fibres Tairyfil TC-35 and FT300B are 1.8 g/cm³ and 1.76 g/cm³ respectively, these values are provided by the manufacturers.

Single fibre samples were prepared by hand under stereo optical microscopy (Zeiss, Germany). An individual fibre was extracted from the carbon fibre bundles. Each fibre was cut using a razor blade (Swann Morton Limited, UK) then bonded onto a piece of silicon 5 x 5 mm (Agar scientific, UK) using conductive carbon tape (Agar scientific, UK) with electrical resistance of 9.5 Ω / (25.4 mm²). The prepared sample is shown in Figure 3-1.

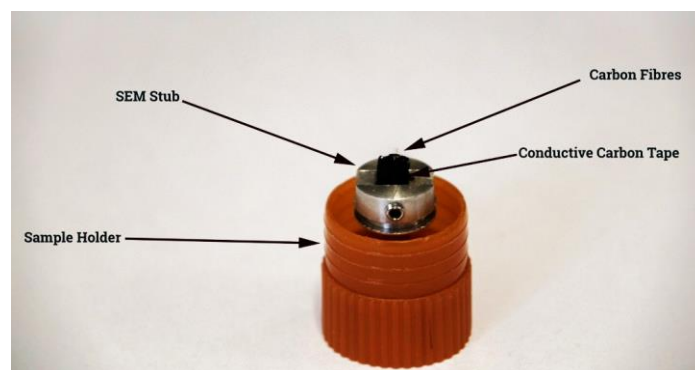


Figure 3-1: Prepared sample for SEM examination

3.2.2.2 Scanning Electron Microscope Setup

Each sample was examined using a high resolution thermal field emission scanning electron microscope, an Inspect F Scanning Electron Microscope (SEM) (FEI, USA). This SEM is operated in the range between 200V – 30 kV. This is an advanced SEM that gives much details of the carbon fibre filament's transverse microstructure due to high vacuum technology that is used in this machine. In addition, the penetration of depth of lower kV electrons into the fibres is less than with the conventional electron microscopes. An Everhardt – Thornley secondary electron detector (ETD-SE) was used to capture the transverse microstructural images. The images dimensions are 1024 x 943 pixels. An extra image processing to adjust the brightness and the contrast of the images was undertaken by using Lightroom CC 2015 (Adobe, USA), the actual image sizes after processing are mentioned on the figures. As it can be noticed from the figures that various magnifications were used to show the carbon fibre filament from different angles. However, the transverse microstructure is responsible for the electrical conductivity in the filament.

3.2.3 Resistivity Measurement of the Sensing System

To prove the reliability of the electrical connection made with the carbon fibre composite laminates. The total resistivity measure by the system was divided into Pyralux FR8510R, connection wires, electrodag 1415 (Agar Scientific, UK), silver epoxy 8331 (MG Chemicals, UK) and carbon fibre composite laminates resistivity. However, electrical resistivity of the measuring system (Pyralux, connection wires, electrodag or silver epoxy 8331) was measured all together at once. This amount of resistivity will be subtracted from the total resistivity to find the real resistivity of the panel. The test was undertaken according to IPC-TM-650-2.5.14A, where the letters IPC denote institution of printed circuit, TM denotes the test manual 650-2.5.14A is a serial number.

3.2.3.1 Resistivity test setup

A four-probe technique was used to measure the resistivity of a 330 X 20 mm strip of Pyralux FR8510R as shown in Figure 3-2. National Instrument mode NI9219 in a chassis NI cDAQ-9172 was used, the accuracy of the system is $\pm 0.1\%$ at the room temperature. The mode was configured to a four-probe electrical resistance method, a default direct electrical current of 500 μA was used, it is found that this amount of electrical current does not generate additional heat in the sample. The electrical resistance readings were taken as shown in Figure 3-3 and then the average reading was considered in the calculations.

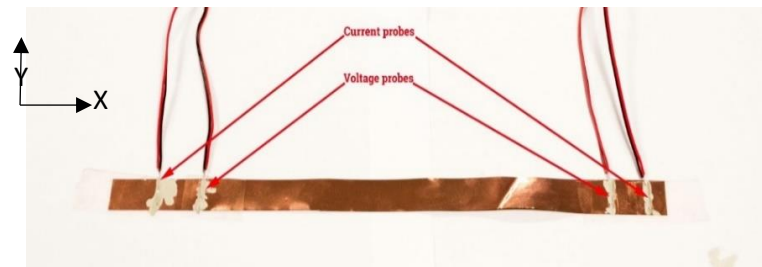


Figure 3-2: Photograph showing a representation of the four-probe technique.

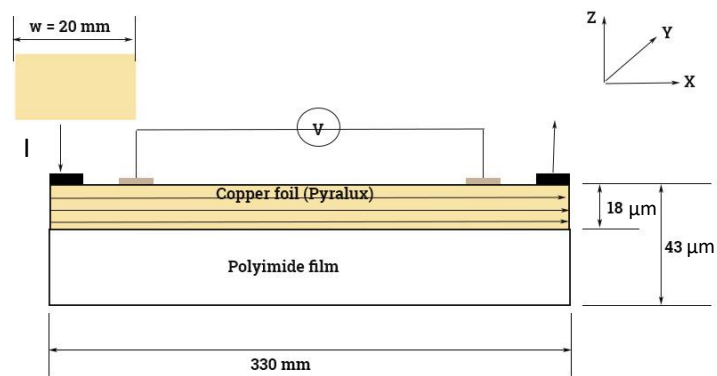


Figure 3-3: Schematic model of the experimental setup that is used to measure the resistivity for Pyralux FR8510R. The thickness dimensions have been magnified for the purpose of clarifications.

RESULTS OF CHARACTERIZATION PROCEDURES FOR RAW MATERIALS

This chapter presents results and discussions of the characterization methods that were described in the previous chapter. The analytical calculations and the diagrams of degree of cure (DOC) for resin systems are explained and discussed. The governing equations and the analytical calculations and the Arrhenius plot to determine the activation energy for IN-2 epoxy infusion resin are also given. The carbon fibres cross-sections were examined using the scanning electron microscope (SEM), and the images are presented in this chapter. The resistivity of Pyralux FR 8510 was also examined, and the results are shown here.

4.1 Differential Scanning Calorimetry

4.1.1 Degree of Cure

The DSC graphs for resin systems IN-2 epoxy infusion resin, and VTC401 are presented in Figure 4-1 and Figure 4-2 respectively. These graphs have been obtained by heating uncured epoxy resin systems at a rate of 10°C/min. It can be seen from the graphs that with the increase in the specimen temperature, the epoxy resins undergo curing and where a large exothermic peak can be observed, in case of liquid resin, and a small peak, in case of cured samples. It can be seen from the graphs that the resins have gone through irreversible chemical reactions during heating-cooling cycles.

The temperature at which the heat flow curve deviates from a linear response is considered the temperature at which the cure has onset. The exothermic peak reflects the maximum rate of curing of the epoxy resin. It is worth to mention here that the test was undertaken using a Perkin Elmer 8500 DSC, the Perkin Elmer DSCs shows exothermic peaks as down. At the end of the curing reaction (crosslinking), the DSC heat flows return to quasi-linear behaviour. The heat of the reaction can be calculated by integrating the area under the exothermic curve. Equation 4-1 was used to calculate the degree of cure (DOC). It was found that the DOC for IN-2 Epoxy infusion resin is 95 % and the degree of cure for VTC401 is 94 %.

$$\text{DOC} = \frac{\Delta H_{\text{liq}} - \Delta H_{\text{sol}}}{\Delta H_{\text{liq}}} \times 100 \quad 4-1$$

Where ΔH_{liq} is the enthalpy of liquid resin and ΔH_{sol} is the enthalpy of solid resin.

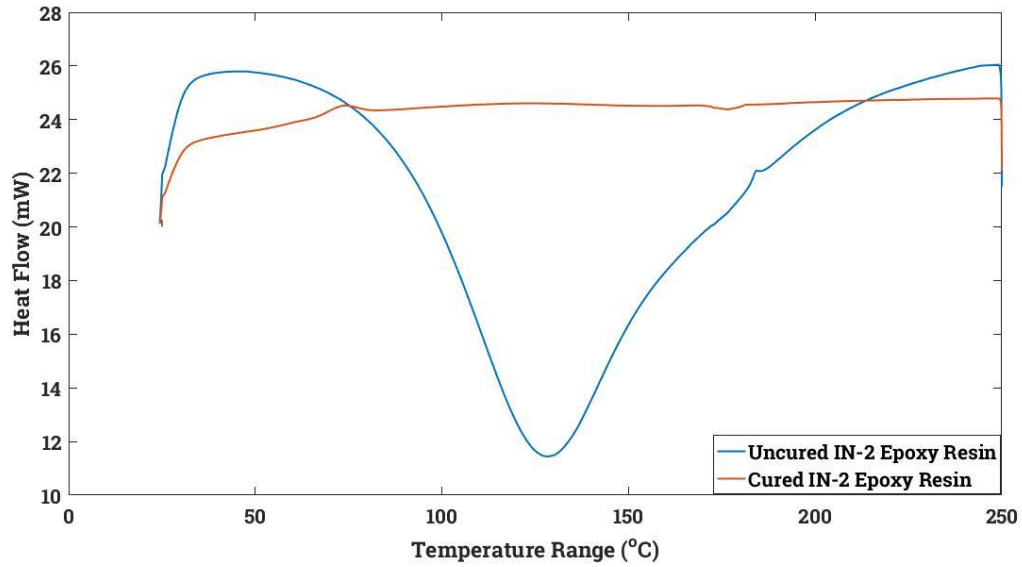


Figure 4-1: Curing reaction IN-2 Epoxy infusion resin as function of temperature.

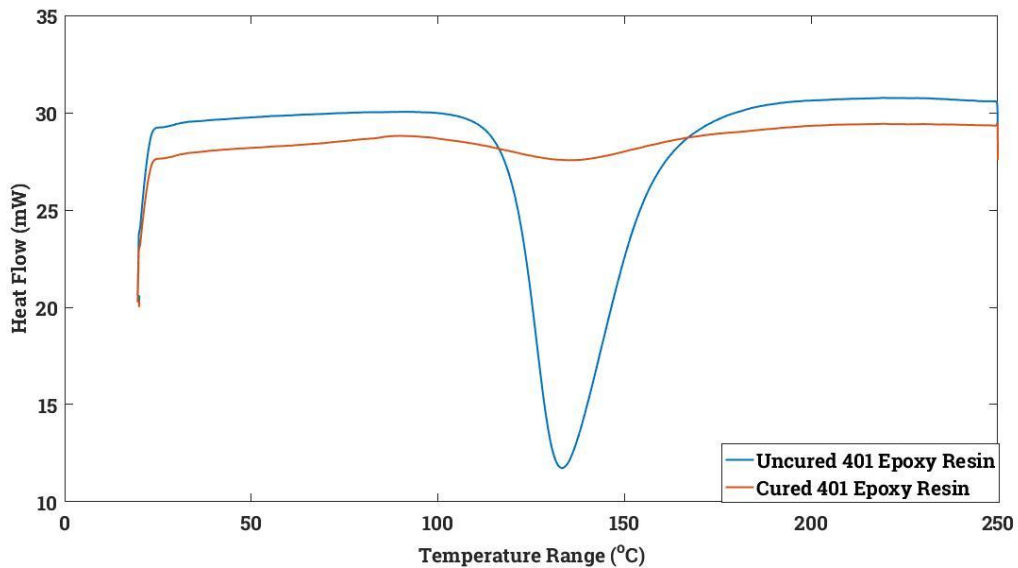


Figure 4-2: Curing reaction of VTC401 resin as function of temperature.

4.1.2 Kinetic Parameters by Differential Scanning Calorimeter Using Isothermal Method

Equation 4-2 represents a direct relationship between the resin viscosity and the temperature [200].

$$\mu = \mu_0 \exp\left(\frac{E}{\psi T}\right) \quad 4-2$$

Where E , Ψ , T and μ_0 are the flow activation energy (J/mol), the universal gas constant (8.314 J/mol. $^{\circ}$ K), the absolute temperature ($^{\circ}$ K) and the viscosity constant (Pa.s) respectively.

The relationship in Equation 4 – 2 showed that the viscosity of the resin can be managed effectively by the infusion temperature. To measure the effect of the infusion temperature on the IN-2 epoxy infusion resin, the activation energy need to be calculated. Therefore, an Arrhenius plot was drawn, the Arrhenius plot represents a logarithmic heating rate versus the inverse of the glass transition temperature, as shown in Figure 4-3.

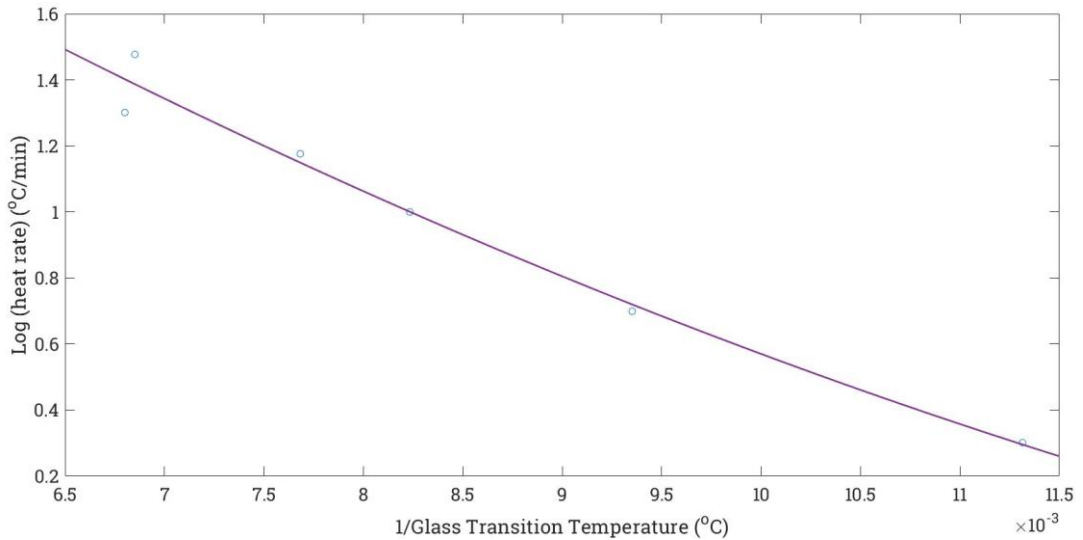


Figure 4-3: Arrhenius plot that represents the relationship between the heating rate and glass transition temperature for IN-2 Epoxy infusion resin.

By applying the Equation 4-3, the activation energy was found to be 37.151 kJ mol $^{-1}$

$$E = \frac{\Psi}{0.4567} * \frac{\Delta \log \beta}{\Delta (1/T)} \quad 4-3$$

A relationship between the heating rate (β) and glass transition temperature (T_g) was established for IN-2 epoxy infusion resin

$$T_g = 98.27 + 2.44 * \beta - 0.09 * (\beta - 13.66)^2 \quad 4-4$$

By applying Equation 4-2 at the room temperature the viscosity constant was found, by substituting the viscosity constant in Equation 4-2 the resin viscosity at the infusion temperature (313.15 $^{\circ}$ K) was found to be 27.88 mPa.s.

4.2 Scanning Electron Microscope Characterization

The transverse cross-section for each fibre was examined using SEM as shown in Figure 4-4 and Figure 4-5 and as described in Section 3.2.2. Figure 4-4 represents Formosa Tairyfil TC-35. It can be observed in the figure, that the fibres have a circular cross-section, the heterogeneity

can be observed too. The structure is mixed of radially oriented sheet-like structures in the core, granular and random structures towards the skin of the fibre.

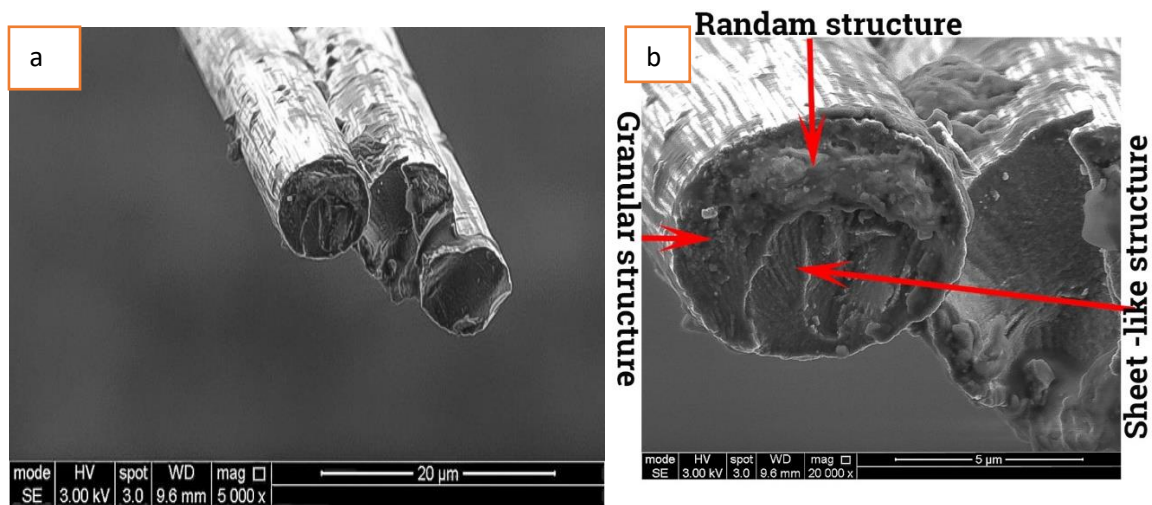


Figure 4-4: SEM micrographs of carbon fibres showing the surface and transverse cross section of Formosa Tairyfil TC-35. a. shows a low magnification image b. shows a high magnification image where the transverse cross section features appear clearly. Image dimensions is 1024 x 943 pixels.

Figure 4-5 shows Toray FT300B carbon fibre. It is noticed that the transverse cross section of this type of carbon fibre is distorted oval and it contains a particulate or a granular structure. The distinct differences in the structures of carbon fibres is attributed to graphitization at different heat treatment temperatures.

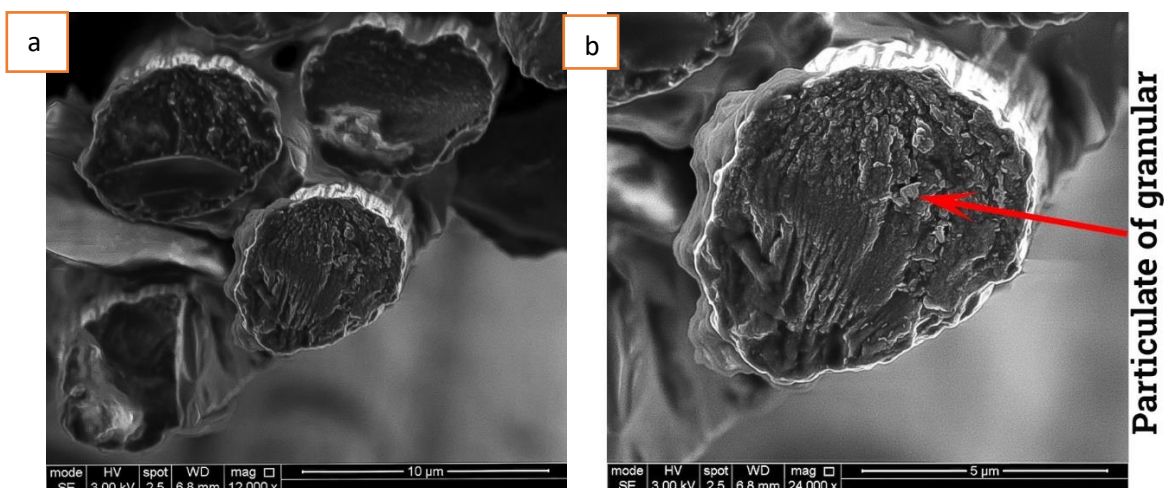


Figure 4-5: SEM micrographs of carbon fibres showing the surface and transverse cross section of Toray FT300B. a. shows a low magnification image 12000x b. shows a high magnification image 20000x where the transverse cross section features appear clearly. Image dimensions is 1024 x 943 pixels.

All the electrical resistivity tests on carbon fibre composite laminates were undertaken at the room temperature (20°C). It is expected that the defects that are shown in the carbon fibre

structure in Figure 4-4 and Figure 4-5 will have a significant impact on the electrical resistivity of the carbon fibre since they may cause a considerable electron scattering. It is expected that the defects, in addition to the electric contact resistance may cause a high resistivity reading as will be shown in electrical resistance results in Section 7.2.3. The electrical resistivity of Toray FT300B and Tairyfil TC-35 are close in value due to the similarity in the transverse cross-section that are (17×10^{-3} and $17.3 \times 10^{-3} \Omega \cdot \text{cm}$ respectively).

4.3 Sensing System Resistivity

The measured resistivity of the whole sensing system, including sensing mats, interconnection and wiring, is $0.499 \times 10^{-8} \Omega \cdot \text{mm}$. The Pyralux FR8510R is made of wrought copper foil. In the wrought condition the grains are distorted in the longitudinal direction and copper that is formed has a high tensile strength, is fairly hard, and has a relatively low elongation [201]. It is expected that a big part of this resistivity was attributed to Pyralux FR8510 as well as the silver paste that was used to attach the flexible circuit boards to the carbon fibre composite laminate panels.

Chapter 5

PRODUCTION OF COMPOSITE PANELS

This chapter describes methods used to produce carbon fibre composite laminate panels using the materials selected in Section 3.1, consumables and variables affecting the manufacturing techniques are also discussed thoroughly.

5.1 Vacuum Assisted Resin Transfer Moulding

This section discusses the production of carbon fibre composite laminates using a vacuum assisted resin transfer moulding (VARTM) technique. The materials used in this technique were mentioned in Section 3.1. The consumables and manufacturing variables such as the resin infusion temperature, the infusion speed, the vacuum pressure, and curing schedules are presented in this section.

5.1.1 Fabricating Process

PAN-based woven twill 2 x 2 mm carbon fibre Tairyfil TC-35 was used to make the carbon fibre composite laminates. Two types of laminates 200 x 200 x 1.09 mm (VB panel) and 200 x 200 x 2.06 mm (VC panel) were fabricated. The set up for a VARTM is illustrated in Figure 5-1. The arrangement of the preform is made in the following way:

1. Carbon fibre plies were placed between two layers of peel plies measuring 300 x 300 mm, (Econolease, Tygavac, UK). Peel plies were cut larger than the carbon fibre plies for easy release from the aluminium plate.
2. A layer of a breather fabric measuring 300 x 300 mm (Air Weave N-10 (AWN-10), Tygavac, UK) was applied on the top of the peel ply.

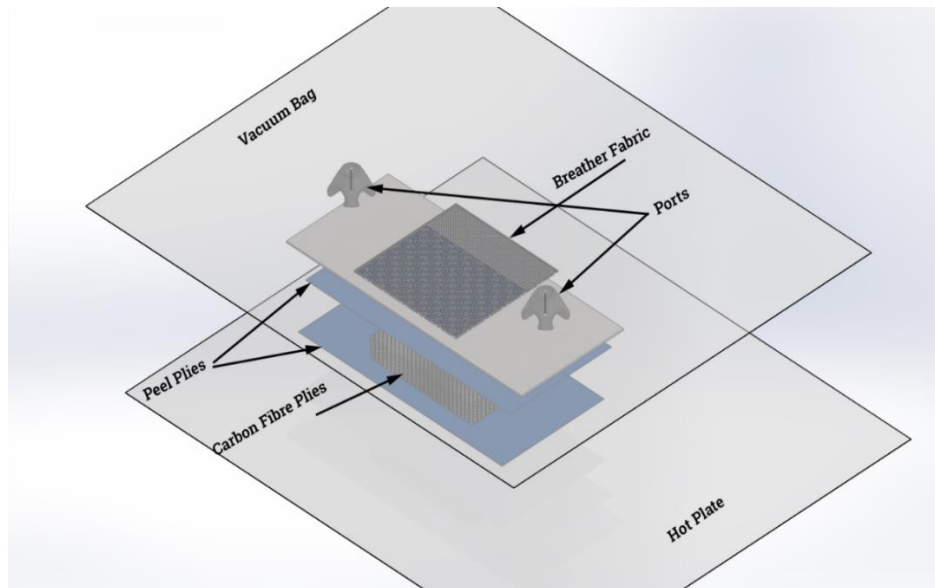


Figure 5-1: A typical schematic diagram shows the setup for a VARTM technique.

Typically, resin distribution mediums are used to enhance and speed up the infusion process, but they are not used in this setup, as the laminates are small in size, and it was found to be unnecessary. In addition, it is found that using the resin distribution mediums will cause dry spots on the upper surface since they are making a direct connection with the vent from one side and the preform from the other side. The breather fabric helps to distribute the pressure inside the vacuum bag evenly and consequently that helps to obtain uniform thickness panels. It is therefore found that removing the distribution medium helps to prevent formation of dry spots by increasing the resin pressure and ensuring a uniform flow front.

Plastic tubes (Easy Composite, UK) were used to inject the ultra-low viscosity resin into the preform. The resin used in this work is IN-2 epoxy infusion resin (Easy Composites, UK). Helical open tubes were used as a resin injection line source on one end and a resin and air collector on the other end. The helical tubes used in this work is commercially called Resin Infusion Spiral Medium Flow 4.5 mm (EasyComposite, UK) as shown in Figure 5-2. Two ports were placed on to the preform, one is resin injection port and the other is a vacuum port. The resin injection port was connected to the helical pipe and they were placed on to the breather fabric. A quick and simultaneous resin infusion into the preform was maintained using set up as shown in Figure 5-2. The vent port was placed slightly away from the preform on top of the peel ply to prevent direct competition against the dry fibre preform for the resin supplied from resin inject port.

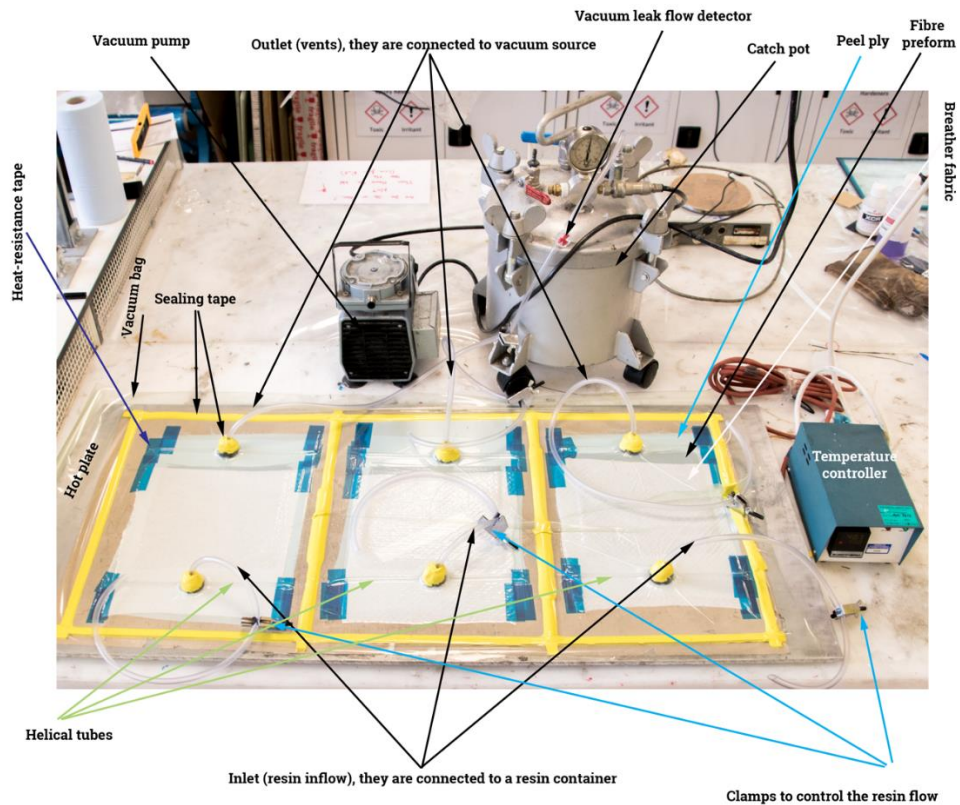


Figure 5-2: A typical vacuum assisted resin transfer moulding setup.

The preform was enveloped by a vacuum bag, which consists of a plastic film, (Wrightlon 7400, Tygavac, UK) that is capable of withstanding temperatures up to 204°C. A sealant tape, (AT-200Y, Tygavac, UK) was used to seal the film to the hotplate. The maximum use temperature for this product is 204°C. However, the infusion was undertaken at 40°C. Flexible plastic pipes are connected to ports on both resin injection and vacuum sides. The plastic pipe, that is linked to resin injection port, goes to the resin container and the plastic pipe on the other side goes to a catch pot that in turn connects to a vacuum pump as shown in Figure 5-2.

The infusion was carried out at a constant pressure of 0.95 bar (95.95 kPa). It was found during the experiments that this pressure was enough to compact the preform and to obtain relatively high fibre volume fraction of 50% by volume. Debulking process was undertaken during the work, that allows better compaction of the fibre preform by cyclically compressing and relaxing it. In this process the vacuum pressure was applied on the preform for five minutes then the inlet was opened to let air in to the preform then the pressure was applied again. This process was carried out for three times. It was found that this helps to obtain panels with uniform thickness. Before the infusion process the ultra-low viscosity resin, IN-2 epoxy infusion resin, was mixed manually then degassed using a vacuum oven (Gallenkamp, UK) for ten minutes. To

reduce the viscosity and ensure a low micro-void content, the resin infusion process was undertaken at 40°C.

The viscosity was decreased from 225 mPa.s to approximately 27 mPa.s by this level of heating, more details are mentioned in Section 3.1.1. The resin flow rate was adjusted by opening the clamps slightly as shown in Figure 5-2. Once the resin reaches the vacuum port, it is allowed to bleed out for five minutes to wash out all the air bubbles from the resin flow front and entrapped air bubbles in the preform. Then the resin injection port was clamped off and the resin was left to partially cure at the room temperature for 24 hours then the carbon fibre composite laminates were removed and post-cured in an oven (Heraeus Instruments GmbH, Germany), the curing schedules are shown in Table 5-1.

Table 5-1: The curing schedules for the epoxy resin system.

Temperature (°C)	RT	40	50	60
Time (Hour)	24	6	6	12

The infusion time is a function of the preform thickness, hence, 20 and 10 minutes was the infusion time that was required to obtain 200 x 200x 2.06 mm (AC panel) and 200 x 200 x 1.09 mm (AB panel) respectively. That included 5 minutes to washout the air bubbles from the preform. No dry spots were noticed on the final panels, which was due to simple panels shape and the resin system that was used (the resin system was discussed in Section 3.1.1) which has 8 to 11 hours gelation time at 25°C. A low micro-voids content was observed in the panels due to use a breather fabric instead of resin distribution medium, where the breather fabric slows the infusion process. Therefore, it reduces the dual scale flow behaviour due to the slow speed of resin infusion that happens between the plies. Dual scale flow behaviour occurs due to the difference in the flow patterns [57, 71, 72]. There are two flow patterns occurring, these being flow inside the fibre tow which is dominated by the capillary effect, and which is significantly slower than the other that happens between the fibre tows and it is governed by Darcy's law.

5.2 Autoclave processing

This section will discuss the production of the carbon fibre composite laminate panels using an autoclave processing technique. The properties of materials (carbon fibres, and epoxy resins) used in the autoclave processing fabricating technique were discussed in 3.1.3. The cutting

of prepreg sheets, the layup technique, bagging, and curing cycles are discussed in the following section.

5.2.1 Fabricating Process

Pre-impregnated carbon fibre (prepreg) VTC 401 (SHD composites, UK) was used to make carbon fibre composite laminate panels. The prepreg sheets were cut using a scalpel (Swann Morton, UK) in to 200 x 200 mm². Hand layup technique was used to stack the prepreg sheets. The prepreg sheets were then placed onto a steel plate, which is covered by a polytetrafluoroethylene (PTFE) sheet to avoid sticking. Then a hot air jet from a hair dryer was applied on each prepreg sheet to soften the uncured resin and improve the stickiness before laying of the consecutive sheets. A squeegee was used to consolidate this sheet along the fibre direction. The prepreg used were woven reinforced carbon fibre/epoxy, therefore, the consolidation process was carried out in the weft and warp directions.

After the layup process, the prepreg stack was covered with various layers of cloth. The first layer was a bleeder (Econolease, Tygavac, UK) that assists to achieve an optimal fibre volume fraction by absorbing excess resin. The second layer is breather (Air Weave N-10, Tygavac, UK) that provides a path for removal of the air and volatile gasses from the component during the cure. Then the assembly was sealed inside a vacuum bag (Wrighton 7400, Tygavac, UK) as shown in Figure 5-3. The tool and assembly were then placed in the autoclave (Premier Autoclave and Solution, UK). In order to cure the panel, the curing cycle is shown in Figure 5-4.

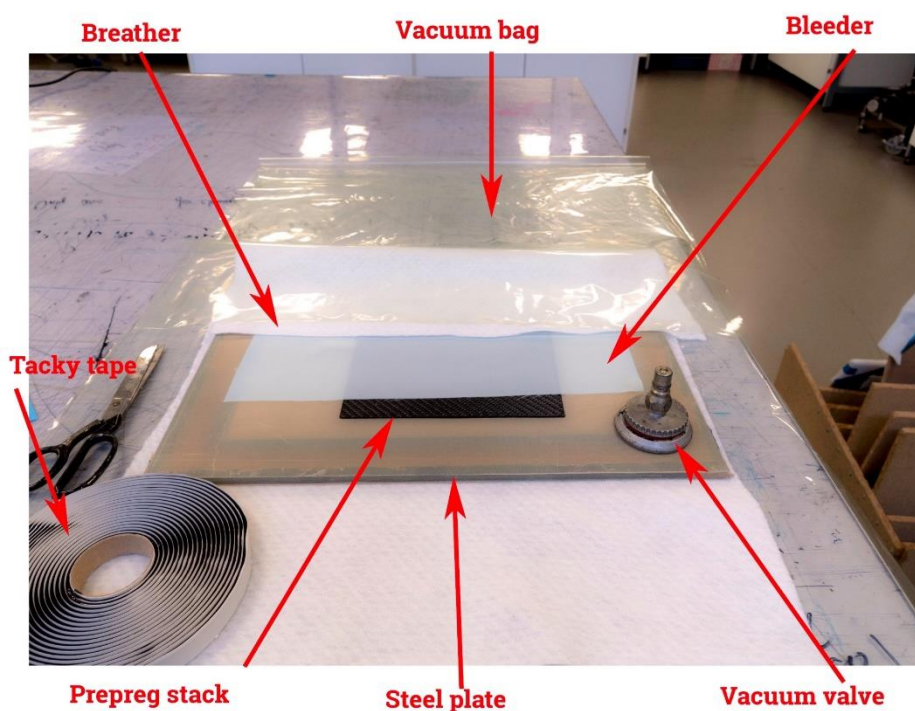


Figure 5-3: Prepreg stacks prepared for autoclave processing.

Initially, inside the vacuum bag a uniform vacuum pressure was applied (101 kPa) to consolidate the prepreg stack and remove the air and volatile gasses. Inside the autoclave chamber, the vessel was filled with a compressed gas at a rate of 0.2 bar/min. The pressure inside the pressure vessel helps to consolidate the prepreg stack and it normally remains on until the end of the curing cycle. When the external pressure (the pressure inside the vessel) increases to higher than 202 kPa (2 bars) the vacuum pressure inside the bag stops working, therefore, the vacuum pressure was set to vent as shown in Figure 5-4. Otherwise, the external pressure might damage the vacuum system in the autoclave.

The temperature inside the autoclave was increased gradually at a rate of 2°C/min to the cure temperature. The cure temperature for the prepreg VTC 401 is 120°C for 45 minutes followed by post curing at 135°C for 120 minutes as shown in Figure 5-4. The autoclave was set to cool down to the room temperature then the assembly was taken out of the chamber the panels were peeled off and prepared for further processing. Composite laminate panels with four various thicknesses were prepared. The panels were AB, AC, AD, and AE with thickness 0.84, 1.64, 2.54, and 3.5 respectively. The composite panels passed through further processing stages prior to convert them to smart composite panels.

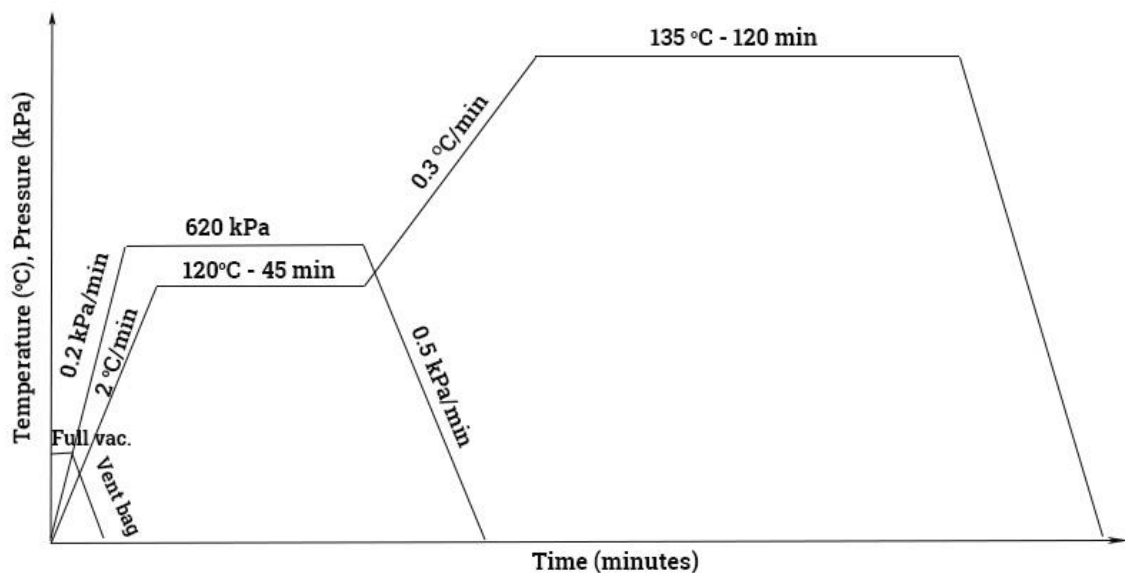


Figure 5-4: Autoclave processing cycle for prepreg VTC 401.

5.3 Producing Sensing Mats

The main goal of this work is to make a reliable, robust, repeatable and applicable self-sensing system. Sensing mats have replaced connection wires to make electrical connections with carbon fibre composite laminates. The materials used to make the sensing mats were chosen carefully as discussed in Section 3.1.2, therefore no reduction in mechanical properties of the CFRP laminates will occur. Section 5.3.1 describes the stages to produce sensing mats from the design stage to ready-to-use sensing mats.

5.3.1 Fabricating Procedure

The first step to make sensing mats is to design artworks. The artworks were designed using photo editor software Photoshop CC 2017 (Adobe, USA) as shown in Figure 5-5 and Figure 5-6 for sensing mat 1 and mat 2 respectively. The electrodes sizes, the tracks width, the distances between tracks and pads sizes were fixed for all sensing mats, they are either 10 x 10 mm or 20 x 20 mm, 1 mm, 2 mm and 2 x 2 mm respectively. The artworks were printed at 1:1 ratio on an A4 translucent polyester drafting film, commercially called LaserStar (Mega Electronics, UK). The software allows print mirror images of the artworks, that means the black areas of the artworks will be in contact to the flexible circuit boards' photo-sensitive side during UV exposure as shown in Figure 5-7.

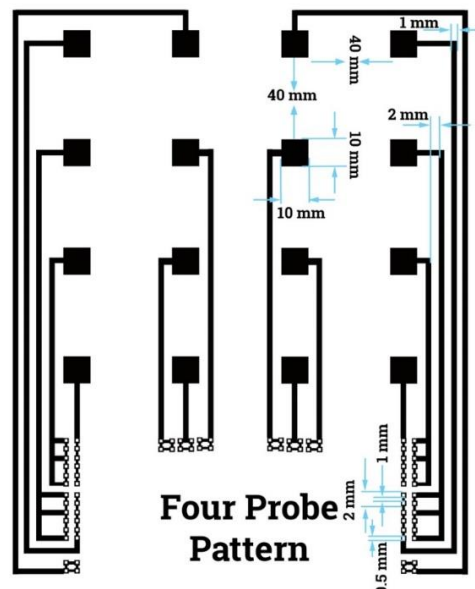


Figure 5-5: Sensing mat 1 designed using Photoshop CC 2017.

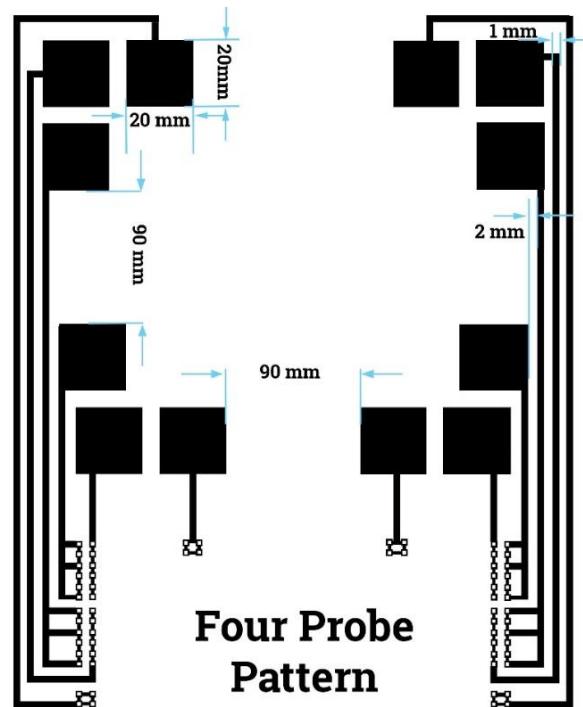


Figure 5-6: Sensing mat 2 designed using Photoshop CC 2017.

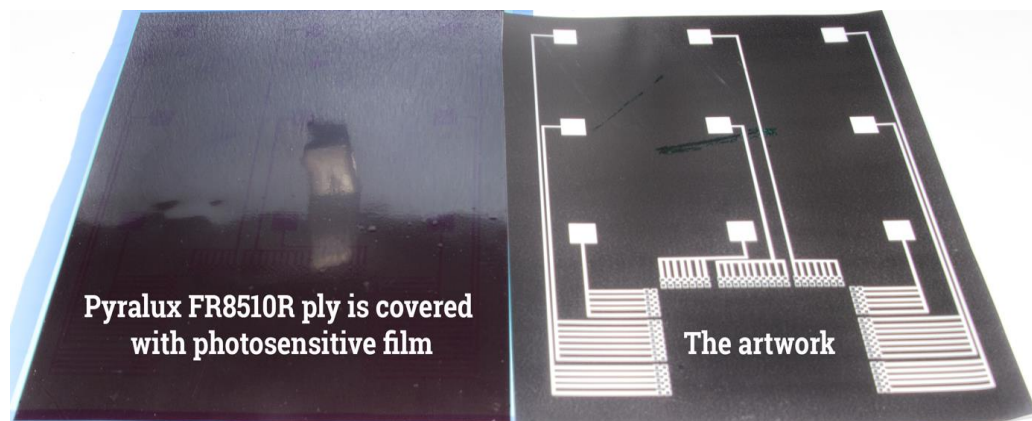


Figure 5-7: Preparation steps for producing sensing mats that are designed specifically for damage sensing in carbon fibres composite laminates. The image on the right shows the artwork for the sensing mat that is going to be printed on the Pyralux FR8510R covered with photosensitive film that is shown in on left image.

The photosensitive side of the flexible circuit was made by applying a photo-sensitive film (dry film) (Mega Electronics, UK) on the copper side of the Pyralux FR8510R (Figure 5-8). Where a layer of Pyralux FR8510R and the photo-sensitive film were cut by a pair of scissors to desired dimensions as shown in Table 5-2. As seen in Table 5-2 and Figure 5-8, the reason the dry film was cut to bigger sizes than the Pyralux FR8510R sizes is to ease removing the plastic film which is required prior to the developing stage.

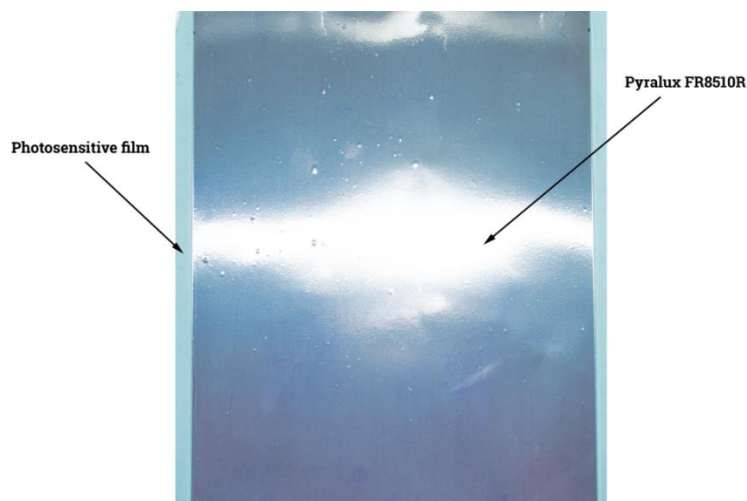


Figure 5-8: Pyralux FR8510R that was covered with photo-resistive film.

Table 5-2: Pyralux FR8510R, Coverlay FR0110 and Dry film dimensions corresponding to sensing mat sizes

Sensing Mat	Pyralux FR8510R dimensions (mm)	Dry film dimensions (mm)	Coverlay FR0110 dimensions (mm)	Sensing mats sizes (mm)	Electrode dimensions (mm)
Mat 1	235 x 200 x 0.043	250 x 160	235 x 140 x 0.025	200 x 200 x 0.068	10 x 10 x 0.018
Mat 2	220 x 200 x 0.043	240 x 160	220 x 140 x 0.025	200 x 200 x 0.068	20 x 20 x 0.018

The combination of Pyralux FR8510R and the dry film were put inside a vacuum bag and then they are placed in an oven, (Heraeus Instruments GmbH, Germany) at 60°C under 101 kPa of vacuum pressure for two hours. It was found that a 3-5°C/min heating rate will maintain the light sensitivity of the dry film. Then the combination of Pyralux FR8510R and the dry film were exposed to UV light using a UV exposure unit (RS Components, UK) for 40 seconds. The protective plastic film was removed from the surface of the dry film prior to developing the exposed sensing mats in a printed circuit board (PCB) etcher (Mega electronics, UK). Then UV exposed boards were placed in a basket holder and immersed in a potassium carbonate solution, that is commercially called Dry Film Photoresist Developer (Conc.) (MEGA Electronics, UK). Potassium carbonate was diluted in distilled water, the dilution ratio is 25:1 (25 parts of distilled water to 1 part of potassium carbonate). The development process occurred at 28°C in the PCB etcher for 15 minutes. Since the artworks were negative, so the dry film removed from all areas apart from areas that were exposed to UV light (electrodes, tracks and pads areas) as shown in Figure 5-9. The developed sensing mats were taken out of the developing tank in the PCB etcher and washed by low pressure water jet at the room temperature. The developed and washed sensing mats were then placed into the basket holder and immersed in the etching tank in the PCB

combination was enveloped in a vacuum bag then placed in an oven (Heraeus Instruments GmbH, Germany) to cure the B-staged acrylic adhesive. The acrylic adhesive was cured at 70°C for 2 hours under 1 bar of pressure. After cure, the peel strength between the coverlay FR0110 and the Pyralux FR8510R was 1.6 N/mm measured according to IPC-TM-650. That peel strength should be enough to prevent any conductive liquids, that will be used to attach the sensing mats to the surface of carbon fibre composite laminates, from penetrating between the coverlay and the sensing mats.

5.4 Attaching Sensing Mats to the Carbon Fibres Composite Laminates

This is the first stage in the process of converting conventional carbon fibre composite laminates panels to smart materials. A good quality electrical contact between the carbon fibre laminate made using VARTM and autoclave processing and the sensing mat this was necessary for electrical sensing analysis. Preparation starts with trimming the sharp edges of the sample that were formed during the VARTM technique. That was followed by grinding and then polishing stages as will be described in the below section. The same method that was described below was applied on prepreg carbon fibre laminates.

5.4.1 Attaching Sensing Mats to Carbon Fibre Composite Laminate Panels Using Conductive Epoxy

A rough grinding for carbon fibre laminates was required to remove the artefacts that were formed because of the nature of the manufacturing technique. Where the samples were in contact with rough surfaces (peel plies), more details about VARTM and autoclave processing setups were described in Section 5.1 and Section 5.2. The rough grinding step was essential to remove the epoxy layer from the surface that will be in contact with the sensing mat. This step started with using 240 grit SiC papers with presence of coolant (water) at the room temperature, where the water has two functions. The first function is dissipating the heat generated due to friction between the abrasive and the sample's surface, the second function is to hold the dust that is generated during the erosion process.

The samples were then ground using 240, and 600 grit silicon carbide (SiC) papers (Metprep, UK) and polished using 1200 grit silicon carbide papers (Metprep, UK). A cleaning grade of isopropyl alcohol (Sigma Aldrich, UK) was used to remove any particulates from the surface. A 10x magnifier (Zeiss, UK) was used to ensure that the epoxy was removed from the targeted area. The grinding and polishing procedure were undertaken by hand since the size of the sample helped to do it manually rather than using automated grinding machines. To maintain a high-

quality flat surface the sample held from one side by one hand and the grinding step starts from one side all the way up to the other side repeatedly in warp then in weft direction consecutively as shown in Figure 5-10. Then the sample was washed with water then dried in the air, then washed using Isopropyl alcohol between each stage. Figure 5-11 shows the final samples before attaching the sensing mat to the panels.

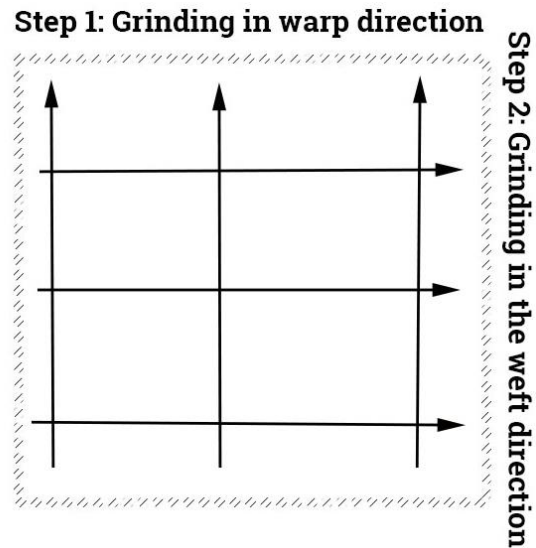


Figure 5-10: Schematic representing directions of grinding and polishing steps.



Figure 5-11: Graphs showing the finish of the same sample before and after abrasion process.

To measure the resistance of carbon fibre composite laminate panels, efficient electrical contacts are vital for this technique, therefore the panels have passed through many preparation stages (as discussed above) before attaching the sensing mats to their surfaces. Contacts were applied with Silver-Epoxy conductive adhesive. Vacuum pressure was applied on the panels to ensure good electrical contacts between them and the sensing mats. Silver-Epoxy conductive adhesive 8331S was a two-component 1:1 mixing ratio silver epoxy paste (MG Chemicals, UK), that cured at the room temperature to form a polymer with a high thermal conduction $10 \text{ W}/(\text{m}\cdot\text{K})$, and low resistivity $0.0010 \mu\Omega\cdot\text{cm}$; It adheres to the carbon fibre/epoxy composites efficiently. This material achieved an operational cure at five hours at room temperature and full cure at 24 hours. It has a strong resistance to water, brine, acids, bases and aliphatic hydrocarbons.

A small quantity of epoxy silver paste was placed carefully on the electrodes (1 g on each electrode in sensing mat 1 and 1.5 g on each electrode in sensing mat 2). Care was taken to ensure all the electrodes were covered with the same amount of the epoxy silver paste. Then the panels were placed onto the sensing mats and were enveloped in a vacuum bag. 101 kPa of vacuum pressure was applied inside the vacuum bag for 24 hours as shown in Figure 5-12. Then the panels were taken out of the vacuum bag for further processing. It was found that the panels were able to undergo further handling and testing when they had been left under the vacuum pressure for 24 hours. The smart carbon fibre composite laminate panel is shown in Figure 5-13.

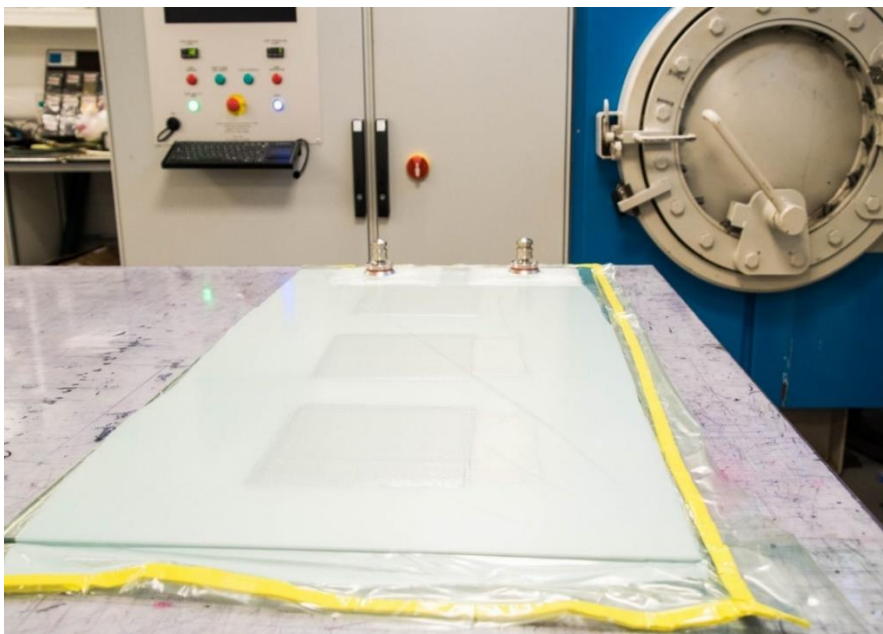


Figure 5-12: The panels were enveloped in a vacuum bag and subjected to 1 bar of vacuum pressure.

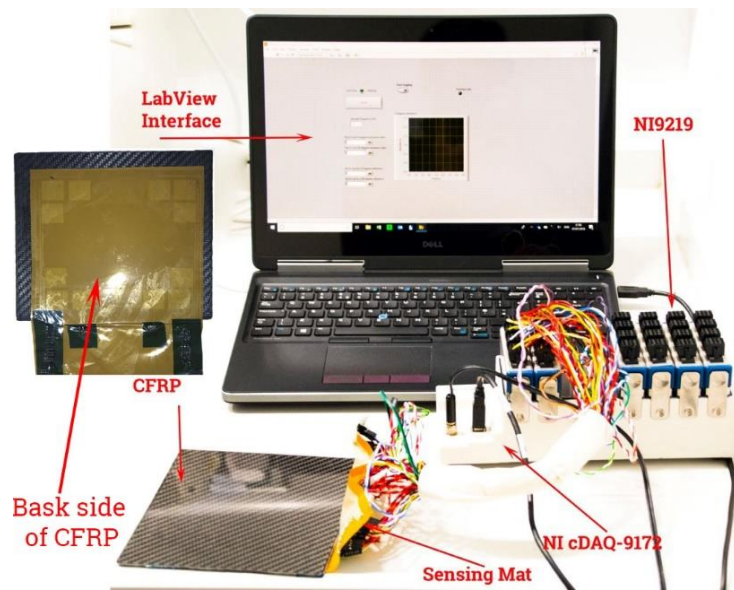


Figure 5-13: Experimental set ups for electrical resistance measurements of a test specimen before being subjected to a low velocity impact test.

Chapter 6

EXAMINATION OF COMPOSITE PANELS

6.1 Specimens and Experimental Procedures

6.1.1 Microscopical Examination of Carbon Fibre Composite Laminate Panels

The optical microscope was adapted in this work to examine electrical contacts between adjacent plies. The electrical contacts are essential to understand electrical conduction in through – thickness direction and understand the damage detection mechanism in the electrical resistance sensing technique in carbon fibre composite laminates. In addition, epoxy resin rich areas and void distribution have been investigated for all types of carbon fibre composite laminates used in the experiments. The following section describes the specimen preparations and optical microscope used.

6.1.1.1 Specimen preparation and optical microscope setup

The specimens (AB, VB, AC, VC, AD, and AE) were sectioned to a manageable size 18 x 18 x t mm, where t is the specimens thickness that is 0.84, 1.09, 1.63, 2.06, 2.54, and 3.5 mm respectively. The specimens were sectioned in the z-axis (through – thickness direction), with a diamond cutter being used. The sectioning was undertaken in the presence of water (the water was used as a cutting fluid and coolant at the same time) to maintain the temperature of the specimens at the room temperature and to avoid creating or altering the artefacts of the specimens. The rotation speed of the diamond cutter was fixed at 3000 rpm (no load speed) while the linear speed of the sample was adjusted manually. The linear speed was low to avoid damaging the specimens. After cutting the specimens were washed by water to remove any remaining particulates after cutting, then dried in an oven (Thermo Scientific, UK) at 50°C.

The specimens were mounted in a mounting compound, EPO-SET resin (Met Prep, UK). The specimens were labelled on the mounting mould during curing then documented on the side opposite to the polishing face during the preparation stage. Thin tip, black colour permanent markers were used to label the mould during the mounting stage. A red colour permanent marker was used to label the specimens during the polishing stage. The purpose behind using different markers was to get a good contrast on the parts. The specimens were mounted in a 23 mm circular plastic moulds (Metprep, UK). The moulds were lubricated using Vaseline oil as a mould release agent. The casting resin used was a two-part resin system that comprises a

resin and a hardener. This is a cold mounting resin; its curing time is 4-5 hours at room temperature. It was noticed that the resin system used in this work gives a good edge retention.

An automated grinder and polisher machine, EcoMet 250 Pro (Buehler, USA) was used. The specimens passed through many grinding and polishing stages to eliminate sectioning and mounting induced artefacts. These stages were essential to adjust the level where the desirable information was found. The grinding and polishing stage started with rough grinding to obtain a planar surface. Silicon carbide papers 600 grit was locked on a planar polishing wheel as described in Table 6-1. Water was used to displace the removed particles. In addition, the water cools down the temperature of the sample and maintain it at the room temperature reducing the heat damage. A 60 RPM head speed and 150 RPM platen rotation speed were used. The head rotation was complimentary to the platen rotation, it was found that this increases the removal rate of the specimen surface without damaging the composite. The head speed was constant during all grinding and polishing stages, where the platen rotation speeds were varied as shown in Table 6-2 and

Table 6-3. The pressure on the sample surface was essential to increase the sample removal rate. The pressure on the sample surface was 25 N that pressure was fixed during all grinding and polishing stages. The grinding and polishing times that are mentioned in Table 6-2 and Table 6-3 are typical for carbon fibre/epoxy composite laminates, however, they were adjusted slightly depending on the condition of the sample surface.

An automated rough polishing stage followed the rough grinding stage to further remove the specimen surface. The rough polishing stage started using cloth (Planocloth H) (Metprep, UK) with 9 μm water-based diamond abrasive suspension. The Planocloth H was locked on the platen rotation of the polishing machine then a small quantity of the abrasive suspension was applied on the surface. The platen rotation speed was fixed in this stage on 250 RPM and the polishing time was 4 minutes. The next stage consisted of using 6 μm water-based abrasive diamond suspension with special type of cloth that (Planocloth). In this stage, the polishing process was the same as mention above, but the polishing time was less than the first polishing stage, 3 minutes.

The next stage transitions to polishing using napless cloths (Durasilk, Metprep, UK), with the 0.06 μm of silica suspension. A small quantity of the silica suspension was applied on Durasilk, the cloth was kept wet with the silica suspension to avoid damaging the specimen since this type of cloth does not retrain lubricant. The platen rotation was fixed at 100 RPM and the polishing time was 5 minutes as shown in Table 6-2. The final polishing stage included using ultra

fine cloth (Chemocloth) with 0.06 μm of silica suspension (Silco, Metprep, UK). The platen rotation speed was fixed at 80 RPM and the polishing time was 2 minutes.

Table 6-1: The primary abrading stage

Surface	Abrasive	Pressure (N)	Head Speed RPM	Plate Speed RPM
SiC paper 600 grit	Water	25	60	150-comp

Table 6-2: The secondary abrading stage

Surface	Abrasive	Pressure (N)	Head Speed RPM	Plate Speed RPM	Time (Minutes)
Planocloth H	9 μm (WB) Diamond	25	60	250-comp	5
Planocloth	6 μm (WB) Diamond	25	60	250-comp	3
Durasilk	0.06 μm (WB) Silco	25	60	100-comp	5

Table 6-3: The polishing stage

Surface	Abrasive	Pressure (N)	Head Speed RPM	Plate Speed (RPM)	Time (Minutes)
Chemocloth	0.06 μm Silco	15	60	80-comp	2

6.1.2 Flexural Properties of Carbon Fibre Composite Laminates

Three-point bending system was used to determine the flexural properties of CFRP panels. The test was carried out according to ASTM D7264/D7264M and ASTM 6856/D6856M. This tests through-thickness flexural properties such as strength, stiffness and load/deflection behaviour. The specimen and testing process are described below

6.1.2.1 Specimen preparation and test setup

Bars of rectangular cross sections ($w \approx 8.2$ mm and $t \approx 0.84, 1.09, 1.63, 2.06, 2.54,$ and 3.5 mm) were prepared from the CFRP panels that were described in Section 5.1 and 5.2. The span-to-thickness ratio was used 32:1 according to ASTM D7264/D7264M, the specimen must be at

least 20% bigger than the support span. Since the CFRP panels were fabric-reinforced, therefore, ~ 8.2 mm the width of the sample was chosen, to ensure that it was at least two-unit cells width. Eighteen samples were tested, twelve samples were made from prepreg VTC 401 using an autoclave fabricating technique; the other six samples were made by a vacuum assisted resin transfer moulding (VARTM).

The specimens were cut into desired dimensions using a 3000-rpm diamond cutter, the linear cutting speed was adjusted manually. To avoid changing the mechanical properties of carbon fibre composite laminates, water was used as a coolant to ensure that the specimen temperature was still at the room temperature. Since the flexural properties will vary depending on which surface of the specimen is in compression, therefore same surface that will be subjected to low velocity impact was compressed by the force member as shown in Figure 6-1 and Figure 6-2. The test was carried using a tensometer (Zwick/roell Z020, Germany). The test was undertaken at the room temperature 23°C . The speed of testing was set at a constant rate at 1 mm/min .

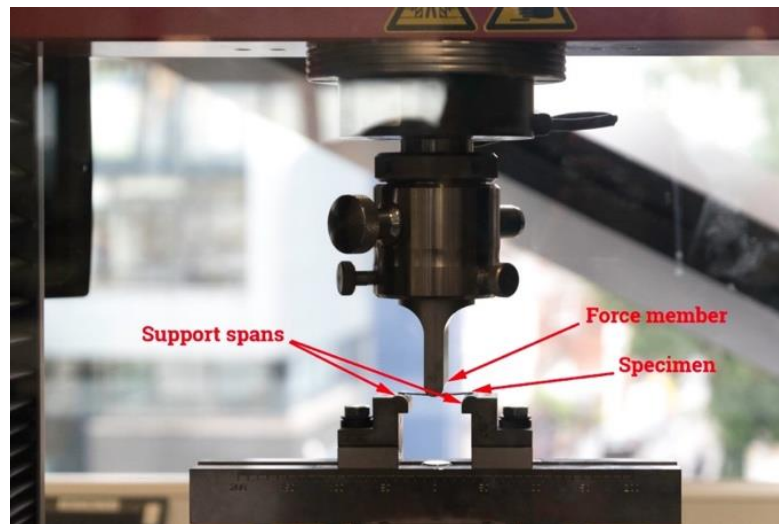


Figure 6-1: Experimental setup for flexural test according to ASTM D7264/D7264M.

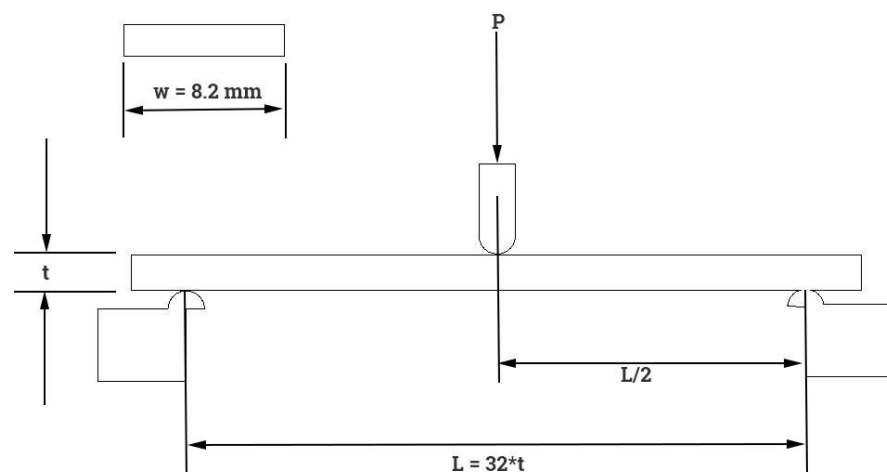


Figure 6-2: Flexural loading diagram according to ASTM D7264/D7264M.

The outputs of the test were bending forces (P) vs deformation (δ) and for the purpose of further analyses to estimate the required energy to cause fibre breakage in low velocity impact events, the flexural strength and flexural strain are calculated by using Equation 6 – 1.

$$\sigma_f = \frac{3PL}{2wt^2} \quad 6-1$$

Where σ_f is the flexural stress at the outer surface in the load span region (MPa), P bending force (N), L support span (mm), w width of the specimen (mm) and t is thickness of the specimen (mm). The maximum deflection (δ) at the mid span (mm). δ was measured as a displacement of the force member, ideally a strain gauge should be used. Therefore, the strain values were not used any further to calculate the impact energy that was required to cause fibre breakage in the CFRP laminates.

6.1.3 Tensile Properties of Carbon Fibre Composite Laminates

ASTM D6856/D6856M for preparation of textile composite fabricated using fabric preforms along with ASTM D3039/D3039M were used in this test. This standard allows the determination of the in-plane tensile properties of carbon fibre composite laminate panels. This test enables to determination of the ultimate tensile strength, the ultimate tensile strain, and the tensile modulus of elasticity (Young's modulus).

6.1.3.1 Specimen Preparation and Test Set up

Eighteen samples were prepared, twelve samples were made from prepreg VTC 401-C275-T300- 2 x 2 mm twill weave- 3K-42 % resin weight (SHD Composites Materials, UK). This material was cut into sheets 200 x 200 mm then they laid up on a flat plate using hand lay-up technique. Then they were placed in an autoclave to cure at 120°C for 1 hour at 606 kPa then post cured at 135°C for 2 hours as detailed in Section 5.2. The other six samples were made by a vacuum assisted resin transfer moulding (VARTM), where an ultra-low viscosity resin IN-2 epoxy infusion resin (Easy Composite, UK) was infused into a 2X2 mm twill weave 200 gsm carbon fibre preform (Easy composite, UK), more details given in Section 5.1.

The samples were then cut using a 3000-rpm diamond cutter, the linear cutting velocity was adjusted manually. All the samples were cut into 150 x 10 mm (LxW). The width of the sample was chosen according to ASTM D6856/D6856M-03 where the width to unit cell width (2 mm) was 5:1. However the thicknesses of the samples were varied, that were 0.84, 1.09, 2.06, 1.63, 2.54, and 3.5 mm. Rapid setting Araldite adhesive (Huntsman, Switzerland) was used to adhere the end tabs to the samples. A Z020 tensometer (Zwick/Roell, Germany) was used to carry out

the tensile test as shown in Figure 6-3. The testing machine was set up according to ASTM D3039/D3039M. The test was undertaken at the room temperature 23°C, and a constant head speed 2 mm/min was used. A standard test method to measure the strain was adopted, where stickers placed on the samples and a camera was set to monitor the movement of stickers and report an error free strain measurement.



Figure 6-3: View of tensile test frame, Zwick/Roell Z020.

6.1.4 Fibres, Resin Volume Fraction and Void Contents

The evaluation of electrical properties of CFRP laminates is a key element in development of the electrical self-sensing carbon fibre composite laminates. In order to make comparative studies, factors that were influencing the electrical properties were considered. Those factors were carbon fibre volume fraction, resin and void contents. The carbon fibre volume fraction has a direct impact on the electrical properties, as it is the element that is responsible for the electrical conduction process in the CFRP laminates. Where the ideal electrical resistivity of the CFRP laminates were calculated by multiplying the fibre volume fraction by electrical resistivity of the carbon fibre filaments.

6.1.4.1 Samples preparation

The first step to measure the fibre volume fraction was to cut the specimens. Three specimens 18 x 18 x t mm (t is the panel thickness 0.84, 1.09, 1.63, 2.06, 2.54, and 3.5 mm as shown in Table 6-8) were prepared carefully, using 3000-rpm diamond cutter with the linear velocity being adjusted manually. The water was used as a cutting fluid and coolant at the same time. Rough grinding of the specimen was undertaken to ensure that the specimens have the same dimensions. The rough grinding was carried out using 240 grit silicon carbide papers. A single wheel grinder and polisher (ATM, SAPHIR 320, Germany) was used, the speed was fixed at 150 rpm.

6.1.4.2 Carbon fibre composite density

The immersion method was adopted to determine the density of CFRP laminates according to ASTM D792 – 13. A density measurement device (Mettler Toledo-Newclassic MS. Model MS104S/01, UK) was used to measure the relative density of the CFRP laminates. The device utilizes Archimedes principle in which the CFRP specimen was immersed in distilled water at known temperature, normally the room temperature $\pm 3^{\circ}\text{C}$. The specimen will undergo an apparent loss in weight which equals to weight of the distilled water it displaces as shown in Figure 6-4.

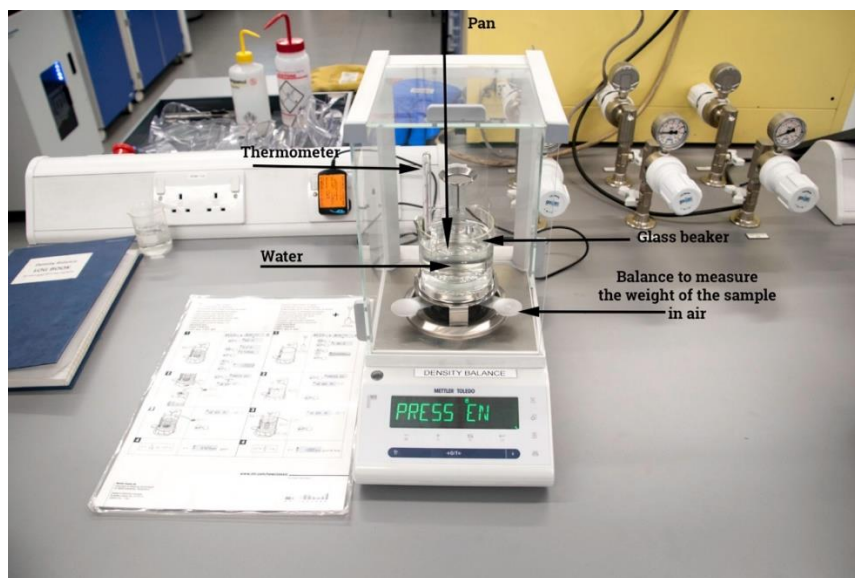


Figure 6-4: Precision balance to measure the density of carbon fibre composite laminates.

The temperature of the distilled water was measured by a thermometer, 23°C . Then the specimen was weighed in air to the nearest 0.1 mg. The specimen was held by tweezers then im-

mersed in the distilled water and weighed. The specimen was tilted and inserted into the distilled water to ensure there are no bubbles adhere to the surface of the specimen. The device used the following formula to calculate the relative density of the CFRP specimen:

$$\rho_{sp} = \frac{a}{(a+w_p-b)} \quad 6-2$$

Where ρ_{sp} is the relative density of the CFRP laminate at 23°C. a is the weight of the specimen in air, b is the weight of the specimen completely immersed in the distilled water. w_p is the weight of the pan. Then the density of the carbon fibre composite laminate can be calculated as follows

$$\rho_c \left(\frac{\text{kg}}{\text{m}^3} \right) = \rho_{sp} (\text{at } 23^\circ\text{C}) * 997.5 \quad 6-3$$

A pycnometer was also used to measure the CFRP density. Where a certain amount of a specimen (from 300-500 mg) was placed in a chamber then the chamber was closed. An inert gas, Helium, was subjected on the sample to measure the volume of the sample under 82047.612 kPa, 20 cycles were used. Each run took 120 minutes to finish, it was found that this method did not give accurate results. A contributing factor in this was the light weight of the carbon fibres. It was found that values were low even though the carbon fibres fill the chambers, and the weight of the sample was less than the required by the machine to obtain accurate results.

6.1.4.3 Acid digestion method

The acid digestion method was used to determine the constituent content of CFRP laminate. According to ASTM D3171-15, it was assumed that the reinforcement, carbon fibres, was unaffected by the digestion medium. The digestion medium chemically dissolved the matrix portion of carbon fibre composite laminates. When dissolving in a digestion medium, the remaining residue, containing the carbon fibres, was then filtered, washed, dried, cooled and weighed. The weight percentage of the carbon fibres was calculated and from that value, and the densities of both the CFRP laminate and carbon fibres, the fibre volume percentage was calculated.

An 18 x 18 x t mm (where t is the specimen thickness that is 0.84, 1.09, 1.63, 2.06, 2.54, and 3.5 mm) specimen was placed in a flask that contained at least 30 mL of 70 % nitric acid. The flask was placed in an oil bath and they were placed on a hot plate. It was found that the optimum digestion time was 120 minutes when the temperature was maintained at $80^\circ\text{C} \pm 2$ as shown in Figure 6-5. It was found that digestion time and temperature give no evidence of fibre attack as shown in Figure 6-6 and Figure 6-7. Those scanning electron microscope images show that the resin was digested without any damage to the carbon fibres.

Once digestion was complete the specimen was taken out of the flask, filtered into pre-weighed sintered glass filter under a vacuum of 101 kPa, using a vacuum pump. The carbon fibres were

then washed using distilled water then placed in an air-circulation oven (Heratherm, Thermo-scientific, USA) to dry at 50°C for 90 minutes. Then the specimens were weighed to nearest 0.0001 g. The specimen was dried again in the oven and reweighed after 90 minutes, and the process continued until constant mass was reached. The following formulas were used to calculate fibre, resin and void contents respectively:

$$\varphi_f = \frac{w_f \times \rho_c}{\rho_f} \quad 6-4$$

$$\varphi_r = \frac{(100-w_f) \times \rho_c}{\rho_r} \quad 6-5$$

$$\varphi_v = 100 - (\varphi_f + \varphi_r) \quad 6-6$$

where φ_f is the fibre content %, φ_r is the resin content %, φ_v is the void content %, w_f is the fibre mass (g), ρ_c is the density of carbon fibre composite (g/cm^3), ρ_f is the density of the carbon fibre (g/cm^3) and ρ_r is the density of the resin (g/cm^3)



Figure 6-5: Set up used to measure the constituent content of carbon fibre composite laminate.

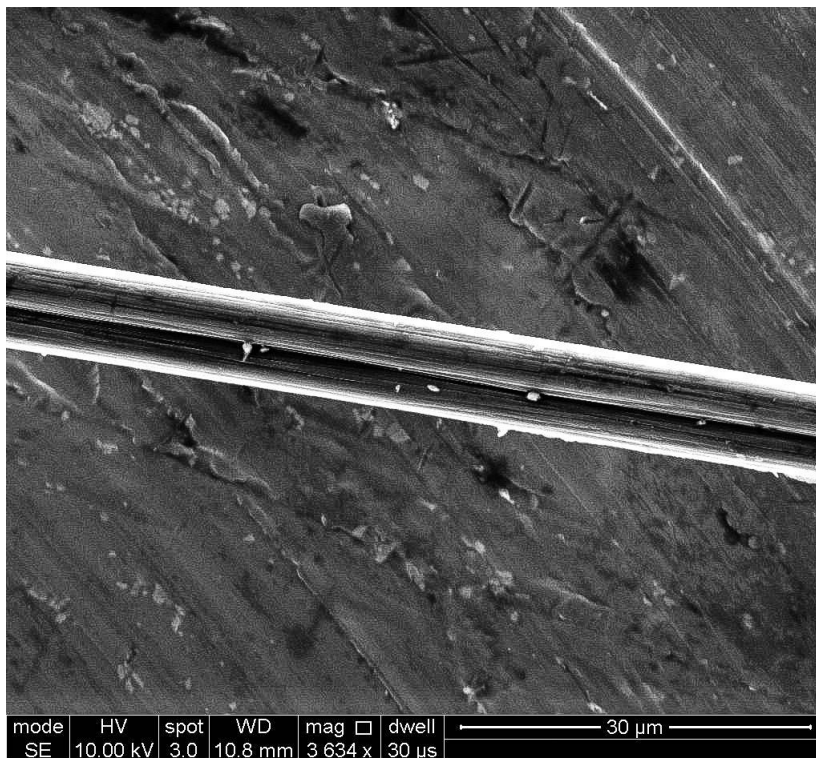


Figure 6-6: SEM image shows the surface of the carbon fibre and residual resin for Tairafil TC-35 carbon fibre.

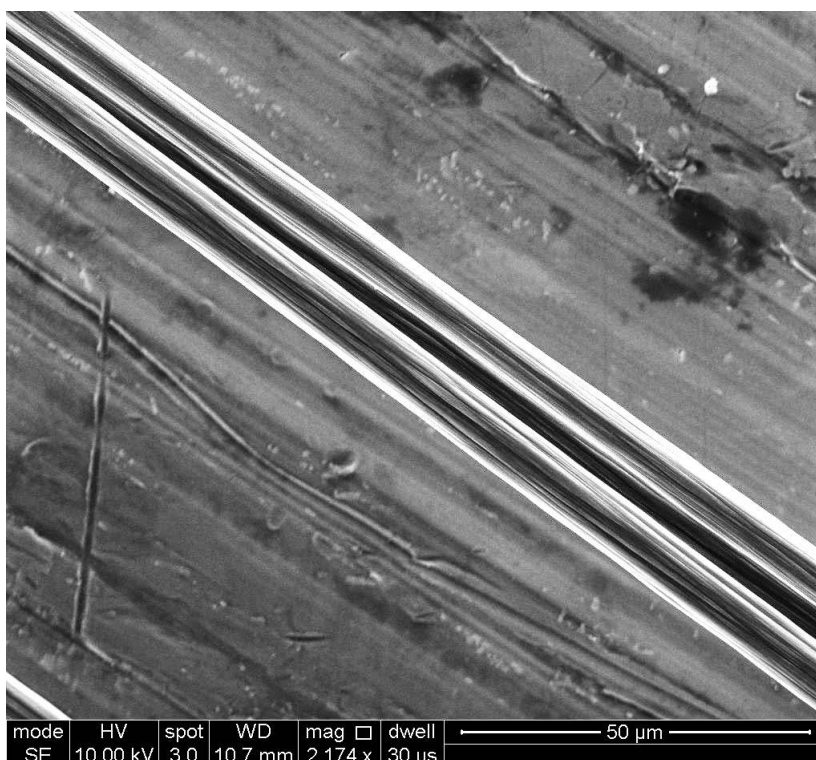


Figure 6-7: SEM image shows the surface of the carbon fibre and residual resin for VTC 401 carbon fibre.

6.2 Results and Discussions

6.2.1 Microscopical Examination of Carbon Fibre Composite Laminate Panels

A Nikon Eclipse LV-150 reflected-light microscope was used to examine specimens. It was found that void content and resin rich areas of CFRP laminates can be examined using low magnification, a 5x objective was used. The voids and resin rich areas were viewed normal to the ZX plane. The ZX plane was chosen as it provided plenty of information about number of plies, ply terminations, and micro-cracks, as well as the electric contacts between plies which was the most important feature in this work. These features were examined using a 10x objective. To identify electrical contacts of some of the laminates a greater magnification was required, therefore, a 20x objective was used.

6.2.1.1 Voids, resin rich areas, bundles drops, and number of plies analysis

Since carbon fibre fabric used in this work was 2 x 2 mm twill weave, therefore, bundle terminations (resin rich areas) can be observed in Figure 6-8 and Figure 6-9. It can be noticed that adjacent plies accommodate bundle-drops. However, the bundle-drops created voids and resin rich areas in the transition areas. In Figure 6-8 and Figure 6-9, the spherical dark areas (black areas) represent voids, while the circular yellow regions represented the fibres and the brown areas were the resin. The panels made by a vacuum assisted resin transfer moulding (VARTM) technique shown in Figure 6-8 have more void contents than the others since they have been formed due to entrapped air during the manufacturing process. On the other hand, the panels made by an autoclave have less voids contents, although the voids could still have been generated due to entrapped air and volatiles.

The voids, which were observed in Figure 6-8, were attributed to the manufacturing technique and the resin systems that were used. The epoxy system that was used in this technique was ultralow viscosity, and although it was degassed in a vacuum oven at the room temperature for 10 minutes prior to infusion into the preform, as described in Section 5.1, some air was expected to be entrapped into the resin during insertion of the inlet plastic pipes in the resin container. In addition, this resin system contains solvents, propylene carbonate and benzyl alcohol, in the formulation that may also form voids in the structure.

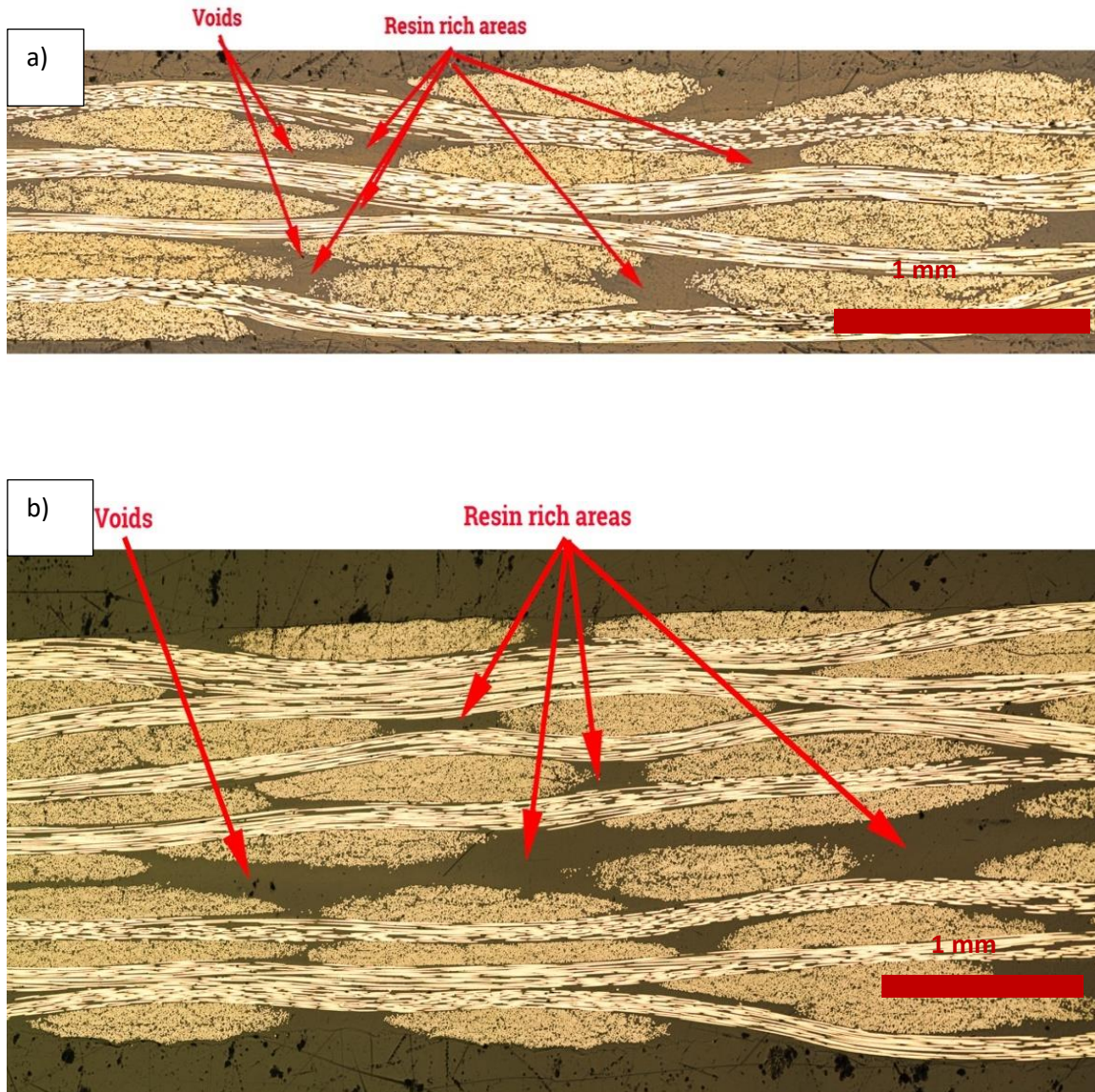
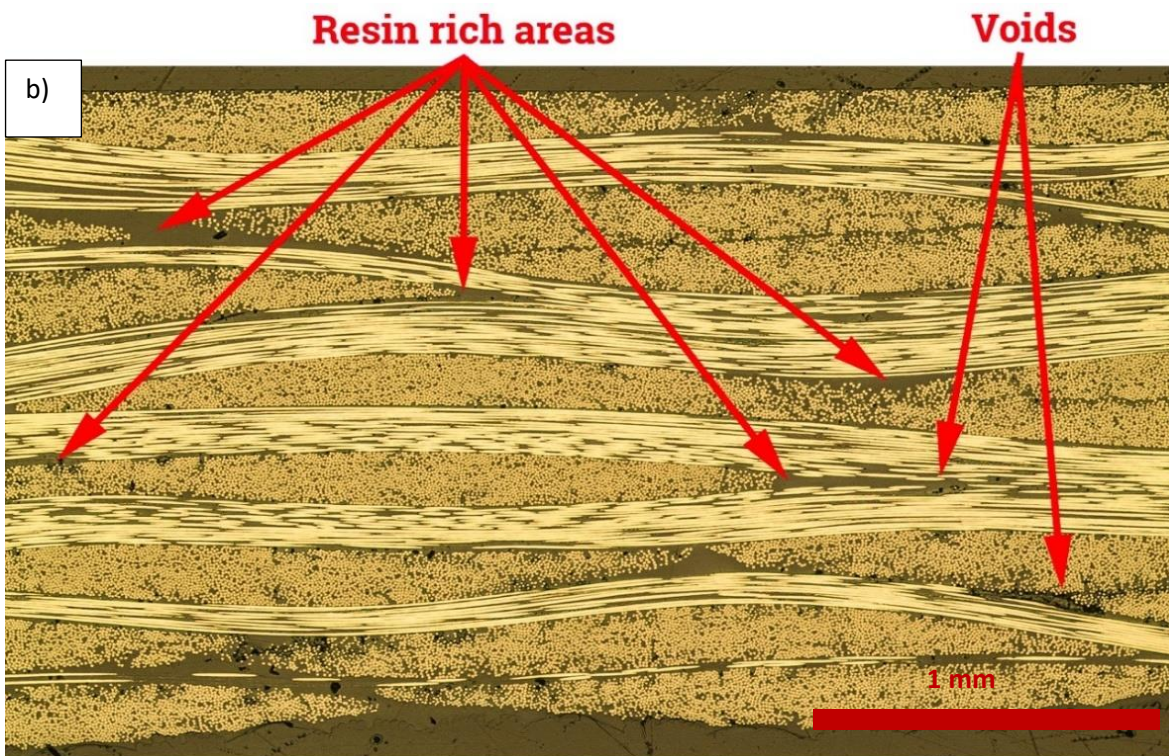
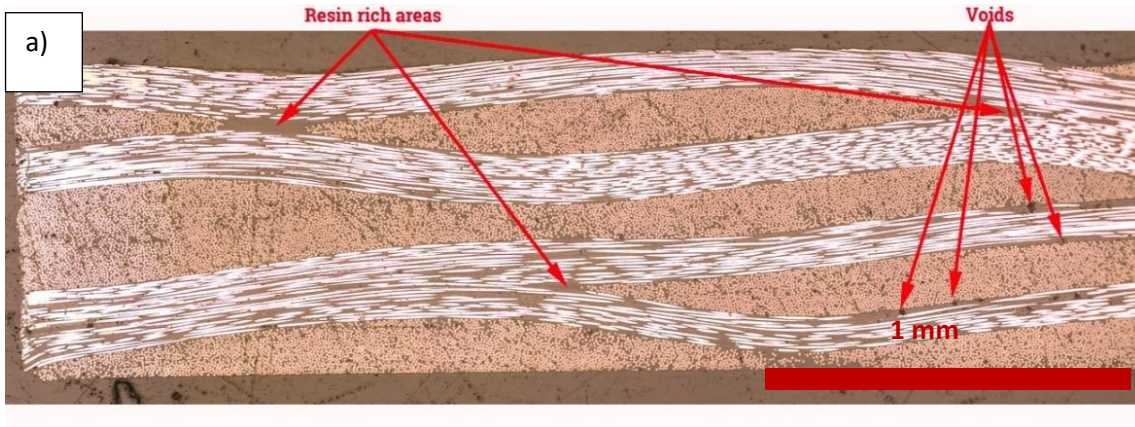


Figure 6-8: Cross sections of a 2 x 2 mm twill weave CFRP laminates panel, reflected-light bright-field illumination, 5x objective. a) represents 4 plies CFRP laminates b) represents 8 plies CFRP laminates. Samples were made by a vacuum assisted resin transfer moulding technique (VARTM).

Since limited information was provided by supplier about the VTC401 resin system, due to confidentiality, the discussion addressed in this section is conclusory. Figure 6-9 shows the voids contents and resin rich areas. Since the epoxy systems, in general, contain between 0.3 – 0.7 wt % water, it was assumed that the water was the main factor in the voids production, as well as other factors such as the manufacturing technique. It was proved elsewhere that the prepreg can absorb considerably high moisture during the layup process, and that may cause a considerable reduction in the mechanical properties [202]. That helps to explain the void formation in VTC 401.



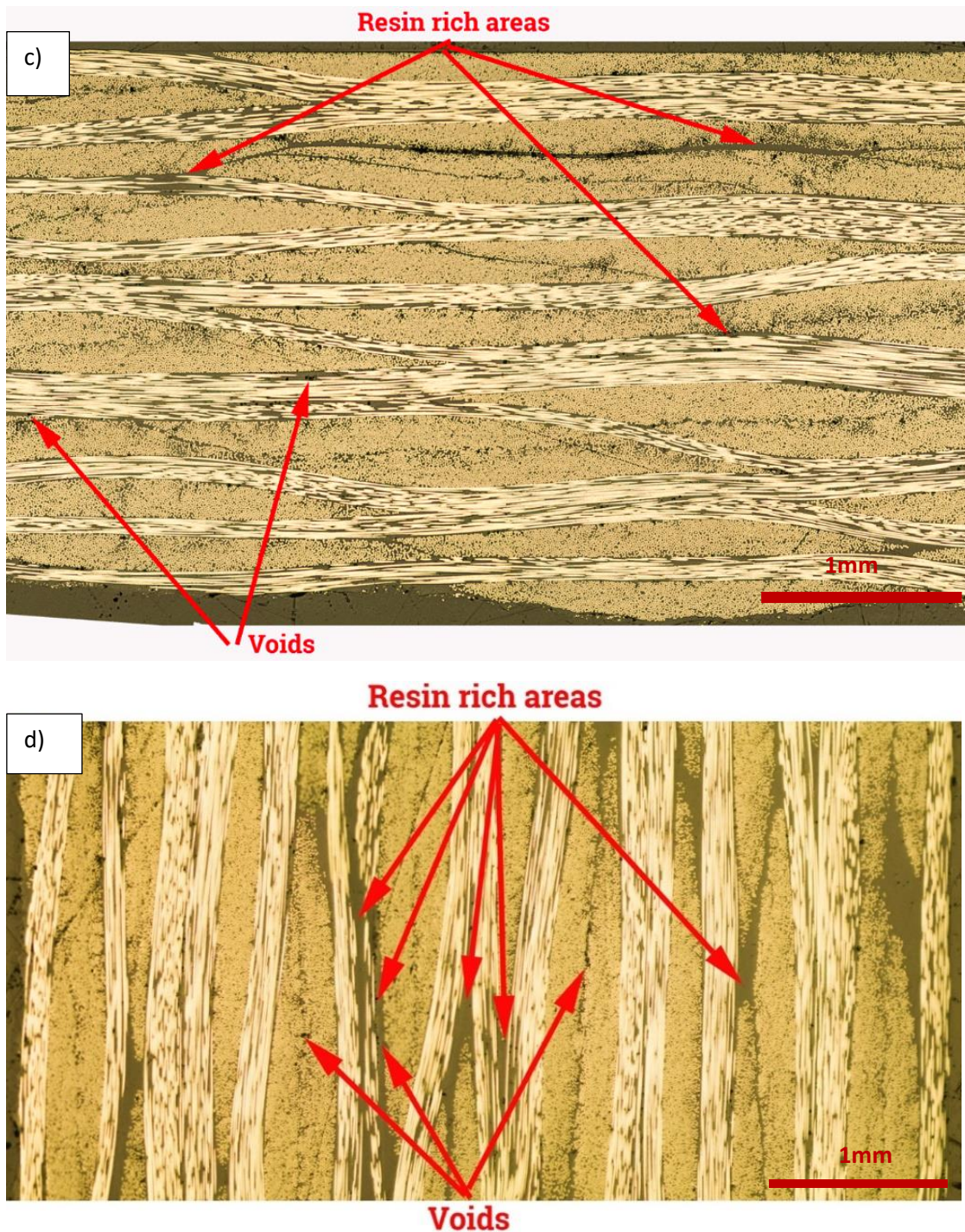


Figure 6-9: Entrapped air, resin rich areas, bundles termination and number of plies in CFRP laminate panels that were made with 2 x 2 mm twill weave carbon fibres by an autoclave. a) represents 4 plies of prepreg VTC401, b) represents 8 plies of prepreg VTC401, c) represents 12 plies of prepreg VTC401, and d) represents 16 plies of prepreg VTC401. A reflected light bright-field illumination, 5x magnification.

The CFRP laminate panels in Figure 6-9 have less void content than the VARTM panels in Figure 6-8. Since the prepreg VTC401 contains less resin content 48% by volume than the VARTM panels, Figure 6-8, those panels that were made of prepreg VTC401, have less resin volume

fraction than panels that were made by a vacuum assisted resin transfer moulding (VARTM) technique.

It is important to mention that the woven fabrics that were used in this work cause low hydrostatic resin pressure. Therefore, voids formed in carbon fibre composite panels when the volatile vapour pressure exceeds the hydrostatic resin pressure before gelation. In general, voids that were observed in all figures were irregular in shape and size and they were concentrated at the interstitial regions in the woven fabrics. It is expected that the high void content has a significant impact on the electric properties of carbon fibre composite laminates as they interrupt the electric paths through the composite laminates by preventing fibre – fibre contacts. The void content was less than 2 % in all composite panels used in this work, therefore, the effect of the void content on the electrical resistance was minimal.

6.2.1.2 Electrical connection analysis

The electrical contacts between consecutive plies (through-thickness contacts) were investigated using a Nikon Eclipse LV-150 reflected-light microscope. The electrical connections between adjacent plies due to fibre – fibre contacts are essential for understanding how efficiently the carbon fibre composite laminates panels will respond to the subjected electrical current in the electrical resistance self-sensing technique. The more fibre – fibre contacts there are between adjacent plies the more similar the electrical resistance of the carbon fibre composite panels will be to the typical resistance of carbon fibres composite laminates.

Factors such as fibre volume fraction, void contents, and fabrication techniques determine the electrical conductivity of CFRP laminates. Higher fibre volume fraction, lower void content and higher pressure applied during the fabricating process ensure higher electrical conductivity of CFRP laminates panels. It can be seen clearly that the panels that were made from prepreg VTC401 by an autoclave processing in Figure 6-11 have higher number of contacts between plies than panels made using a vacuum assisted resin transfer moulding VARTM (Figure 6-10). That is due to higher pressure used during the fabrication process (606 kPa). It is therefore expected to be more sensitive for damage detection in through-thickness direction.

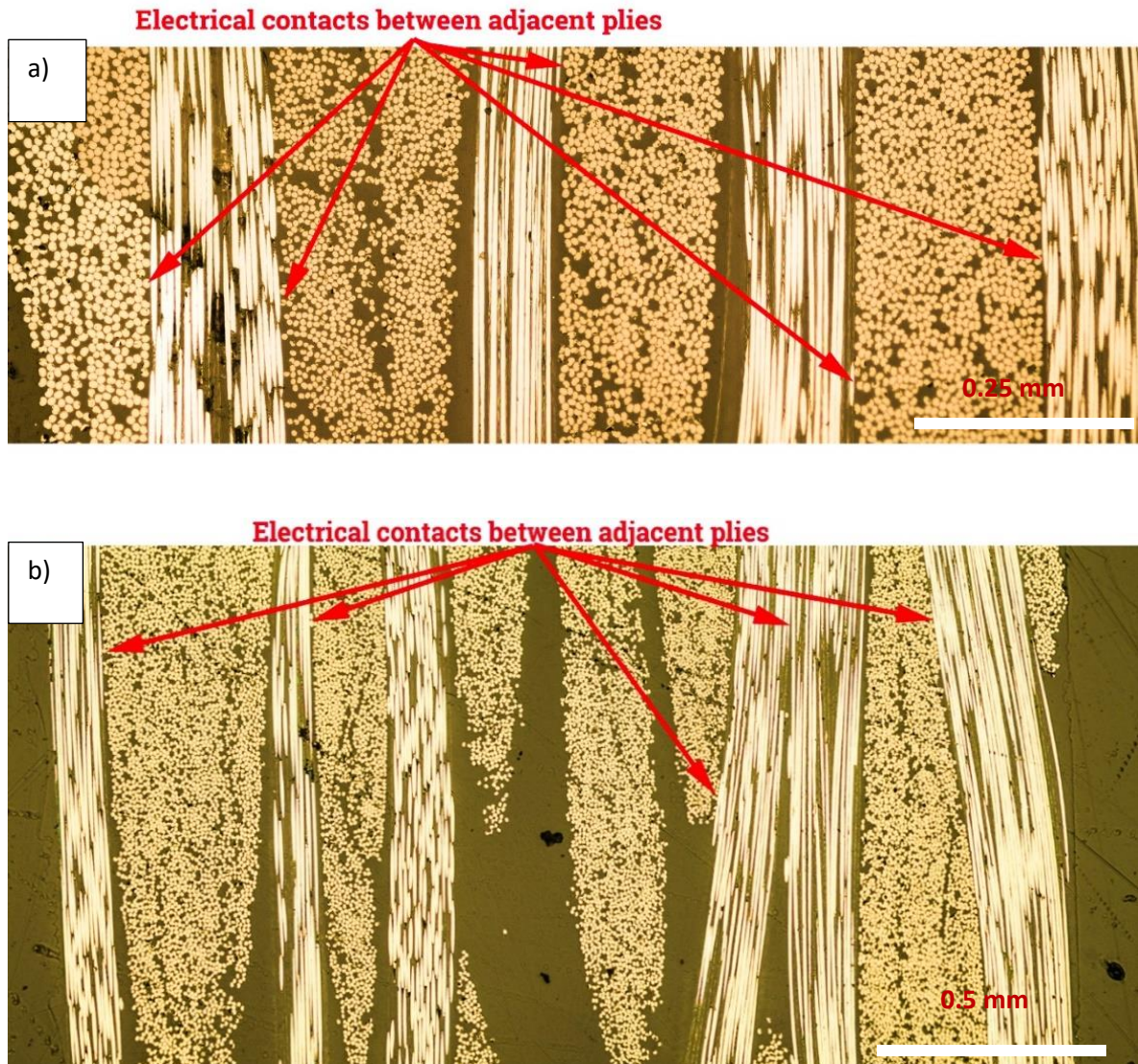
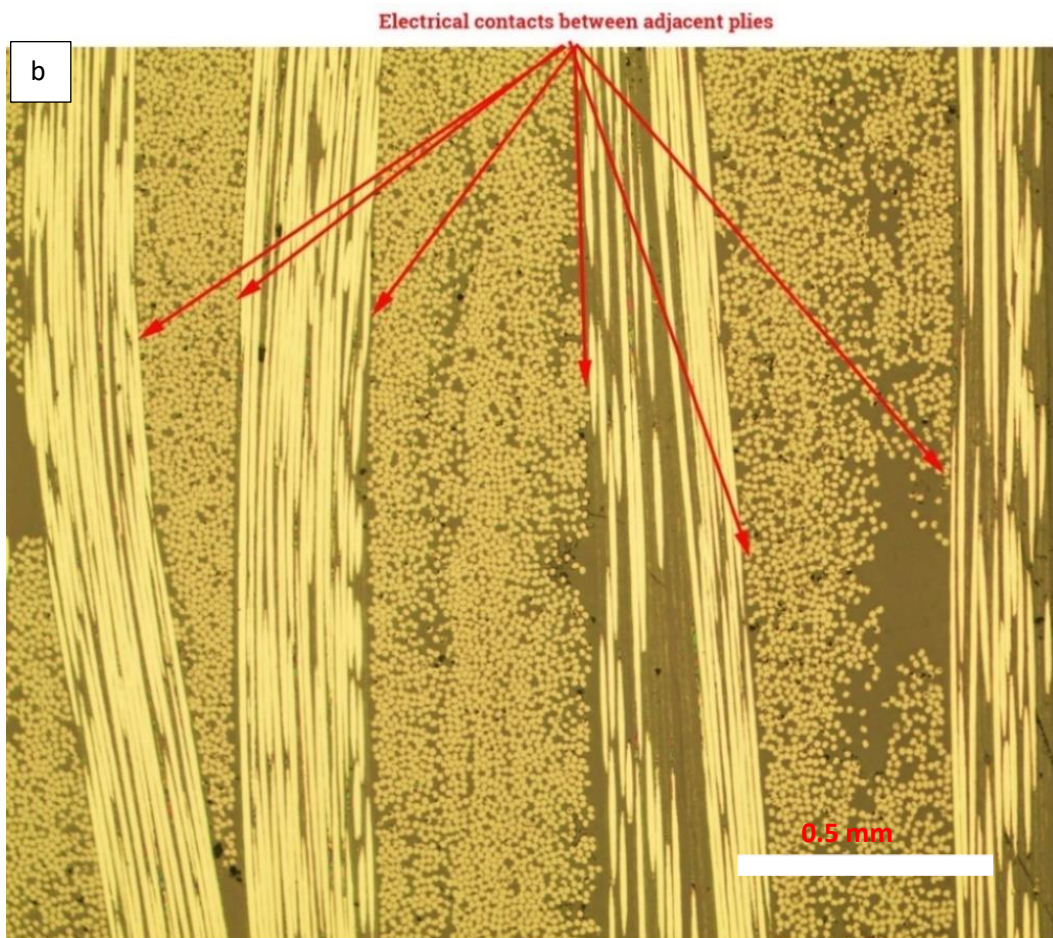
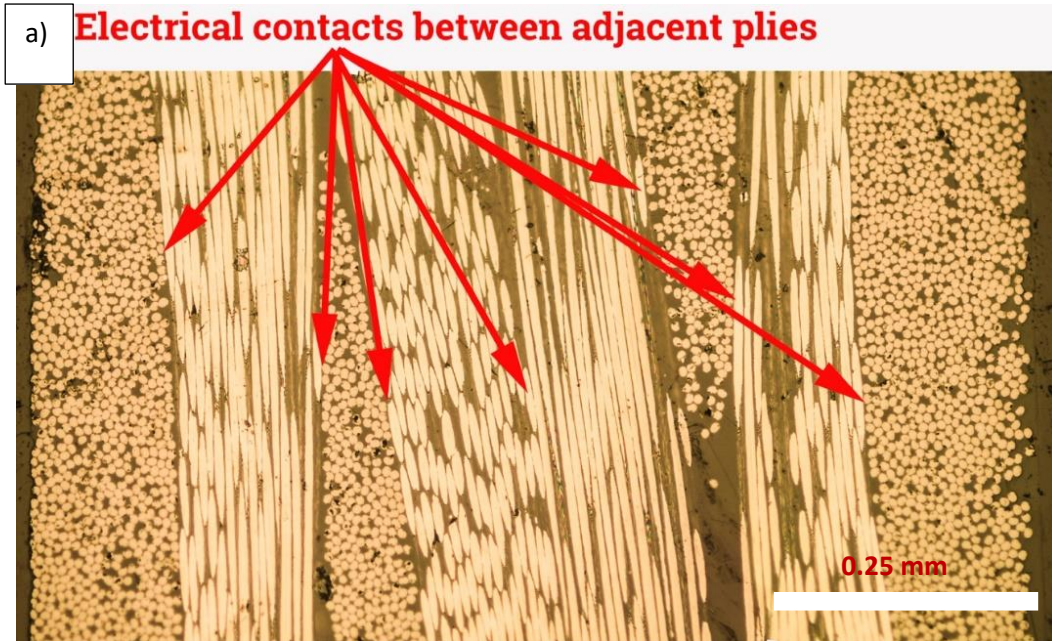


Figure 6-10: Cross-section of CFRP laminate panels that were made by a vacuum assisted resin transfer moulding (VARTM), through-thickness electrical conduction due to fibre – fibre contacts are shown in a) 4-ply panel (VB) that was examined using bright-field illumination, 20x objective, and b) 8-ply panel (VC) that was examined using bright-field illumination, 10x objective.



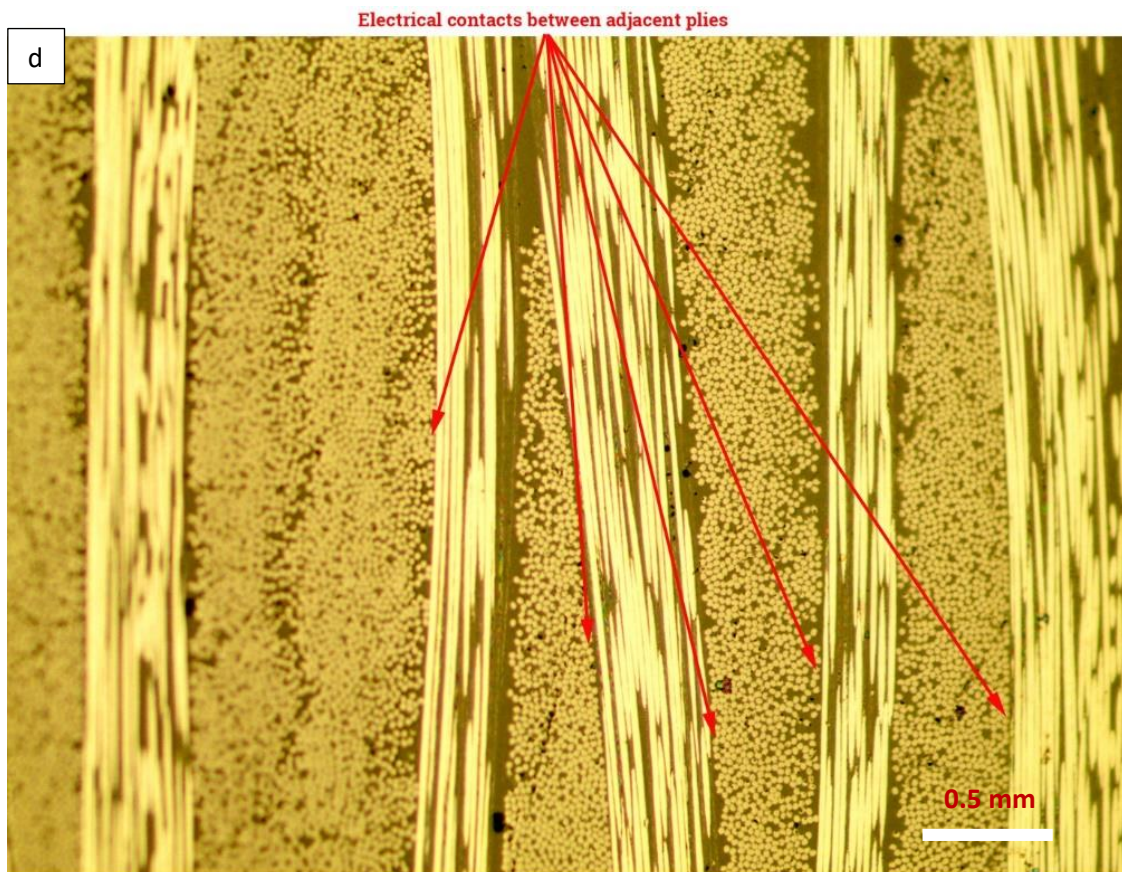
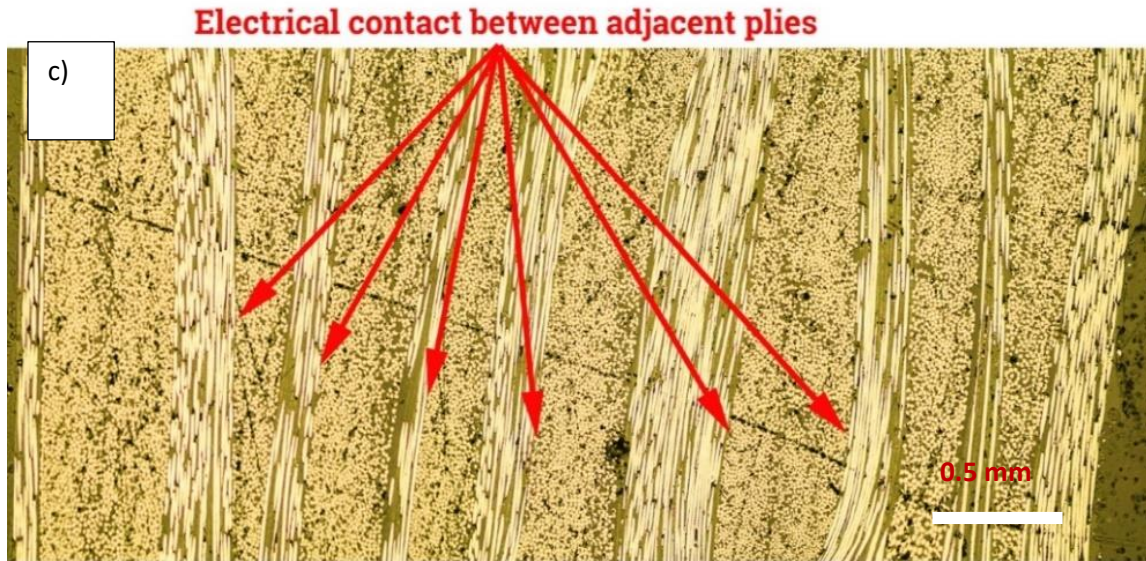


Figure 6-11: Cross-section of CFRP laminate panels that were made from prepreg VTC401 by using an autoclave processing technique. The electrical contacts between adjacent plies occurred due to fibre – fibre contacts that can be seen in all images. a) 4-ply panel (AB), b) 8-ply panel (AC), c) 12-ply panel (AD), and d) 16-ply panel (AE). All the panels were examined using bright-field illumination, 10x objective apart from the panel that was showed in a that was examined under 20x objective.

6.2.2 Flexural Strength of Carbon Fibre Composite Laminate Panels

The flexural profile for AB CFRP panel is depicted in Figure 6-12, the other data used in this work given in Appendix A. The flexural test was carried out on three specimens of each panel according to ASTM D7264/D7264M and ASTM 6856/D6856M as shown in Figure 6-12. The average values were considered in further calculations to estimate the required energy to cause fibre breakage in low velocity impact events. The non-linearity in the $\sigma - \epsilon$ flexural curve was caused by structural change in the fabric during the deformation [203]. The flexural test showed that the dominant mode of failure, apart from AB specimen, was tension under the loading nose at the bottom surface of the laminates. The damage in the lower surface was from tensile failure, however a close observation showed that there was small visible damage at the compressive side of laminate (upper surface). As the amount of load increased a crack initiated in the outer layer on the tensile side, this crack initiated when the tensile stress exceeded the epoxy matrix tensile strength [203-205] Table 6-4 classifies the flexural failure modes according to ASTM D7264/D7264M. **Error! Reference source not found.** shows the flexural properties of CFRP laminates that were made in the autoclave processing and the VARTM processing techniques. The carbon fibre composite laminates, which were made using a VARTM technique, have higher flexural strength than the CFRP laminates made using autoclave processing. This was attributed to the fibre type (Tairyfill TC-35) and the toughened resin system (IN-2 Epoxy Resin). It was found that the thicker the laminate the higher the carbon fibre volume fraction and the higher flexural properties and this agrees with the rule of mixture [204].

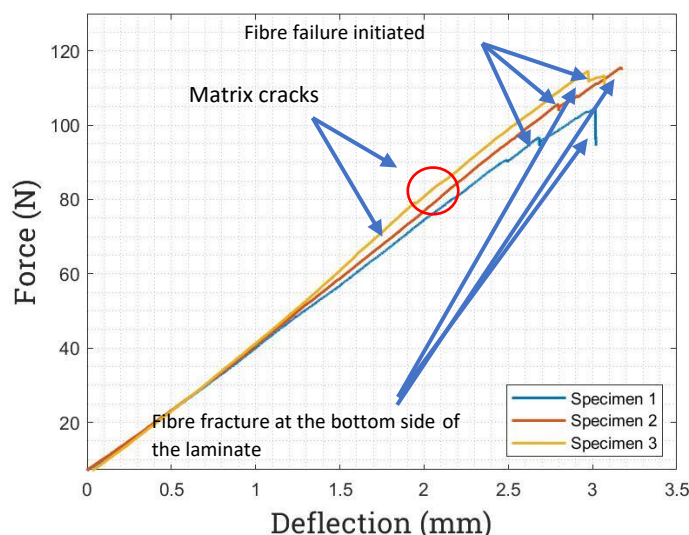


Figure 6-12: Three-point flexural test for AB panel, the average $\sigma_f = 790$ MPa.

Table 6-4: Flexural fracture shapes and failure identification codes according to ASTM D7264/D7264M.

Specimen Failure shape and failure identification code

Tension and compression at the loading nose top and bottom (TAB) (CAT)

AB



Tension at the loading nose bottom (TAB)

AC



Tension at the loading nose bottom (TAB)

AD



Tension at the loading nose bottom (TAB)

AE



Specimen Failure shape and failure identification code

Tension at the loading nose bottom (TAB)

VB



Tension at the loading nose bottom (TAB)

VC



Table 6-5: Flexural properties of CFRP laminates considered in the experiments.

Specimen	Maximum Flexural Stress (MPa)	Percent Coefficient of Variant %
AB	790	11.43
AC	810	5.42
AD	870	1.5
AE	890	1.01
VB	610	5.42
VC	690	4.4

6.2.3 Tensile Strength of Carbon Fibre Composite Laminate Panels

A typical representation stress – strain curve that was obtained from tensile test for an auto-clave processed panel (AC) is shown in Figure 6-13, the stress – strain curves for all panels used in this work is given in Appendix A. All the specimens showed a similar behaviour, where the strain increased with the applied stress and the failure occurred suddenly. Typical fracture modes for all the specimens are presented in Table 6-6. Table 6-6 classifies the tensile failure mode in each specimen according ASTM D6856/D6856M and ASTM D3039/D3039M. Table 6-7 reports the results of the tensile properties for all the panels used in this work. The reported data have been compared to data in [206-208]. Ultimate tensile strength (UTS) varied from a specimen to the other since the value of UTS depends on many factors that are manufacturing

processes, void content, fibre volume fraction, and surface roughness. UTS increased when fibre volume fraction increased (see Table 6-8).

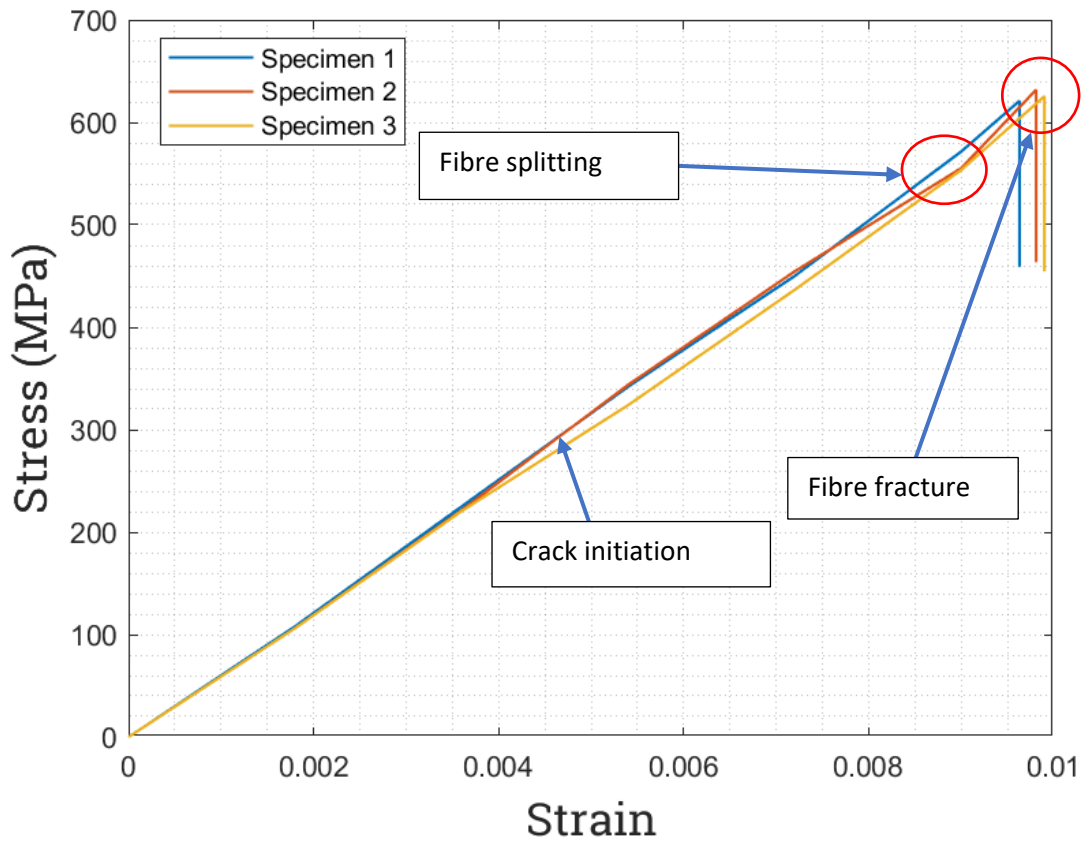


Figure 6-13: Tensile stress-strain curve for AC panel.

Table 6-6: Tensile fracture shape and fracture codes according to ASTM 3039/3039M for all panels used in this work.

Specimen	Failure shape and failure identification code
	Lateral gage various (LGV)
AB	
	Lateral gage middle (LGM)
AC	

Specimen	Failure shape and failure identification code
AD	<p style="text-align: center;">Lateral gage various (LGV)</p> 
AE	<p style="text-align: center;">Grip at grip top (GAT)</p> 
VB	<p style="text-align: center;">Lateral gage middle (LGM)</p> 
VC	<p style="text-align: center;">Lateral gage middle (LGM)</p> 

Table 6-7: Tensile properties of carbon fibre composite laminates panel used in this work.

Specimen	Young's Modulus (GPa)	UTS (MPa)	Coefficient of Variation %
AB	55	607	9.1
AC	57	620	1.2
AD	57	690	4.72
AE	57	735	5.67
VB	53	419	6.1
VC	55	450	8.5

It can be noticed in Table 6-7 that although AB, AC, AD, and AE panels were made from the same prepreg but they have different Young's modulus because their carbon fibre volume fraction was varied as shown in Table 6-8, and this comply with the rule of mixture where modulus of elasticity is a function of carbon fibre volume fraction.

6.2.4 Fibres, Resin Volume Fraction, and Void Contents in Carbon Fibre Composite Laminate Panels

Results of acid digestion for fibre volume fraction, resin and void content analyses, showing mean and standard deviation values are listed in Table 6-8. To minimize the errors in this analysis, three samples of each panels were tested, and the results are shown in Table 6-8. The fibre volume fraction was increased when the thickness of a panel was increased. The same pattern applies equally on the panels that were made by a VARTM or autoclave techniques. However, the panels that were made in a VARTM technique have lower fibre volume fraction than their counterparts that were made using an autoclave technique.

The void content was less than 2% in all panels under investigation as shown in Table 6-8. However, it was obvious from the table that they do not follow a regular pattern. It is worth to mention that the void content can differ greatly from one panel to another at a specific thickness since they were subject to varying manufacturing conditions and raw materials preparations. Those factors were in such a complexity to control. It was expected that the highest void contents can be observed in the panels that were made using a VARTM technique due to increased sources for voids in the fabricating process.

Table 6-8: The fibres, resin, voids contents volume fraction for carbon fibres composite laminates panels.

Specimen Type	Sample No.	Fibre Volume Fraction %	Resin Volume Fraction %	Void Volume Fraction %
AB	1	45.52	54.2	0.28
	2	43.99	55.34	0.67
	3	43.30	56	0.7
Mean		44.27	55.18	0.55
Standard Deviation		1.136	0.91	0.234
AC	1	52.46	45.5	2.04
	2	50.67	48.2	1.13
	3	48.88	50.1	1.02
Mean		50.67	49.93	1.39
Standard Deviation		1.76	2.311	0.559
AD	1	55.39	44	0.6
	2	53.65	45.6	0.75
	3	54.01	44.9	1
Mean		54.35	44.83	0.78

Standard Deviation		0.918	0.802	0.202
AE	1	53.05	45.26	1.69
	2	54.98	44.2	0.82
	3	5.30	43.6	1.1
Mean		54.44	44.35	1.2
Standard Deviation		1.21	0.84	0.444
VB	1	39.35	59.2	1.45
	2	44.43	54.87	0.7
	3	47.84	51.36	0.8
Mean		43.87	55.14	0.98
Standard Deviation		4.272	3.927	0.407
VC	1	45.01	53.39	1.6
	2	48.3	49.9	1.78
	3	48.2	50.8	1
Mean		47.17	51.36	1.46
Standard Deviation		1.871	1.811	0.408

Chapter 7

DAMAGE GENERATION AND DETECTION IN COMPOSITE PANELS

The aim of the current chapter is to describe the introduction of barely visible impact damage into CFRP laminates panels using a drop – weight method (Section 7.1) and to detect the damage. Section 7.2 presents the data acquisition system that was used to acquire through – thickness electrical resistivity, surface electrical resistance and changes in electrical resistance due to bending loads. A non-destructive testing technique (C-scan) is presented in Section 7.2.5 to validate the electrical resistance sensing technique data. A destructive technique (fluorescent microscope Section 7.2.6) was used to provide further evidence to results and discussions in Section 7.3. Section 7.3 presents the results and discussions of the electrical resistance self – sensing technique; supported by C – Scan and fluorescent microscope data.

7.1 Damage Generation (Drop – Weight Impact Test)

Damage was generated using a drop – weight impact tester according to ASTM D7136/D7136M-15. Where a flat CFRP laminate panel 200 x 200 x t mm (t = 0.84, 1.09, 1.63, 2.02, 2.54, and 3.5 mm) was subjected to through-thickness, concentrated impact energy. The weight (1.456 kg) was left to fall from pre-determined heights. Various heights were used, these being 70, 105, 140, 245, 375 and 700 mm, to strike a CFRP laminate panel. A hemi-spherical impactor, 13 mm in diameter, was used. The CFRP laminate panel was supported on the horizontal plane using G-clamps. The impact energies are shown in Table 7-1.

Those impact energies and velocities were chosen according to the literature and trials and error so as to cause barely visible impact damage, where no destruction of the CFRP laminate panels should occur [81, 90]. The incident energy was the kinetic energy (KE) of the impactor before impact events took place. While the potential energy (PE) was the energy of the impactor at certain heights as given in Equation 7-1.

$$\left. \begin{aligned} PE &= mgh \\ KE &= 0.5 m v^2 \end{aligned} \right\} \quad 7-1$$

Where m is the total mass of the impactor plus the carriage that is 1456 g. g is the acceleration due to gravity, taken as 9.81 ms⁻², and h is the height of the impactor above the CFRP panel. v

is the incident velocity (m/s). The drop height, PE, KE, and incident velocities are presented in Table 7-1. Ideally the force – displacement and force – time curves for various impact energies should be presented but the available impact tester does not provide this data.

Table 7-1: Experimental data of low velocity impact tests.

Specimen	Striker Type	Drop Height (m)	PE (J)	Incident velocity (m/s)	KE (kg.m ² /s ²)
AB	13 mm round	0.07	1	0.75	0.409
		0.105	1.5	0.95	0.657
		0.14	2	1.4	1.426
		0.245	3.5	2.14	3.333
		0.35	5	2.61	4.959
AC	13 mm round	0.14	2	1.4	1.426
		0.245	3.5	2.14	3.333
		0.35	5	2.61	4.959
AD	13 mm round	0.35	5	2.61	4.959
		0.7	10	3.7	9.966
AE	13 mm round	0.35	5	2.61	4.959
		0.7	10	3.7	9.966
VB	13 mm round	0.14	2	1.4	1.426
		0.245	3.5	2.14	3.333
		0.35	5	2.71	4.959
VC	13 mm round	0.14	2	1.4	1.426
		0.245	3.5	2.14	3.333
		0.35	5	2.61	4.959

7.2 Damage Detection in Carbon Fibre Composite Laminates

7.2.1 Data Acquisition System

A data acquisition system (DAQ) that was used in this technique consists of modules of NI9219 (National instrument, US). Those modules are analogue to digital converters (ADC). Each module has four channels, those channels having a 24bit resolution. A total of twenty-four analogue inputs were used, and they are able to acquire 100 S/s/ch simultaneously. The modules were installed in a NI cDAQ-9172 (National instruments, US) chassis. The input range that was used

in this study, varied from 0 Ω to 10.5 k Ω . Those modules were thus low noise and they have low distortion effects that gives high-accuracy measurements.

A four-probe electrical resistance configuration was used. The NI9219 computed the electrical resistance from the resulting electrical potential readings according to Ohm's law. In the four-probe technique the contact resistance (Pin headers, soldering materials, and connection wires) were neglected since there is only a small amount or none of electrical current flowing across the electrical potential terminals. Figure 7-1 represents the four-wire resistance connection map. The four-wire resistance technique is more sensitive, accurate and more precise than the two-probe method in sensing impact damage and fatigue in CFRP laminates [31]. It is proved elsewhere that it can present a subsurface behaviour [209]. However, it is more complicated than the two-wire resistance technique.

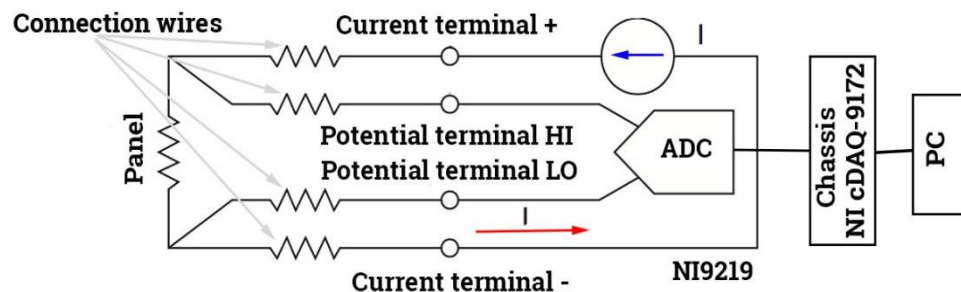


Figure 7-1: Schematic diagram of 4-wire resistance circuit.

The connection between sensing mats (Section 5.3) and the dedicated modules was made by connection pin headers (RS, UK) that were soldered to sensing mats using a lead-free solder (Sn, 3% Ag, 0.5% Cu) (Weller, UK). These are plugged into the terminals in NI9219 modules through special connection wires. The data collection was triggered and collected using a dedicated software that was written in LabView 2015 (National Instruments, USA); the software was written on a Windows PC platform. The terminals in the modules were executed consecutively to avoid the electric interference between a terminal and the others during the data collection process.

The NI9219 modules were placed in a chassis cDAQ-9172. Each module has four channels, the channels were set to execute consecutively; structural loops were used. One channel measures the electrical resistance between a certain pair of electrodes while the other channels in the same loop were configured to measure the voltage Figure 7-2. Eight structural loops were used to acquire the electrical resistance readings for sensing mat shown in Figure 5-5. Each channel has a dedicated structural loop, Appendix B. Four structural loops were used to obtain the electrical resistance for sensing mat shown in Figure 5-6. Each loop measures the electrical re-

sistance between a certain pair of electrodes as shown in Figure 7-2. This strategy was successful to avoid the electric interference between channels if they were set to measure the electrical resistance between all electrodes at the same time as shown in Figure 7-1 and Figure 7-2.

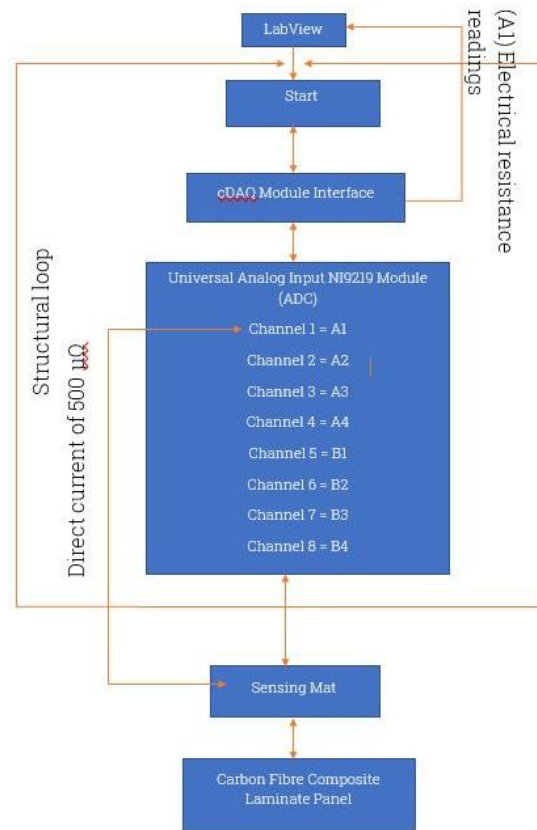


Figure 7-2: Data collection flow chart using NI cDAQ-9127 and NI9219 modules.

A 500 μA electrical current was selected to be injected into the panels. It was found that this amount of the electrical current did not generate Joule heating during electrical tests. 10 readings were taken for each channel before and after barely visible impact damage was generated in the panels. A statistical software (Matlab R-2017b) was used to organize and analyses the data. Matlab sorts the raw data obtained from the electrical tests into matrices then it calculates the mean value and standard deviation for each channel to determine whether changes have occurred as shown in Table 7-2.

7.2.2 Through – Thickness Electrical Resistance Measurements and Electrical Conductivity Calculations

Measurements of electrical resistance of carbon fibre composite laminates were conducted using a four-probe electrical resistance method. Through – thickness electrical resistivity was

measured using National Instrument data acquisition system NI cDAQ-9172 chassis with NI9219 modules as was shown in Figure 5-13. A 200 x 200 x t mm CFRP laminate was used, where t represents the thickness of the panels AB, AC, VB, VC, AD, and AE that are 0.84, 1.63, 1.09, 2.06, 2.54, and 3.5 mm respectively. The laminates manufacturing processes were detailed in Section 5.1 and 5.2. The laminates were ground and polished as described in Section 5.4.1 prior to attaching sensing mats. Two sensing mats (either 2 sensing mat 1 or 2 sensing mat 2) were attached to the upper and lower surface of the CFRP laminate panels to measure the through – thickness electrical resistance as shown in Figure 7-3.

The experimental set up to measure the through – thickness electrical resistance is shown in Figure 7-3. 500 μ A of direct current that flows from the negative electrode at the bottom surface of the laminate to the positive electrodes at the upper surface of the laminate and the voltage was measured using two other electrodes that were placed next to the current electrodes on the upper and lower surface of the laminate (red colour). This process was reversed for one main purpose that was to acquire more electrical resistance readings at a shorter time. 10 readings were taken, and the average values were considered in further calculations. The through – thickness electrical resistivity of the panel (η_t) was calculated using the following equation

$$\eta_t = R \cdot (A/L) \quad 7-2$$

Where R is the electrical resistance (Ω), A is the electrode area (mm^2), L is the distance between the voltage electrodes (mm). Equation 7 – 3 was used to calculate the distance between the voltage electrodes (sensing electrodes)

$$L = \sqrt{t^2 + b^2} \quad 7-3$$

Where t is the thickness of the panels AB, AC, AD, AE, VB, and VC that being 0.84, 1.63, 2.54, 3.5, 1.09, and 2.06 mm and b = 60 mm for sensing mat 1 and 130 for sensing mat 2. The angle between the voltage electrodes on the upper and lower surface was calculated using Equation 7 – 4, therefore θ was 0.8, 1.55, 2.42, 3.33, 1.04 and 1.96° for panels AB, AC, AD, AE, VB, and VC using sensing mat 1, and θ was 0.37, 0.71, 1.11, 1.54, 0.48, and 0.90° for panels AB, AC, AD, AE, VB, and VC using sensing mat 2. The electrical resistivity data is presented and discussed in Section 7.3.1.

$$\tan \theta = \frac{t}{b} \quad 7-4$$

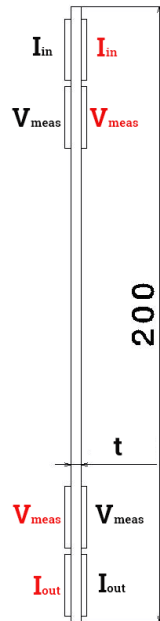


Figure 7-3: Schematic diagram illustrate through – thickness electrical resistance experimental set ups.

The electrical conductivity of composites (C_c) is a fundamental property that determines the oppose of CFRP laminate panels for the flow of the electrical current. The electrical conductivity of composite (C_c) was calculated for each type of CFRP laminates that were used in this work and presented in Table 7-4. The rule of mixture was used to calculate the electrical conductivity (C_c) in the CFRP laminate panels. Equation 7 – 5 describes the relationship between C_c of composites and their constituents

$$C_c = C_f \cdot V_f + C_m \cdot (1 - V_f) \quad 7-5$$

Where C_f is the electrical conductivity of the carbon fibre (carbon filaments), there were two types of carbon fibres used in this work that were Toray FT300B and Tairyfil TC – 35 their electrical conductivity, which were obtained from the data sheet, was 58827 and 57803 S/m respectively, V_f is the fibre volume fraction, C_m is the electric conductivity of the epoxy matrix. The epoxy matrix is an insulator, therefore C_m is vanished and the rule of mixture equation will be simplified to Equation 7 – 6. V_f is the mean value of three specimens of each panel as presented in Table 6-8. The panels electrical conduction data is depicted and discussed in Section 7.3.1

$$C_c = C_f \cdot V_f \quad 7-6$$

7.2.3 Surface Electrical Resistance Measurements and Global Electrical Resistance Calculations

Six types of CFRP laminate panels, which were AB, AC, AD, AE, VB, and VC, were examined. These panels were made using two different manufacturing techniques that were VARTM (VB and VC) and autoclave processing techniques (AB, AC, AD, and AE). The fabrication processes

were detailed in Section 5.1 and 5.2 respectively. On each panel, the measurements of the surface electrical resistance were taken as shown in Figure 7-4 using the data acquisition system that was presented in Section 7.2.1, along with the sensing mats that were described in Section 5.3. A $500\ \mu\text{A}$ of direct current was injected into CFRP laminate panels. 10 electrical resistance readings were taken of each electric channel (A1, A2, A3, A4, B1, B2, B3 and B4) and the average values were used in further calculations. Noise was calculated by dividing the standard deviation on the mean value of electrical resistance in each channel and presented in Table 7-2.

Table 7-2 shows electrical resistances for all panels measured using sensing mat 1 and sensing mat 2 (Section 5.3 detailed each sensing mat), the electrical resistances were measured before and after damage was generated. The current sensing system adopted a four probe electrical resistance technique (discussed in Section 2.6.3), in this technique the electrical resistance of the contact is neglected, where $500\ \mu\text{A}$ of direct current was injected by the outer electrodes and the voltage was measured by the inner electrodes, (inner electrodes sometimes are called sensing electrodes) as shown in Figure 7-4. The outputs of the sensing code that is shown in Figure 7-2 and Appendix B give the electrical resistance changes following the measurement process.

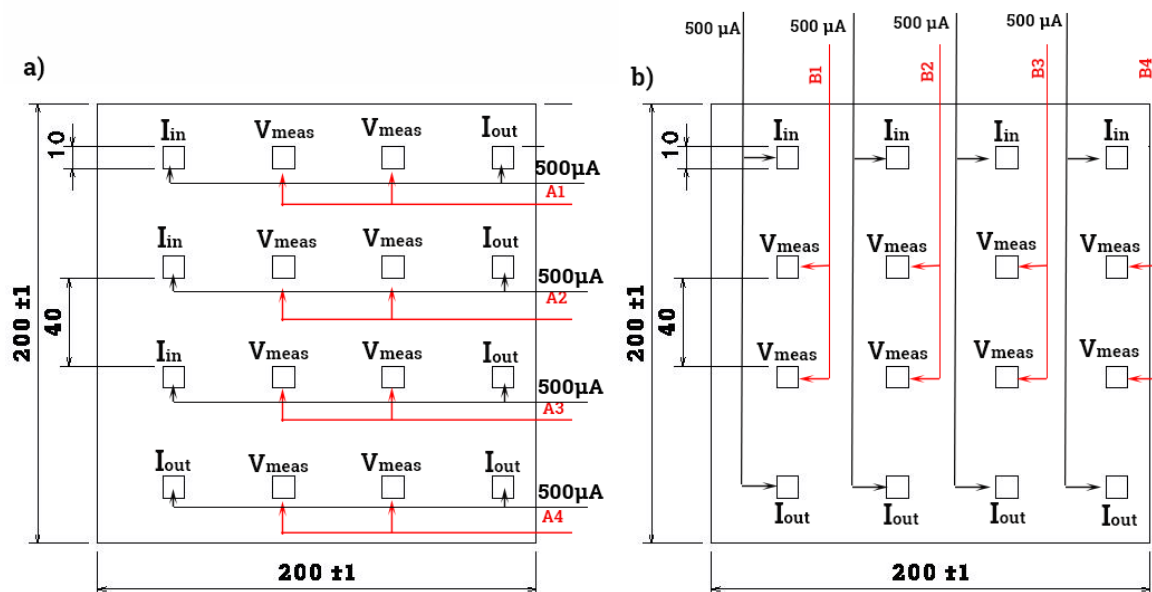


Figure 7-4: Electrical resistance measurement map using sensing mat 1 a) electrical resistance along 0° and b) electrical resistance along 90° .

The sensing mats attached to the bottom surface of the CFRP laminate panels (Section 5.3.1), whereas the impact events occurred on the top surface (Section 7.1). It can be seen in Table 7-2 that the pre-impact electrical resistance readings all differ, since the initial resistance is a function of the manufacturing technique of the panels, the sensing mats and the amount of electrical contacts made with carbon fibres. Also, it strongly depends on procedure that was

used to attach the sensing mat to the panel, the factors that affect electrical sensing techniques where presented in Section 2.4.4. Once this project will be upscaled, this issue can be partially resolved by automating this procedure to obtain more consistent data. There are other variables that have a significant impact on electrical resistances, such as exact amount of pressure, resin viscosity, surface quality of electrodes, fabricating procedures for sensing mats and CFRP laminates, shape and size of electrodes, materials of electrodes, amounts and types of an electric current, the place on the CFRP laminates that electrical measurements were taken at. The most important factor is how much contacts can be made with carbon fibres since that determines the electrical resistance in each point of measurements. The data obtained in Table 7-2 clearly shows the change in electrical resistance due to damage occurrence. This is raw data that was acquired from the data acquisition system directly as shown in Figure 7-2, further processing was undertaken to detect, quantify and locate the damage, with more details being shown in Section 7.3.3, Section 7.3.4, and Section 7.3.5.

It was found that increasing the contacts area from 100 mm² (mat 1) to 400 mm² (mat 2) increased the baseline electrical resistances up to $\approx 55\%$, this occurs due to the decrease in the current density and the increase in the distance between the electrodes from 40 mm to 90 mm. It was also found that the change in the baseline electrical resistance over time has been minimal that is an advantage of the four-probe electrical resistance method over other electrical sensing methods. Where the separation of current and voltage electrodes in this technique has eliminated the contacts electrical resistance, therefore, the contacts aging did not have an effect on the resistance baseline. An aging test was undertaken on the AC, AD, and VC specimens, where the electrical resistances were measured at the room temperature (20°C), the samples were kept in the lab for seven months and after seven months the electrical resistance was measured again at the room temperature (20°C), it was found that a very small change in electrical resistance had occurred, which was as low as $\approx 0.00001\%$. It can be noticed from Table 7-2 that the damage can be detected using both sensing mats, however, the sensing mat 2 has reduced the cost of the sensing system from £3200 to £1800, as discussed in Section 5.3, where sensing mat 2 has less sensors and therefore it required less number of NI9219 modules. It can be seen in Table 7-2 that the electrical resistance readings of mat 2 are more consistent in comparison with electrical resistance readings of mat 1. This can be attributed to surface area of the electrodes, where the current is distributed on a larger area. However, the change in electrical resistances due to damage using mat 1 is higher than the change in electrical resistance using mat 2 since the distance between consecutive electrodes is smaller (Section 5.3).

Table 7-2: Electrical resistance changes due to impact events measured using both sensing mat 1 and mat 2.

Sensing Channel	R_o before impact (Ω)	Im-STD	Noise	R_i after impact (Ω)	Im-STD	Noise
AB – 0.406 J – Mat 1						
A1	0.0404031	0.0000002	0.0000050	0.0405122	0.0000002	0.0000049
A2	0.0355110	0.0000001	0.0000028	0.0362349	0.0000001	0.0000028
A3	0.0348322	0.0000002	0.0000057	0.0355153	0.0000001	0.0000028
A4	0.0418006	0.0000001	0.0000024	0.0418005	0.0000001	0.0000024
B1	0.0441643	0.0000002	0.0000045	0.0442150	0.0000001	0.0000023
B2	0.0351508	0.0000002	0.0000057	0.0382359	0.0000001	0.0000026
B3	0.0376009	0.0000001	0.0000027	0.0400007	0.0000009	0.0000225
B4	0.0472153	0.0000001	0.0000021	0.0475101	0.0000002	0.0000042
AB – 0.657 J – Mat 1						
A1	0.0385211	0.0000002	0.0000052	0.0389305	0.0000002	0.0000051
A2	0.0295404	0.0000001	0.0000034	0.0305142	0.0000001	0.0000033
A3	0.0324331	0.0000001	0.0000031	0.0339517	0.0000009	0.0000265
A4	0.0416248	0.0000001	0.0000024	0.0418109	0.0000002	0.0000048
B1	0.0417141	0.0000001	0.0000024	0.0421115	0.0000002	0.0000047
B2	0.0328025	0.0000002	0.0000061	0.0341245	0.0000002	0.0000059
B3	0.0355412	0.0000001	0.0000028	0.0370016	0.0000002	0.0000054
B4	0.0426344	0.0000001	0.0000023	0.0434287	0.0000001	0.0000023
AB – 0.607 J – Mat 2						
A1	0.0420061	0.0000004	0.0000095	0.0422731	0.0000003	0.0000071
A2	0.0351252	0.0000001	0.0000028	0.0374185	0.0000001	0.0000027
B1	0.0385016	0.0000002	0.0000052	0.0392619	0.0000002	0.0000051
B2	0.0248331	0.0000006	0.0000242	0.0251384	0.0000003	0.0000119
AB – 1.426 J – Mat 1						
A1	0.0341926	0.0000001	0.0000029	0.0353401	0.0000002	0.0000057
A2	0.0332224	0.0000005	0.0000151	0.0374307	0.0000001	0.0000027
A3	0.0328002	0.0000003	0.0000091	0.0383504	0.0000002	0.0000052
A4	0.0383212	0.0000002	0.0000052	0.0395006	0.0000001	0.0000025
B1	0.0425232	0.0000003	0.0000071	0.0431356	0.0000005	0.0000116
B2	0.0341237	0.0000002	0.0000059	0.0362223	0.0000003	0.0000083
B3	0.0339011	0.0000001	0.0000029	0.0354602	0.0000001	0.0000028
B4	0.0382112	0.0000001	0.0000026	0.0391406	0.0000002	0.0000051
AB – 1.426 J – Mat 2						
A1	0.0325033	0.0000005	0.0000154	0.0328214	0.0000005	0.0000152
A2	0.0328331	0.0000002	0.0000061	0.0332117	0.0000002	0.0000060
B1	0.0248007	0.0000006	0.0000242	0.0254408	0.0000005	0.0000197
B2	0.0248114	0.0000006	0.0000242	0.0255444	0.0000005	0.0000196

Sensing Channel	R_o before pact (Ω)	Im- STD	Noise	R_i after pact (Ω)	Im- STD	Noise
AB – 3.333 J – Mat 1						
A1	0.0365441	0.0000003	0.0000082	0.0386403	0.0000003	0.0000078
A2	0.0365215	0.0000002	0.0000055	0.0448504	0.0000002	0.0000045
A3	0.0356351	0.0000002	0.0000056	0.0384488	0.0000002	0.0000052
A4	0.0397113	0.0000002	0.0000053	0.0413175	0.0000002	0.0000048
B1	0.0412122	0.0000002	0.0000049	0.0426921	0.0000002	0.0000047
B2	0.0423216	0.0000002	0.0000047	0.0455513	0.0000002	0.0000044
B3	0.0354652	0.0000001	0.0000028	0.0369127	0.0000003	0.0000081
B4	0.0412708	0.0000002	0.0000048	0.0424364	0.0000002	0.0000047
AB – 3.333 J – Mat 2						
A1	0.0553675	0.0000002	0.0000036	0.0567819	0.0000002	0.0000035
A2	0.0668332	0.0000002	0.0000030	0.0688545	0.0000020	0.0000290
B1	0.0664117	0.0000001	0.0000015	0.0689343	0.0000001	0.0000015
B2	0.0678233	0.0000002	0.0000029	0.0682346	0.0000002	0.0000029
AB – 4.96 J – Mat 1						
A1	0.0367455	0.0000003	0.0000082	0.0435715	0.0000003	0.0000069
A2	0.0337773	0.0000020	0.0000592	0.0500398	0.0000002	0.0000040
A3	0.0342124	0.0000010	0.0000292	0.0510739	0.0000002	0.0000039
A4	0.0462213	0.0000020	0.0000433	0.0520562	0.0000002	0.0000038
B1	0.0387667	0.0000002	0.0000052	0.0422191	0.0000002	0.0000047
B2	0.0381234	0.0000002	0.0000052	0.0445923	0.0000002	0.0000045
B3	0.0319852	0.0000001	0.0000031	0.0410791	0.0000001	0.0000024
B4	0.0448197	0.0000002	0.0000045	0.0430045	0.0000002	0.0000047
AB – 4.96 J – Mat 2						
A1	0.0677433	0.0000001	0.0000015	0.0699001	0.0000001	0.0000014
A2	0.0794217	0.0000004	0.0000050	0.0861423	0.0000004	0.0000046
B1	0.0719006	0.0000002	0.0000028	0.0857825	0.0000002	0.0000023
B2	0.0732657	0.0000002	0.0000027	0.0890519	0.0000003	0.0000034
AC – 1.426 J – Mat 1						
A1	0.0251127	0.0000001	0.0000040	0.0253005	0.0000002	0.0000079
A2	0.0210582	0.0000010	0.0000475	0.0217132	0.0000002	0.0000092
A3	0.0231484	0.0000011	0.0000475	0.0240315	0.0000014	0.0000583
A4	0.0320041	0.0000013	0.0000406	0.0323651	0.0000016	0.0000494
B1	0.0304711	0.0000012	0.0000394	0.0302118	0.0000020	0.0000662
B2	0.0202493	0.0000010	0.0000494	0.0231478	0.0000017	0.0000734
B3	0.0230029	0.0000015	0.0000652	0.0238414	0.0000015	0.0000629
B4	0.0270715	0.0000000	0.0000001	0.0271351	0.0000012	0.0000442
AC – 1.426 J – Mat 2						
A1	0.0408331	0.0000011	0.0000269	0.0412131	0.0000011	0.0000267

Sensing Channel	R_o before pact (Ω)	Im- STD	Noise	R_i after pact (Ω)	Im- STD	Noise
A2	0.0376171	0.0000002	0.0000053	0.0385583	0.0000005	0.0000130
B1	0.0424008	0.0000012	0.0000283	0.0432019	0.0000007	0.0000162
B2	0.0484604	0.0000009	0.0000186	0.0492814	0.0000006	0.0000122
AC – 3.33 J – Mat 1						
A1	0.0253477	0.0000001	0.0000039	0.0271932	0.0000010	0.0000368
A2	0.0195712	0.0000001	0.0000051	0.0220084	0.0000003	0.0000136
A3	0.0223004	0.0000002	0.0000090	0.0251316	0.0000004	0.0000159
A4	0.0296071	0.0000001	0.0000034	0.0315574	0.0000001	0.0000032
B1	0.0272017	0.0000002	0.0000074	0.0274043	0.0000006	0.0000219
B2	0.0221705	0.0000002	0.0000090	0.0222223	0.0000009	0.0000405
B3	0.0192447	0.0000002	0.0000104	0.0212012	0.0000004	0.0000189
B4	0.0234278	0.0000002	0.0000085	0.0235901	0.0000007	0.0000297
AC – 3.33 J – Mat 2						
A1	0.0381121	0.0000004	0.0000105	0.0401932	0.0000001	0.0000025
A2	0.0473246	0.0000002	0.0000042	0.0487119	0.0000004	0.0000082
B1	0.0376816	0.0000010	0.0000265	0.0383147	0.0000008	0.0000209
B2	0.0407342	0.0000001	0.0000025	0.0416912	0.0000005	0.0000120
AC – 4.96 J – Mat 1						
A1	0.0246814	0.0000003	0.0000122	0.0252471	0.0000003	0.0000119
A2	0.0207324	0.0000001	0.0000048	0.0246817	0.0000001	0.0000041
A3	0.0222091	0.0000001	0.0000045	0.0263181	0.0000001	0.0000038
A4	0.0257415	0.0000006	0.0000233	0.0264652	0.0000004	0.0000151
B1	0.0247214	0.0000008	0.0000324	0.0268133	0.0000008	0.0000298
B2	0.0234306	0.0000004	0.0000171	0.0280029	0.0000004	0.0000143
B3	0.0286173	0.0000002	0.0000070	0.0356919	0.0000002	0.0000056
B4	0.0286323	0.0000001	0.0000035	0.0327213	0.0000001	0.0000031
AC – 4.96 J – Mat 2						
A1	0.0421742	0.0000001	0.0000024	0.0443121	0.0000001	0.0000023
A2	0.0405611	0.0000002	0.0000049	0.0441249	0.0000002	0.0000045
B1	0.0413701	0.0000002	0.0000048	0.0432167	0.0000002	0.0000046
B2	0.0436516	0.0000004	0.0000092	0.0448115	0.0000003	0.0000067
AD – 4.96 J – Mat 1						
A1	0.0388162	0.0000002	0.0000052	0.0383011	0.0000002	0.0000052
A2	0.0363006	0.0000004	0.0000110	0.0374381	0.0000004	0.0000107
A3	0.0373024	0.0000004	0.0000107	0.0386695	0.0000004	0.0000103
A4	0.0382163	0.0000001	0.0000026	0.0390158	0.0000001	0.0000026
B1	0.0350083	0.0000007	0.0000200	0.0355009	0.0000007	0.0000197
B2	0.0363318	0.0000001	0.0000028	0.0372541	0.0000001	0.0000027
B3	0.0372612	0.0000002	0.0000054	0.0379011	0.0000002	0.0000053

Sensing Channel	R_o before pact (Ω)	Im- STD	Noise	R_i after pact (Ω)	Im- STD	Noise
B4	0.0340156	0.0000004	0.0000118	0.0345114	0.0000005	0.0000145
AD – 4.96 J – Mat 2						
A1	0.0350047	0.0000002	0.0000057	0.0360892	0.0000002	0.0000055
A2	0.0365031	0.0000002	0.0000055	0.0369017	0.0000001	0.0000027
B1	0.0373814	0.0000002	0.0000054	0.0377513	0.0000002	0.0000053
B2	0.0326113	0.0000001	0.0000031	0.0325073	0.0000004	0.0000123
AD – 9.95 J – Mat 1						
A1	0.0248114	0.0000002	0.0000081	0.0273549	0.0000002	0.0000073
A2	0.0212319	0.0000001	0.0000047	0.0264151	0.0000001	0.0000038
A3	0.0209041	0.0000001	0.0000048	0.0220039	0.0000001	0.0000045
A4	0.0282516	0.0000001	0.0000035	0.0294211	0.0000001	0.0000034
B1	0.0287212	0.0000001	0.0000035	0.0290094	0.0000001	0.0000034
B2	0.0238015	0.0000004	0.0000168	0.0244384	0.0000003	0.0000123
B3	0.0293313	0.0000003	0.0000102	0.0312633	0.0000003	0.0000096
B4	0.0340307	0.0000001	0.0000029	0.0343131	0.0000001	0.0000029
AD – 9.95 J – Mat 2						
A1	0.0381212	0.0000002	0.0000052	0.0391751	0.0000003	0.0000077
A2	0.0405413	0.0000002	0.0000049	0.0410528	0.0000002	0.0000049
B1	0.0476035	0.0000001	0.0000021	0.0482846	0.0000001	0.0000021
B2	0.0393375	0.0000003	0.0000076	0.0411639	0.0000003	0.0000073
AE – 4.96 J – Mat 1						
A1	0.0241023	0.0000001	0.0000041	0.0242761	0.0000001	0.0000041
A2	0.0268131	0.0000001	0.0000037	0.0273442	0.0000001	0.0000037
A3	0.0286315	0.0000003	0.0000105	0.0291623	0.0000003	0.0000103
A4	0.0316172	0.0000002	0.0000063	0.0319041	0.0000002	0.0000063
B1	0.0280104	0.0000005	0.0000179	0.0283022	0.0000004	0.0000141
B2	0.0274322	0.0000002	0.0000073	0.0282518	0.0000002	0.0000071
B3	0.0264174	0.0000004	0.0000151	0.0274109	0.0000004	0.0000146
B4	0.0279151	0.0000002	0.0000072	0.0281111	0.0000002	0.0000071
AE – 4.96 J – Mat 2						
A1	0.0452542	0.0000002	0.0000044	0.0461521	0.0000002	0.0000043
A2	0.0413411	0.0000002	0.0000048	0.0420105	0.0000002	0.0000048
B1	0.0409022	0.0000001	0.0000024	0.0413019	0.0000001	0.0000024
B2	0.0419428	0.0000001	0.0000024	0.0424307	0.0000001	0.0000024
AE – 9.95 J – Mat 1						
A1	0.0248151	0.0000002	0.0000081	0.0252862	0.0000002	0.0000079
A2	0.0212742	0.0000001	0.0000047	0.0230967	0.0000001	0.0000043
A3	0.0209055	0.0000001	0.0000048	0.0219381	0.0000001	0.0000046
A4	0.0282931	0.0000005	0.0000177	0.0294092	0.0000003	0.0000102

Sensing Channel	R_o before pact (Ω)	Im- STD	Noise	R_i after pact (Ω)	Im- STD	Noise
B1	0.0287032	0.0000006	0.0000209	0.0280434	0.0000006	0.0000214
B2	0.0238004	0.0000004	0.0000168	0.0256728	0.0000004	0.0000156
B3	0.0252666	0.0000004	0.0000158	0.0263321	0.0000003	0.0000114
B4	0.0340642	0.0000002	0.0000059	0.0343842	0.0000002	0.0000058
AE – 9.95 J – Mat 2						
A1	0.0450912	0.0000001	0.0000022	0.0455406	0.0000001	0.0000022
A2	0.0434164	0.0000001	0.0000023	0.0440652	0.0000001	0.0000023
B1	0.0417403	0.0000001	0.0000024	0.0422543	0.0000001	0.0000024
B2	0.0484531	0.0000001	0.0000021	0.0489049	0.0000001	0.0000020
VB – 1.426 J – Mat 1						
A1	0.0345473	0.0000002	0.0000058	0.0347751	0.0000002	0.0000058
A2	0.0343592	0.0000002	0.0000058	0.0370486	0.0000002	0.0000054
A3	0.0347971	0.0000002	0.0000057	0.0352251	0.0000001	0.0000028
A4	0.0447481	0.0000003	0.0000067	0.0450082	0.0000003	0.0000067
B1	0.0320129	0.0000001	0.0000031	0.0330231	0.0000003	0.0000091
B2	0.0374884	0.0000001	0.0000027	0.0397501	0.0000003	0.0000075
B3	0.0290041	0.0000002	0.0000069	0.0320829	0.0000005	0.0000156
B4	0.0310023	0.0000001	0.0000032	0.0330139	0.0000003	0.0000091
VB – 1.426 J – Mat 2						
A1	0.0572431	0.0000003	0.0000052	0.0593212	0.0000003	0.0000051
A2	0.0776125	0.0000002	0.0000026	0.0784132	0.0000002	0.0000026
B1	0.0685014	0.0000001	0.0000015	0.0701609	0.0000004	0.0000057
B2	0.0670046	0.0000002	0.0000030	0.0673214	0.0000002	0.0000030
VB – 3.33 J – Mat 1						
A1	0.0461254	0.0000004	0.0000087	0.0493631	0.0000004	0.0000081
A2	0.0523836	0.0000004	0.0000076	0.0630023	0.0000004	0.0000063
A3	0.0413412	0.0000002	0.0000048	0.0505333	0.0000002	0.0000040
A4	0.0420222	0.0000004	0.0000095	0.0424951	0.0000004	0.0000094
B1	0.0316678	0.0000001	0.0000032	0.0330002	0.0000001	0.0000030
B2	0.0301667	0.0000002	0.0000066	0.0398194	0.0000002	0.0000050
B3	0.0405554	0.0000002	0.0000049	0.0490199	0.0000002	0.0000041
B4	0.0350002	0.0000002	0.0000057	0.0390023	0.0000002	0.0000051
VB – 3.33 J – Mat 2						
A1	0.0624323	0.0000006	0.0000096	0.0635304	0.0000005	0.0000079
A2	0.0204561	0.0000005	0.0000244	0.0220647	0.0000005	0.0000227
B1	0.0710325	0.0000005	0.0000070	0.0730239	0.0000002	0.0000027
B2	0.0927146	0.0000001	0.0000011	0.0940321	0.0000002	0.0000021
VB – 4.96 J – Mat 1						
A1	0.0270023	0.0000001	0.0000037	0.0331032	0.0000002	0.0000060

Sensing Channel	R_o before pact (Ω)	Im- STD	Noise	R_i after pact (Ω)	Im- STD	Noise
A2	0.0280041	0.0000001	0.0000036	0.0321661	0.0000002	0.0000062
A3	0.0270130	0.0000002	0.0000074	0.0312924	0.0000001	0.0000032
A4	0.0260311	0.0000003	0.0000115	0.0320023	0.0000003	0.0000094
B1	0.0406802	0.0000002	0.0000049	0.0566789	0.0000002	0.0000035
B2	0.0381485	0.0000001	0.0000026	0.0416608	0.0000001	0.0000024
B3	0.0312925	0.0000002	0.0000064	0.0405551	0.0000002	0.0000049
B4	0.0371128	0.0000002	0.0000054	0.0390082	0.0000002	0.0000051
VB – 4.96 J – Mat 2						
A1	0.0488131	0.0000002	0.0000041	0.0552393	0.0000002	0.0000036
A2	0.0950112	0.0000002	0.0000021	0.0980372	0.0000002	0.0000020
B1	0.0246235	0.0000003	0.0000122	0.0285234	0.0000003	0.0000105
B2	0.0406211	0.0000002	0.0000049	0.0440133	0.0000002	0.0000045
VC – 1.426 J – Mat 1						
A1	0.0212790	0.0000001	0.0000047	0.0215946	0.0000001	0.0000046
A2	0.0227809	0.0000002	0.0000088	0.0228308	0.0000002	0.0000088
A3	0.0205278	0.0000003	0.0000146	0.0206000	0.0000003	0.0000146
A4	0.0289768	0.0000004	0.0000138	0.0291007	0.0000004	0.0000137
B1	0.0270000	0.0000005	0.0000185	0.0270000	0.0000005	0.0000185
B2	0.0233442	0.0000006	0.0000257	0.0233442	0.0000006	0.0000257
B3	0.0202774	0.0000007	0.0000345	0.0202774	0.0000007	0.0000345
B4	0.0220298	0.0000001	0.0000045	0.0220298	0.0000001	0.0000045
VC – 3.33 J – Mat 1						
A1	0.0224053	0.0000002	0.0000089	0.0229686	0.0000002	0.0000087
A2	0.0220925	0.0000002	0.0000091	0.0240203	0.0000002	0.0000083
A3	0.0219047	0.0000003	0.0000137	0.0250040	0.0000003	0.0000120
A4	0.0326692	0.0000002	0.0000061	0.0327945	0.0000002	0.0000061
B1	0.0291646	0.0000002	0.0000069	0.0297132	0.0000002	0.0000067
B2	0.0257849	0.0000002	0.0000078	0.0290049	0.0000002	0.0000069
B3	0.0250711	0.0000003	0.0000120	0.0273322	0.0000003	0.0000110
B4	0.0240320	0.0000003	0.0012483	0.0241576	0.0000003	0.0000124
VC – 3.33 J – Mat 2						
A1	0.0200222	0.0000001	0.0000050	0.0210343	0.0000001	0.0000048
A2	0.0670231	0.0000001	0.0000015	0.0681135	0.0000002	0.0000029
B1	0.0287327	0.0000002	0.0000070	0.0291343	0.0000003	0.0000103
B2	0.0530237	0.0000002	0.0000038	0.0535722	0.0000002	0.0000037
VC – 4.96 J – Mat 1						
A1	0.0212790	0.0000002	0.0000094	0.0235946	0.0000002	0.0000085
A2	0.0227809	0.0000002	0.0000088	0.0255308	0.0000002	0.0000078
A3	0.0205278	0.0000003	0.0000146	0.0234026	0.0000003	0.0000128

Sensing Channel	R _o before impact (Ω)	Im-STD	Noise	R _i after impact (Ω)	Im-STD	Noise
A4	0.0289768	0.0000002	0.0000069	0.0281007	0.0000002	0.0000071
B1	0.0240099	0.0000002	0.0000083	0.0260022	0.0000002	0.0000077
B2	0.0233442	0.0000002	0.0000086	0.0242775	0.0000003	0.0000124
B3	0.0181304	0.0000003	0.0000165	0.0227741	0.0000003	0.0000132
B4	0.0261042	0.0000002	0.0000077	0.0290372	0.0000001	0.0000034
VC – 4.96 J – Mat 2						
A1	0.0397212	0.0000006	0.0000151	0.0420135	0.0000004	0.0000095
A2	0.0668013	0.0000005	0.0000075	0.0700296	0.0000004	0.0000057
B1	0.0420134	0.0000002	0.0000048	0.0470704	0.0000002	0.0000042
B2	0.0700297	0.0000006	0.0000107	0.0560921	0.0000005	0.0000089

The global electrical resistance change refers to the whole change in electrical resistance of the CFRP laminate panels due to damage. The surface electrical resistances that were presented in Table 7-2, were deployed to calculate the global electrical resistances. Equation 7 – 7 and Equation 7 – 8 were used to calculate the global electrical resistance change for the CFRP laminate panels.

$$\xi_1 = \left(\frac{\sum_{A1}^{A4} \left(\frac{\Delta R}{R_0} \right) + \sum_{B1}^{B4} \left(\frac{\Delta R}{R_0} \right)}{8} \right) * 100 \quad 7-7$$

$$\xi_2 = \left(\frac{\sum_{A1}^{A2} \left(\frac{\Delta R}{R_0} \right) + \sum_{B1}^{B2} \left(\frac{\Delta R}{R_0} \right)}{4} \right) * 100 \quad 7-8$$

ξ_1 is the global electrical resistance using sensing mat 1 (Ω), ξ_2 is the global electrical resistance using sensing mat 2 (Ω). ΔR is $(R_i - R_0)$; R_i represents mean value of ten electrical resistance readings after impact acquired using electrical channels A1, A2, A3, A4, B1, B2, B3, and B4 as shown in Table 7-2, R_0 represents the mean value of ten electrical resistance readings before the impact A1, A2, A3, A4, B1, B2, B3, and B4 shown in Table 7-2.

The following formula was used to calculate the standard error (Y) in the global electrical resistances.

$$Y = s/\sqrt{n} \quad 7-9$$

Where s is standard deviation of the electrical resistance readings and n is the number of electrical resistance readings.

7.2.4 Electrical Resistance Change Due to Flexural Loads

Changes in electrical resistance due to applied flexural loading was investigated using a four – probe electrical resistance method as described in the previous section. A 200 x 20 x t mm specimen (AC and VC panel) was used. The specimen was cut using 3000 rpm diamond cutter, the cutting was undertaken in the presence of water to keep the specimen at the room temperature and to avoid damaging the specimen due to cutting heat. The specimen was ground using silicon carbide papers (240 and 600 grit) and polished using 1200 silicon carbide papers prior to attach the sensing mats to the specimens. A1 channel of sensing mat 1 and sensing mat 2 were attached to the bottom surface of the specimen using Silver – Epoxy conductive adhesive as described in Section 5.3.1. However, due to size constraints (the size of the bar is 200 x 20 (L x W) mm and the sizes of the sensing mats are 200 x 200 (L x W)), therefore only A1 readings were taken.

Figure 7-5 shows the specimen and the test set up, the outer electrodes are current electrodes and inner electrodes are voltage electrodes (sensing electrodes). The specimen was subjected to four loading cycles and the deflection due to applied force was measured using camera installed on the testing frame as shown in Figure 7-6. The test speed was set at 2 mm / min and the test was paused four times to measure the electrical resistance at various deflections that were (2, 4, 6, and 8 mm), the pausing time was 3 minutes. 10 electrical resistance readings were acquired, and the average values were considered in further calculations. The electrical resistance changes due to deflection are depicted and discussed in Section 7.3.2.

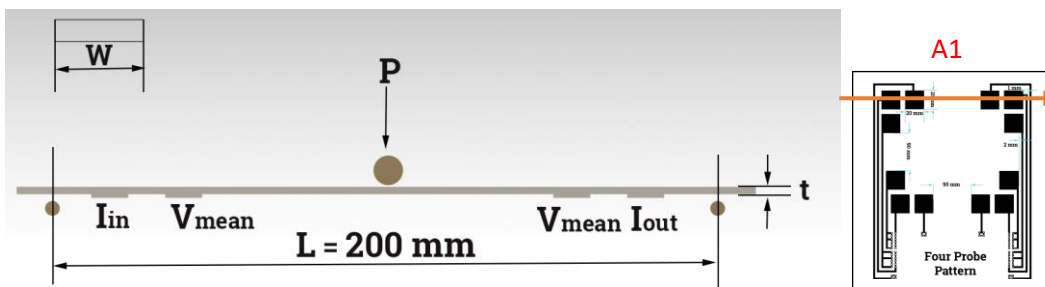


Figure 7-5: Flexural test and specimen configuration.

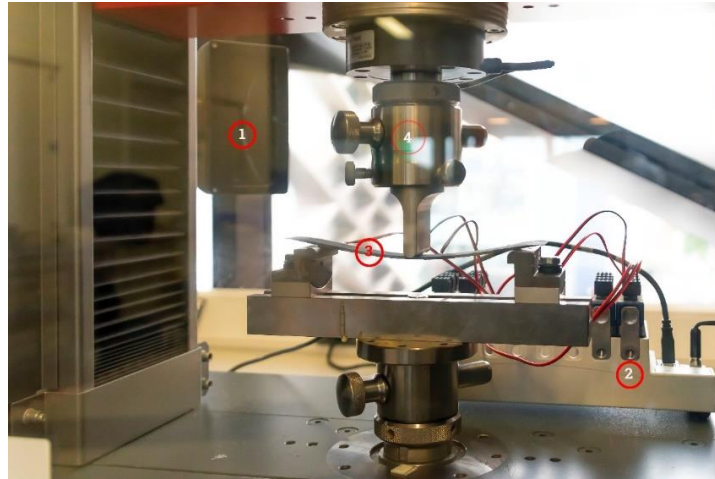


Figure 7-6: Experimental set-up; 1. Digital camera to monitor the movement of the specimen and record the deflection, 2. DAQ system to measure electrical resistance data from the CFRP laminate, 3. CFRP laminate, 4. Flexural testing rig.

7.2.5 Non-Destructive Testing Technique (C-scan)

In this non-destructive testing technique, the sound waves that are simply organized mechanical vibrations travel through the CFRP laminate. The waves will be reflected once they hit a discontinuity in the materials, such as delamination, matrix crackings and voids. The damage profile, the damage size, and the location of the damaged region were investigated using a C-scan camera (DolphiCam, UK), the software (DolphiCam, UK) was used to analyse the images, further image processing was carried out using Photoshop CC 2017 (Adobe, USA).

7.2.5.1 Specimen preparation and C-scan setup

DolphiCam is a hand-held real-time imaging ultrasound camera with dry-coupling front surface that enables inspection of CFRP laminates without any liquid couplants. However, the CFRP laminate panels under investigation must be dust free. The C-scan camera shoots up to 4 frames per second (fps) due to the field programmable gate array (FPGA) that is installed on-camera. The transducer is a 30 x 30 mm, the transducer consists of a piezoelectric two-dimensional 124 x 124 element array as shown in Figure 7-7. When a high electric pulse is applied to the transducer, a mechanical vibration generated which travels through a 2.84 mm dry coupling pad and into the material under inspection. The reflected waves are then picked up by the same element in the array. The waves are then converted from mechanical energy to electrical signals. DolphiCam CF08 can inspect CFRP laminates up to 8 mm thickness.

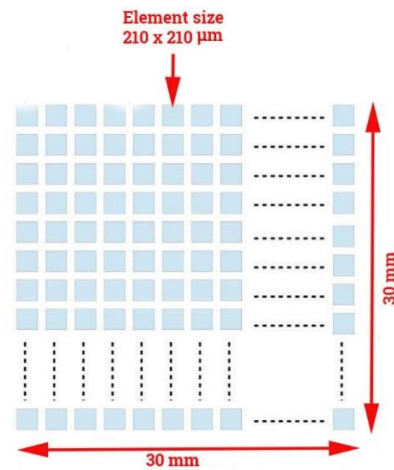


Figure 7-7: DolphiCam C08 transducer.

The C-scan camera was calibrated prior to the start of the scan. The velocity of the sound in CFRP laminate was fixed at 3000 m / s, longitudinal mode of propagation was used, and a 3.8 MHz ultrasonic beam was applied on the specimen. A few drops of Sonagel-w (Sonatest, UK) was used to allow smooth probe movement during testing. The output of the C-scan camera includes A-scan, B-scan and C-scan (Figure 7-8). A-scan is presented as a signal processed time series of the ultrasound reflection from the material at the intersection between the cross-hairs on the main C-scan images, over the depth of the material (Graph in the bottom left hand-corner of Figure 7-8). The B-scan is presented as the cross-section through the material, shown in the top left-hand graph and bottom centre graph of Figure 7-8. There are two B-scan lines, those being vertical and horizontal sections through the material coinciding with the position of the cross-hair on the main C-scan images. The vertical B-scan displays the vertical cross-section at the position of the vertical line in the C-scan. While the horizontal B-scan displays the cross-section at the horizontal line in the C-scan. B-scan information is vital to determine the location of the damage through the thickness as shown in Figure 7-8. Of the 3 C-scan images, the most clear representation of damage is shown in the C – scan (Time of Flight) image in the top right hand corner, where the depth of damage within the structure can be seen in the changes of colour. In this case, a cross-shaped damage area can be seen in the image at a depth of about 1.5 mm from the surface.

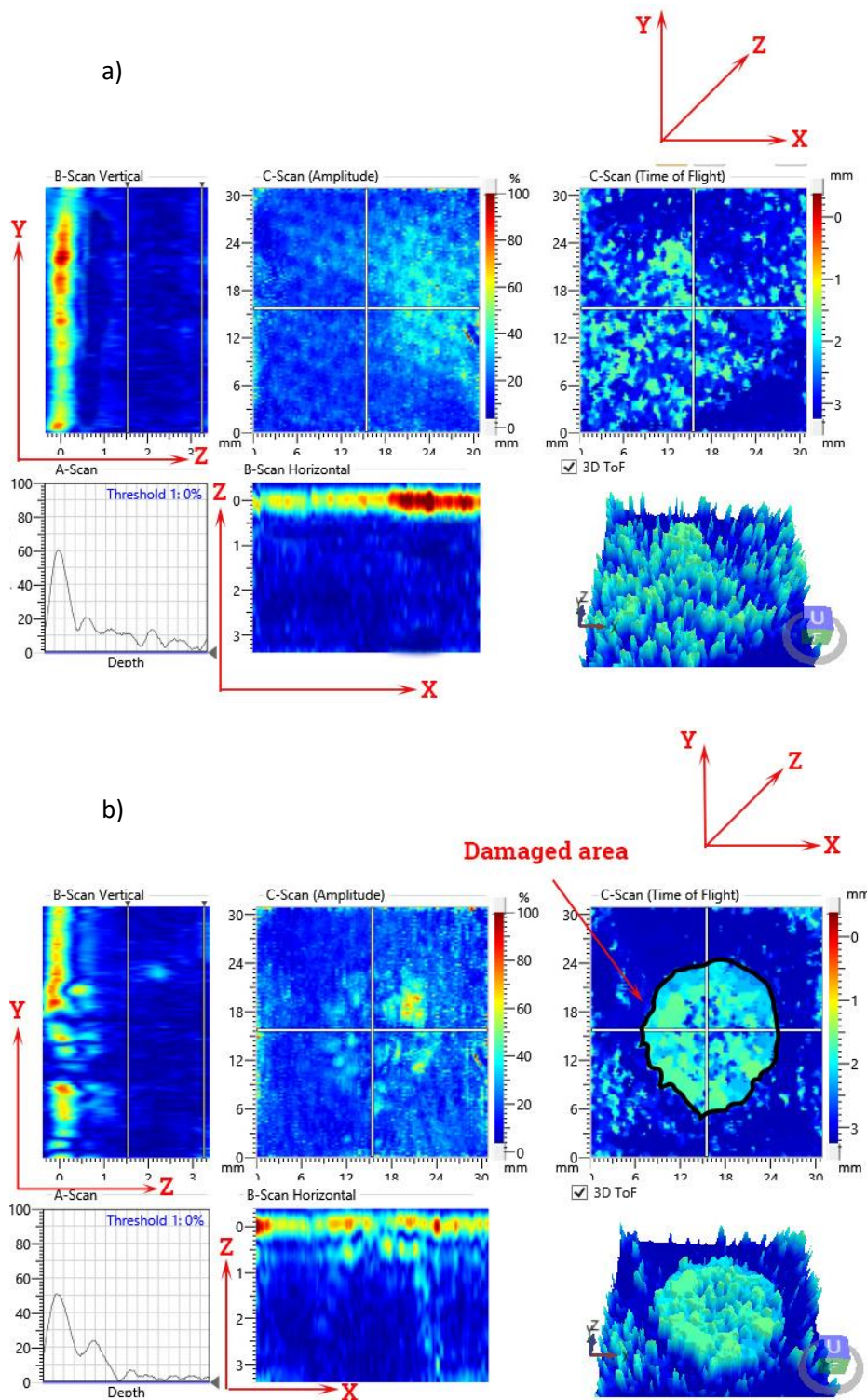


Figure 7-8: C – scan, B – scan, and A – scan images for a) damage free CFRP laminates (AE panel) and b) the same panel but impacted at 10 J. In C – scan TOF image in top right corner, the dark blue colour represents the back face of the panel and the light blue colour represents the top surface roughness. B – scan images in the left top corner and bottom middle represent the depth of damage through – thickness. A – scan in the bottom left corner shows reflection of ultrasound wave due to damage.

7.2.6 Destructive Testing Technique (Fluorescent Microscope Test)

Epi-fluorescent microscopy is a valuable tool to observe the micro-cracks and macro-cracks and their extent in composite materials. In thermosetting carbon fibre/epoxy composites, some of the micro-cracks cannot be observed in a conventional microscope (dark-field and bright-field illumination), therefore using an Epi-fluorescence microscopy is essential to see these cracks. In addition, there are many types of features that can benefit from the high contrast that can be obtained from a fluorescing dye. This is especially true if the fluorescing contrast can impregnate the damaged areas.

7.2.6.1 Sample Preparation and Machine Setup

Firstly, representative areas were cut from the impacted panels using a cutting wheel, the cutter speed was fixed at 3000 rpm (no load speed), the linear speed was adjusted manually, the linear cutting speed was low with a water spray as a coolant. Then the specimens were ground down using a grinder and polisher (ATM Saphir 320, Germany). A rough silicon carbide paper (grit 180) at 150 RPM of platen rotation speed was used with water as a coolant to avoid creating or changing artefacts at the surface. The specimens were washed and dried for 12 hours at 50°C in an oven (Thermo Scientific, UK) to obtain a clean interface to bond to the mounting resin.

The specimens were potted at the room temperature in a cold-setting mounting resin (Epofix, Struers, Denmark) in mounting cups. This is a two-components resin with a low-viscosity, it is suitable for vacuum impregnation. Its mixing ratio by weight is 25 parts of resin to 3 parts of hardener. To achieve greater contrast between the micro-cracks, macro-cracks and other features, a fluorescent dye (EpoDye, Struers, Denmark) was mixed with the mounting resin Epofix (component A) prior to adding the hardener (component B) to the resin. This dye will fluoresce under the UV-light, therefore, it provides high contrast to distinguish between various types of features in the panels.

The necessary quantity of the mounting resin and the hardener were mixed manually and then placed in a vacuum oven at the room temperature for 10 minutes to remove entrapped air. The specimens were placed in plastic mounting cups (Buehler, Germany), the mounting cups were release-coated using release agent (Marbocote CEO 75, US), clips were used to support the samples to ensure a flat planar surface will be obtained. The resin was then slowly poured into the cups and the cups were placed in a vacuum chamber at 101 kPa for 2 hours at the room temperature then they were taken out and left to cure at the room temperature for 12 hours. Then the mounted specimens were ejected from the mould and they were ready for grinding and polishing stages as shown in Table 7-3.

Table 7-3: Grinding and polishing stages for CFRP laminates for fluorescence microscopy.

Stage	Abrasive	Lubricant	Extender Force (N)	Time (min:sec)	Platen Speed (RPM)	Head Speed (RPM)	Relative Rotation
1	P600	Water	22	Until planar	175	60	Contra
2	P1200	Water	22	0:50	175	60	Contra
3	15 μm diamond	15 μm Polycrystalline Diamond suspension	22	0:50	175	60	Contra
4	6 μm diamond	6 μm Polycrystalline Diamond suspension	18	4	100	60	Contra
5	0.05 μm diamond	0.05 μm Diamond suspension	18	1:30	75	60	Contra
6	0.05 μm diamond	0.05 μm Diamond suspension	18	1:30	75	60	Comp

An automated polishing head with circular openings EcoMet 250 Pro (Buehler, Germany) was used. This machine used compressed air to clamp the samples in a place. In the first stage the samples were ground on wet silicon carbide abrasive papers (grit size 600), the head speed was 175 RPM and using counter-direction rotation of the platen, the platen speed was 60 RPM as shown in Table 7-3. This stage ended when the damaged areas were reached. The specimens after this stage had a high roughness and were ready for the next stage that was rough polishing.

An automated rough polishing stage included reduction in abrasive size and the use of abrasive suspensions. 1200 grit size silicon carbide papers were used with water for cooling the sample. A 22 N pressure was applied on the sample when the head speed was 175 RPM in counter-direction to the platen that was at 60 RPM for 50 seconds. A 15 μm polycrystalline diamond suspension (Buehler, Germany) was then used on a polishing cloth (Buehler, Germany). Moderate pressure 22 N was applied on the sample when the head speed was 175 RPM for 50 seconds as shown in Table 7-3. The final rough polishing stage started using 6 μm polycrystalline diamond suspension (Buehler, Germany) applied to a 15 μm diamond cloth (Buehler, Germany). The fine polishing stage started using non-nap cloths with a 0.05 μm diamond suspension (Buehler, Germany) with low pressure 18 N and low head speed 75 RPM counter-direction to platen speed that was 60 RPM. The final polishing stage used a 0.05 μm diamond cloth (Bueh-

ler, Germany) with a 0.05 μm diamond suspension in this stage the head rotation was complimentary to platen rotation direction that were 75 and 60 RPM respectively. Then the samples were placed in distilled water in an ultrasonic cleaner for 5 minutes, then dried using a hair dryer then specimens with smooth surfaces were ready to be examined under a fluorescence microscopy.

7.3 Results and Discussions

7.3.1 Through – Thickness Electrical Resistivity Measurements and Electrical Conductivity Calculations

Table 7-4 shows through – thickness electrical resistivity for all CFRP laminate panels that were used in this thesis, the through – thickness electrical resistivity measured using the set up described in Section 7.2.2 using both sensing mats (sensing mat 1 and sensing mat 2). It can be seen that the baseline of the through – thickness electrical resistivity decreases when the panel thickness increases that is due to increase of carbon fibre volume fraction as shown in Table 7-4. When carbon fibre volume fraction increases and because of the wavy shapes of the carbon fibre that all combined helps to increase the fibre – fibre contacts between adjacent plies and decrease the through – thickness electrical resistivity baseline. This in turn means the fibre volume fraction has more effect than thickness on electrical resistance. Table 7-4 shows that the baseline electrical resistivity using mat 2 is higher than the electrical resistivity baseline measured using mat 1, this is attributed to the distance between the voltage electrodes (sensing electrodes) that were 130 mm in sensing mat 2 and 60 mm in sensing mat 1. The electrical conductivity follows the same pattern where it increases when the carbon volume fraction increases.

Table 7-4: Through – thickness electrical resistivity and electrical conductivity of composites at various carbon fibre volume fractions.

Panel	AB	AC	AD	AE	VB	VC
Vf %	44.27	50.67	54.35	54.44	43.87	47.17
η_t (mat 1) Ω .mm	0.052	0.037	0.036	0.029	0.050	0.032
η_t (mat 2) Ω .mm	0.124	0.115	0.094	0.093	0.152	0.116
Cc S/mm	2604	2980	3197	3202	2535	2726

The effect of panel thicknesses and the fibre volume fraction on the through – thickness electrical resistivity is shown in Figure 7-9 and Figure 7-10. Where the through – thickness electrical resistivity was measured using sensing mat 1 and sensing mat 2 as detailed in Section 7.2.2. It can be seen in both figures that with the increasing of carbon fibre volume fraction and due to waviness of carbon fibre the number of fibre – fibre contacts also increase, resulting in a decrease in through – thickness electrical resistivity. Because of losing these fibre – fibre contacts will increase the electrical resistance of the panels this makes the electrical resistance sensing method very suitable to detect internal damage. It can be seen from the figures that the maximum carbon fibre volume fraction obtained was 54.44 % that is due to carbon fibre texture (twill

fabric weave), where the fabric weave does not allow the resin to bleed out of the layup stack during the curing process.

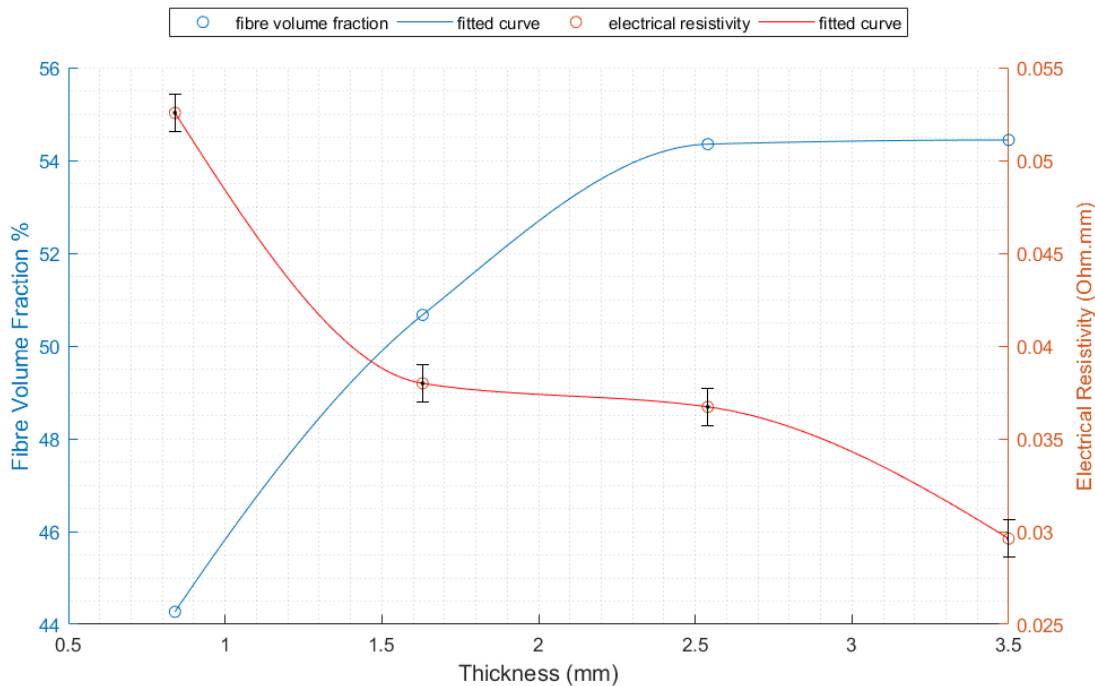


Figure 7-9: Dependence of through – thickness electrical resistivity of CFRP laminate panels on thickness and fibre volume fraction. The electrical resistivity was measured using sensing mat 1.

The electrical resistivity increased by up to 50 % when measured using sensing mat 2 (Figure 7-10) that is due to electrode size and the sensing length that were 400 mm² and 90 mm for sensing mat 2 and 100 mm² and 40 mm for sensing mat 1. However, sensing mat 2 was less sensitive for damage detection than sensing mat 1 as will be discussed in Section 7.3.3. The straight line in electrical resistivity curve in the region between 2.54 and 3.5 mm means that sensing mat 2 was not able to measure the reduction in electrical resistivity due to increase in fibre volume fraction.

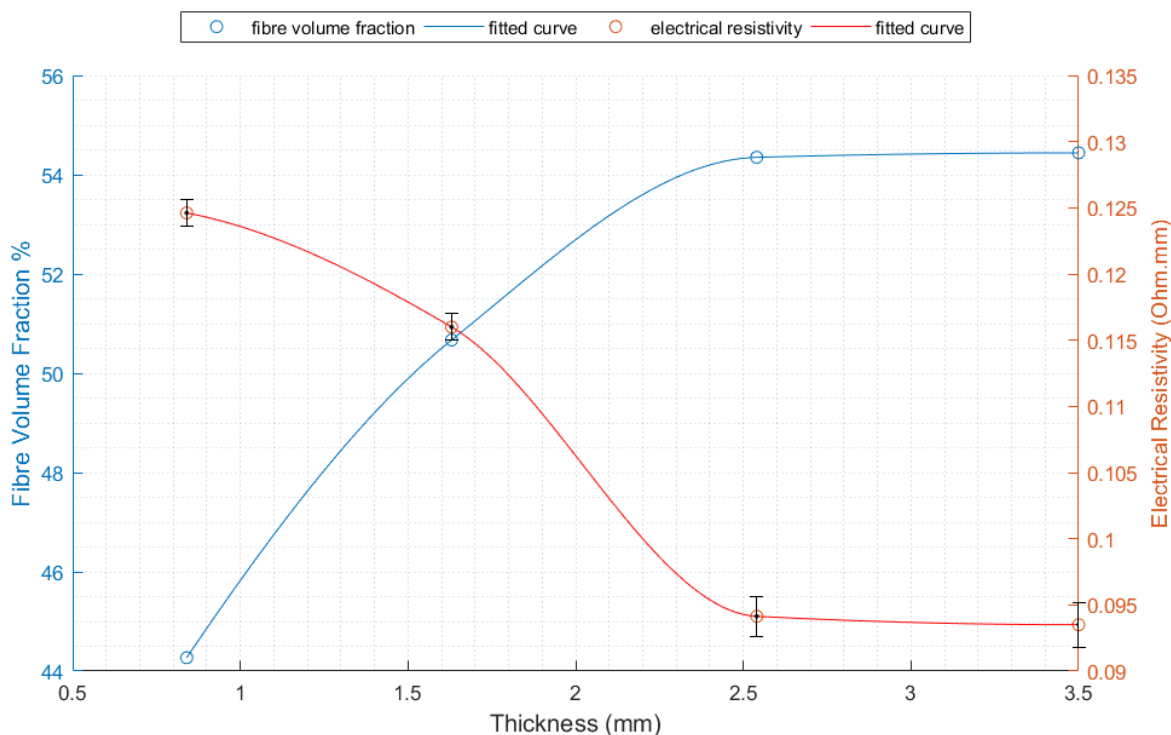


Figure 7-10: Dependence of through – thickness electrical resistivity of CFRP laminate panels on thickness and fibre volume fraction. The electrical resistivity was measured using sensing mat 2.

7.3.2 Changes in Electrical Resistance Due to Flexural Loads

Flexural test was performed on an autoclave processing CFRP laminate panel (AC) and vacuum assisted resin transfer moulding panel (VC) using both sensing mats (sensing mat 1 and sensing mat 2). The typical experimental set up was illustrated in Figure 7-5. Four loading cycles were used, the electrical resistance was measured prior to applying flexural loads and then it was measured while the specimen was loaded, due to the limitations in the data acquisition system (DAQ system was not capable of monitoring changes in electrical resistance in real time) the test was paused several times to measure the changes in electrical resistance while the specimen was loaded. A strong relationship was observed between the applied load and the changes in electrical resistance, the electrical resistance increased with the deflection. Figure 7-11 shows the changes in electrical resistance acquired using sensing mat 1 due to applied loads, at loading cycle one and loading cycle two where the maximum deflection was 2 and 4 mm respectively, the electrical resistance increased reversibly. However, in loading cycle three and cycle four where the maximum deflection was 6 and 8 mm, the change in electrical resistance was increased irreversibly by up to 0.02 % and 0.032 % respectively. This change in electrical resistance was attributed to minor damage where matrix crackings were heard during the test.

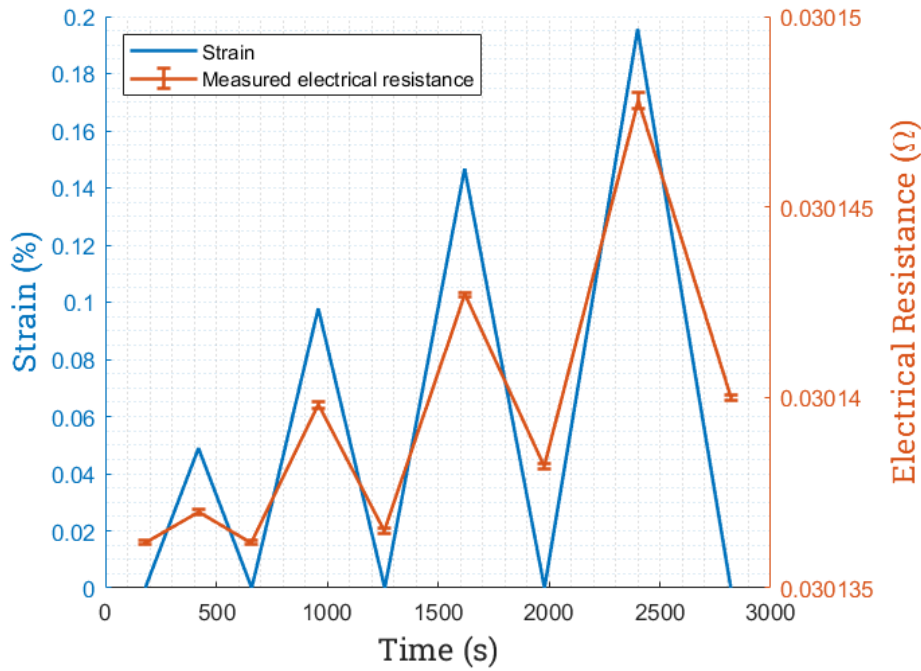


Figure 7-11: Changes in electrical resistance due to deflection at 2, 4, 6, and 8 mm in AC panel. The electrical resistance readings were acquired using sensing mat 1.

These matrix cracks presumably reduce the number of fibre – fibre contacts in plies and between adjacent plies and decrease the surface electrical conduction and through – thickness electrical conduction and increase the electrical resistance consequently. It was noticed that the irreversible changes in electrical resistance increased when the deflection increased that was because the minor damage (matrix cracks) becomes more defined. Figure 7-12 shows the changes in electrical resistance due to applied loads for VC panel, the electrical resistance was measured using sensing mat 1. The changes in electrical resistance was reversible in loading cycle one and cycle two, however the VC panel showed irreversible changes in electrical resistance when it was loaded at loading cycle three and cycle four, the change in electrical resistance at loading cycle three and cycle four was 0.017 % and 0.024 % respectively. It can be seen that the changes in electrical resistance in VC panel was smaller than AC panel because IN – 2 Epoxy Infusion Resin was tougher than VTC 401 resin, thanks to presence of 1,6 bis (2,3-epoxypropoxy) hexane in its formula (more details mentioned in Section 3.1.1), a comparison between damage size due to impact loading between VC and AC panel is presented in Table 7-6.

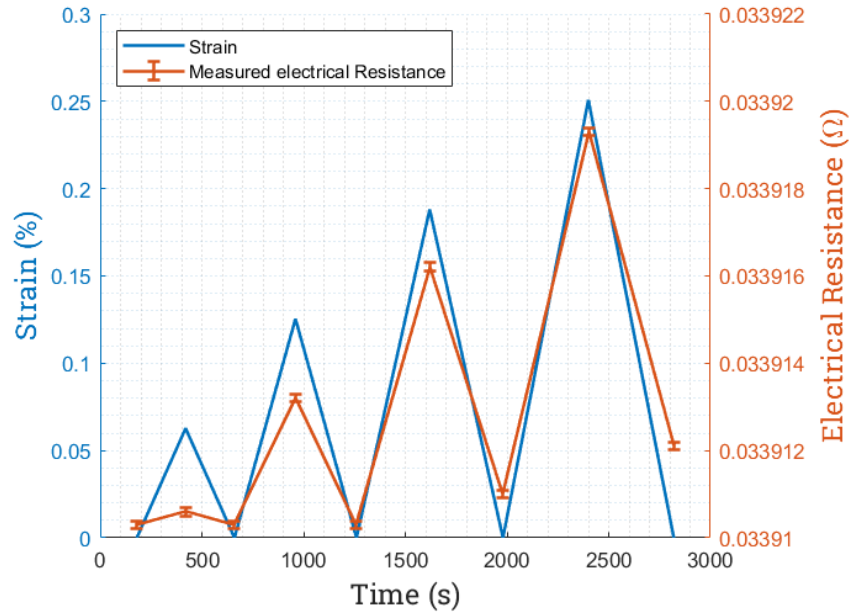


Figure 7-12: Changes in electrical resistance due to deflection at 2, 4, 6, and 8 mm in VC panel. The electrical resistance readings were acquired using sensing mat 1.

In Figure 7-13 the changes in electrical resistance due to applied loads were measured in AC panel using sensing mat 2. Loading cycle one and cycle two were undetectable, therefore no change in electrical resistance occurred. The AC panel showed reversible changes in electrical resistance at loading cycle three. 0.027 % irreversible change in electrical resistance was observed when the specimen was loaded at loading cycle 4, this was attributed to minor damage as mentioned above. Sensing mat 2 was less sensitive to strain monitoring and damage detection as it will be discussed in Section 7.3.4. Figure 7-14 shows the change in electrical resistance in VC panel, the irreversible change in the electrical resistance was as low as 0.01 % that is due to toughened epoxy matrix as explained above.

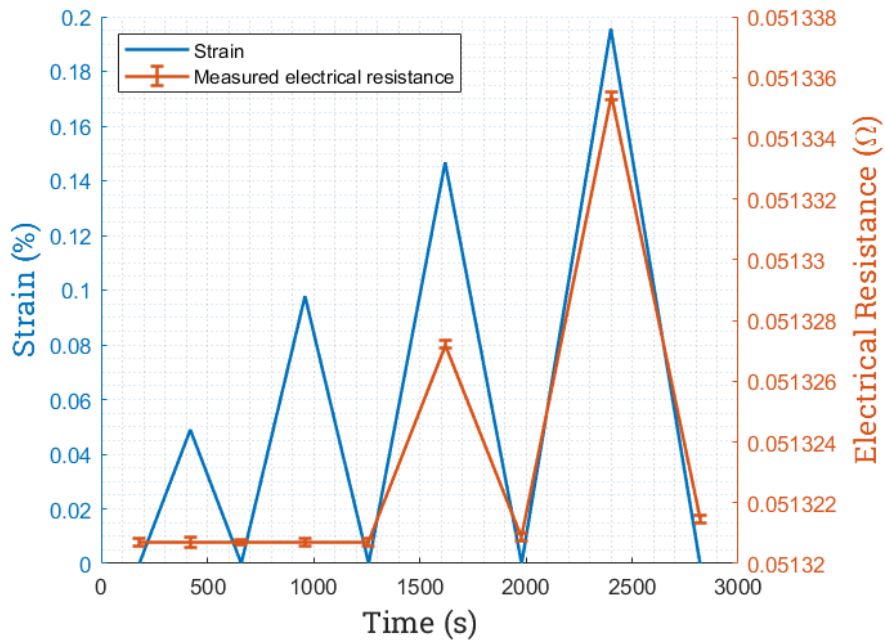


Figure 7-13: Changes in electrical resistance due to deflection at 2, 4, 6, and 8 mm in AC panel. The electrical resistance readings were acquired using sensing mat 2.

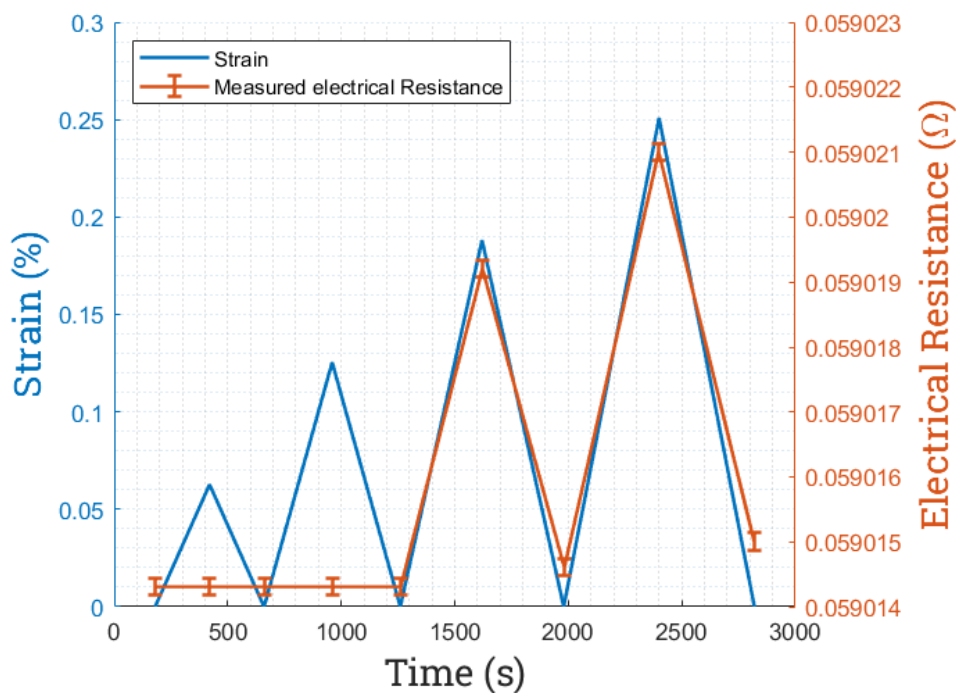


Figure 7-14: Changes in electrical resistance due to deflection at 2, 4, 6, and 8 mm in VC panel. The electrical resistance readings were acquired using sensing mat 2.

7.3.3 Damage Detection in Woven Fabric Carbon Fibre Reinforced Composite Laminates

The aim of this section is to investigate the ability of the current sensing system using a four-probe electrical resistance technique to detect damage in woven fabric CFRP laminate panels.

To study the sensitivity of the sensing system to detect barely visible impact damage (BVID) a range of impact energies were used as shown in Figure 7-15. Those energies were chosen based on trial and error so as to cause barely visible impact damage. In Figure 7-15 sensing mat 1 was attached to the bottom surface of the CFRP laminate panels, while impact energies were applied on upper surface of the panels. The scatter graph in Figure 7-15 shows that there is a strong relationship between the percentage in the global electrical resistance changes (ξ) of the CFRP laminate panels and the impact energies. The global electrical resistance change (ξ) calculations were detailed in Section 7.2.3.

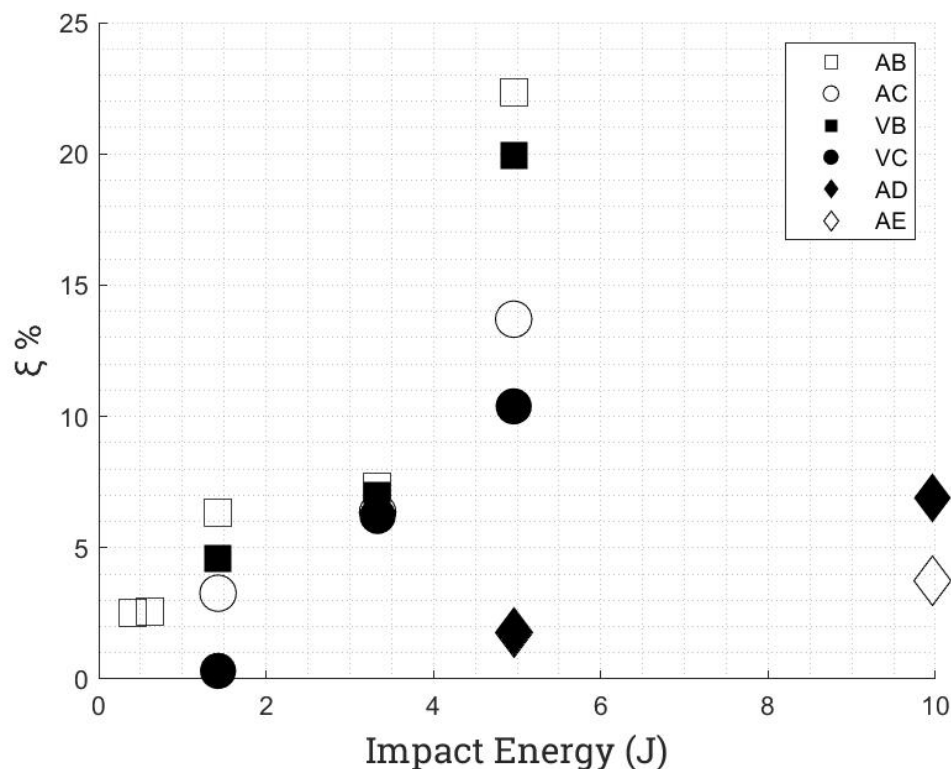


Figure 7-15: The percentage change in electrical resistance in carbon fibre composite laminate panels due to impact damage using sensing mat 1.

Fundamentally, the amount of changes in electrical resistance depends on the panel thicknesses, the fabricating processes, the epoxy matrix, the impact energies, and sensing mats (variables that govern the electrical conduction in CFRP laminate panels were detailed Section 2.4.4). When 0.405 J of impact energy was applied on the panels, it was noticed that BVID was created in the panel AB, while the other panels were not affected by that amount of impact energy. As C-scan images in Figure 7-16 shows, damage in the form of matrix cracks and delamination were generated in AB panel due to impact events. The Time of Flight (TOF) mode shows the damage clearly, the dark blue area represents the bottom face of the laminate and

the light blue area is upper surface roughness that comes from using cloth – type release film during the curing process, the light green area is the damaged area that is a combination of matrix cracks and delamination. The B-scan (B-scan vertical and B-scan horizontal) shows the damage profile through-thickness direction along the horizontal and vertical cross-section of the specimen where the crosshair of the C-scan was placed. The thickness of each carbon fibre ply before the cure is 0.275 mm and because the damage occurred in the thickness between 0 – 0.5 mm (as shown in B – scan vertical), therefore, that implies that matrix cracks occurred in ply number 1 and ply number 2 right under the impact point and delamination occurred between ply number 1 and ply number 2. However, there was no damage observed in VB, and VC panel.

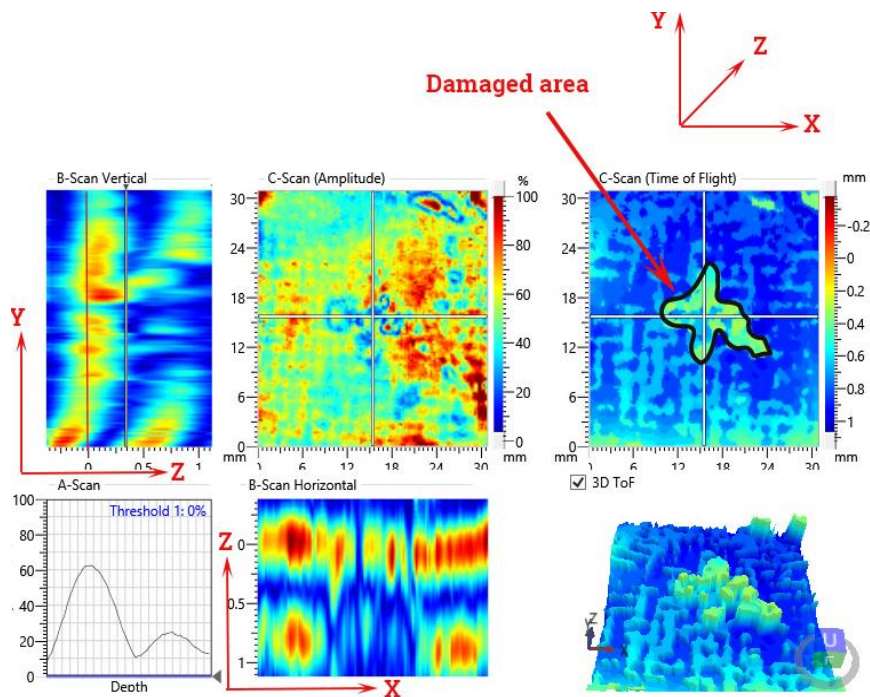


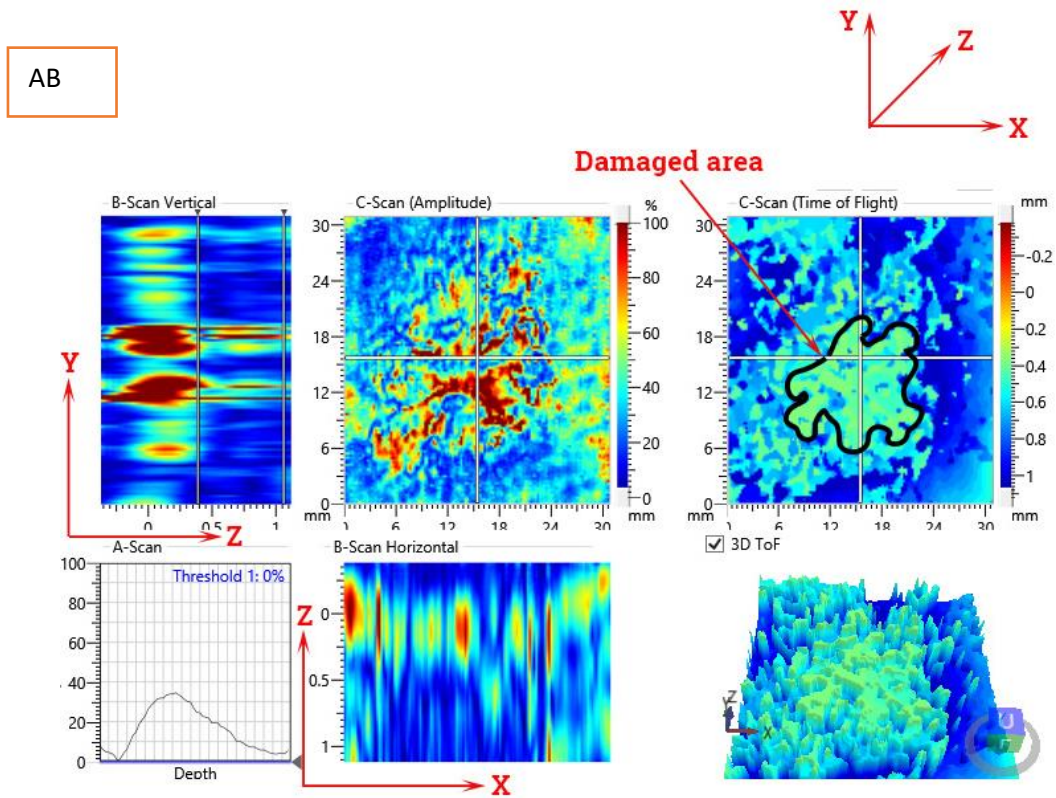
Figure 7-16: Impact damage distribution in CFRP laminates panel (AB). The panel was subjected to 0.405 J impact energy using a semi-spherical impactor with a 13 mm diameter head. The damage is a combination of matrix cracks and delamination.

When damage becomes observable in C-scan images, due to increase in impact energies, the changes in electrical resistance increased in both sensing mats (Mat 1 and Mat 2). When the impact energy increased to 1.426 J, all the panels apart from AD and AE panels showed signs of damage as shown in the C-scan images in Figure 7-17. The amount of changes in electrical resistance was varied depending on the size of damage and that in turn differs due to size effect as discussed in Section 2.3, at a given impact energy the severity of damage decreased when the panel thickness increased. At 1.426 J of impact energy the AB panel showed a bigger damage size than AC panel (122 and 71 mm² consequently). The damage in AB was a combination of matrix cracks, delamination and intralaminar crack. Figure 7-18 shows a fluorescent image

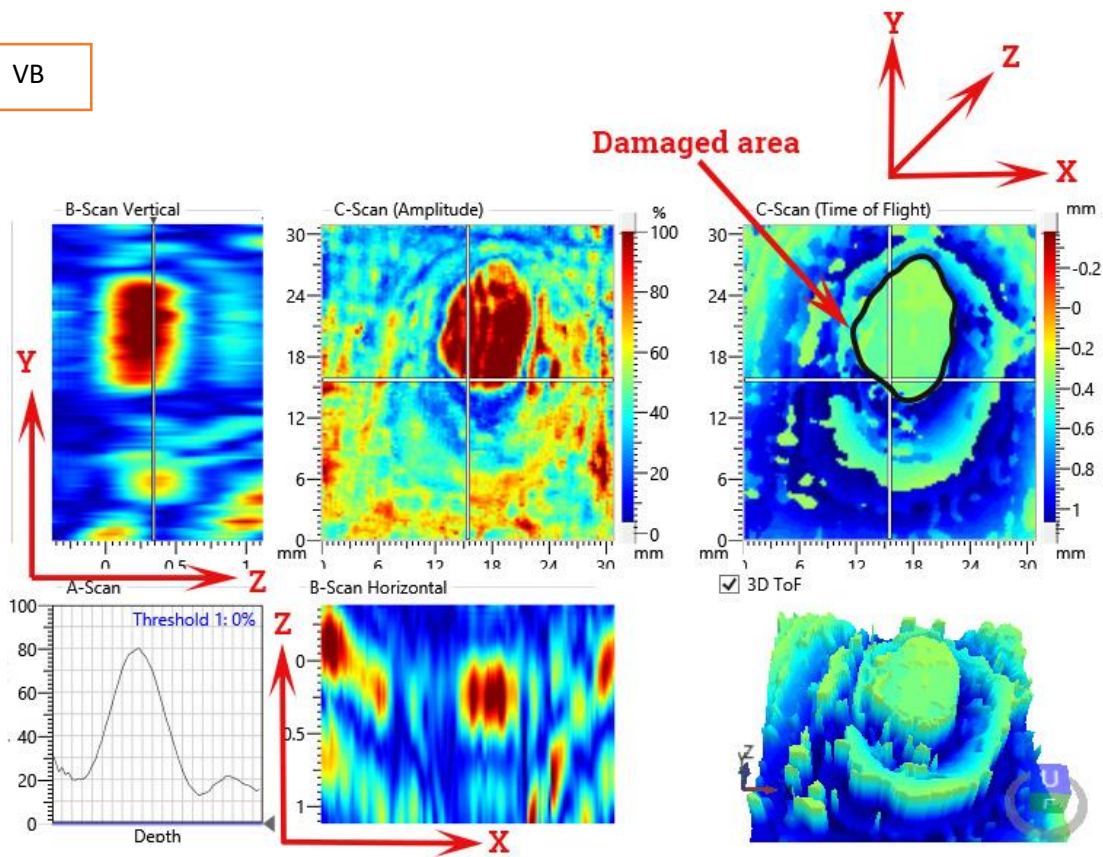
of AB panel, the figure shows a montage of several images of impact damage in the panel. As can be seen, the montage allows a larger field of view than a single image. Although most of the researchers in optical microscopy field consider that making the montage is time consuming, an innovative way was used to obtain the images. Multiple images were taken of the sample, then the images were converted to JPEG extension format before being imported into Lightroom CC 2015.12 (Adobe, USA). In Lightroom CC the images were merged and developed to give the final images. The whole process, converting the images extensions, importing images, merging them and developing the images took less than a minute for each sample. The figure shows different types of damage (interlaminar crack, delamination, and matrix crack) that occurred due to impact events. It can be seen that damage in a form of delamination was generated and grew between layer number 1 and layer number 2 another delamination was created between layer number 3 and layer number 4. The intralaminar crack was observed on the tensile surface of the panel (the bottom surface) due to tension at bottom surface of the panel. However, AC panel showed only matrix cracks and delamination and no fibre breakage was observed as shown in Figure 7-19. The above pattern applies on VB and VC panel, however, the damage size was smaller than AB and AC panel and no fibre breakage was observed.

The highest electrical resistance change was observed in the AB panels. At a given impact energy the size of damage in AB panels were bigger than their equivalent VB panels that maybe attributed to many factors, such as the manufacturing process, the type of carbon fibre and the type of epoxy matrix (detailed in Section 2.4.4). Where AB panels were processed in an autoclave under pressure of 606 kPa while VB panels were cured in a vacuum bag under 101 kPa of pressure. The high processing pressure helped to create fibre – fibre contacts in autoclave processing panels higher than vacuum assisted resin transfer moulding panels as discussed in Section 6.2.1.2 and shown in Figure 6-10 and Figure 6-11. Table 7-4 shows that the through – thickness electrical resistivity of panels made using a vacuum assisted resin transfer moulding technique was higher than their equivalent of autoclave processing panels. This in turn has increased changes in electrical resistance due to damage in autoclave processing panels more than their equivalent of vacuum assisted resin transfer moulding processing panels. Once the delamination was initiated and grew in autoclave processing panels (AB, AC, AD, and AE), it disrupt higher number of fibre – fibre contacts between adjacent plies than VARTM processing panels (VB and VC). In spite of the fact that Tory FT300B has higher electrical conductance than Tairyfil TC – 35 (Table 7-4), the autoclave processing panels showed higher change in electrical resistance due to damage under all energy levels as shown in Figure 7-15. It is worth mentioning that the IN – 2 Epoxy Infusion Resin (the epoxy matrix for VB and VC panels) had a

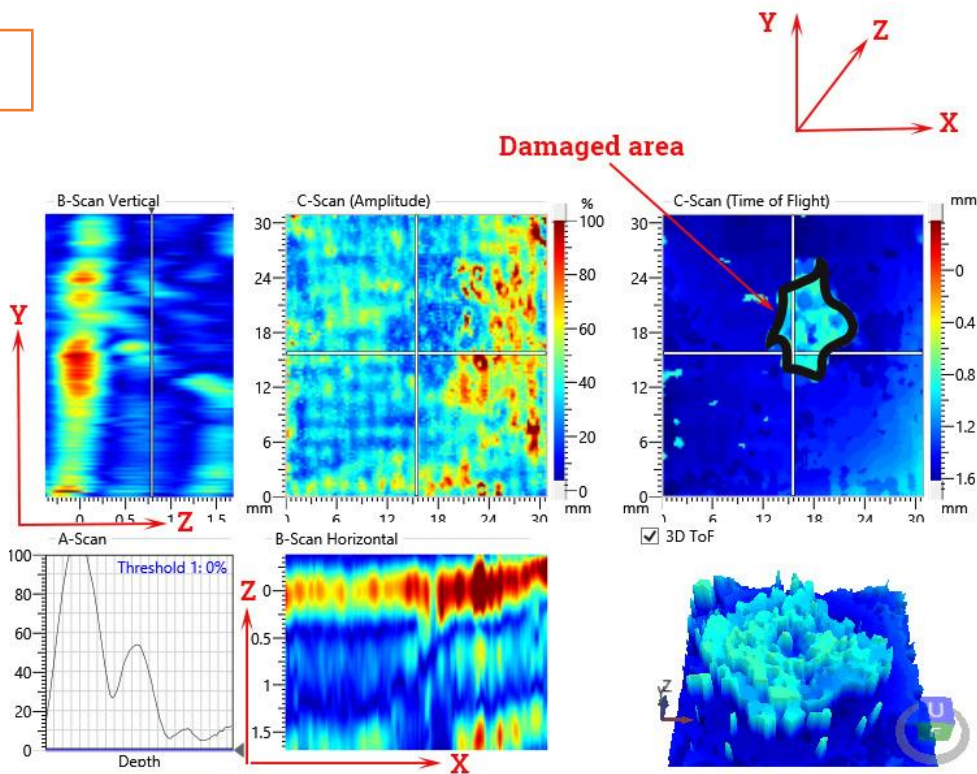
toughening component in its structure that was epoxypropoxy hexane that helped to reduce the damage size due to impact and the electrical resistance change consequently. On the other hand, the brittle nature of the epoxy matrix in VTC 401 along with the weak fibre – matrix interface allowed the translation of the impact energy to destroy the composite laminate throughout the thickness direction. It was expected that the void content in all panels have a minor impact on the electrical resistance since it was less than 2% as shown in Table 6-8.



VB



AC



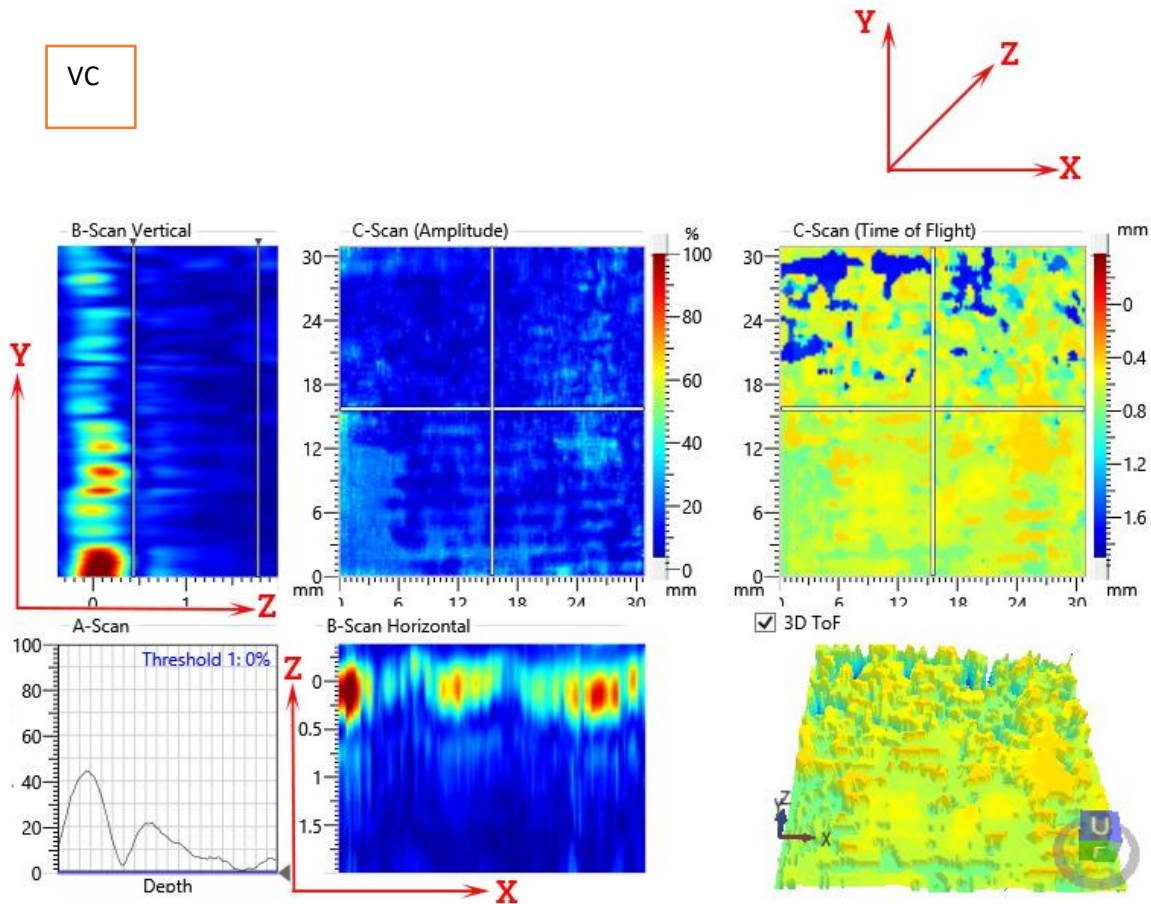


Figure 7-17: Impact damage distribution in different CFRP laminates. The panels were subjected to 1.426 J of impact energy using a semi-spherical impactor with a 13 mm diameter head.

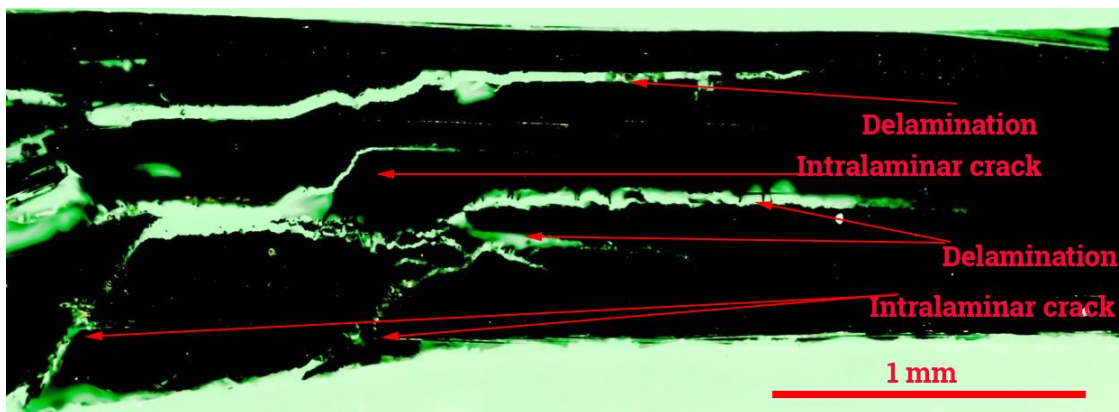


Figure 7-18: Montage image of impact damage of AB panel. The panel was subjected to drop weight impact at 1.426 Joules. Epi-fluorescence, 390-440 nm excitation, 4x objective.

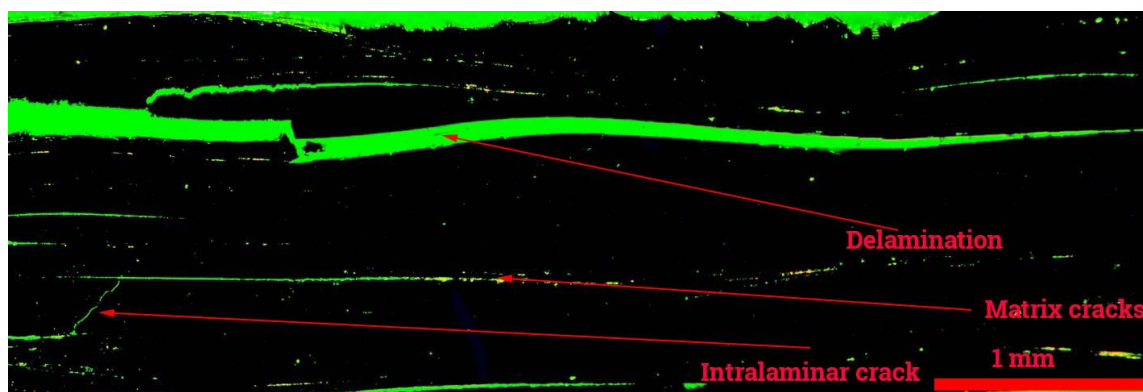


Figure 7-19: Montage image of impact damage of AC panel, the panel was mounted in with EpoDye. Epi-fluorescent, 4x objective. The laminate was subjected to a 1.426 Joules impact energy.

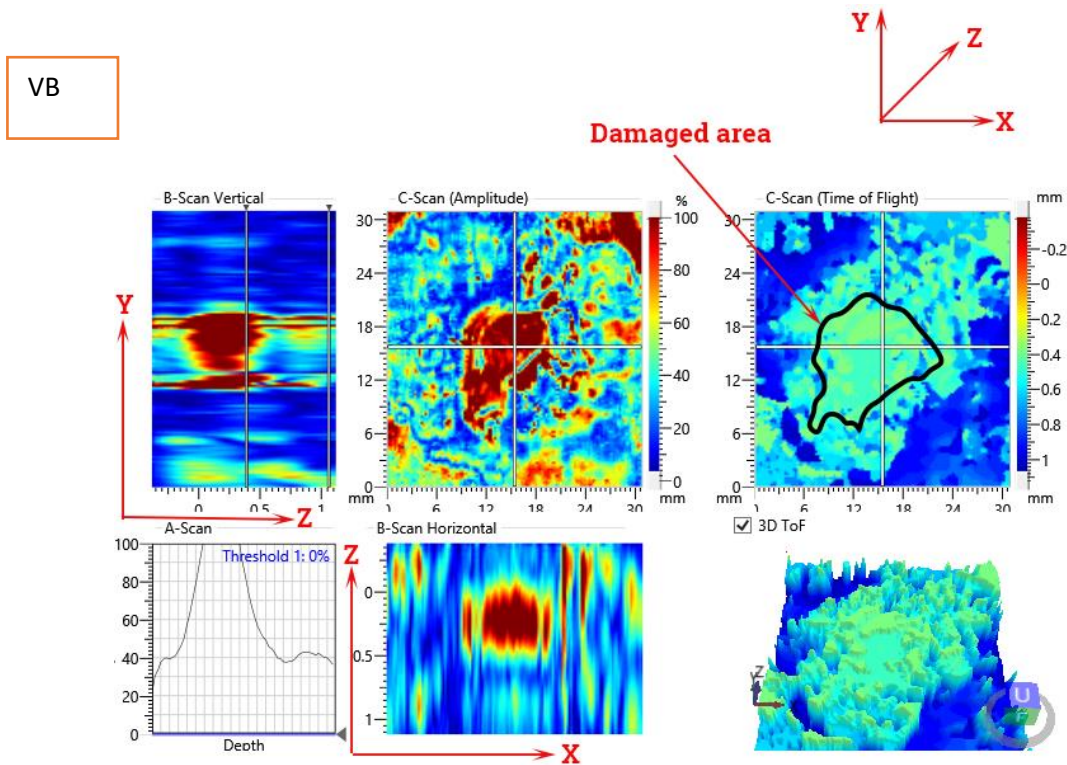
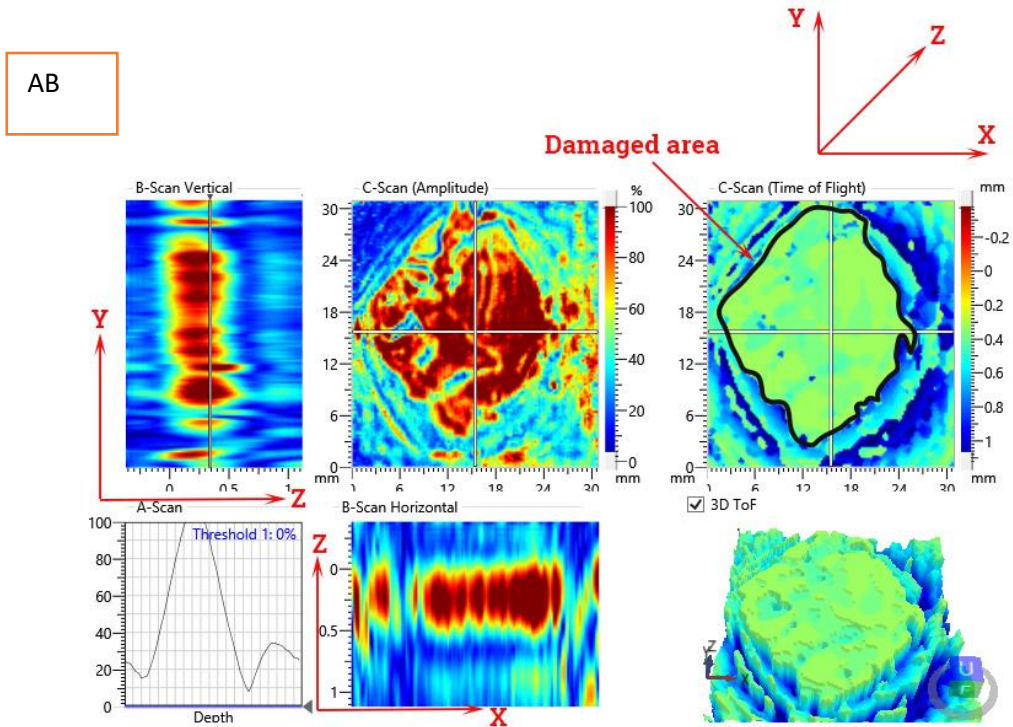
Table 7-5 shows the threshold impact energy for fibre breakage for each panel, the values in Table 7-5 were calculated using Equation 2-2 and data in **Error! Reference source not found.** and Table 6-7. It was noticed that when the impact energy level was below the threshold in Table 7-5, the dominant form of damage was delamination and matrix cracks, therefore changes in electrical resistance were relatively low. However, when the impact energy exceeded the threshold energy a considerable change in electrical resistance was observed as shown in Figure 7-15, since all types of damage, which were fibre breakage, delamination and matrix cracking, occur. It is important to mention that even when the impact energy was lower than fibre breakage threshold impact energy for (AB, VB, and AC), fibre breakage was observed; that may be attributed to the accuracy of an impact tester and the way the CFRP laminate panels were installed in the tester as discussed in Section 7.1.

Table 7-5: The impact energies required for fibre failure due to back surface flexure.

AB (J)	VB (J)	AC (J)	VC (J)	AD (J)	AE (J)
3.22	2.56	6.26	5.91	11.30	16.34

When the CFRP laminate panels (AB, AC, VB and VC panel) were subjected to 3.333 J of impact energy, fibre failure was observed in AB and VB panel as shown in Figure 7-20 and Figure 7-21. Fibre ruptured on the bottom surface of the CFRP laminate panels, therefore the damage in these panels (AB and VB panel) was a combination of delamination, matrix cracking and fibre breakage. The damage in AB and VB panel was classified as visible impact damage, while the damage in AC and VC panel was smaller in size and less in severity, therefore, it was classified

as barely visible impact damage as shown in Figure 7-22 and Figure 7-23 respectively, although an extensive delamination occurred between almost every ply as can be seen in Figure 7-22.



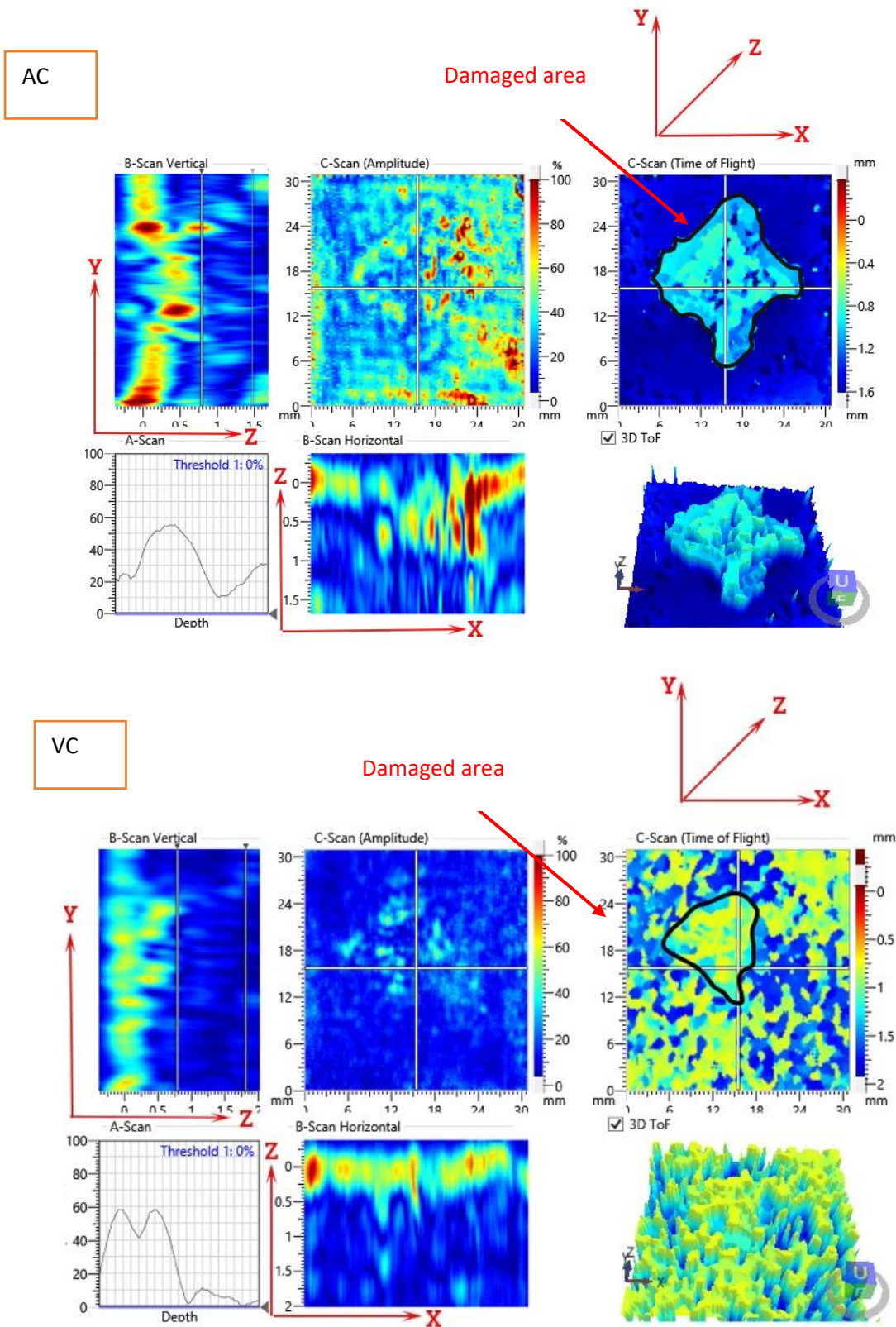


Figure 7-20: Impact damage distribution in different CFRP laminates. The panels were subjected to 3.33 J of impact energy using a semi-spherical impactor with a 13 mm diameter head.



Figure 7-21: Montage image of impact damage of VB panel, epi-fluorescence, 4x objective. The laminate was subjected to low velocity impact at 3.33 Joules.

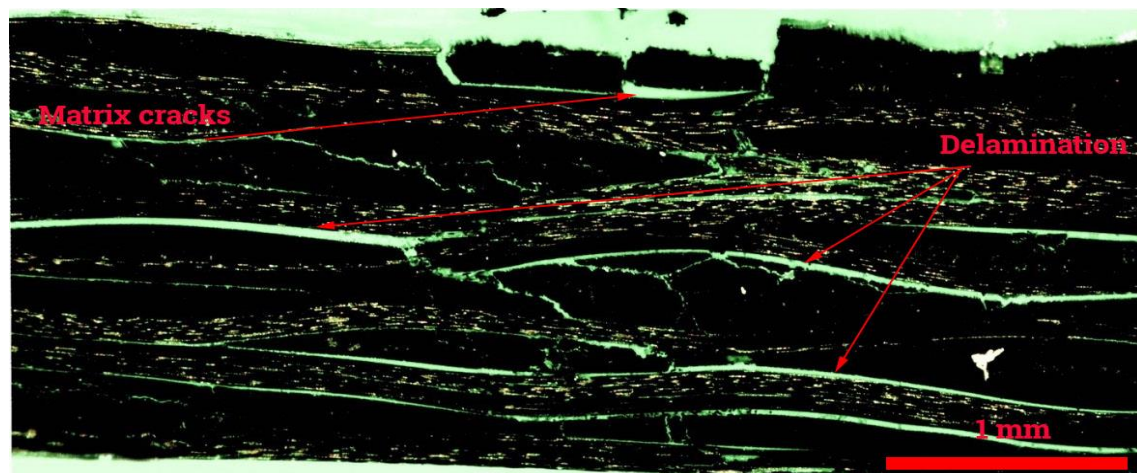


Figure 7-22: Montage image of impact damage of AC panel, epi-fluorescence, 4x objective. The laminate was subjected to low velocity impact at 3.33 Joules.

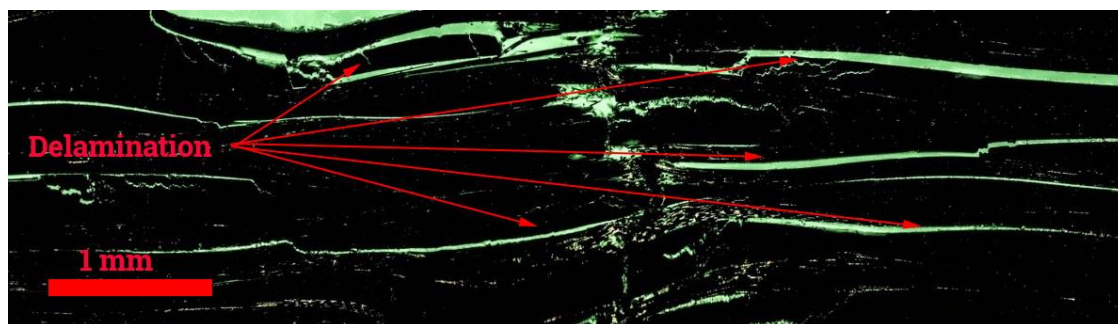
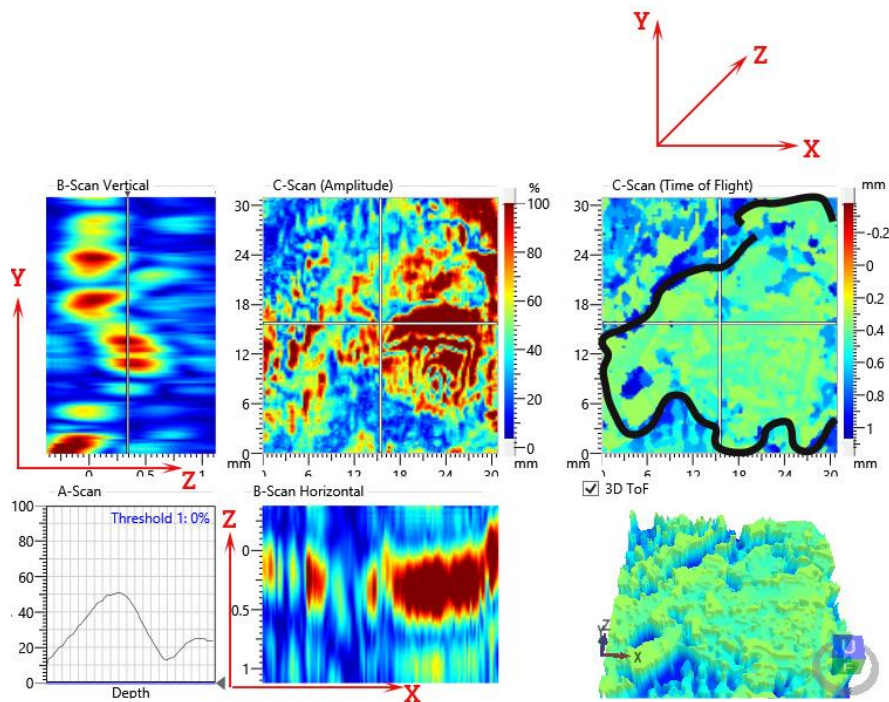


Figure 7-23: Montage image of impact damage of VC panel, epi-fluorescence, 4x objective. The laminate was subjected to low velocity impact at 3.33 Joules.

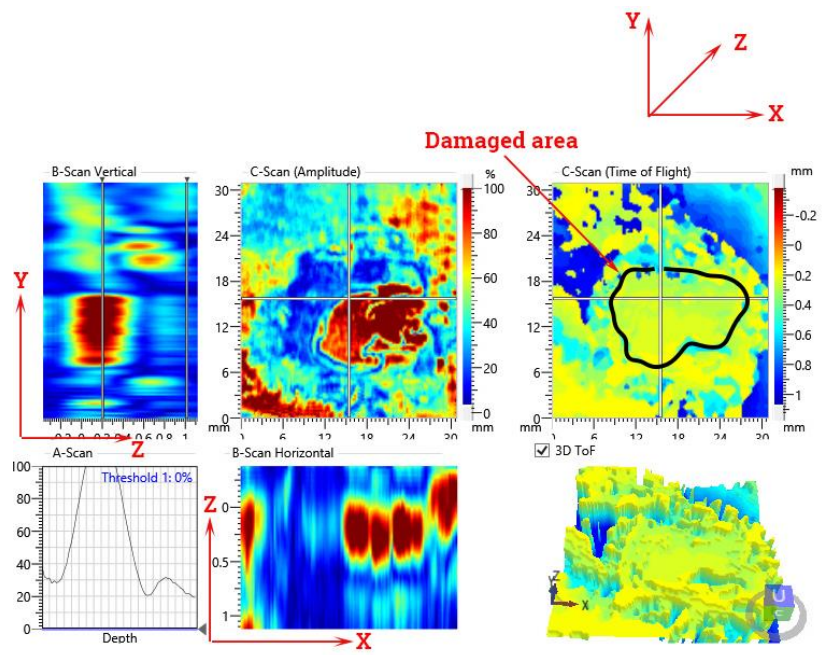
4.96 J of impact caused significant changes in electrical resistances in the impacted regions of AB, AC, VB and VC panels shown in Figure 7-15. The impactor perforated AB panel, it caused a significant damage in VB panel (the damaged area was 210 mm²) as shown in Figure 7-24, this led to high increase in electrical resistance $\approx 23\%$. In addition to matrix cracks, and delamination this impact energy caused fibre breakage in AC panel as shown in Figure 7-25. Fibre breakage was not observed in all other panels. However, VC panel undergo a significant delamination (Figure 7-26) that caused a high increase in electrical resistance Figure 7-15. 4.96 J of

impact energy created damage of 200 and 170 mm² in AD and AE panel respectively, however, it was found that the electrical resistances of AD and AE changed by up to 2 % due to impact at 4.96 J. This indicated that there was a critical thickness at which the current sensing system cannot be used to detect damage. Through – thickness electrical resistivity of CFRP laminates has an inverse relationship to laminate thicknesses as presented in Table 7-4. Through – thickness current density decreased when the composite cross section area increased (as detailed in Section 2.5.2), this means the sensitivity of the current sensing system decreased.

AB



VB



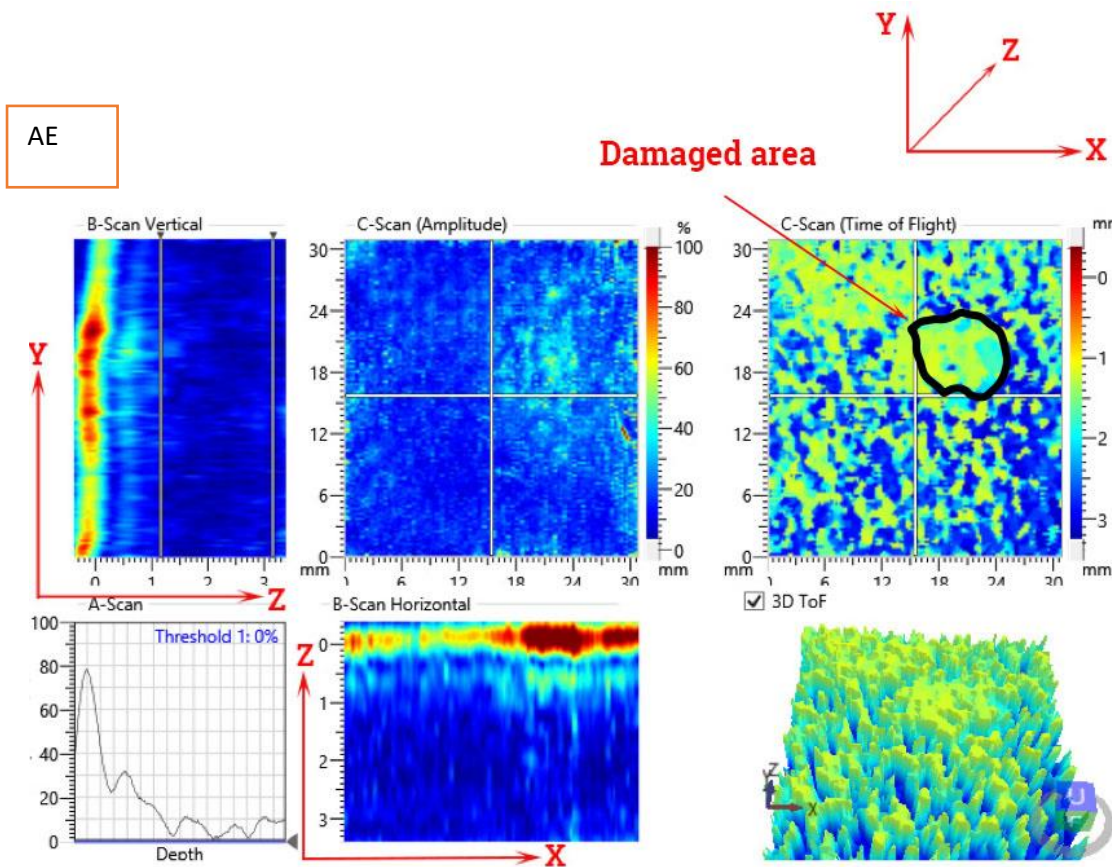
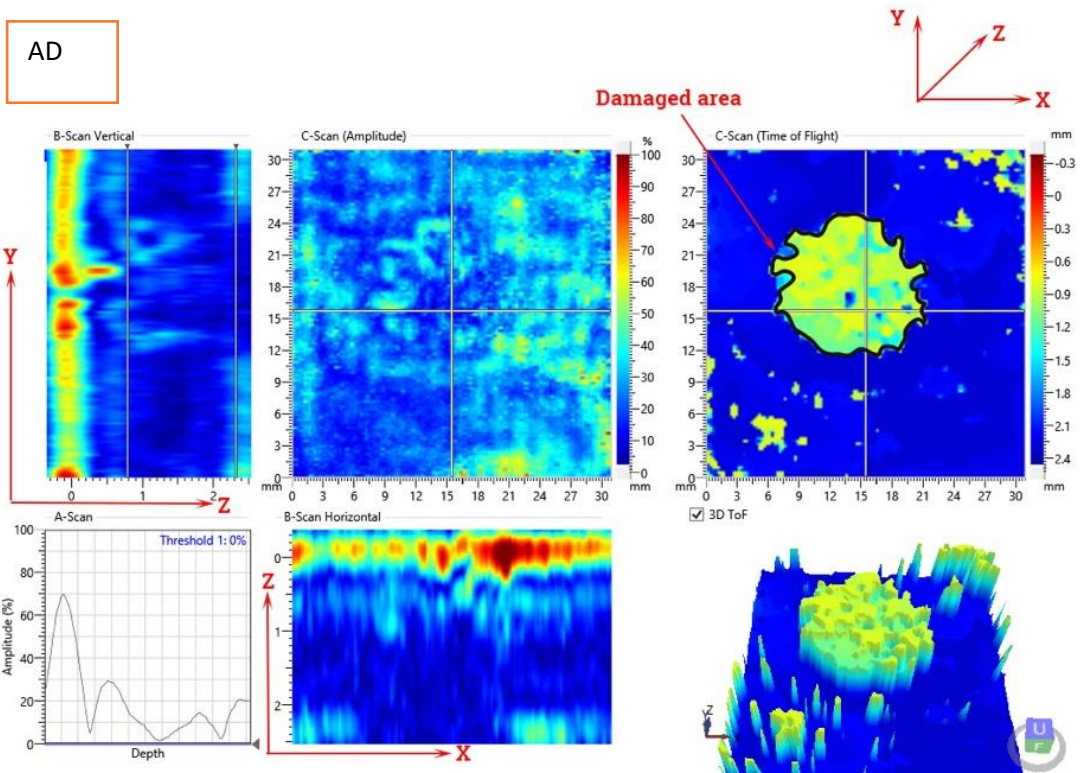


Figure 7-24: Impact damage distribution in CFRP laminates panels (AB, VB, AC, VC, AD and AE). The panels were subjected to 4.96 J impact energy using a semi-spherical impactor with a 13 mm diameter head.

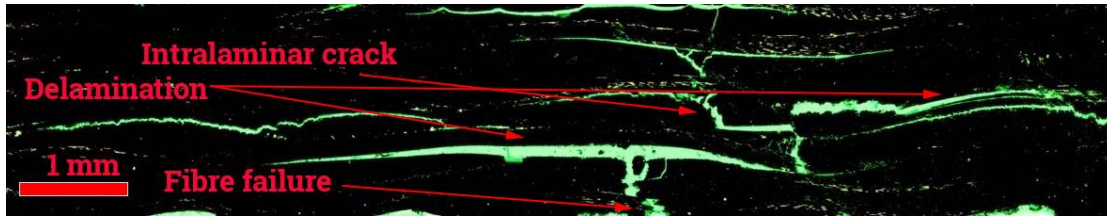


Figure 7-25: Montage image of impact damage of AC panel, epi-fluorescence, 4x objective. The laminate was subjected to low velocity impact at 4.96 Joules.

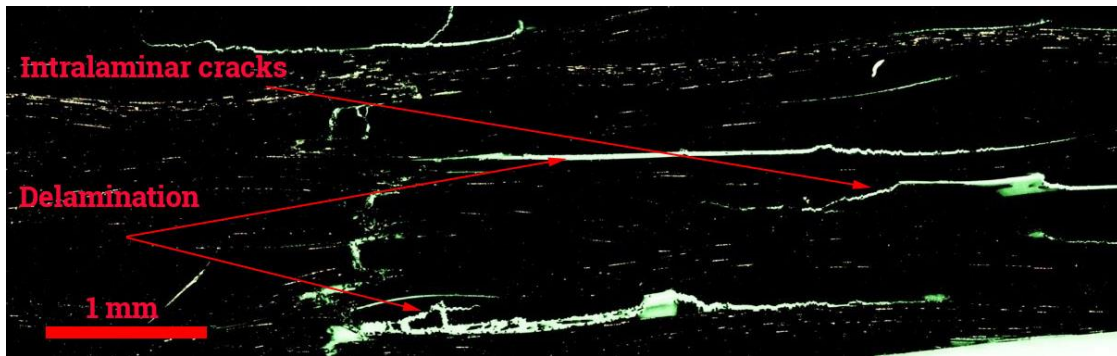
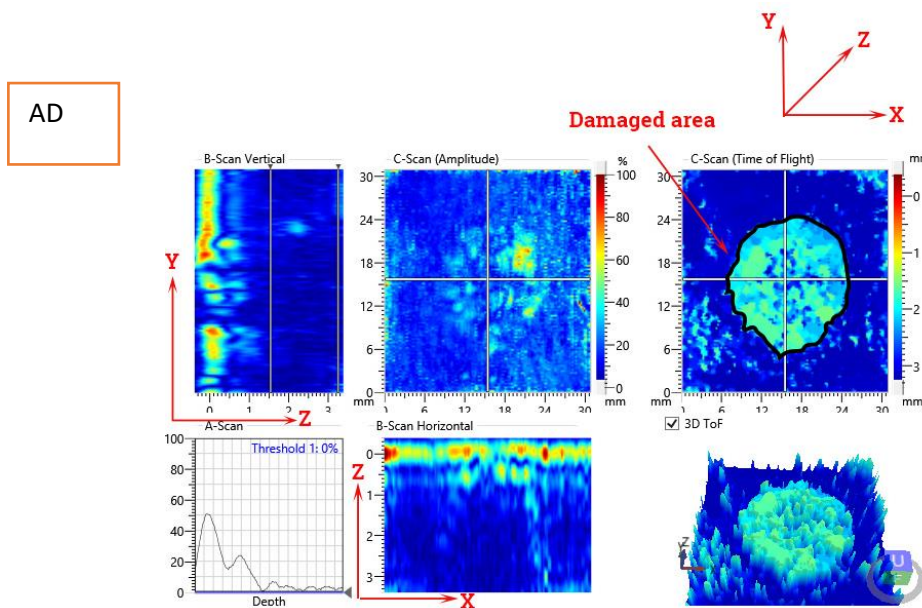


Figure 7-26: Montage image of impact damage of VC panel, epi-fluorescence, 4x objective. The laminate was subjected to low velocity impact at 4.96 Joules.

To investigate the suitability of the current sensing system to detect damage in thick CFRP laminates, AD and AE panels were subjected to 9.96 J of impact energy. The C – scan images in Figure 7-27 show damage in a form of delamination that occurred in both AD and AE panels, the damaged areas were 293 and 232 mm² respectively. The electrical resistance changed by only 7 % in AD panel and 3.8 % in AE panel as shown in Figure 7-15.



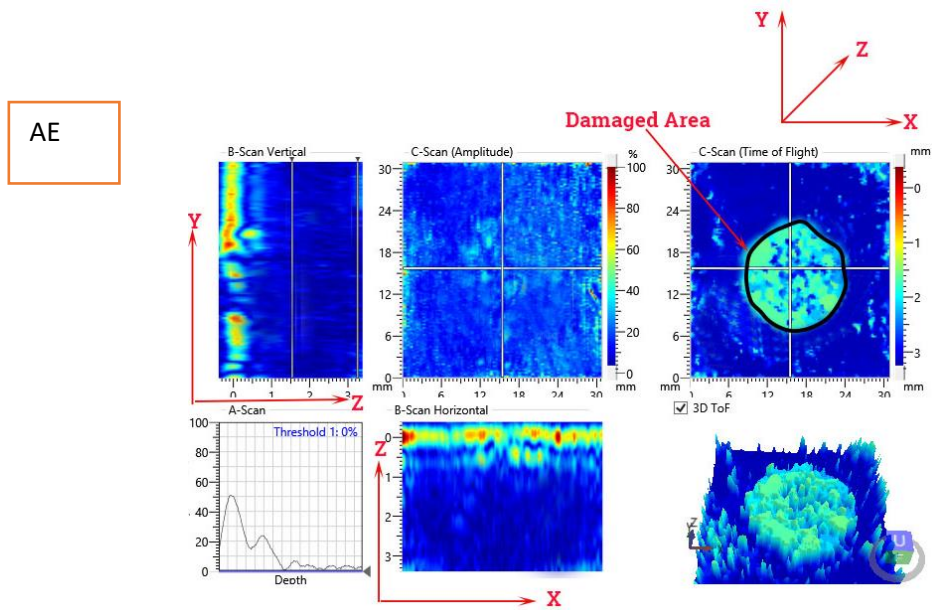


Figure 7-27: Impact damage distribution in CFRP laminates panels (AD and AE). The panels were subjected to 9.96 J impact energy using a semi-spherical impactor with a 13 mm diameter head.

As the current electrical sensing system was proved to be successful in detecting damage in various CFRP laminates made by both autoclave processing and VARTM processing techniques and in order to make this sensing system economically viable, the effect of the sensor size and spacing between electrodes on the sensitivity of the technique was studied as it can be seen in Figure 7-28, where sensing mat 2 was used to collect electrical resistance data from carbon fibre composite laminates panels. In sensing mat 2 the electrode area was 400 mm² and the distance between electrodes was 90 mm. The data in Figure 7-28 was extracted from Table 7-2 as explained earlier in this section. At a given impact energy the changes in electrical resistance using sensing mat 2 in all panels (AB, AC, AD, AE, VB, and VC panel) were less than the changes in electrical resistance using sensing mat 1 as shown in Figure 7-15 and Figure 7-28. In fact, when 0.406 J caused damage of 61 mm² in AB panel, this damage caused a measurable electrical resistance change using mat 1 (the damage was detectable), however, it was not detectable when mat 2 was used.

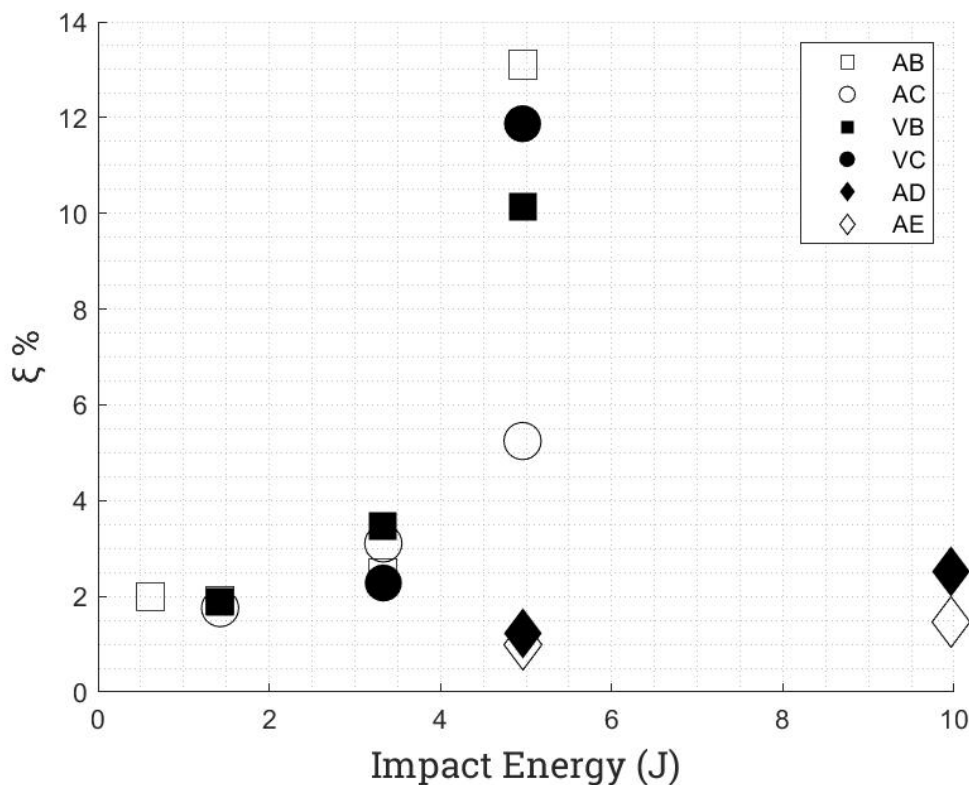


Figure 7-28: The percentage changes in electrical resistance in CFRP laminate panels due to impact damage using sensing mat 2.

7.3.4 Quantification of Damage

After the investigation of the applicability of the current sensing system to detect damage using two different sensing mats (sensing mat 1 and sensing mat 2) in different CFRP laminates, this section aims to investigate the ability of the sensing system to quantify the damage using both sensing mats. Therefore, electrical resistances of the panels were measured before and after the damage was created as detailed in Section 7.2.3, and then C – scan was deployed to measure the damage size as shown in Table 7-6. To calculate the damaged size precisely, the C – scan images were imported to Adobe Photoshop CC 19.1.5 (Adobe, US). The total number of pixels of C - scan transducer pad that was shown in Figure 7-7 was counted and it was found to be 40716 pixel, and then number of pixels in the damaged region was counted. The percentage of the damaged size to the total size of the C – scan transducer pad was calculated by dividing the number of pixels of the damaged size by the whole C – scan transducer pad's pixels. The C – scan transducer pad area is known that is 900 mm² as shown in Figure 7-7, therefore, the damaged areas were calculated by multiplying 900 mm² by the percentage of damaged area, therefore the damaged areas were presented in Table 7-6.

It can be seen from the table that the damaged area was a function of impact energy, the fabricating process, and the panel thicknesses. At a given impact energy autoclave processed panels showed bigger damaged areas than the VARTM processed panels, that may be attributed to epoxy resin system as well as curing processes where higher pressure and temperatures were used. It was found that the damage areas decrease when the thickness increases, where the panels become stiffer and their ability to disperse the impact energies into bigger areas increases.

Table 7-6: Damaged areas due to various impact energies for CFRP laminate panels used in this thesis, measured by C - scan.

Specimen	Impact energy (J)	Damaged area (mm ²)
AB	0.409	61.60
	0.657	100.06
	1.426	122.01
	3.333	400.13
	4.959	654.06
AC	1.426	71.68
	3.333	250.77
	4.959	338.88
AD	1.426	No damage observed
	3.333	No damage observed
	4.959	200.36
	9.966	293.52
AE	1.426	No damage observed
	3.333	No damage observed
	4.959	170.46
	9.96	232.53
VB	1.426	82.22
	3.333	174.11
	4.959	210.43
VC	1.426	No damage observed
	3.333	107.58
	4.959	138.50

The damaged area measured by C – scan was plotted against the percentage of global electrical resistance changes, the global electrical resistance changes (ξ) were calculated and described in Section 7.3.3. Figure 7-29 shows the damage identification using the electrical self-sensing system, sensing mat 2 was attached to bottom surface of the CFRP laminate panels and the impact test was applied to the upper surface of the CFRP laminate panels. The electrical resistance along A1, A2, B1, and B2 was measured before and after the damage generation, then the global electrical resistance (ξ) was calculated for each panel at each impact energy and then ξ was plotted against the damaged areas that were acquired from C – scan tests as shown in Figure 7-30 to Figure 7-35.

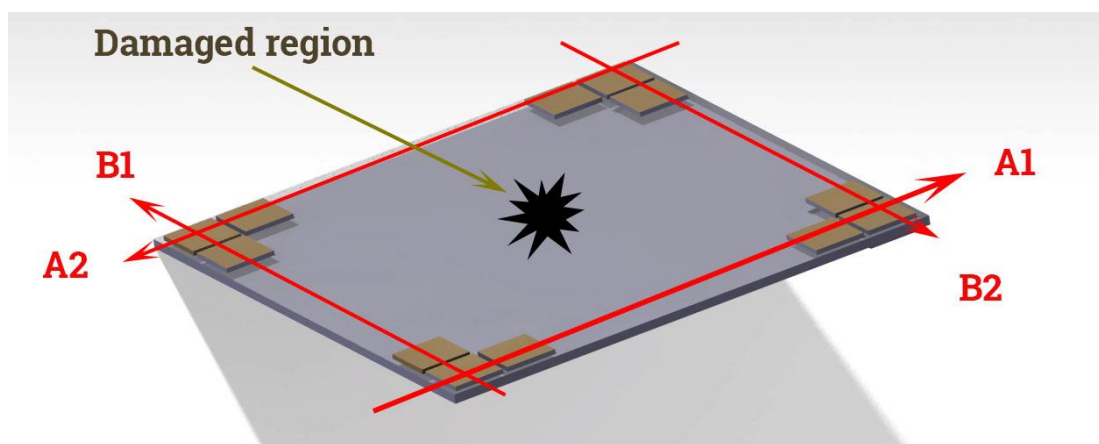


Figure 7-29: Illustration of damage identification and quantification using the electrical resistance change method. The figure illustrates the bottom face of a CFRP laminate panel where sensing mat 2 was attached. The panel was subjected to impact energy on the upper face of the composite panel.

It was found that low impact energy levels produce measurable changes in the electrical resistance of the panels using both sensing mats, however, all damage types were clearly defined and approximately quantified when sensing mat 1 was used. Figure 7-30 to Figure 7-35 present the relationship between the global electrical resistance changes (ξ) and the damaged areas in AB, VB, AC, VC, AD and AE panel respectively, the points represent the actual data that was acquired from Table 7-2 and processed as described in Section 7.2.3. It was evident that both sensing mats were able to identify the damage, however, it can be seen that the changes in electrical resistance in sensing mat 2 were lower than the changes in electrical resistance in sensing mat 1, in spite of the fact that the electrical resistance baseline for sensing mat 2 was higher than mat 1 (discussed in Section 7.2.3) the changes in electrical resistance were lower. According to Equation 2 – 4, increasing the surface area of the electrode decreased the current density, therefore the sensitivity of the sensor decreased. It is worth mentioning that the area

of the electrode in sensing mat 2 was higher than sensing mat 1, 400 mm^2 and 100 mm^2 respectively. That in turn meant sensing mat 2 made contacts with higher number of carbon fibres and since the distance between electrodes in mat 2 was higher (90 mm) while the distance between the electrodes in mat 1 was 40 mm. This helps the electric current to find alternative paths to follow when damage occurs that makes the reduction in electrical resistance less obvious than mat 1. An important point can be concluded that the spacing between electrode had greater effect on damage detection than the electrode sizes.

In this thesis the effects of other variables such as humidity and temperature have been excluded due to time, facilities, and funding constraints. For the purpose of an inverse analysis an exponential fit was used to fit the data in Figure 7-30. It is important to mention that the bigger the data set is the more accurate the fitting, and more accurate the relationship between damaged areas and changes in electrical resistance will be. It can be seen in all the figures that changes in electrical resistance measured by sensing mat 2 were smaller than changes in electrical resistance measured sensing mat 1, that means the sensing mat 2 was less sensitive to quantify the damage. That was proved in AB in Figure 7-30. AB panel was subjected to 0.406 J of a low velocity impact test, the impact test generated damage of 61 mm^2 , this damage produced a measurable change in electrical resistance using sensing mat 1 but this damage size was below the damage threshold of sensing mat 2, therefore this damage was not detected and therefore it was not quantified using mat 2 but it was both detectable and quantifiable using mat 1. It can be concluded that there was an inverse proportional relationship between the global changes in electrical resistance (ξ) and the distance between the electrodes, the higher the distance the lower the accuracy of the sensing system was. On the other hand, the higher the distance between the electrodes the more economical the sensing system was.

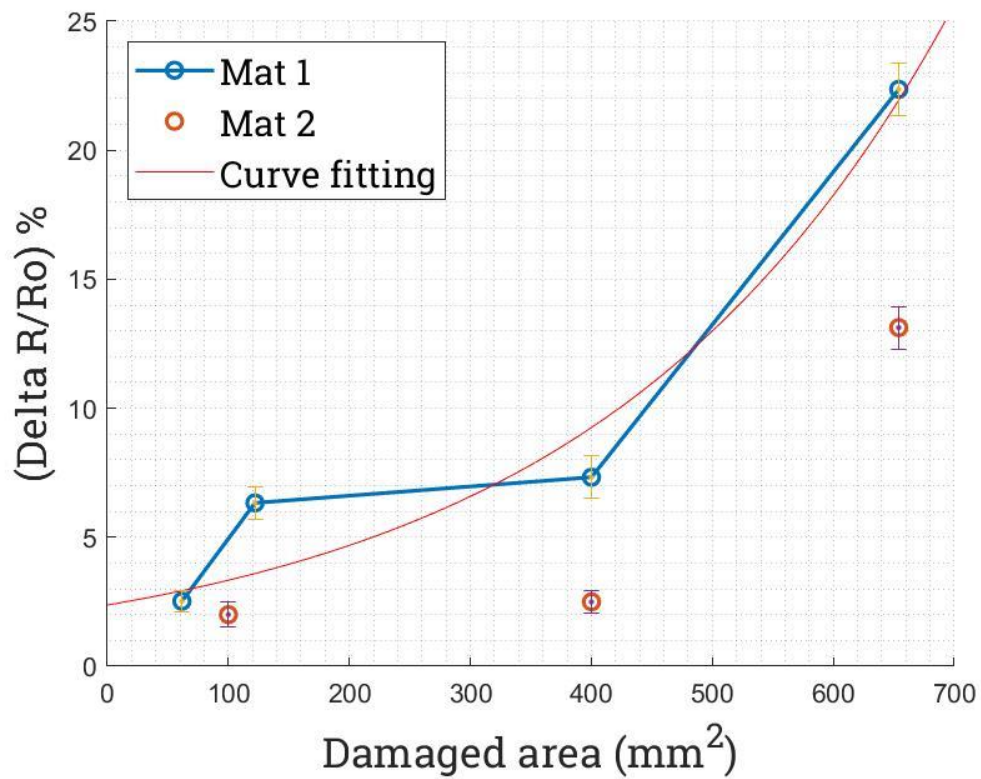


Figure 7-30: Relationships between the damaged areas and the percentage in electrical resistance changes for AB panel using both sensing mats. 0.607 J impact energy was excluded from the graph to be used for inverse analysis later in this section.

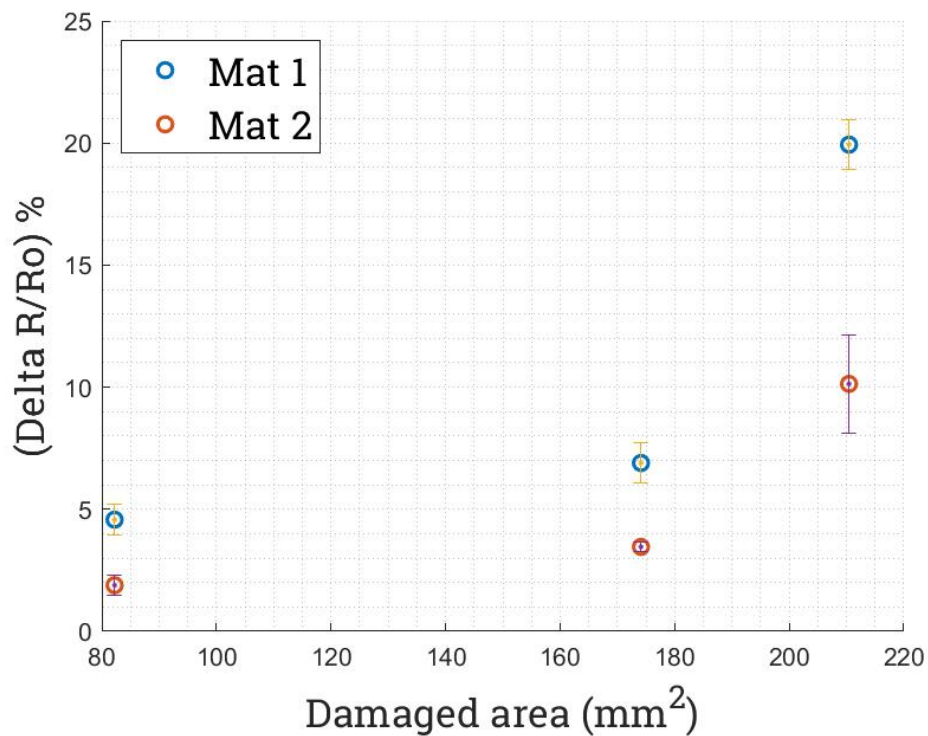


Figure 7-31: Relationships between the damaged areas and the percentage in electrical resistance change for VB panel using both sensing mats.

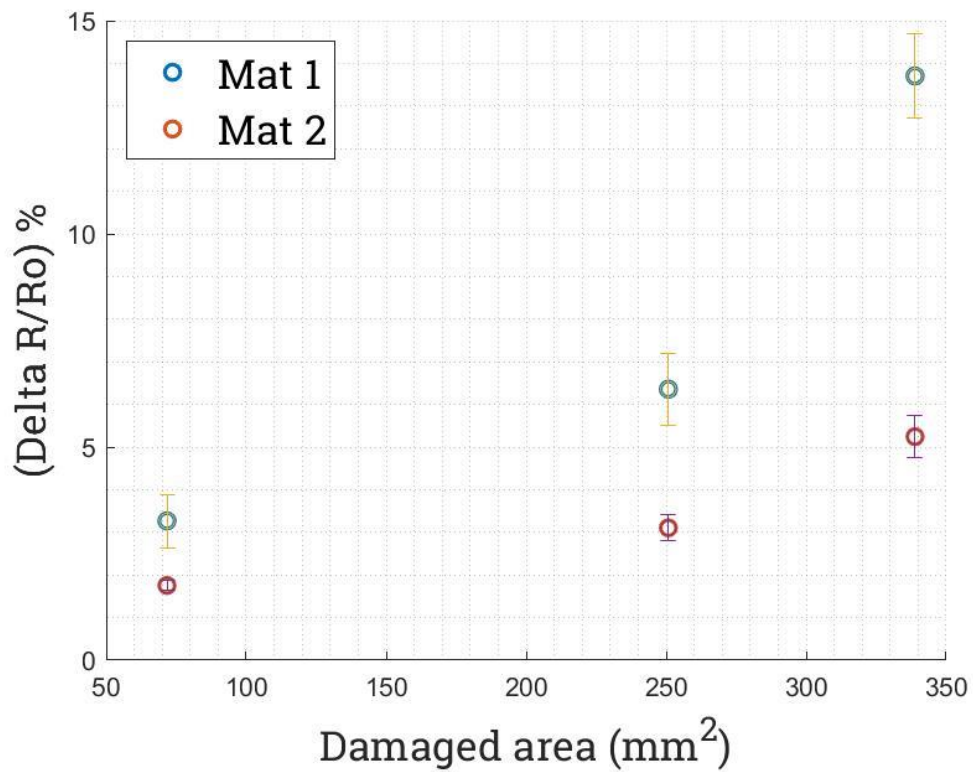


Figure 7-32: Relationships between the damaged areas and the percentage in electrical resistance change for AC panel using both sensing mats.

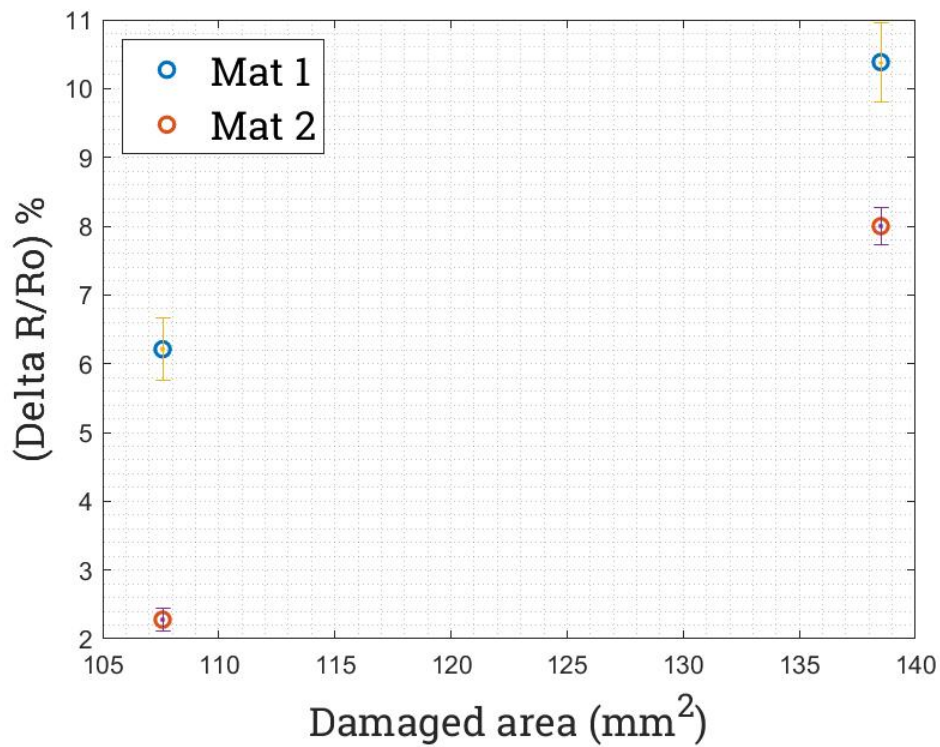


Figure 7-33: Relationships between the damaged areas and the percentage in electrical resistance change for VC panel using both sensing mats.

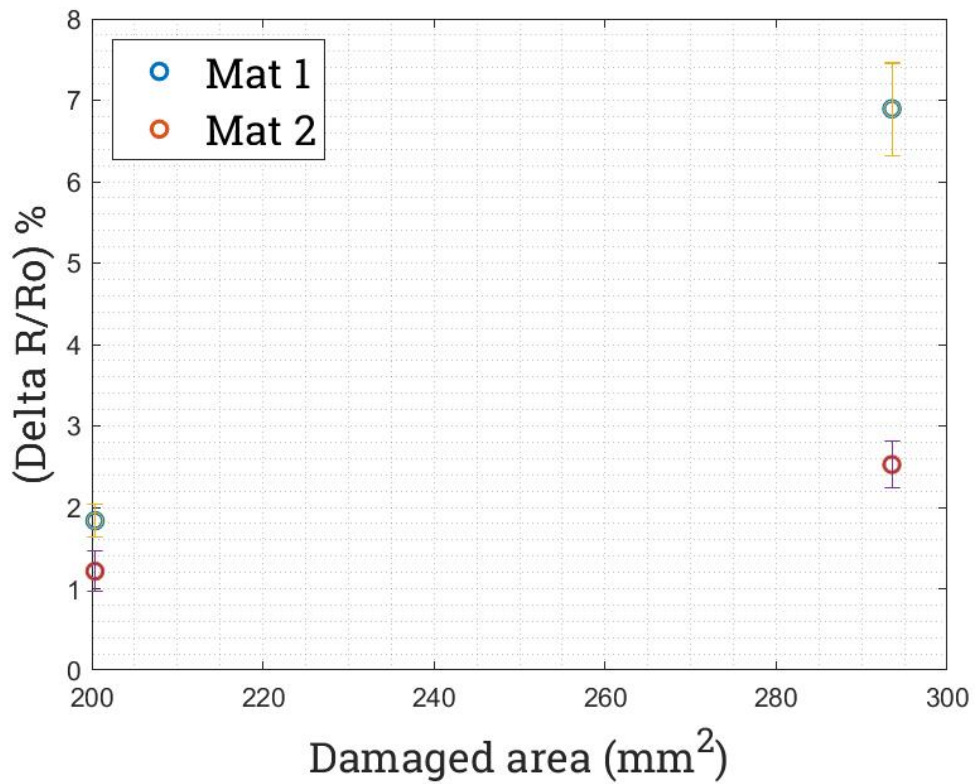


Figure 7-34: Relationships between the damaged areas and the percentage in electrical resistance change for AD panel using both sensing mats.

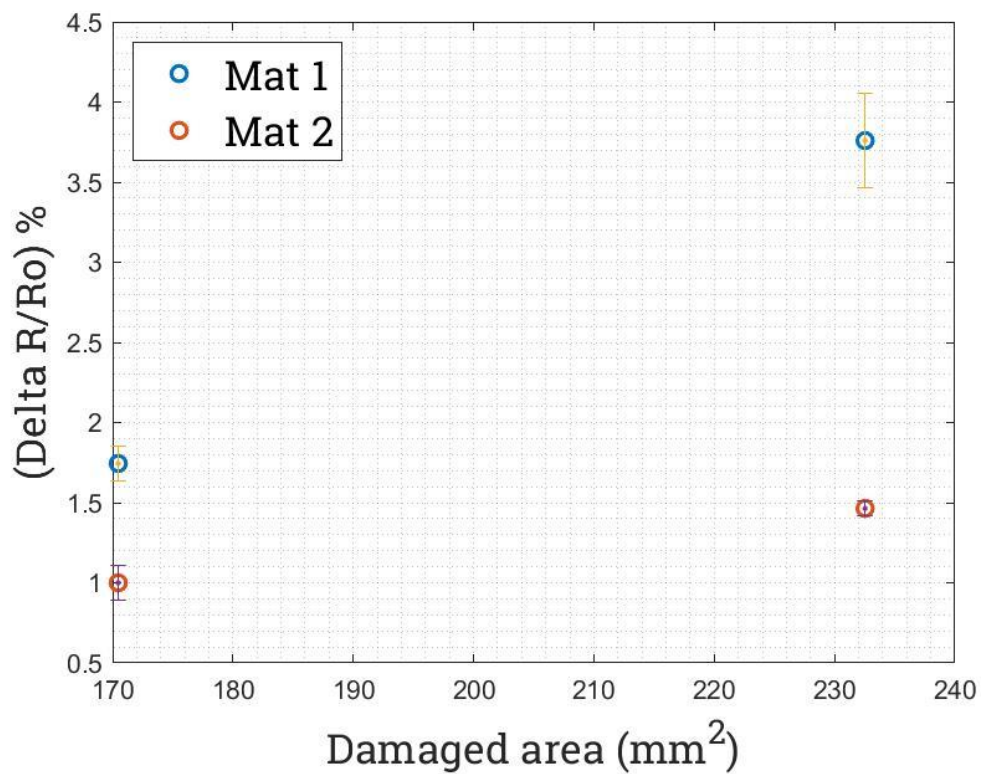


Figure 7-35: Relationships between the damaged areas and the percentage in electrical resistance change for AE panel using both sensing mats.

In an attempt to quantify damage using electrical resistance data, an inverse analysis was undertaken on AB panel. The AB panel was subjected to a 0.607 J of low velocity impact energy. The global electrical resistance change (ξ) was measured using sensing mat 1, it was found that ξ equals to 2.555 % then this value was projected on the fitting line in Figure 7-30, the damaged area was estimated to be 85 mm² then the damage was estimated using non-destructive test (C- scan test) and the damaged area was found to be 100 mm² as shown in Figure 7-36. The error of estimation was found to be 15 mm², the difference between the measurements can be attributed to three factors that were low through – thickness electrical conductance (discussed in Section 7.3.1), the fitting line, which requires a large set of data to obtain an accurate slope to improve prediction, and the negative electric current at the panel surface. Ideally in metals the electric current flows from the negative electrode to the positive electrode directly. However, in CFRP laminate panels due to orthotropic nature of CFRP laminates the electric current flows from the negative electrode to the positive electrode, but electric current passes the positive electrode and then flows back to the positive electrode (as shown in Figure 2-12). This circular flow causes a reduction in electrical resistance changes due to damage, this means the actual electrical resistance changes were higher than the measured ones, therefore the damage area predicted using electrical resistance changes was smaller than the actual damaged area.

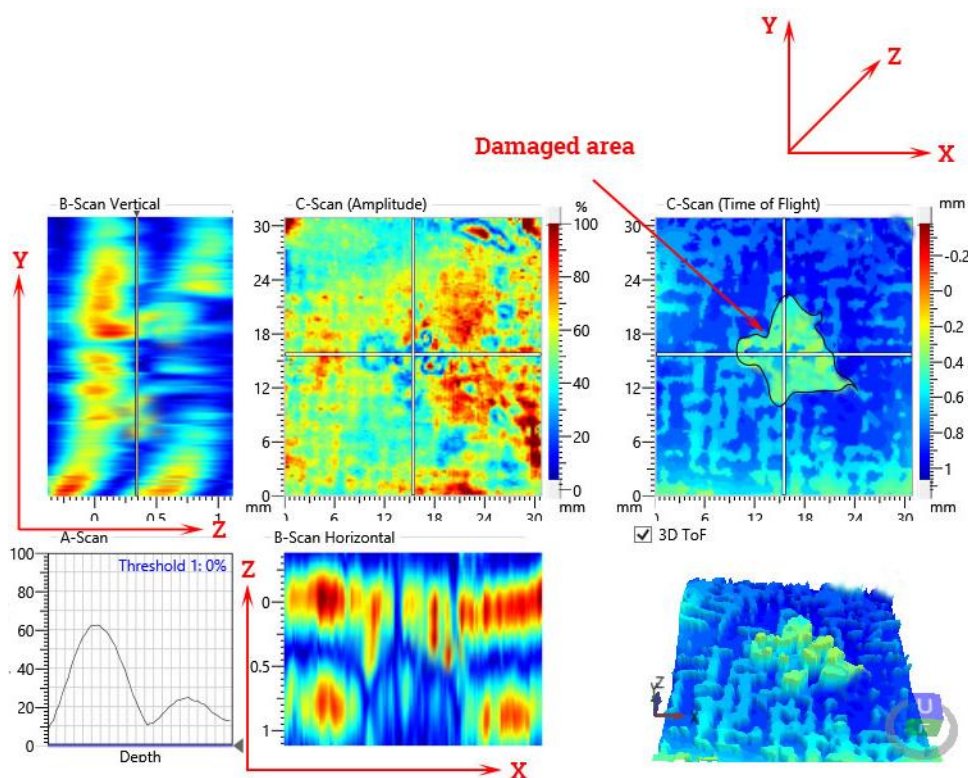


Figure 7-36: C – scan image for AB panel impacted at 0.607 J.

7.3.5 Damage Location

After investigating the effectivity of the electrical resistance sensing system to measure the severity of damage and discussions in the areas that are needed to be researched to improve the accuracy of the current sensing system. Another challenging subject was the investigation of the sensor to enable damage location within the panel. The main advantage of this technique was the ease with which the damage can be located. This technique has an advantage over C-scan in that it located the damaged area within few seconds while C-scan is a point-test and it requires an extensive work to locate internal damage such as delamination. However, a four-probe electrical resistance technique cannot map the damage while C-scan can do that in 2D and 3D view. The ease with which the damage can be located was attributed to innovative sensing mats, four-probe electrical resistance technique, and a simple data processing procedure.

The data acquired from the DAQ system was presented Table 7-2. The sensing mats divided the CFRP laminate panels into segments as shown in Figure 7-37, at which the electrical resistances were measured before and after each impact events. the four-probe electrical resistance technique offered a precise way to measure the resistance by eliminating electrical contact resistances. The electrical resistance at each segment was measured and then the electrical resistance changes at each segment were measured again at various impact energies. The electrical resistance readings were analysed by plotting the change in electrical resistance (ΔR) using Equation 7 – 10 against the sensing electrodes that were used to measure them.

$$\Delta R = R_i - R_o \quad 7-10$$

Where ΔR is the change in resistance at a segment, R_i is the electrical resistance after an impact event, and R_o is the electrical resistance before the impact event as shown Table 7-2.

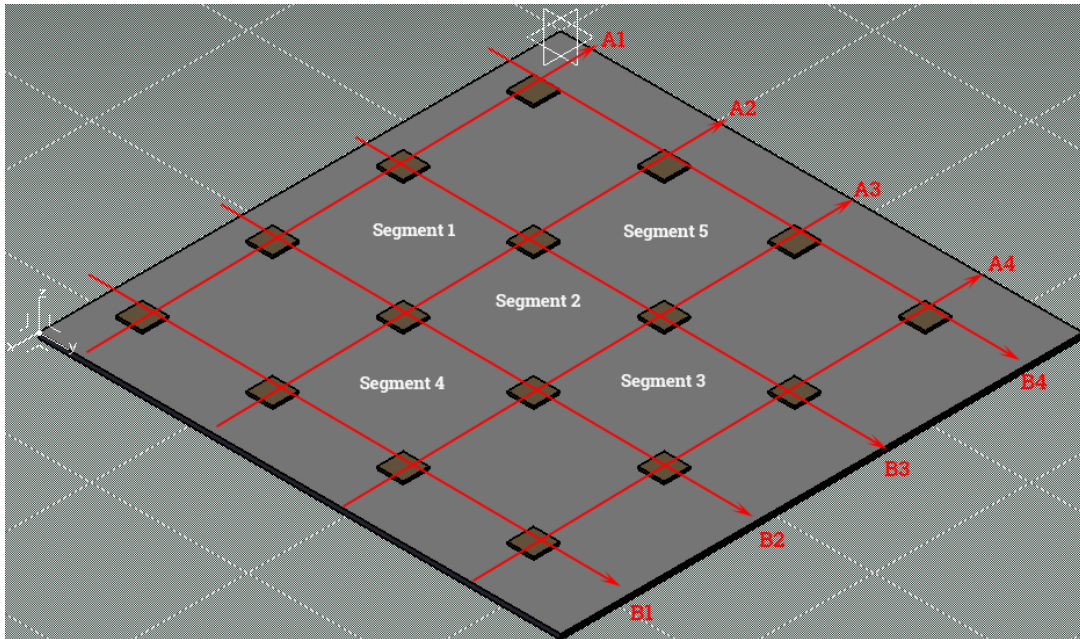


Figure 7-37: Representation of damage identification technique using electrical resistance change method.

The damage was located by significant local variations in the electrical resistances occurred in a panel as shown in Figure 7-38 to Figure 7-43. Those figures were generated in the following method: changes in electrical resistance in the horizontal direction were ($\Delta R_{A1}, \Delta R_{A2}, \Delta R_{A3}, \Delta R_{A4}$) and changes in electrical resistance in the vertical direction were ($\Delta R_{B1}, \Delta R_{B2}, \Delta R_{B3}, \Delta R_{B4}$); changes in horizontal and vertical directions were multiplied to generate a 4 x 4 matrix and then a cubic interpolation function was used to expand the matrix from 4 x 4 to 7 x 7 matrix. The purpose interpolation function was that to make the transition between damage and undamaged regions smooth and then the contour was plotted using "contourf" function in MATLAB.

It can be seen from the figures that when impact energy was low, the changes in electrical resistance were low, therefore, it was hard to locate damage precisely since the local variations in electrical resistances were high in comparison with undamaged areas in a CFRP laminate panel. This can be seen clearly in Figure 7-38a, however when the impact energy increased damage became more defined hence damage was located accurately.

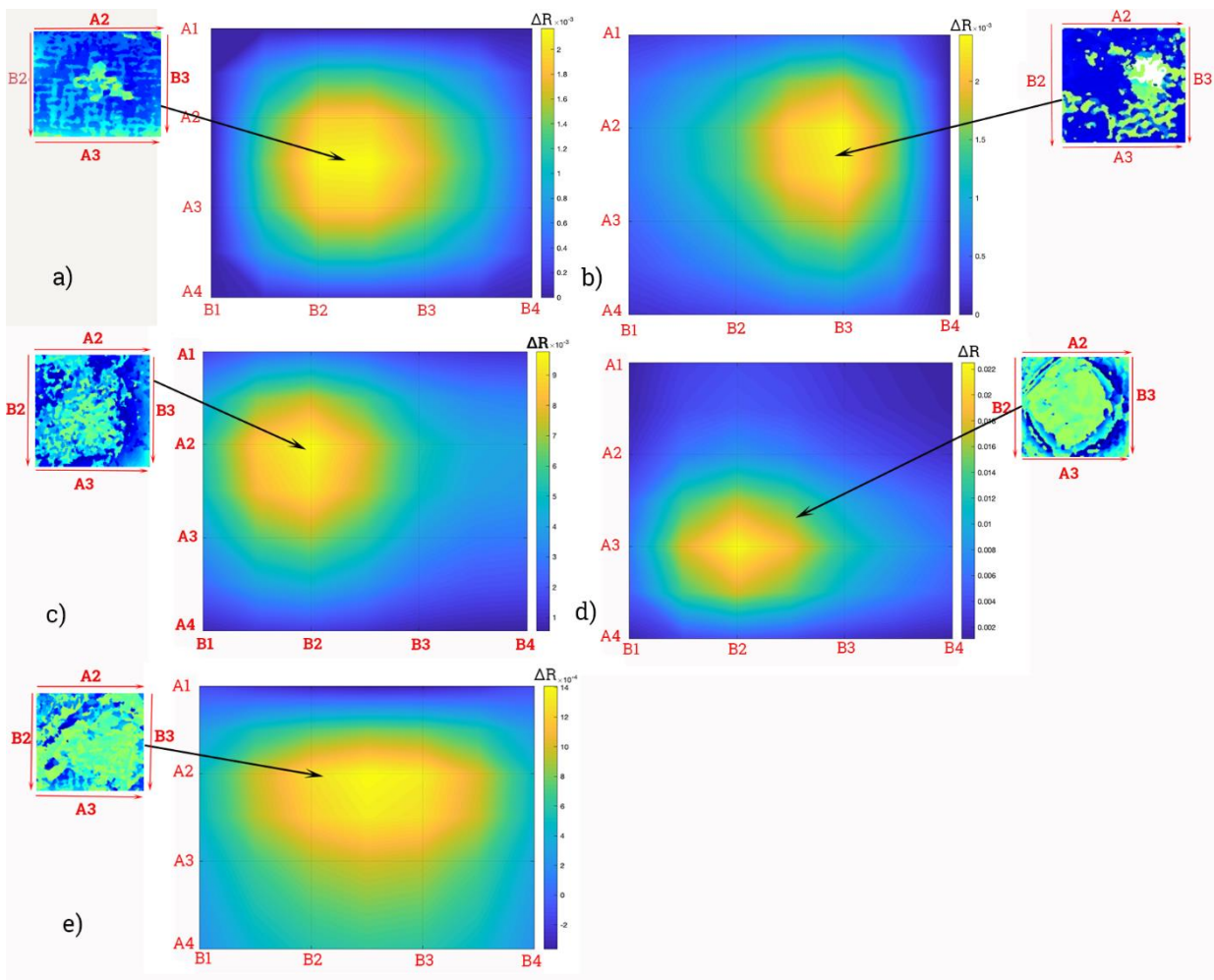


Figure 7-38: Damage location in AB panel that was impacted at a) 0.406 J, b) 0.607 J, c) 1.426 J, d) 3.333 J, and e) 4.96 J. The arrows on C – scan image at the top left and right corners represent the current flow direction.

It can also be seen that C-scan images helped to determine damage profiles. The smaller the damage the more spread the contours were. The arrows around C-scan images represent the direction of electrical current applied into the CFRP laminate panels. All panels were impacted in Segment 2 (Figure 7-37), therefore the highest changes in electrical resistance were occurred in the region between A2, A3, B2, and B3. In spite of the fact that the sensing electrode in this region experienced the highest electrical resistance changes, however the changes in electrical resistance were varied from a sensing electrode to the others. This in turn was shifted damaged areas on the contours from Segment 2 to other segments slightly. This challenge was attributed to amount of electrical contacts made with the carbon fibres in CFRP laminate panels during attaching the sensing mats to CFRP laminate panels. It is important to state that this type of error was inherited in the electrical resistance sensing technique and it required an advanced

signal processing technique to overcome it. In this thesis a simple and straightforward relationship was used to determine the damage location as given in Equation 7-10.

When impact energy increased to 4.96 J, all types of damage occurred (matrix crack, fibre breakage and delamination), therefore the damaged area was big as shown in Figure 7-38e.

When the thickness of the CFRP laminate panel increased to 1.63 mm (Figure 7-39), the changes in electrical resistance were less than CFRP laminate (Figure 7-38). When the thickness increased to 2.54 mm the changes in electrical resistance were as low as $11 \times 10^{-4} \Omega$ when the panel impacted at 4.96 J (Figure 7-40). However, damage was located, and damage was more localised when the CFRP panel was impacted at 9.996 J.

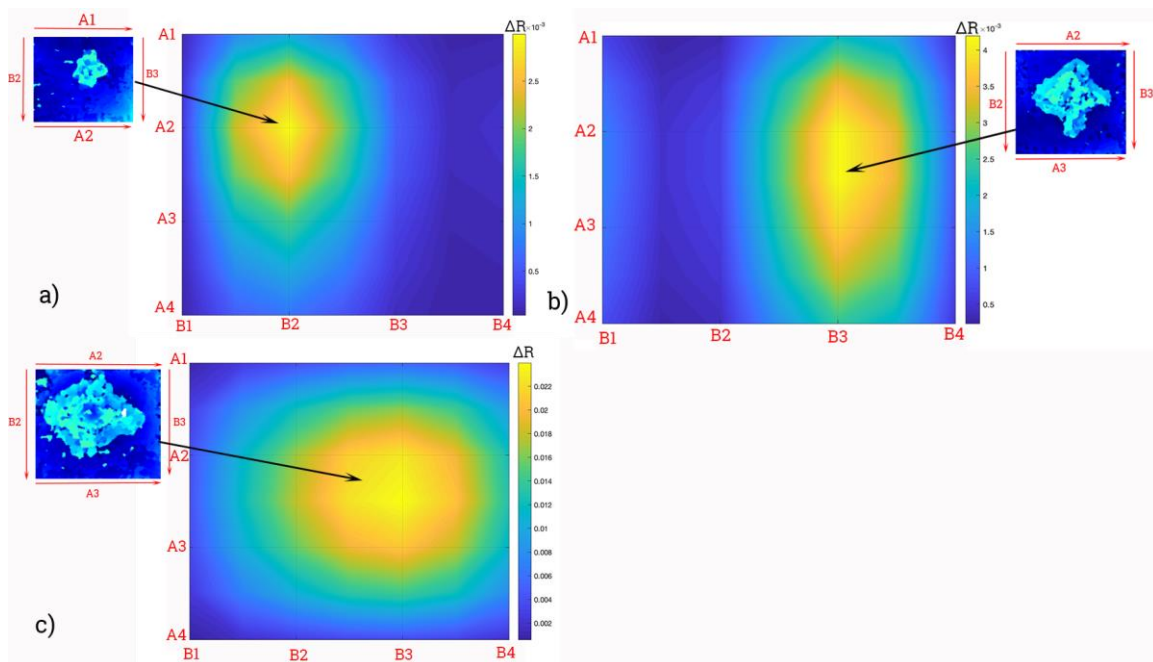


Figure 7-39: Damage location in AC panels that were impacted at a) 1.426 J, b) 3.333 J, and c) 4.96 J. The C-scan images at the top left and right corners show the damage profile, the arrows around C-scan images show the current flow direction.

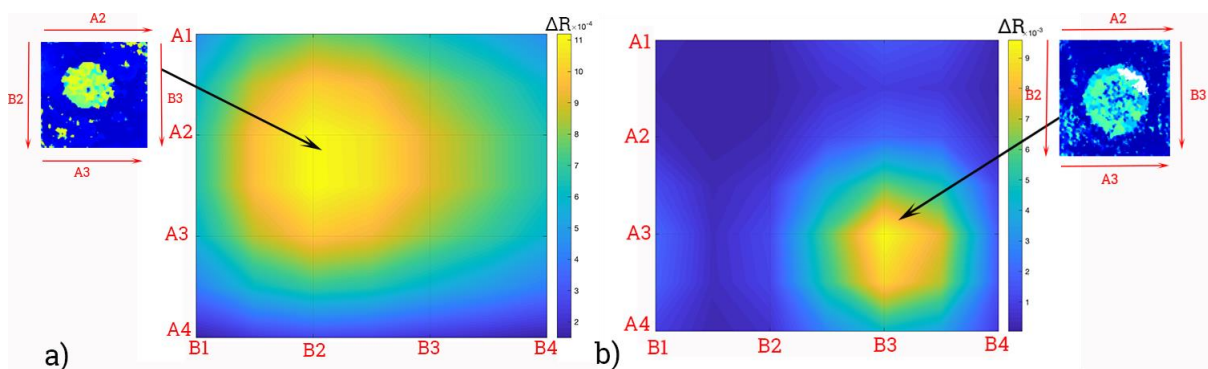


Figure 7-40: Damage location in AD panels that were impacted at a) 4.96 J, and b) 9.996 J. The C-scan images at the top left and right corners show the damage profile, the arrows around C-scan images show the current flow direction.

4.96 J and 9.996 J impacted energies caused barely visible impact damage in 3.5 mm CFRP laminate panel; the changes in electrical resistance was as low as 3.5×10^{-4} and $2.5 \times 10^{-3} \Omega$ respectively. It can be concluded according to Equation 7 – 1 that fibre volume fraction has higher impact on the electrical resistance sensing system than panel thicknesses.

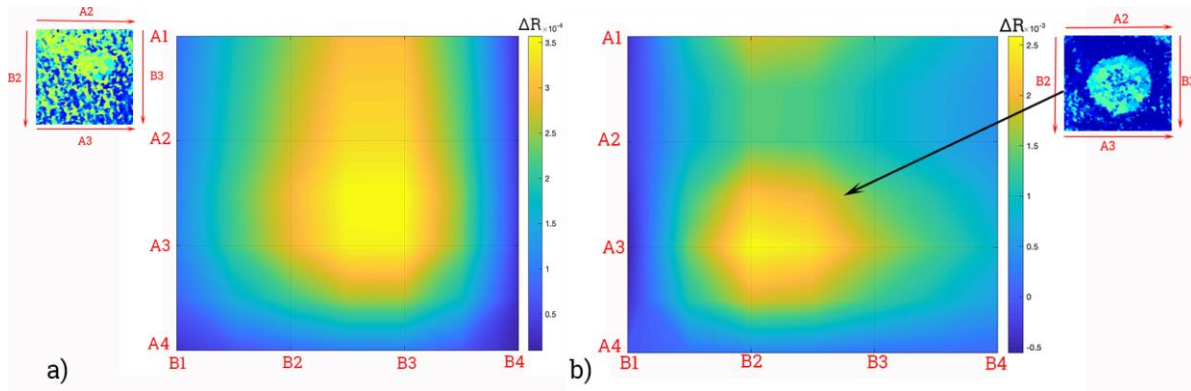


Figure 7-41: Damage location in AE panels that were impacted at a) 4.96 J, and b) 9.996 J. The C-scan images at the top left and right corners show the damage profile, the arrows around C-scan images show the current flow direction.

Damage location in two CFRP laminate panels, that were made using a VARTM technique, was investigated. It was found that VB panel in Figure 7-42 followed the same pattern as AB panel in Figure 7-38, however the changes in electrical resistance were higher which was attributed to the manufacturing technique, where fibre volume fraction was lower as discussed in Section 6.2.4. Also fibre-fibre contact network was lower than AB panel, therefore disruptions caused to fibre-fibre contact network caused due to damage had a higher impact on the electrical resistance of the panels. The CFRP laminate panels made using a VARTM technique had bigger resin rich areas and void contents than their equivalent made in an autoclave as discussed in Section 6.2.1 and Section 6.2.4. All those factors played an important role in damage detection and location.

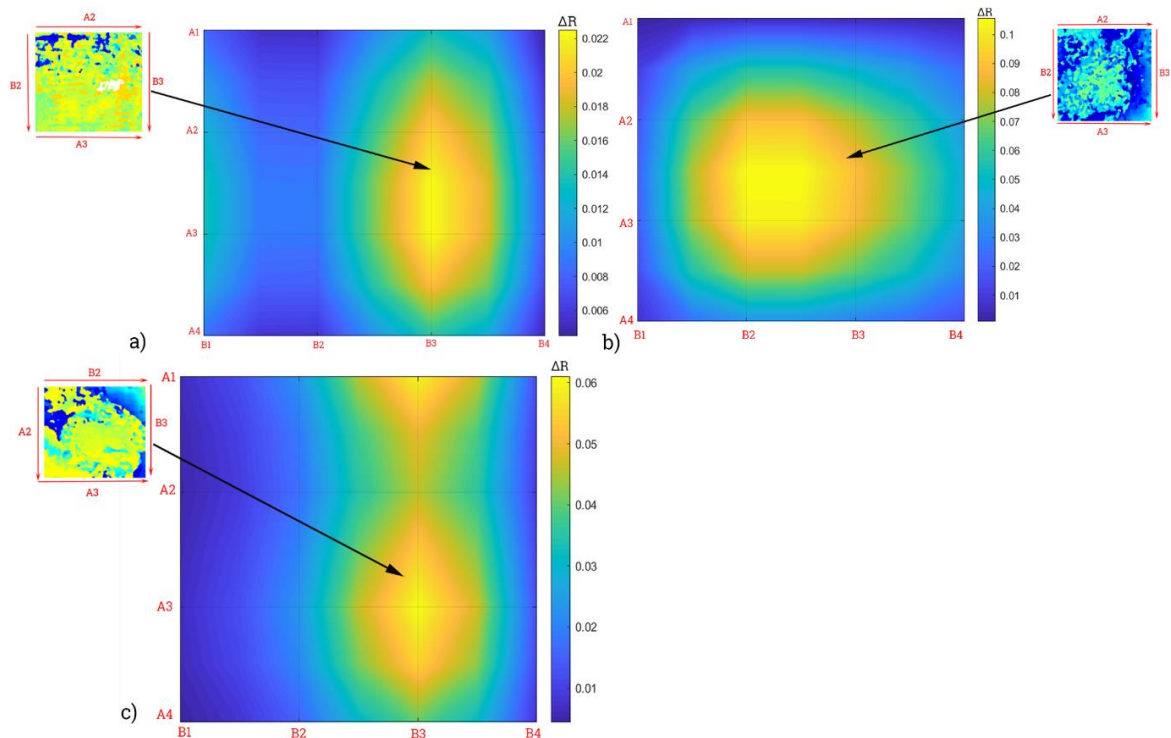


Figure 7-42: Damage location in VB panels that were impacted at a) 1.426 J, b) 3.33 J, and c) 4.96 J. The C-scan images at the top left and right corners show the damage profile, the arrows around C-scan images show the current flow direction.

Impact energy of 4.96 J caused visible damage in VB panel (full perforation was occurred) and that caused damage not only to the CFRP laminate panel but also to sensing electrodes, therefore damage was spread over a large area. Although VC panel had higher fibre volume fraction than VB panel (Table 6-8) but it also had a bigger resin rich area, therefore that was reduced fibre-fibre contact network in through-thickness direction as show in Figure 6-8. Hence the changes in electrical resistance due to BVID was lower than VB panel as shown in Figure 7-43. Given these results the electrical resistance sensing system showed a great advantage to locate damage in a short time (few seconds) over conventional non-destructive techniques, such as C-scan.

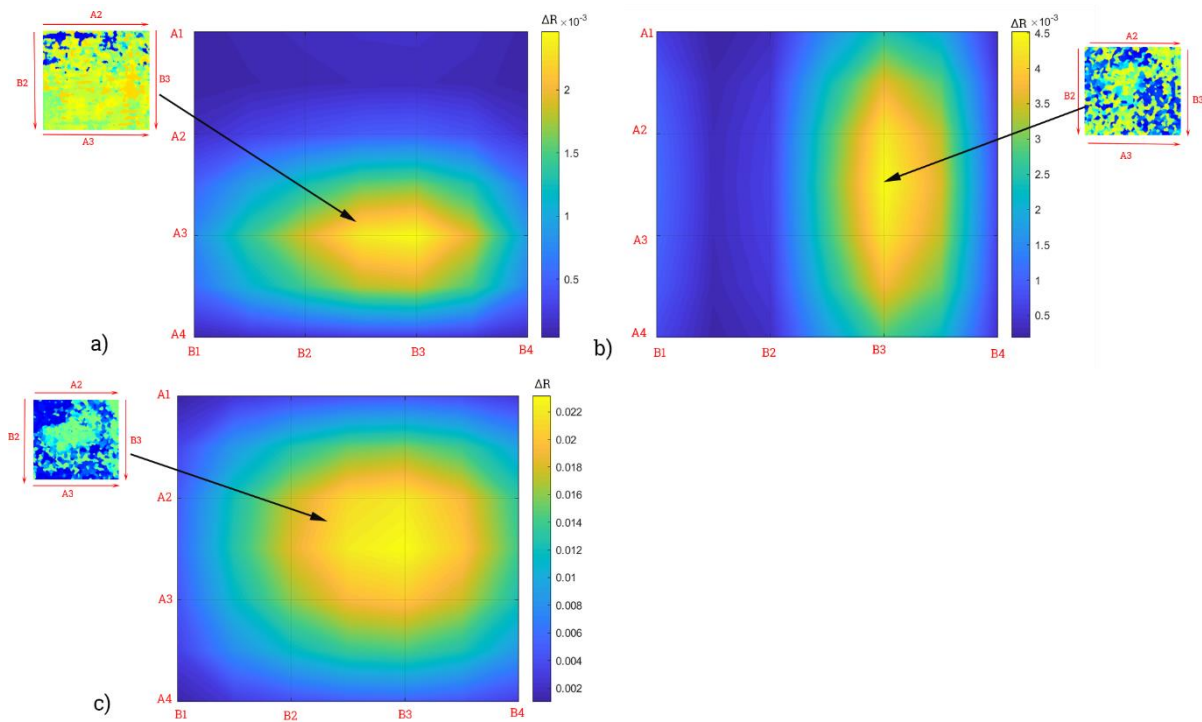


Figure 7-43: Damage location in VC panels that were impacted at a) 1.426 J, b) 3.33 J, and c) 4.96 J. The C-scan images at the top left and right corners show the damage profile, the arrows around C-scan images show the current flow direction

7.3.6 Summary of the Findings

The current sensing system was tested on six different CFRP laminate panels that were made using two different manufacturing techniques that were autoclave processing and vacuum assisted resin transfer moulding techniques. Two different sensing mats (sensing mat 1 and sensing mat 2) were attached to the bottom surface of the CFRP laminate panels. The CFRP laminate panels were subjected to impact energies at the upper surface using a low velocity impact tester, a range of impact energies were used (0.406 – 9.996 J), the purpose was to investigate the ability of the electrical resistance sensing system to detect, locate, and quantify barely visible impact damage (BVID). The results showed that the sensing system using sensing mat 1 cannot detect damage below a threshold that is 61, 71, 200, 170, 82, and 107 mm² in panel AB, AC, AD, AE, VB, and VC respectively. It was found that at a given damage size the change in global electrical resistance (ξ) was significantly lower (as twice as lower) when sensing mat 2 was used than sensing mat 1.

In order to quantify the damage using the current sensing system an inverse analysis was undertaken on AB panel, the panel was impacted at 0.607 J, then depending on the global electrical resistance changes the damage was estimated to be 85 mm², however the actual damage size was measured using C – scan and it was found 100 mm². The error of estimation was 15

mm², this error was inevitable since it was attributed to the electrical properties of CFRP laminate panels. There were two sources of error when damage was quantified, the first source was the through – thickness electrical resistivity that depends on the fibre – fibre contact network between adjacent plies, these fibre – fibre contacts depends on the manufacturing techniques and even if the CFRP laminate panels made using the same manufacturing technique, the density of fibre – fibre contacts differ from region to the other in the same panel. The second source of error was due to negative electrical current flow, this flow creates a circular pattern flow around the positive electric electrode and this in turn decreases the change in electrical resistance due to damage and reduce the estimated damage size consequently. Damage was located in all CFRP laminate panels that were used in this work using an innovative sensing mat that breaks down the panel into segments. The sensing system measures electrical resistance variations in these segments, and then it was assumed that the damage in a particular segment when the highest electrical resistance variations occurred in that segment. The locating damage process takes few seconds for each panel used in this thesis.

Chapter 8

CONCLUSIONS AND FUTURE WORK

8.1 Summary and Conclusions

The aim of this thesis was to develop a sensing system for damage detection in woven fabric CFRP laminate panels. The sensing system utilizes the electrical properties of the reinforcing element (carbon fibres) in CFRP laminates. The main goal is to introduce an integrated structural health monitoring system that can potentially replace the expensive non-destructive testing techniques and reduce the periodical check-up time. During early stages of this work, promising results were obtained from CFRP laminate panels made using an autoclave processing technique, therefore, the sensing system was extended to cover CFRP panels made using a VARTM technique.

Using the VARTM technique to produce panels that are suitable for electrical self-sensing is challenging due to the quality of the panels and low fibre volume fractions. Therefore, the second aim was to produce high quality CFRP laminates using the VARTM. The conventional process to produce CFRP laminates using the VARTM technique was amended in terms of preform sequence, infusion temperature and vacuum pressure. CFRP laminate panels with less than 2% void content and fibre volume fraction $\approx 45\%$ were obtained; those CFRP laminate panels were suitable for electrical self-sensing.

The third aim was to design a sensing mat to maximize the performance of the sensing system; two sensing mats were designed and investigated.

The following conclusions were obtained:

- The electrical resistance sensing technique can be used to detect, locate and quantify damage in woven fabric CFRP laminate panels.
- Many parameters affected the electrical resistance readings, such as carbon fibre types, CFRP processing techniques, fibre volume fractions, specimen thicknesses, electrical measurement techniques, size of sensing electrodes, location of sensing electrodes, type of sensing electrodes, integration of sensing electrodes, electrical current type, electrical current amount, connection wires, and the data acquisition system. Most of all, the amount of electrical contacts between the electrodes and carbon fibres in CFRP laminate panels determine the accuracy and sensitivity the sensing system as well as the readings of electrical resistance. This is, in turn, is very difficult to control and it is

varied from location to the other on the same panel. This explains why there is a significant difference in the published data in the literature.

- Fibre-fibre contacts between the consecutive layers in CFRP laminate panels improved the damage detection sensitivity of the electrical sensing system but it decreased damage quantification ability of the system because it causes negative electrical current flow.
- The impact of the sensor area (100 mm^2 and 400 mm^2) on the accuracy of the electrical sensing technique was significant. The bigger the sensor the higher accuracy, on the other hand the bigger distance between sensors the less the resolution. However, in the cases assessed it was always possible to detect damage within the structure.
- Spacing distance between sensing electrodes had a greater impact on the sensitivity of the sensing system than the electrode size.
- Carbon fibre volume fraction had a greater impact on the sensing system than panel thicknesses.
- This technique showed its capabilities in detecting change in electrical resistance due to BVID, it also can detect the change in electrical resistance when the sample was loaded below BVID energy threshold as determined using C-scanning.
- The electrical resistance sensing technique can map the damage area in 2D, however, the accuracy of the map requires improvements as will be discussed in the following section.

8.2 Future work

To further develop this project beyond the successful results that were obtained. The following points need to be addressed to fully utilize this technique and extend it to an industrial scale.

- In this thesis 200 x 200 mm (LXW) panel size was studied, the future work could investigate the effect of a bigger panel size on the changes in electrical resistance for impact damage detection.
- To reduce the cost of the sensing system, the number of the sensing electrodes and the number of channels in the data acquisition system consequently could potentially decrease. This can be achieved by exploring a larger spacing between sensing electrodes in the sensing mats; this will reduce the sensitivity of the sensing system but establishing a precise relationship between the very small change in electrical resistance due to damage and damage size and location would resolve this issue. This relationship could be obtained by undertaking a large set of experiments.
- In this thesis the effect of humidity and temperature on the electrical resistance were excluded. Future work could investigate the effects of these factors on the electrical resistance readings.
- Develop a remote sensing system by implanting a transceiver into the composite structure, that could communicate with the sensing mats, the transceiver collects and sends the electrical resistance data to a data processing unit that analyses and presents the data. This could expedite the implementation of this technique in the aerospace industry.
- In this thesis, the sensing system was tested on a woven fabric CFRP laminate, future work could explore the suitability of the sensing system to unidirectional CFRP laminates.
- In this thesis, two types of manufacturing techniques, which are autoclave processing and VARTM techniques, were used to fabricate the CFRP laminate panels. Future work could explore using CFRP laminate panels that are made by RTM and press forming manufacturing techniques. These techniques generate fibre – fibre contact density in the through - thickness direction between the adjacent plies somewhere between autoclave processing panels and VARTM processing panels.
- In this thesis a 2 x 2 mm twill weave carbon fibre reinforcing mat was used, other weave architectures could be explored.
- Use FE to simulate the electrical behaviour of CFRP laminates. However, for time being there is no electrical conduction theory for CFRP laminate available in the literature.

REFERENCES

-
- [1] E. J. Barbero, *Introduction to composite materials design*. CRC press, 2017.
- [2] B. Fattouh, L. Kilian, and L. Mahadeva, "The Role of Speculation in Oil Markets: What Have We Learned So Far?," *The Energy Journal*, vol. 34, no. 3, pp. 7-33, 2013.
- [3] F. C. Campbell Jr, *Manufacturing processes for advanced composites*. Elsevier, 2003.
- [4] M. Harris, "Carbon fibre: the wonder materials with a dirty secret " in *Guardian sustainable business* ed, 2017.
- [5] G. V. Research, *Aerospace Plastics Market Analysis By Application (Aerostructure, Components, Cabin Interiors, Propulsion Systems, Satellites), By End-use, And Segment Forecasts, 2014 - 2025*, 2017. [Online]. Available: <https://www.grandviewresearch.com/industry-analysis/aerospace-plastics-market>. Accessed on April, 2017.
- [6] V. M. Karbhari et al., "Durability gap analysis for fiber-reinforced polymer composites in civil infrastructure," *Journal of composites for construction*, vol. 7, no. 3, pp. 238-247, 2003.
- [7] S. Pimenta and S. T. Pinho, "Recycling carbon fibre reinforced polymers for structural applications: technology review and market outlook," *Waste management*, vol. 31, no. 2, pp. 378-392, 2011.
- [8] S. V. Prasad and R. Asthana, "Aluminum metal-matrix composites for automotive applications: tribological considerations," *Tribology letters*, vol. 17, no. 3, pp. 445-453, 2004.
- [9] C. Soutis, "Fibre reinforced composites in aircraft construction," *Progress in Aerospace Sciences*, vol. 41, no. 2, pp. 143-151, 2005/02/01/ 2005.
- [10] J. D. Buckley and D. D. Edie, *Carbon-carbon materials and composites*. William Andrew, 1993.
- [11] A. P. Mouritz, E. Gellert, P. Burchill, and K. Challis, "Review of advanced composite structures for naval ships and submarines," *Composite structures*, vol. 53, no. 1, pp. 21-42, 2001.
- [12] L. C. Hollaway and J.-G. Teng, *Strengthening and rehabilitation of civil infrastructures using fibre-reinforced polymer (FRP) composites*. Elsevier, 2008.
- [13] J. R. Duflou, J. De Moor, I. Verpoest, and W. Dewulf, "Environmental impact analysis of composite use in car manufacturing," *CIRP Annals*, vol. 58, no. 1, pp. 9-12, 2009/01/01/ 2009.
- [14] P. Beardmore and C. F. Johnson, "The potential for composites in structural automotive applications," *Composites Science and Technology*, vol. 26, no. 4, pp. 251-281, 1986/01/01/ 1986.
- [15] T. Gurunathan, S. Mohanty, and S. K. Nayak, "A review of the recent developments in biocomposites based on natural fibres and their application perspectives," *Composites Part A: Applied Science and Manufacturing*, vol. 77, pp. 1-25, 2015/10/01/ 2015.
- [16] S. Das, "The cost of automotive polymer composites: a review and assessment of DOE's lightweight materials composites research," Oak Ridge National Lab., TN (US)2001.

- [17] D. R. Cramer, D. F. Taggart, and H. Inc, "Design and manufacture of an affordable advanced-composite automotive body structure."
- [18] A. A. B. Baker, *Composite materials for aircraft structures*. AIAA, 2004.
- [19] C. Soutis, "1 - Introduction: Engineering requirements for aerospace composite materials," in *Polymer Composites in the Aerospace Industry*. Woodhead Publishing, 2015, pp. 1-18.
- [20] J. Renard and A. Thionnet, "Damage in composites: From physical mechanisms to modelling," *Composites science and technology*, vol. 66, no. 5, pp. 642-646, 2006.
- [21] A. S. D. Wang and F. W. Crossman, "Initiation and growth of transverse cracks and edge delamination in composite laminates Part 1. An energy method," *Journal of Composite Materials*, vol. 14, no. 1, pp. 71-87, 1980.
- [22] R. Smith and B. Hawkins, *Lean maintenance: reduce costs, improve quality, and increase market share*. Butterworth-Heinemann, 2004.
- [23] A. Kelly, R. Davidson, K. Uchino, N. Shanmuga Priya, and M. Shanmugasundaram, "7.18 Smart Composite Materials Systems☆," in *Comprehensive Composite Materials II*Oxford: Elsevier, 2018, pp. 358-363.
- [24] K. Diamanti and C. Soutis, "Structural health monitoring techniques for aircraft composite structures," *Progress in Aerospace Sciences*, vol. 46, no. 8, pp. 342-352, 2010/11/01/ 2010.
- [25] F. Ansari, "Fiber optic health monitoring of civil structures using long gage and acoustic sensors," *Smart Materials and Structures*, vol. 14, no. 3, pp. S1-S7, 2005.
- [26] B. Hofer, "Fibre optic damage detection in composite structures," *Composites*, vol. 18, no. 4, pp. 309-316, 1987/09/01/ 1987.
- [27] R. D. Finlayson, M. Friesel, M. Carlos, P. Cole, and J. C. Lenain, "Health monitoring of aerospace structures with acoustic emission and acousto-ultrasonics," *Insight-Wigston then Northampton-*, vol. 43, no. 3, pp. 155-158, 2001.
- [28] G. Riegert, K. Pfeleiderer, H. Gerhard, I. Solodov, and G. Busse, "Modern methods of NDT for inspection of aerospace structures," *ECNDT, Berlin, Germany*, 2006.
- [29] W. J. Staszewski, S. Mahzan, and R. Traynor, "Health monitoring of aerospace composite structures—Active and passive approach," *composites Science and Technology*, vol. 69, no. 11-12, pp. 1678-1685, 2009.
- [30] L. F. Donald and H. K. Murat, "Experimental Determination of the In Situ Transverse Lamina Strength in Graphite/Epoxy Laminates," *Journal of Composite Materials*, vol. 16, no. 2, pp. 103-116, 1982/03/01 1982.
- [31] X. Wang and D. D. L. Chung, "Self-monitoring of fatigue damage and dynamic strain in carbon fiber polymer-matrix composite," *Composites Part B: Engineering*, vol. 29, no. 1, pp. 63-73, 1998/01/01/ 1998.
- [32] A. Todoroki, Y. Tanaka, and Y. Shimamura, "Delamination monitoring of graphite/epoxy laminated composite plate of electric resistance change method," *Composites Science and Technology*, vol. 62, no. 9, pp. 1151-1160, 7// 2002.
- [33] A. Todoroki, M. Tanaka, and Y. Shimamura, "Measurement of orthotropic electric conductance of CFRP laminates and analysis of the effect on

- delamination monitoring with an electric resistance change method," *Composites Science and Technology*, vol. 62, no. 5, pp. 619-628, 4// 2002.
- [34] A. Todoroki, Y. Tanaka, and Y. Shimamura, "Multi-probe electric potential change method for delamination monitoring of graphite/epoxy composite plates using normalized response surfaces," *Composites Science and Technology*, vol. 64, no. 5, pp. 749-758, 2004.
- [35] S. Wang, D. Wang, D. D. L. Chung, and J. H. Chung, "Method of sensing impact damage in carbon fiber polymer-matrix composite by electrical resistance measurement," *Journal of Materials Science*, vol. 41, no. 8, pp. 2281-2289, 2006/04/01 2006.
- [36] W. Chung-Yue and C. H. Yew, "Impact damage in composite laminates," *Computers & structures*, vol. 37, no. 6, pp. 967-982, 1990.
- [37] S. Liu, Z. Kutlu, and F.-K. Chang, "Matrix cracking and delamination in laminated composite beams subjected to a transverse concentrated line load," *Journal of Composite Materials*, vol. 27, no. 5, pp. 436-470, 1993.
- [38] W. J. Cantwell and J. Morton, "Detection of impact damage in CFRP laminates," *Composite Structures*, vol. 3, no. 3-4, pp. 241-257, 1985.
- [39] B. Harris, *Fatigue in composites: science and technology of the fatigue response of fibre-reinforced plastics*. Woodhead Publishing, 2003.
- [40] Q. Ji, P. Zhu, J. Lu, and C. Zhu, "Experimental study and modeling of fatigue life prediction of plain weave carbon/polymer composite under constant amplitude loading," *Advanced Composite Materials*, vol. 26, no. 4, pp. 295-320, 2017/07/04 2017.
- [41] T. Roberts, *The carbon fibre industry: Global strategic market evaluation 2006-2010*. Materials Technology Publications, 2006.
- [42] M. S. Dresselhaus, G. Dresselhaus, K. Sugihara, I. L. Spain, and H. A. Goldberg, M. Cardona, Ed. *Graphite Fibers and Filaments*, 1 ed. (Springer Series in Materials Science). Springer-Verlag Berlin Heidelberg, 1988, pp. X, 382.
- [43] R. Bacon, "Growth, structure, and properties of graphite whiskers," *Journal of Applied Physics*, vol. 31, no. 2, pp. 283-290, 1960.
- [44] D. D. Edie, "The effect of processing on the structure and properties of carbon fibers," *Carbon*, vol. 36, no. 4, pp. 345-362, 1998.
- [45] G. Henrici-Olivé and S. Olivé, "The chemistry of carbon fiber formation from polyacrylonitrile," in *Industrial Developments* Berlin, Heidelberg: Springer Berlin Heidelberg, 1983, pp. 1-60.
- [46] S. C. Bennett, D. J. Johnson, and W. Johnson, "Strength-structure relationships in PAN-based carbon fibres," *Journal of Materials Science*, vol. 18, no. 11, pp. 3337-3347, 1983/11/01 1983.
- [47] H. Q. Pham and M. J. Marks, "Epoxy resins," *Kirk-Othmer encyclopedia of chemical technology*, 2004.
- [48] B. Ellis, *Chemistry and technology of epoxy resins*. Springer, 1993.
- [49] R. J. Gritter, "Reactions of cyclic ethers," *The Ether Linkage (1967)*, pp. 373-443, 1967.
- [50] W. R. Ashcroft, "Curing agents for epoxy resins," in *Chemistry and technology of epoxy resins*: Springer, 1993, pp. 37-71.
- [51] L. Shechter, J. Wynstra, and R. P. Kurkky, "Glycidyl ether reactions with amines," *Industrial & Engineering Chemistry*, vol. 48, no. 1, pp. 94-97, 1956.

- [52] E. M. Petrie, *Epoxy adhesive formulations*. McGraw Hill Professional, 2005.
- [53] O. Hara, "Curing Agents for Epoxy Resin," 32). 1990, p.^pp. Pages.
- [54] N. Odagiri, H. Kishi, and M. Yamashita, "Development of TORAYCA prepreg P2302 carbon fiber reinforced plastic for aircraft primary structural materials," *Advanced Composite Materials*, vol. 5, no. 3, pp. 249-254, 1996.
- [55] U. P. Breuer, "Repair," in *Commercial Aircraft Composite Technology*: Springer, 2016, pp. 141-162.
- [56] P. K. Mallick, *Fiber-reinforced composites: materials, manufacturing, and design*. CRC press, 2007.
- [57] S. G. Advani and K.-T. Hsiao, *Manufacturing techniques for polymer matrix composites (PMCs)*. Elsevier, 2012.
- [58] P. Hubert, G. Fernlund, and A. Poursartip, "Autoclave processing for composites," in *Manufacturing techniques for polymer matrix composites (PMCs)*: Elsevier, 2012, pp. 414-434.
- [59] J. Schlimbach and A. Ogale, "14 - Out-of-autoclave curing process in polymer matrix composites," in *Manufacturing Techniques for Polymer Matrix Composites (PMCs)*: Woodhead Publishing, 2012, pp. 435-480.
- [60] E. M. Sozer, P. Simacek, and S. G. Advani, "9 - Resin transfer molding (RTM) in polymer matrix composites," in *Manufacturing Techniques for Polymer Matrix Composites (PMCs)*: Woodhead Publishing, 2012, pp. 245-309.
- [61] A. Goren and C. Atas, "Manufacturing of polymer matrix composites using vacuum assisted resin infusion molding," *Archives of materials Science and Engineering*, vol. 34, no. 2, pp. 117-120, 2008.
- [62] C. I. ltd, "Resin Transfer Moulding " in *On line ed*, 2017, p. Schematic of a typical resin tranfer moulding technique
- [63] W. D. Brouwer, E. C. F. C. van Herpt, and M. Labordus, "Vacuum injection moulding for large structural applications," *Composites Part A: Applied Science and Manufacturing*, vol. 34, no. 6, pp. 551-558, 2003.
- [64] K. K. Verma, B. L. Dinesh, K. Singh, K. M. Gaddikeri, and R. Sundaram, "Challenges in Processing of a Cocured Wing Test Box Using Vacuum Enhanced Resin Infusion Technology (VERITy)," *Procedia Materials Science*, vol. 6, pp. 331-340, 2014.
- [65] S. Laurenzi, A. Casini, and D. Pocci, "Design and fabrication of a helicopter unitized structure using resin transfer moulding," *Composites Part A: Applied Science and Manufacturing*, vol. 67, pp. 221-232, 2014.
- [66] H. A. Materials. (2015). *Vacuum Infusion Process Guide*
 ARALDITE® FST 40002 / ARALDITE® FST 40003. Available:
www.huntsman.com/advanced_materials
- [67] K.-T. Hsiao, M. Devillard, and S. G. Advani, "Simulation based flow distribution network optimization for vacuum assisted resin transfer moulding process," *Modelling and Simulation in Materials Science and Engineering*, vol. 12, no. 3, pp. S175-S190, 2004.
- [68] L. Labat, J. Bréard, S. Pillut-Lesavre, and G. Bouquet, "Void fraction prevision in LCM parts," *The European Physical Journal Applied Physics*, vol. 16, no. 2, pp. 157-164, 2001.
- [69] J. M. Lawrence, P. Frey, A. A. Obaid, S. Yarlagadda, and S. G. Advani, "Simulation and validation of resin flow during manufacturing of composite

- panels containing embedded impermeable inserts with the VARTM process," *Polymer Composites*, vol. 28, no. 4, pp. 442-450, 2007.
- [70] E. Sevkat and M. Brahim, "The bearing strength of pin loaded woven composites manufactured by vacuum assisted resin transfer moulding and hand lay-up techniques," *Procedia Engineering*, vol. 10, pp. 153-158, 2011.
- [71] G. Francucci, A. Vázquez, E. Ruiz, and E. S. Rodríguez, "Capillary effects in vacuum-assisted resin transfer molding with natural fibers," *Polymer Composites*, vol. 33, no. 9, pp. 1593-1602, 2012.
- [72] V. R. Kedari, B. I. Farah, and K.-T. Hsiao, "Effects of vacuum pressure, inlet pressure, and mold temperature on the void content, volume fraction of polyester/e-glass fiber composites manufactured with VARTM process," *Journal of composite materials*, vol. 45, no. 26, pp. 2727-2742, 2011.
- [73] U. K. Vaidya, N. C. Jadhav, M. V. Hosur, J. W. Gillespie Jr, and B. K. Fink, "Assessment of flow and cure monitoring using direct current and alternating current sensing in vacuum-assisted resin transfer molding," *Smart materials and structures*, vol. 9, no. 6, p. 727, 2000.
- [74] T. Luthy and P. Ermanni, "Flow monitoring in liquid composite molding based on linear direct current sensing technique," *Polymer composites*, vol. 24, no. 2, pp. 249-262, 2003.
- [75] D. Modi, N. Correia, M. Johnson, A. Long, C. Rudd, and F. Robitaille, "Active control of the vacuum infusion process," *Composites Part A: Applied Science and Manufacturing*, vol. 38, no. 5, pp. 1271-1287, 2007.
- [76] S. Konstantopoulos, "Monitoring the production of FRP composites: A review of in-line sensing methods," *Express Polymer Letters*, vol. 8, no. 11, pp. 823-840, 2014.
- [77] Q. Govignon, S. Bickerton, J. Morris, and P. A. Kelly, "Full field monitoring of the resin flow and laminate properties during the resin infusion process," *Composites Part A: Applied Science and Manufacturing*, vol. 39, no. 9, pp. 1412-1426, 9// 2008.
- [78] B. Yenilmez and E. Murat Sozer, "A grid of dielectric sensors to monitor mold filling and resin cure in resin transfer molding," *Composites Part A: Applied Science and Manufacturing*, vol. 40, no. 4, pp. 476-489, 2009.
- [79] C. Lekakou, S. Cook, Y. Deng, T. W. Ang, and G. T. Reed, "Optical fibre sensor for monitoring flow and resin curing in composites manufacturing," *Composites Part A: Applied Science and Manufacturing*, vol. 37, no. 6, pp. 934-938, 2006/06/01/ 2006.
- [80] P. Kumar and B. Rai, "Delaminations of barely visible impact damage in CFRP laminates," *Composite Structures*, vol. 23, no. 4, pp. 313-318, 1993.
- [81] M. O. W. Richardson and M. J. Wisheart, "Review of low-velocity impact properties of composite materials," *Composites Part A: Applied Science and Manufacturing*, vol. 27, no. 12, pp. 1123-1131, 1996/01/01/ 1996.
- [82] K. D. Challenger, "The damage tolerance of carbon fiber reinforced composites—A workshop summary," *Composite Structures*, vol. 6, no. 4, pp. 295-318, 1986/01/01 1986.
- [83] J. C. Prichard and P. J. Hogg, "The role of impact damage in post-impact compression testing," *Composites*, vol. 21, no. 6, pp. 503-511, 1990.
- [84] H. Y. Choi, H.-Y. T. Wu, and F.-K. Chang, "A new approach toward understanding damage mechanisms and mechanics of laminated

- composites due to low-velocity impact: Part II—analysis," *Journal of Composite Materials*, vol. 25, no. 8, pp. 1012-1038, 1991.
- [85] S. Abrate, *Impact on composite structures*. Cambridge university press, 2005.
- [86] W. J. Cantwell and J. Morton, "The impact resistance of composite materials – a review," *Composites*, vol. 22, no. 5, pp. 347-362, 1991/09/01/ 1991.
- [87] K. B. Katnam, L. F. M. Da Silva, and T. M. Young, "Bonded repair of composite aircraft structures: A review of scientific challenges and opportunities," *Progress in Aerospace Sciences*, vol. 61, pp. 26-42, 2013/08/01/ 2013.
- [88] J. Morton and E. W. Godwin, "Impact response of tough carbon fibre composites," *Composite Structures*, vol. 13, no. 1, pp. 1-19, 1989/01/01/ 1989.
- [89] B. Vieille, V. M. Casado, and C. Bouvet, "About the impact behavior of woven-ply carbon fiber-reinforced thermoplastic- and thermosetting-composites: A comparative study," *Composite Structures*, vol. 101, pp. 9-21, 2013/07/01/ 2013.
- [90] S. Abrate, *Impact engineering of composite structures*. Springer Science & Business Media, 2011.
- [91] S. R. Reid and G. Zhou, *Impact behaviour of fibre-reinforced composite materials and structures*. Elsevier, 2000.
- [92] R. M. Jones, *Mechanics of composite materials*. Scripta Book Company Washington, DC, 1975.
- [93] S. A. Hitchen and R. M. J. Kemp, "The effect of stacking sequence on impact damage in a carbon fibre/epoxy composite," *Composites*, vol. 26, no. 3, pp. 207-214, 1995/03/01/ 1995.
- [94] N. K. Naik, Y. Chandra Sekher, and S. Meduri, "Damage in woven-fabric composites subjected to low-velocity impact," *Composites Science and Technology*, vol. 60, no. 5, pp. 731-744, 2000.
- [95] P. J. Hazell, C. Stennett, and G. Cooper, "The effect of specimen thickness on the shock propagation along the in-fibre direction of an aerospace-grade CFRP laminate," *Composites Part A: Applied Science and Manufacturing*, vol. 40, no. 2, pp. 204-209, 2009/02/01/ 2009.
- [96] R. Thévenin, "Composites@ Airbus Maintenance & Repairs Validations."
- [97] R. Jones and R. J. Callinan, "A design study in crack patching," *Fibre Science and Technology*, vol. 14, no. 2, pp. 99-111, 1981.
- [98] C. S. Lopes, O. Seresta, Y. Coquet, Z. Gürdal, P. P. Camanho, and B. Thuis, "Low-velocity impact damage on dispersed stacking sequence laminates. Part I: Experiments," *Composites Science and Technology*, vol. 69, no. 7, pp. 926-936, 2009/06/01/ 2009.
- [99] D. Feng and F. Aymerich, "Finite element modelling of damage induced by low-velocity impact on composite laminates," *Composite Structures*, vol. 108, pp. 161-171, 2014/02/01/ 2014.
- [100] H. R. Wang, S. C. Long, X. Q. Zhang, and X. H. Yao, "Study on the delamination behavior of thick composite laminates under low-energy impact," *Composite Structures*, vol. 184, pp. 461-473, 2018/01/15/ 2018.
- [101] Y. Wang and H. Waisman, "Progressive delamination analysis of composite materials using XFEM and a discrete damage zone model," *Computational Mechanics*, vol. 55, no. 1, pp. 1-26, 2014.

- [102] L. Dahsin and E. M. Lawrence, "Matrix Cracking in Impacted Glass/Epoxy Plates," *Journal of Composite Materials*, vol. 21, no. 7, pp. 594-609, 1987/07/01 1987.
- [103] G. A. O. Davies and X. Zhang, "Impact damage prediction in carbon composite structures," *International Journal of Impact Engineering*, vol. 16, no. 1, pp. 149-170, 1995/02/01/ 1995.
- [104] G. Dorey, P. Sigety, K. Stellbrink, and W. G. Hart, "Impact Damage Tolerance of Carbon Fibre and Hybrid Laminates," ROYAL AIRCRAFT ESTABLISHMENT FARNBOROUGH (ENGLAND)1987.
- [105] N. Takeda, R. L. Sierakowski, and L. E. Malvern, "Microscopic observations of cross sections of impacted composite laminates," *Journal of Composites, Technology and Research*, vol. 4, no. 2, pp. 40-44, 1982.
- [106] S. P. Joshi and C. T. Sun, "Impact induced fracture in a laminated composite," *Journal of Composite Materials*, vol. 19, no. 1, pp. 51-66, 1985.
- [107] A. C. Garg, "Delamination—a damage mode in composite structures," *Engineering Fracture Mechanics*, vol. 29, no. 5, pp. 557-584, 1988.
- [108] J. C. Dendis and V. Captain, "DAMAGE INITIATION IN TWO-DIMENSIONAL, WOVEN, CARBON-CARBON COMPOSITES," Master of Science in Aeronautical Engineering School of Engineering of Air Force Institute of Technology Air University AD-A202 617, 1988.
- [109] L. Asp, S. J. Ouml, A. gren, and E. Greenhalgh, "Delamination Growth and Thresholds in a Carbon/Epoxy Composite Under Fatigue Loading," 2001.
- [110] L. J. Broutman and A. Rotem, "Impact strength and toughness of fiber composite materials," in *Foreign object impact damage to composites*: ASTM International, 1975.
- [111] A. Todoroki, K. Suzuki, Y. Mizutani, and R. Matsuzaki, "Durability Estimates of Copper Plated Electrodes for Self-sensing CFRP Composites," *Journal of Solid Mechanics and Materials Engineering*, vol. 4, no. 6, pp. 610-620, 2010.
- [112] A. Todoroki, M. Ueda, and Y. Hirano, "Strain and Damage Monitoring of CFRP Laminates by Means of Electrical Resistance Measurement," *Journal of Solid Mechanics and Materials Engineering*, vol. 1, no. 8, pp. 947-974, 2007.
- [113] M. X. Xu, W. G. Liu, Z. X. Gao, L. P. Fang, and K. D. Yao, "Correlation of change in electrical resistance with strain of carbon fiber-reinforced plastic in tension," *Journal of Applied Polymer Science*, vol. 60, no. 10, pp. 1595-1599, 1996.
- [114] M. X. Xu, W. G. Liu, Z. X. Gao, L. P. Fang, and K. D. Yao, "Correlation of change in electrical resistance with strain of carbon fiber-reinforced plastic in tension," *Journal of applied polymer science*, vol. 60, no. 10, pp. 1595-1599, 1996.
- [115] "<Wang, Chung - 1997 - Sensing delamination in a carbon fiber polymer - matrix composite during fatigue by electrical resistance measureme.pdf>."
- [116] H. Wittich, K. Schulte, M. Kupke, H. Kliem, and W. Bauhofer, "The measurement of electrical properties of CFRP for damage detection and strain recording," *Proc. 2. ECCM-CTS, Hamburg*, pp. 447-457, 1994.
- [117] L. Hou and S. A. Hayes, "A resistance-based damage location sensor for carbon-fibre composites," *Smart Materials and Structures*, vol. 11, no. 6, p. 966, 2002.

- [118] J. Qiu, F. Li, and S. Abbas, "A Review on SHM Techniques and Current Challenges for Characteristic Investigation of Damage in Composite Material Components of Aviation Industry," *Materials Performance and Characterization*, vol. 7, no. 1, 2018.
- [119] A. Ciliberto *et al.*, "Porosity detection in composite aeronautical structures," *Infrared Physics & Technology*, vol. 43, no. 3, pp. 139-143, 2002/06/01/ 2002.
- [120] D. Balageas *et al.*, "Thermal (IR) and Other NDT Techniques for Improved Material Inspection," *Journal of Nondestructive Evaluation*, vol. 35, no. 1, p. 18, 2016/01/19 2016.
- [121] C. P. Hiremath, K. Senthilnathan, N. K. Naik, A. Guha, and A. Tewari, "Microstructural damage based modeling of thermal conductivity of cyclically loaded CFRP," *Composites Science and Technology*, vol. 154, pp. 37-44, 2018/01/18/ 2018.
- [122] M. Naebe, M. M. Abolhasani, H. Khayyam, A. Amini, and B. Fox, "Crack Damage in Polymers and Composites: A Review," *Polymer Reviews*, vol. 56, no. 1, pp. 31-69, 2016/01/02 2016.
- [123] T. J. Ahmed, G. F. Nino, H. E. N. Bersee, and A. Beukers, "Heat emitting layers for enhancing NDE of composite structures," *Composites Part A: Applied Science and Manufacturing*, vol. 39, no. 6, pp. 1025-1036, 2008.
- [124] I. De Baere, W. Van Paepegem, and J. Degrieck, "The use of rivets for electrical resistance measurement on carbon fibre-reinforced thermoplastics," *Smart Materials and Structures*, vol. 16, no. 5, pp. 1821-1828, 2007.
- [125] D. Bates, G. Smith, D. Lu, and J. Hewitt, "Rapid thermal non-destructive testing of aircraft components," *Composites Part B: Engineering*, vol. 31, no. 3, pp. 175-185, 2000/04/01/ 2000.
- [126] N. P. Avdelidis, D. P. Almond, A. Dobbinson, B. C. Hawtin, C. Ibarra-Castanedo, and X. Maldague, "Aircraft composites assessment by means of transient thermal NDT," *Progress in Aerospace Sciences*, vol. 40, no. 3, pp. 143-162, 2004.
- [127] P.-y. Hung, K.-t. Lau, L.-k. Cheng, J. Leng, and D. Hui, "Impact response of hybrid carbon/glass fibre reinforced polymer composites designed for engineering applications," *Composites Part B: Engineering*, vol. 133, pp. 86-90, 2018/01/15/ 2018.
- [128] I. G. Scott and C. M. Scala, "A review of non-destructive testing of composite materials," *NDT international*, vol. 15, no. 2, pp. 75-86, 1982.
- [129] P. E. Irving and C. Thiagarajan, "Fatigue damage characterization in carbon fibre composite materials using an electrical potential technique," *Smart Materials and Structures*, vol. 7, no. 4, p. 456, 1998.
- [130] O. Ceysson, M. Salvia, and L. Vincent, "Damage mechanisms characterisation of carbon fibre/epoxy composite laminates by both electrical resistance measurements and acoustic emission analysis," *Scripta Materialia*, vol. 34, no. 8, pp. 1273-1280, 4/15/ 1996.
- [131] J. P. McCrory *et al.*, "Damage classification in carbon fibre composites using acoustic emission: A comparison of three techniques," *Composites Part B: Engineering*, vol. 68, pp. 424-430, 2015/01/01/ 2015.
- [132] P. W. R. Beaumont and C. Soutis, "Structural integrity of engineering composite materials: a cracking good yarn," *Philosophical transactions*.

- Series A, Mathematical, physical, and engineering sciences*, vol. 374, no. 2071, p. 20160057, 03/02/accepted 2016.
- [133] M. Ourak, B. Nongaillard, J. M. Rouvaen, and M. Ouaftouh, "Ultrasonic spectroscopy of composite materials," *NDT & E International*, vol. 24, no. 1, pp. 21-28, 1991.
- [134] D. Crivelli *et al.*, "Localisation and identification of fatigue matrix cracking and delamination in a carbon fibre panel by acoustic emission," *Composites Part B: Engineering*, vol. 74, pp. 1-12, 2015/06/01/ 2015.
- [135] V. Carvelli, A. D'Ettorre, and S. V. Lomov, "Acoustic emission and damage mode correlation in textile reinforced PPS composites," *Composite Structures*, vol. 163, pp. 399-409, 2017/03/01/ 2017.
- [136] W. Roundi, A. El Mahi, A. El Gharad, and J.-L. Rebiere, "Acoustic emission monitoring of damage progression in Glass/Epoxy composites during static and fatigue tensile tests," *Applied Acoustics*, vol. 132, pp. 124-134, 2018/03/01/ 2018.
- [137] A. Vary, "The Acousto-Ultrasonic Approach," in *Acousto-Ultrasonics: Theory and Application*, J. C. Duke, Ed. Boston, MA: Springer US, 1988, pp. 1-21.
- [138] B. F. Sørensen *et al.*, "Fundamentals for remote structural health monitoring of wind turbine blades-a preproject," 2002.
- [139] R. M. Crane, A. B. Macander, and J. Gagorik, "Fiber optics for a damage assessment system for fiber reinforced plastic composite structures," in *Review of Progress in Quantitative Nondestructive Evaluation*: Springer, 1983, pp. 1419-1430.
- [140] G. Zhou and L. Sim, "Damage detection and assessment in fibre-reinforced composite structures with embedded fibre optic sensors-review," *Smart Materials and Structures*, vol. 11, no. 6, p. 925, 2002.
- [141] S. Wang, D. D. L. Chung, and J. H. Chung, "Impact damage of carbon fiber polymer-matrix composites, studied by electrical resistance measurement," *Composites Part A: Applied Science and Manufacturing*, vol. 36, no. 12, pp. 1707-1715, 2005.
- [142] G. F. Fernando, "Fibre optic sensor systems for monitoring composite structures," *Reinforced Plastics*, vol. 49, no. 11, pp. 41-49, 2005/12/01/ 2005.
- [143] G. P. Carman and G. P. Sendekyj, "Review of the mechanics of embedded optical sensors," *Journal of Composites, Technology and Research*, vol. 17, no. 3, pp. 183-193, 1995.
- [144] T. Liu, M. Wu, Y. Rao, D. A. Jackson, and G. F. Fernando, "A multiplexed optical fibre-based extrinsic Fabry-Perot sensor system for in-situ strain monitoring in composites," *Smart Materials and Structures*, vol. 7, no. 4, p. 550, 1998.
- [145] T. Liu, G. F. Fernando, L. Zhang, I. Bennion, Y.-J. Rao, and D. A. Jackson, "Simultaneous strain and temperature measurement using an integrated fiber Bragg grating/extrinsic Fabry-Perot sensor," vol. 3330, pp. 324-332: International Society for Optics and Photonics.
- [146] C.-C. Chang and J. S. Sirkis, "Optical fiber sensors embedded in composite panels for impact detection," in *Smart Structures and Materials '95*, 1995, vol. 2444, p. 12: SPIE.

- [147] P. M. Schindler, R. G. May, R. O. Claus, and J. K. Shaw, "Location of impacts on composite panels by embedded fiber optic sensors and neural network processing," in *Smart Structures and Materials '95*, 1995, vol. 2444, p. 9: SPIE.
- [148] E. Oromiehie, B. G. Prusty, P. Compston, and G. Rajan, "Characterization of process-induced defects in automated fiber placement manufacturing of composites using fiber Bragg grating sensors," *Structural Health Monitoring*, vol. 17, no. 1, pp. 108-117, 2018.
- [149] P. Shrestha, Y. Park, and C.-G. Kim, "Low velocity impact localization on composite wing structure using error outlier based algorithm and FBG sensors," *Composites Part B: Engineering*, vol. 116, pp. 298-312, 2017/05/01/ 2017.
- [150] M. Mira and S. Gopalakrishnan, "Guided wave based structural health monitoring: A review," *Smart Materials and Structures*, vol. 25, no. 5, p. 053001, 2016.
- [151] P. J. Schubel, R. J. Crossley, E. K. G. Boateng, and J. R. Hutchinson, "Review of structural health and cure monitoring techniques for large wind turbine blades," *Renewable Energy*, vol. 51, no. Supplement C, pp. 113-123, 2013/03/01/ 2013.
- [152] J. S. Leng and A. Asundi, "Real-time cure monitoring of smart composite materials using extrinsic Fabry-Perot interferometer and fiber Bragg grating sensors," *Smart materials and structures*, vol. 11, no. 2, p. 249, 2002.
- [153] E. Hecht, "Optics 4th edition, vol. 1," ed: Addison Wesley, 2001.
- [154] M. LeBlanc and R. M. Measures, "Impact damage assessment in composite materials with embedded fibre-optic sensors," *Composites Engineering*, vol. 2, no. 5, pp. 573-596, 1992/01/01/ 1992.
- [155] J. C. Abry, Y. K. Choi, A. Chateauminois, B. Dalloz, G. Giraud, and M. Salvia, "In-situ monitoring of damage in CFRP laminates by means of AC and DC measurements," *Composites Science and Technology*, vol. 61, no. 6, pp. 855-864, 5// 2001.
- [156] O. Pirgon, G. H. Wostenholm, and B. Yates, "Thermal expansion at elevated temperatures IV. Carbon-fibre composites," *Journal of Physics D: Applied Physics*, vol. 6, no. 3, p. 309, 1973.
- [157] U. Escher, "Thermal expansion of epoxy resins with different cross-link densities at low temperatures," *Cryogenics*, vol. 35, no. 11, pp. 775-778, 1995/11/01/ 1995.
- [158] K. Schulte and C. Baron, "Load and failure analyses of CFRP laminates by means of electrical resistivity measurements," *Composites Science and Technology*, vol. 36, no. 1, pp. 63-76, 1989/01/01 1989.
- [159] J. C. Abry, S. Bochard, A. Chateauminois, M. Salvia, and G. Giraud, "In situ detection of damage in CFRP laminates by electrical resistance measurements," *Composites Science and Technology*, vol. 59, no. 6, pp. 925-935, 5// 1999.
- [160] M. Kemp, "Self-sensing composites for smart damage detection using electrical properties," in *Second European Conference on Smart Structures and Materials*, 1994, vol. 2361, pp. 136-140: International Society for Optics and Photonics.
- [161] A. Todoroki, K. Omagari, Y. Shimamura, and H. Kobayashi, "Matrix crack detection of CFRP using electrical resistance change with integrated surface

- probes," *Composites Science and Technology*, vol. 66, no. 11, pp. 1539-1545, 2006/09/01/ 2006.
- [162] D. Kranbuehl et al., "Use of in-situ dielectric sensing for intelligent processing and health monitoring," vol. 2779, pp. 112-118: International Society for Optics and Photonics.
- [163] M. Kahali Moghaddam et al., "Design, fabrication and embedding of microscale interdigital sensors for real-time cure monitoring during composite manufacturing," *Sensors and Actuators A: Physical*, vol. 243, pp. 123-133, 2016/06/01/ 2016.
- [164] F. Pegorin, K. Pingkarawat, and A. P. Mouritz, "Electrical-based delamination crack monitoring in composites using z-pins," *Composites Part A: Applied Science and Manufacturing*, vol. 104, pp. 120-128, 2018/01/01/ 2018.
- [165] T. J. Swait, F. R. Jones, and S. A. Hayes, "A practical structural health monitoring system for carbon fibre reinforced composite based on electrical resistance," *Composites Science and Technology*, vol. 72, no. 13, pp. 1515-1523, 2012.
- [166] R. J. Hart and O. I. Zhupanska, "Influence of low-velocity impact-induced delamination on electrical resistance in carbon fiber-reinforced composite laminates," *Journal of Composite Materials*, p. 0021998318776361, 2018.
- [167] D.-C. Seo and J.-J. Lee, "Damage detection of CFRP laminates using electrical resistance measurement and neural network," *Composite Structures*, vol. 47, no. 1, pp. 525-530, 1999/12/01/ 1999.
- [168] A. S. Kaddour, F. A. R. Al-Salehi, S. T. S. Al-Hassani, and M. J. Hinton, "Electrical resistance measurement technique for detecting failure in CFRP materials at high strain rates," *Composites Science and Technology*, vol. 51, no. 3, pp. 377-385, 1994/01/01 1994.
- [169] S. Wang and D. D. L. Chung, "Self-sensing of flexural strain and damage in carbon fiber polymer-matrix composite by electrical resistance measurement," *Carbon*, vol. 44, no. 13, pp. 2739-2751, 2006/11/01/ 2006.
- [170] A. Todoroki, Y. Shimazu, Y. Mizutani, and R. Matsuzaki, "Using Electrical Resistance Change to Monitor the Damage in a Thick CFRP Plate Caused by a Dent," *Journal of Solid Mechanics and Materials Engineering*, vol. 5, no. 1, pp. 44-53, 2011.
- [171] M. Zappalorto, F. Panozzo, P. A. Carraro, and M. Quaresimin, "Electrical response of a laminate with a delamination: modelling and experiments," *Composites Science and Technology*, vol. 143, pp. 31-45, 2017/05/03/ 2017.
- [172] J. Gadomski and P. Pyrzanowski, "Experimental investigation of fatigue destruction of CFRP using the electrical resistance change method," *Measurement*, vol. 87, pp. 236-245, 2016/06/01/ 2016.
- [173] D.-J. Kwon, P.-S. Shin, J.-H. Kim, Z.-J. Wang, K. L. DeVries, and J.-M. Park, "Detection of damage in cylindrical parts of carbon fiber/epoxy composites using electrical resistance (ER) measurements," *Composites Part B: Engineering*, vol. 99, pp. 528-532, 2016/08/15/ 2016.
- [174] N. Angelidis, C. Y. Wei, and P. E. Irving, "The electrical resistance response of continuous carbon fibre composite laminates to mechanical strain," *Composites Part A: Applied Science and Manufacturing*, vol. 35, no. 10, pp. 1135-1147, 2004.

- [175] A. Todoroki, Y. Samejima, Y. Hirano, and R. Matsuzaki, "Piezoresistivity of unidirectional carbon/epoxy composites for multiaxial loading," *Composites Science and Technology*, vol. 69, no. 11-12, pp. 1841-1846, 2009.
- [176] Y. V. Nazarov, "Generalized Ohm's law," in *Quantum Dynamics of Submicron Structures*: Springer, 1995, pp. 687-704.
- [177] M. B. Heaney, "Electrical conductivity and resistivity," *The measurement, instrumentation and sensors handbook*, pp. 1332-1345, 2000.
- [178] H. C. Montgomery, "Method for Measuring Electrical Resistivity of Anisotropic Materials," *Journal of Applied Physics*, vol. 42, no. 7, pp. 2971-2975, 1971.
- [179] B. F. Logan, S. O. Rice, and R. F. Wick, "Series for Computing Current Flow in a Rectangular Block," *Journal of Applied Physics*, vol. 42, no. 7, pp. 2975-2980, 1971.
- [180] S. Wang and D. D. L. Chung, "Piezoresistivity in continuous carbon fiber polymer-matrix composite," *Polymer Composites*, vol. 21, no. 1, pp. 13-19, 2000.
- [181] P. Jae Beom, O. Tomonaga, and T. Nobuo, "New concept for modeling the electromechanical behavior of unidirectional carbon-fiber-reinforced plastic under tensile loading," *Smart Materials and Structures*, vol. 12, no. 1, p. 105, 2003.
- [182] Z. Xia, T. Okabe, J. B. Park, W. A. Curtin, and N. Takeda, "Quantitative damage detection in CFRP composites," *Composites Science and Technology*, vol. 63, no. 10, pp. 1411-1422, 2003.
- [183] V. Antonucci *et al.*, "Resin flow monitoring in resin film infusion process," *Journal of Materials Processing Technology*, vol. 143-144, pp. 687-692, 2003.
- [184] M. Danisman, G. Tuncol, A. Kaynar, and E. M. Sozer, "Monitoring of resin flow in the resin transfer molding (RTM) process using point-voltage sensors," *Composites Science and Technology*, vol. 67, no. 3-4, pp. 367-379, 2007.
- [185] R. Matsuzaki, S. Kobayashi, A. Todoroki, and Y. Mizutani, "Full-field monitoring of resin flow using an area-sensor array in a VaRTM process," *Composites Part A: Applied Science and Manufacturing*, vol. 42, no. 5, pp. 550-559, 2011.
- [186] N. Angelidis and P. E. Irving, "Detection of impact damage in CFRP laminates by means of electrical potential techniques," *Composites Science and Technology*, vol. 67, no. 3-4, pp. 594-604, 2007.
- [187] Y. Suzuki, A. Todoroki, Y. Mizutani, and R. Matsuzaki, "Impact Damage Detection in CFRP Using Statistical Analysis of Resistance-Temperature Characteristics," *Journal of Solid Mechanics and Materials Engineering*, vol. 5, no. 1, pp. 33-43, 2011.
- [188] A. Todoroki and J. Yoshida, "Electrical Resistance Change of Unidirectional CFRP Due to Applied Load," *JSME International Journal Series A Solid Mechanics and Material Engineering*, vol. 47, no. 3, pp. 357-364, 2004.
- [189] N. Angelidis, "Damage Sensing in CFRP Composites Using Electrical Potential Techniques," Doctor of Philosophy School of Industrial and Manufacturing Science Cranfield University 2003-2004.
- [190] D. D. L. Chung, "Continuous carbon fiber polymer-matrix composites and their joints, studied by electrical measurements," *Polymer Composites*, vol. 22, no. 2, pp. 250-270, 2001.

- [191] S. Wang and D. D. L. Chung, "Apparent negative electrical resistance in carbon fiber composites," *Composites Part B: Engineering*, vol. 30, no. 6, pp. 579-590, 9// 1999.
- [192] I. De Baere, W. Van Paepegem, and J. Degrieck, "Electrical resistance measurement for in situ monitoring of fatigue of carbon fabric composites," *International Journal of Fatigue*, vol. 32, no. 1, pp. 197-207, 2010.
- [193] P. Conor and C. Owston, "Electrical resistance of single carbon fibres," 1969.
- [194] C. Owston, "Electrical properties of single carbon fibres," *Journal of Physics D: Applied Physics*, vol. 3, no. 11, p. 1615, 1970.
- [195] B. Berg, B. v. Hofsten, and G. Pettersson, "Electronmicroscopic observations on the degradation of cellulose fibres by *Cellvibrio fulvus* and *Sporocytophaga myxococcoides*," *Journal of Applied Bacteriology*, vol. 35, no. 2, pp. 215-219, 1972.
- [196] X. Wang and D. Chung, "Continuous carbon fibre epoxy-matrix composite as a sensor of its own strain," *Smart materials and structures*, vol. 5, no. 6, p. 796, 1996.
- [197] P. Irving and C. Thiagarajan, "Fatigue damage characterization in carbon fibre composite materials using an electrical potential technique," *Smart materials and structures*, vol. 7, no. 4, p. 456, 1998.
- [198] I. L. Spain, "Electronic Transport-Properties Of Graphite, Carbons, And Related Materials," *Chemistry and physics of carbon*, vol. 16, pp. 119-304, 1981.
- [199] I. Spain, K. Volin, H. Goldberg, and I. Kalnin, "Electronic properties of pan-based carbon fibers—I: Experiment and comparison with properties of bulk carbons," *Journal of Physics and Chemistry of Solids*, vol. 44, no. 8, pp. 839-849, 1983.
- [200] K.-T. Hsiao and D. Heider, "Vacuum assisted resin transfer molding (VARTM) in polymer matrix composites," in *Manufacturing Techniques for Polymer Matrix Composites (PMCs)*: Elsevier, 2012, pp. 310-347.
- [201] M. W. Jawitz, *Printed circuit board materials handbook (electronic packaging and interconnection)*. McGraw-Hill, New York, 1997.
- [202] R. Delasi and J. B. Whiteside, "Effect of moisture on epoxy resins and composites," in *Advanced Composite Materials—Environmental Effects*: ASTM International, 1978.
- [203] B. Yang, V. Kozey, S. Adanur, and S. Kumar, "Bending, compression, and shear behavior of woven glass fiber–epoxy composites," *Composites Part B: Engineering*, vol. 31, no. 8, pp. 715-721, 2000/01/01/ 2000.
- [204] R. A. Naik, "Failure Analysis of Woven and Braided Fabric Reinforced Composites," *Journal of Composite Materials*, vol. 29, no. 17, pp. 2334-2363, 1995/11/01 1995.
- [205] S. Dai, P. R. Cunningham, S. Marshall, and C. Silva, "Influence of fibre architecture on the tensile, compressive and flexural behaviour of 3D woven composites," *Composites Part A: Applied Science and Manufacturing*, vol. 69, pp. 195-207, 2015/02/01/ 2015.
- [206] N. Oya and H. Hamada, "Mechanical properties and failure mechanisms of carbon fibre reinforced thermoplastic laminates," *Composites Part A: Applied Science and Manufacturing*, vol. 28, no. 9, pp. 823-832, 1997/01/01/ 1997.

- [207] T. Bru, P. Hellström, R. Gutkin, D. Ramantani, and G. Peterson, "Characterisation of the mechanical and fracture properties of a uni-weave carbon fibre/epoxy non-crimp fabric composite," *Data in Brief*, vol. 6, pp. 680-695, 2016/03/01/ 2016.
- [208] S. Composite. *VTC 401 Epoxy Component Prepreg* Available: <http://shdcomposites.com/wp-content/uploads/2016/03/VTC401-TDS.pdf>
- [209] J. Wen, Z. Xia, and F. Choy, "Damage detection of carbon fiber reinforced polymer composites via electrical resistance measurement," *Composites Part B: Engineering*, vol. 42, no. 1, pp. 77-86, 2011.

APPENDIX A

1. Tensile Test for Carbon Fibre Composite Laminates Panels

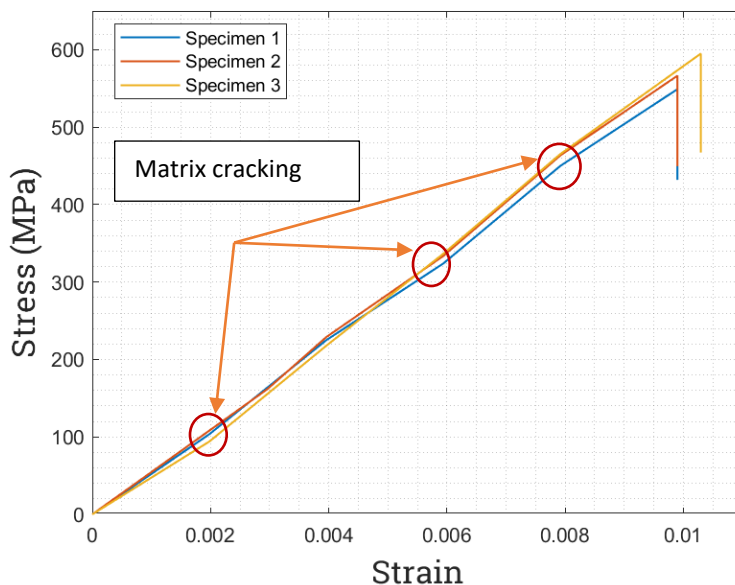


Figure A-1: Stress – Strain curve for AB panel, the average UTS = 607.33 MPa and $E = 55$ GPa. E was calculated at a strain range of 0.002 in the region between 0.002 and 0.004 for specimen 1, 0.004 and 0.006 for specimen 2, and 0.006 and 0.008 for specimen 3.

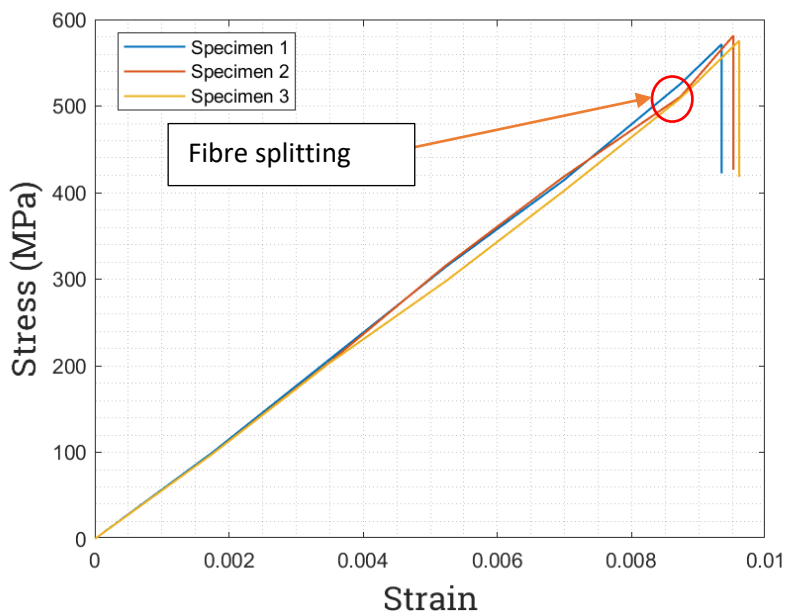


Figure A-2: Stress – Strain curve for AC panel, the average UTS = 620.6 MPa and $E = 57.744$ GPa. E was calculated at a strain range of 0.002 in the region between 0.002 and 0.004 for all the specimens.

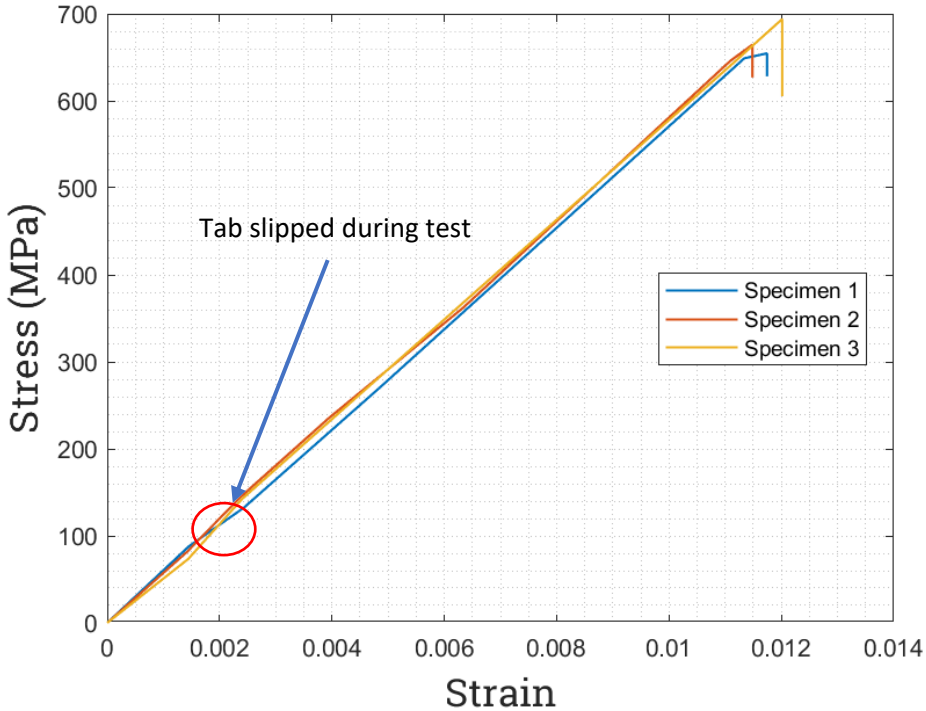


Figure A-3: Stress – Strain curve for AD panel, the average UTS = 690 MPa and E = 57.46 GPa. E was calculated at a strain range of 0.002 in the region between 0.0052 and 0.0072 for all the specimens.

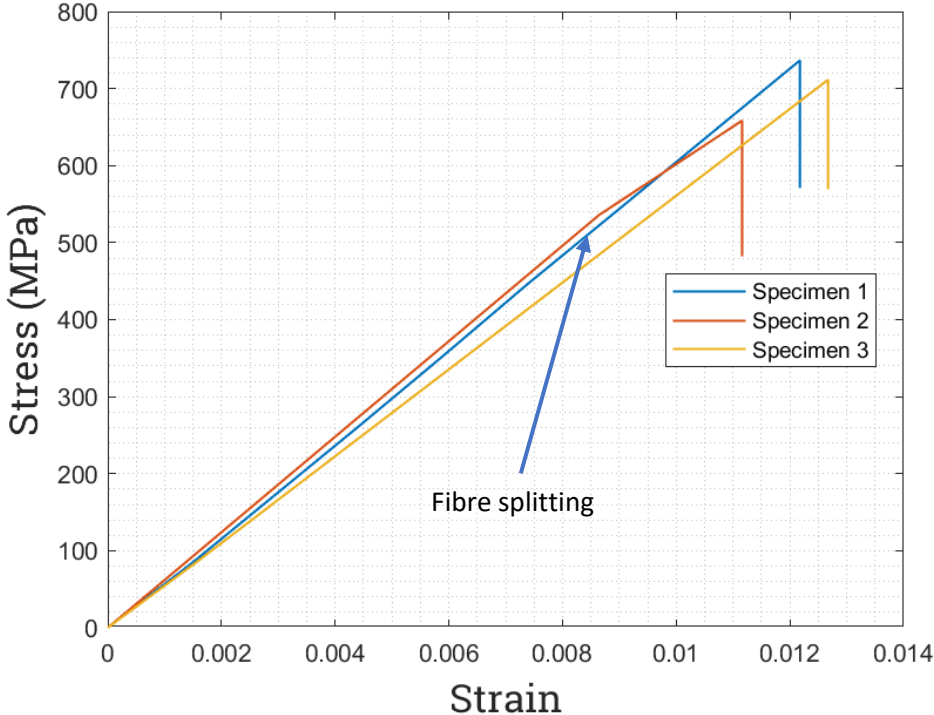


Figure A-4: Stress – Strain curve for AE panel, the average UTS = 735.5 MPa and E = 57.33 GPa. E was calculated at a strain range of 0.002 in the region between 0.002 and 0.004 for all the specimens.

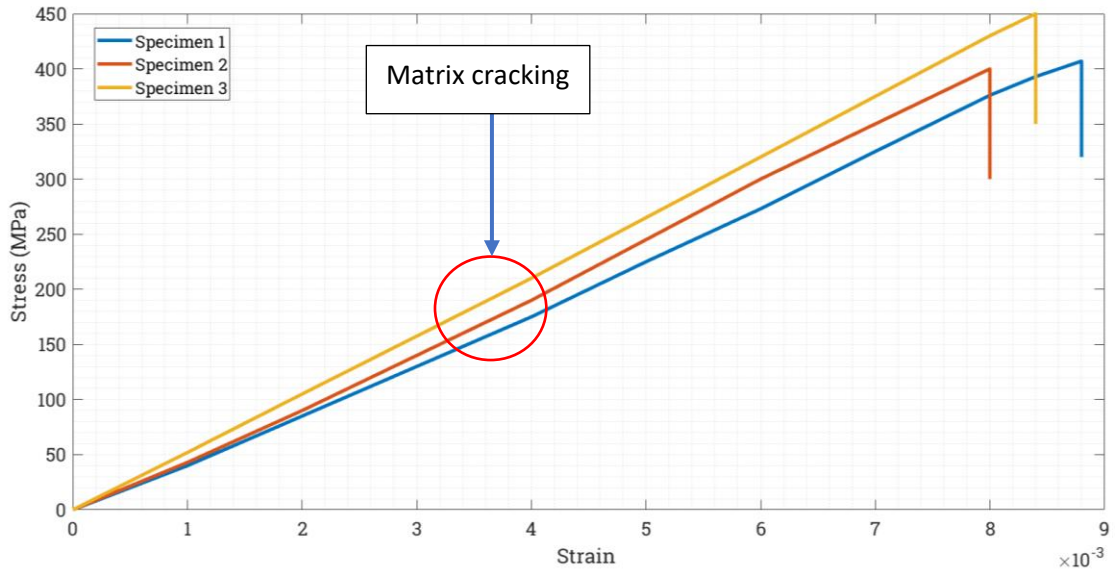


Figure A-5: Stress – Strain curve for VB panel, the average UTS = 419 MPa and $E = 53$ GPa. E was calculated at a strain range of 0.002 in the region between 0.003 and 0.005 for all specimens.

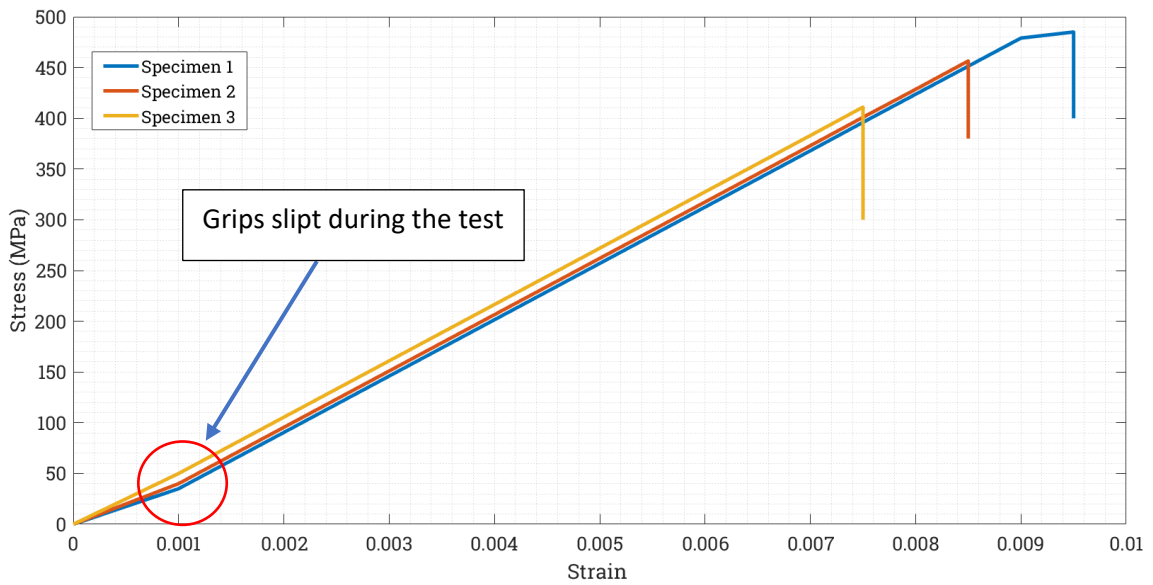


Figure A-6: Stress – Strain curve for VC panel, the average UTS = 450 MPa and $E = 55$ GPa. E was calculated at a strain range of 0.002 in the region between 0.004 and 0.006 for all the specimens.

2. Flexural Tests for Carbon Fibre Composite Laminates Panels

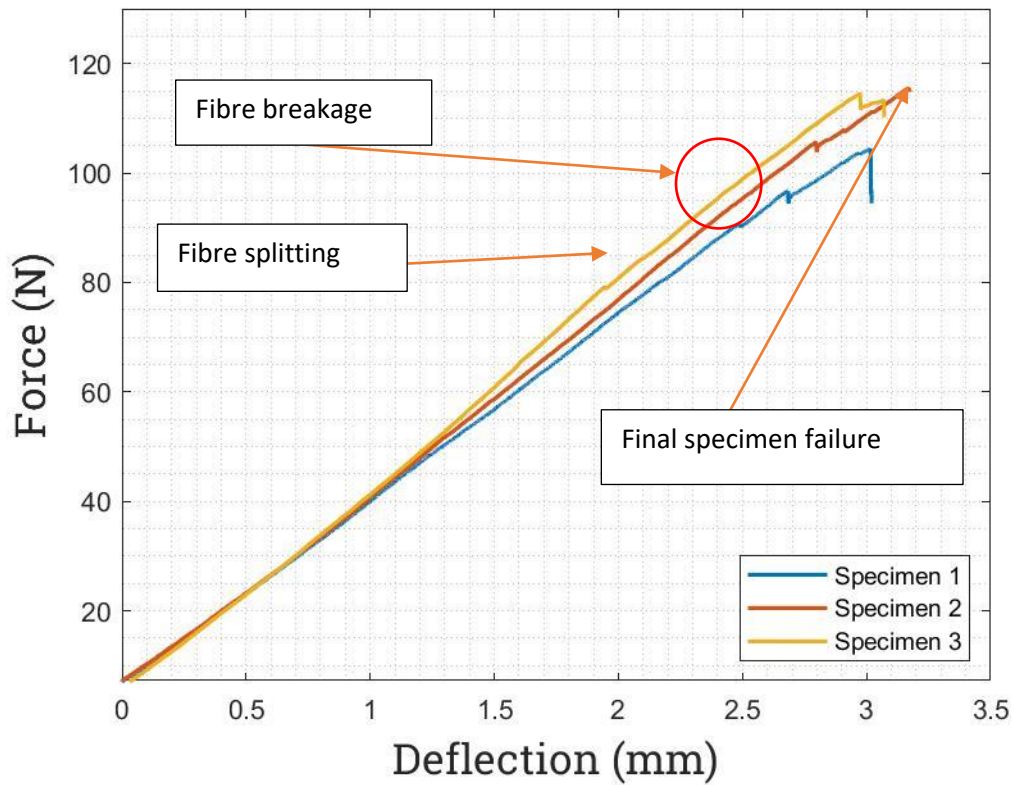


Figure A-7: Three-point bending test for AB panel. The average $\sigma_f = 790$ MPa.

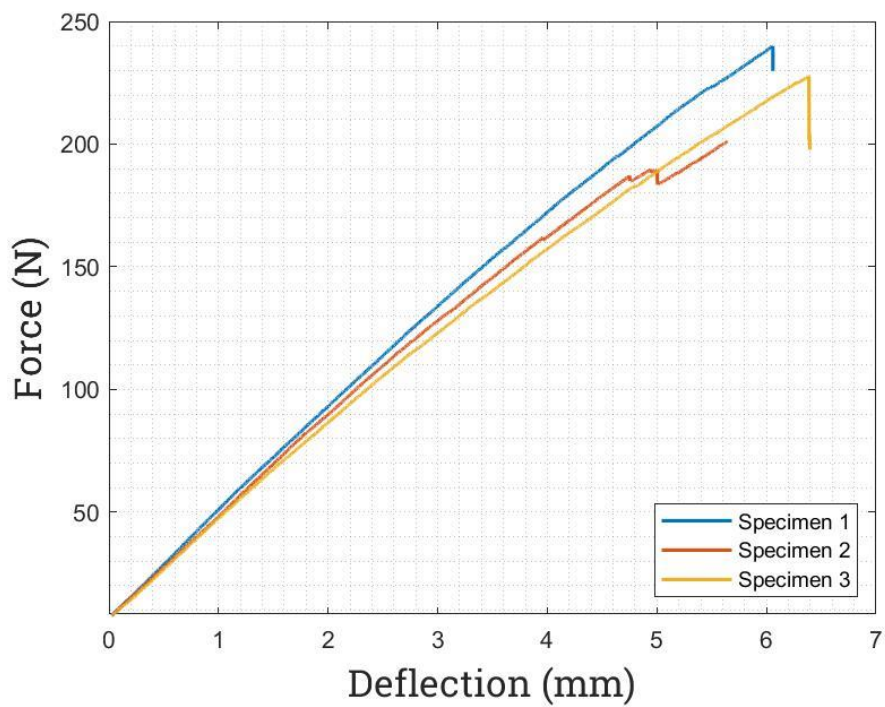


Figure A-8: Three-point flexural test for AC panel. The average $\sigma_f = 810$ MPa.

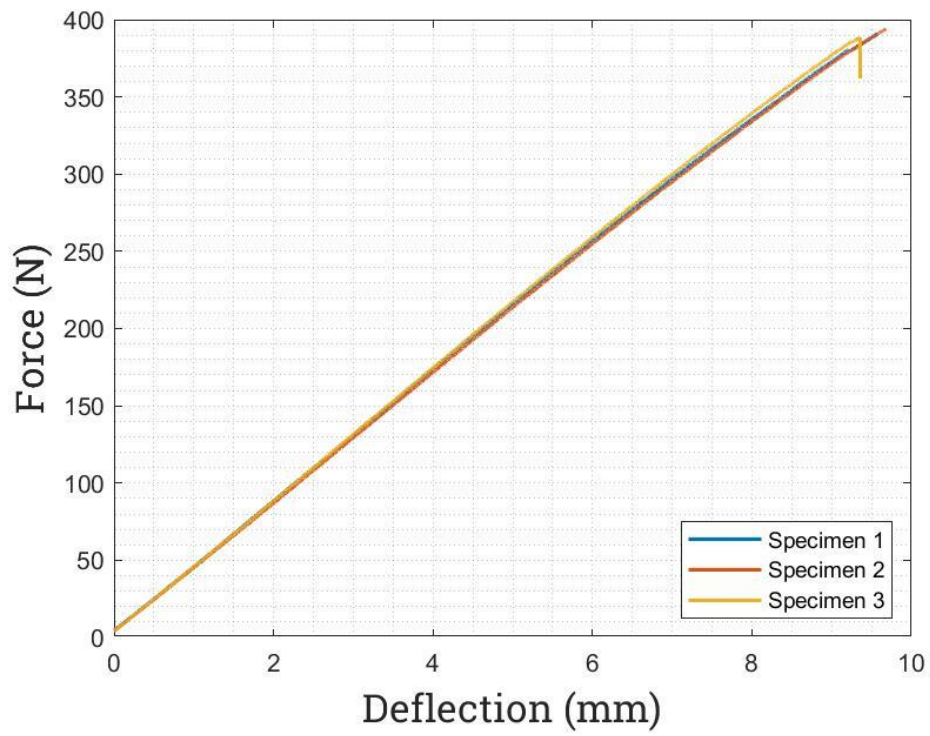


Figure A-9: Three-point flexural test for AD panel. The average $\sigma_f = 870$ MPa.

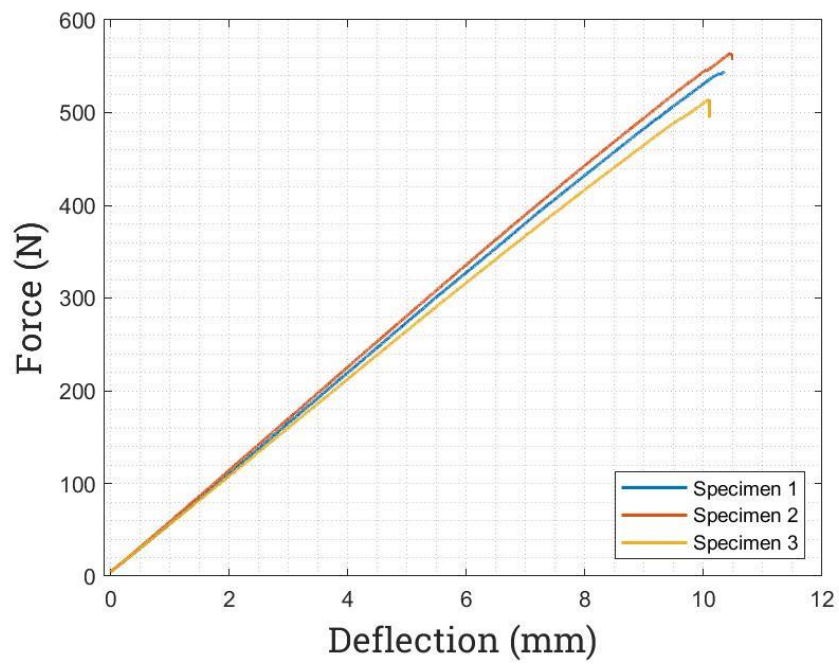


Figure A-10: Three-point flexural test for AE panel. The average $\sigma_f = 890$ MPa.

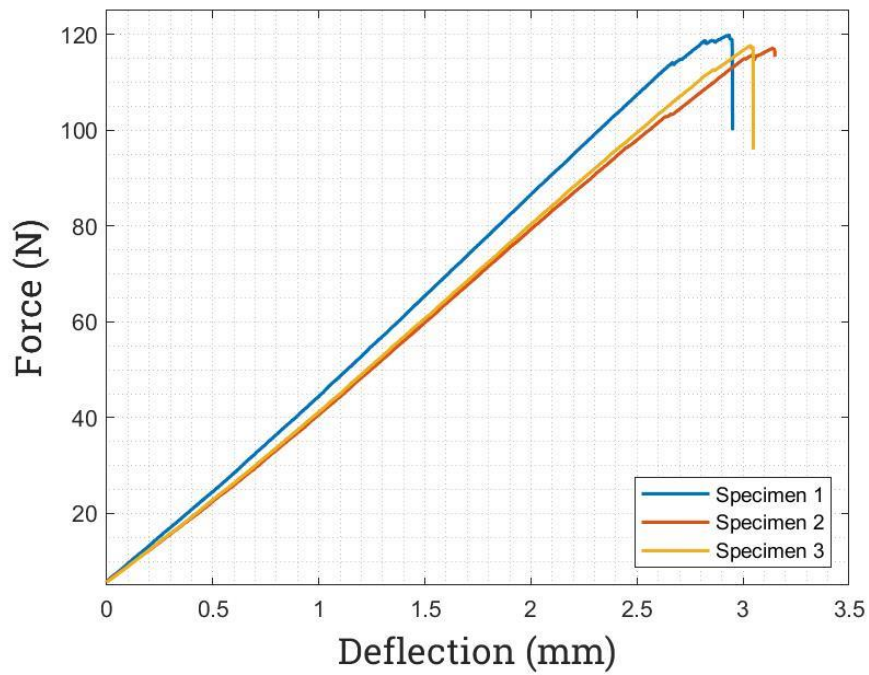


Figure A-11: Three-point flexural test for VB panel. The average $\sigma_f = 610$ MPa.

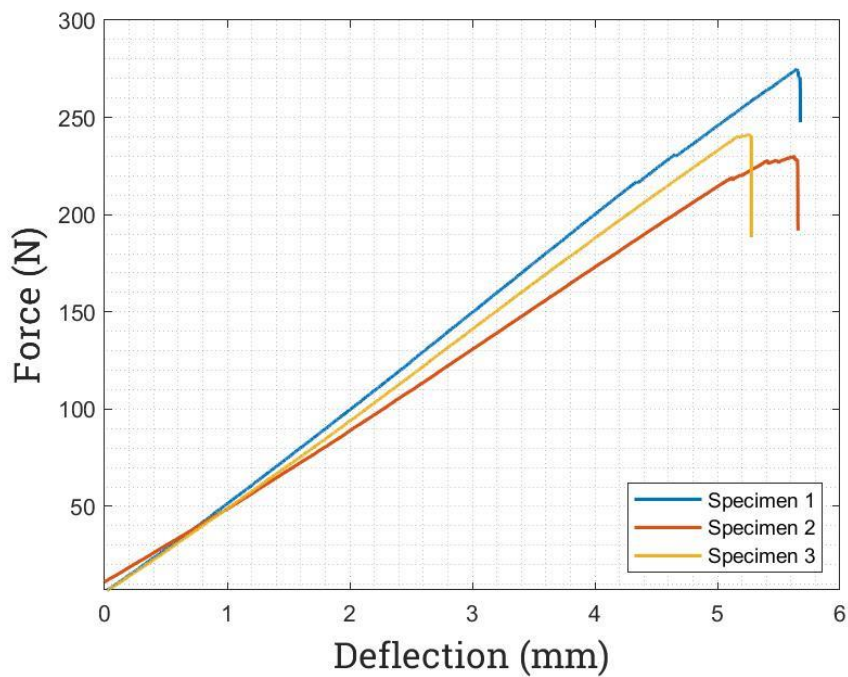


Figure A-12: Three-point flexural test for VC panel. The average $\sigma_f = 690$ MPa.

